A Comparison Study of Intermediate Frequency BL Lacs and High Frequency BL Lacs Detected by VERITAS and Fermi LAT

Anna Louise Cannon

Submitted to University College Dublin
for the degree of Ph.D. in the College of Physics

Febuary 2011

UCD School of Physics
Prof. Lorraine Hanlon

Supervised by Dr. John Quinn

Abstract

This thesis presents the comprehensive analysis and results of an extensive comparison study between two subclasses of blazars : Intermediate Frequency BL Lacs and High Frequency BL Lacs Detected by VERITAS and Fermi LAT. VERITAS (the Very Energetic Radiation Imaging Telescope Array System) is an array of four 12m telescopes, located at the Fred Lawrence Whipple Observatory in Southern Arizona and is sensitive in the energy range of 100 GeV - 30 TeV. Fermi LAT (Large Area Telescope) is a pair production satellite sensitive between 20 MeV - 300 GeV. Since the launch of Fermi LAT, there is for the first time, continuous coverage from MeV to TeV with an overlap between 100 and 300 GeV, crucial for constraining the inverse Compton peak and providing a clearer picture of the sources themselves, their environments and the processing taking place between 20 MeV and 30 TeV.

Three HBLs (1ES 0502+675,1ES 0806+524 and 1ES 1959+650) and three IBLs (W Comae, 3C66A and PKS 1424+240) were selected based on previous results and publications. Quasi-contemporaneous Fermi LAT and VERITAS data for each source were analysis and combined to look closely at spectra. The inverse Compton peak was constrained and temporal analysis was performed. Multiwavelength spectral energy distributions were constructed and fit with both a single zone synchrotron model and synchrotron-external Compton combination model.

Acknowledgements

I would first like to express my utmost gratitude to my thesis supervisor Dr. John Quinn for his constant encouragement and patience throughout the course of my PhD. To everybody in the High Energy Astrophysics group in UCD, thank you for your help and efforts in the last few months of my write up, in particular, Anna O'Faolain deBhroithe for proof-reading endless pages of my thesis (I'll return the favour when it's your turn, I promise!). I would like to mention Dr Remo Huglii for the hours of conversation on just about everything from statistics to traveling and Leonard English for the music supply, most of it good. Thank you to Professor Lorraine Hanlon, Bairbre Fox and Marian Hanson who were always so approachable and willing to help out with anything. A special cheers to Dr. John Ward for his friendship over the last four years and was answering my never-ending questions.

I wish to thank Dr Trevor Weekes for organizing my observing trips to Arizona and for being supportive. Also, thank you to Dr. Ken Gibbs who will be missed at basecamp. To Dr. Julie McEnery, thank you for the opportunity to work within the Fermi LAT collaboration and for organizing my trips to Goddard. To my good friends Arun Madhavan (co-creator of "tpg") and Dr. Sagar Godambe for making 12 hour observing shifts fun and for their advice and encouragement over the last year. Thank you to Dr. Teddy Cheung for the many, many laughs and for making my Maryland trips so entertaining.

I would also like to mention Dr. Luis Reyes, Dr. Jeff Grube, Dr. Tyrel Johnson, William McConville and Sean Griffin who were always willing to answer physics/analysis queries and help out. It was greatly appreciated.

Finally, I'd like to thank my my family and friends. To my parents for their unwavering support and encouragement, my sisters Christine (for helping me proof-read) and Mariosa (for keeping me entertained while I was writing up), my uncle Joseph and aunt Caitriona for making sure I was always fed and watered while in Dublin and my uncle John for the hours of science conversations. A special thank you to my closest friends Orla O'Neill and Susan Moore for their friendship and well-needed distractions.

For Louis

There are more things in heaven and earth, Horatio
Than are dreamt of in your philosophy.
- William Shakespeare, Hamlet

Contents

List of Figures vii

List of Tables xix

Chapter 1. Introduction 1
1.1. History of γ-ray astronomy 1
1.2. Brief Account of Satellite Experiments 1
1.3. Brief Account of Ground Based Experiments 7
1.4. Thesis Outline 10
1.5. My Contributions 11

Chapter 2. Active Galactic Nuclei 13
2.1. Introduction 13
2.2. Blazars 17
2.3. Variability 20
2.4. Relativistic Jets 21
2.5. Jet Dynamics 25
2.6. Synchrotron Radiation 27
2.7. Leptonic Models of Gamma-Ray Production 30
2.8. Hadronic Models 34
2.9. Motivation 36

Chapter 3. Cherenkov Radiation and its Detection from Extensive Air Showers 47
3.1. Cherenkov Radiation 47
3.2. Gamma-ray interactions with matter 49
3.3. Extensive Air Showers 50
3.4. Detection 51
3.5. Atmospheric Cherenkov Telescopes 52
3.6. Imaging Atmospheric Cherenkov Technique 53

Chapter 4. VERITAS and Fermi LAT Instrument Description 55
4.1. The VERITAS array 55
4.2. The Fermi LAT satellite 65

Chapter 5. Data Analysis 76
5.1. Introduction 76
5.2. VERITAS 76
5.3. Fermi LAT 94

Chapter 6. Results 107
6.1. Introduction 107
6.2. Data Analysis 107
6.3. 1ES 0502+675 109
6.4. 1ES 0806+524 119
6.5. 1ES 1959+650 130
6.6. W Comae 139
6.7. 3C66A 150
6.8. PKS 1424+240 160
6.9. Constraining the IC peak 170
6.10. SED modeling 177
6.11. GeV dip 199
6.12. Discussion 201

Chapter 7. Conclusions and Future work 206
7.1. Thesis results 206
7.2. The Future of γ-ray Blazar Science 207

Bibliography 209

Appendix A. Astronomer's Telegrams 217

List of Figures

1.1 Schematic drawing of the γ-ray detector onboard NASA's Explorer satellite, taken from Kraushaar et al.,1965. 3

1.2 The second COS-B satellite catalog sky map, displaying 25 detections of γ-ray emitting sources above 100 MeV. The filled circles denote fluxes above 1.3×10^{-6} ph cm^{-2} cm^{-1} and the open circles denote fluxes below this. This flux value is chosen to demonstrate the flux magnitude concentration in the galactic plane. The shaded region indicates unsearched areas - (Swanenberg et al., 1981) 4

1.3 Schematic diagram of EGRET's spark chamber, calorimeter and anti-coincidence shield (Thompson et al., 1993) 5

1.4 The third EGRET catalog γ-ray emission sky map, taken from (Hartman et al., 1999). The black diamonds represent AGN with the exception of Cen A, the black squares represent pulsars, the black triangle represents the Large Magellanic Cloud (LMC), the black circle represent solar flares and the open circles represent unidentified EGRET sources. 6

1.5 The Whipple 10m telescope located in Southern Arizona - (www.astro.wisc.edu/~larson/Webpage/Gamma.html) 9

1.6 A HEGRA γ-ray telescope (www.sciencephoto.com/media/322268/enlarge). 10

2.1 Illustration of an AGN, highlighting the main components of AGNs and the classification dependent on orientation (http://www.auger.org/news/PRagn/about_AGN.html). 15

2.2 AGN Classification including types 0, 1 and 2 classification (Adapted from Toner, 2008). 16

2.3 How AGN classification is influenced by viewing angle (Toner, 2008). 17

2.4 Multiwavelength SED of the blazar Markarian 421, including XMM-Newton OM (triangles), XMM-Newton EPN (filled circles), MAGIC (squares), Whipple (diamonds) and VERITAS (crosses). SSC model for 2006 data (green) and 2008 data (red) (Acciari et al., 2009). 18

2.5 From top to bottom (referring to radio luminosity) FSRQs (empty boxes), 1 Jy BL Lac sample (filled boxes) and Slew survey BL Lac sample (triangles) - (Fossati et al., 1998). 20

2.6 Radio power at 5 GHz vs. the synchrotron peak frequency for FSRQ (filled points) and BL Lacs (crosses) for the DXRBS sample. The dotted lines denote the two quadrants (top-left and bottom-right) occupied by the sources studied by Fossati et al 1998. (Padovani, 2007). 21

2.7 Whipple 10m lightcurve for Markarian 421 from May 15th 1996, binned in 4.5 minute intervals - (Gaidos et al.,1996) 22

2.8 Illustrations of Toroidal Magnetic Field Acceleration (a) and Magneto-centrifugal acceleration from the accretion disk (b), (Sauty, Tsinganos & Trussoni, 2002) 23

2.9 Illustration of superluminal motion (physicsmadeeasy.wordpress.com/physics-made-easy/cosmology-iii/). 26

2.10 The spectrum of the synchrotron radiation of a single electron with linear axes. 28

2.11 The spectrum of the synchrotron radiation of a single electron with logarithmic axes. 28

2.12 An illustration of Inverse Compton scattering of a low energy photon up to γ-ray energies (www.cv.nrao.edu). 30

2.13 Daily average Whipple 10m lightcurve for 1ES 1959+650 for May - July 2002, with rate displayed in Crab units. The dashed line corresponds to the quickest flux change, indicating a variability timescale on the order of 7 hours (Holder et al., 2003) 38

2.14 Multiwavelength SED of 1ES 1959+650 using November - December 2007 data, with the addition of 2002 HEGRA data. (Bottacini et al, 2010) 39

2.15 Lightcurve in months bins in units of integral flux about 300 GeV from 1ES 0806+524 observations. A Chi-squared probability of being constant yields a value of 0.24, indicating little to no variability (Acciari et al., 2009). 40

2.16 Broadband multiwavelength SED of 1ES 0806+524. The Swift data was taken on two separate days: grey points - 8th March 2008 and black points - 12th March 2008. The solid (March 8th) and dashed (March 12th) lines are the SSC fits to the data (Acciari et al., 2009). 41

2.17 W Comae lightcurves. Bottom panel: Integrated flux above 200 GeV. Each data point is a 3 week period of observations, except for the period of flaring around MJD 54538, which is binned nightly. Top panel: Quasi-simultaneous Swift X-ray data (Acciari et al., 2008). 42

2.18 Quasi-simultaneous multiwavelength observations SED for W Comae. The EGRET, optical and X-ray data are archival and shown in grey (Acciari et al., 2008). 43

2.19 Multiwavelength observations SED of PKS1424+240. The lines represent different SSC model fits as a function of redshift. The zoomed in area is the υF_{υ} VERITAS spectrum. The Fermi LAT upper limits correspond to TS < 25, with a 95% confidence level (Acciari et al., 2010). 44

2.20Smoothed Fermi LAT counts map for the 3C66A region, E > 100 MeV, between September 2008 and December 2008. The magenta circle represents the VERITAS 3C66A location, the blue circle corresponds to the 95% error radius of the LAT position (Abdo et al., 2011). 45

2.21Broadband 3C66A SED during the October 2008 flare. The fit is a SSC+EC model, EBL absorption corrected with a redshift of z = 0.3 (Abdo et al, 2011). 45

2.223C66A multiwavelength lightcurves for the period 22nd August 2008 to 31st December 2002, including the October 2008 flare. The dashed and dotted lines correspond to the average 2007 and 2008 data respectively. The VERITAS data is binned nightly and the Fermi LAT data is divided up into 3 day bins (Abdo et al., 2011). 46

3.1 Illustration of the electromagnetic field distortion caused by a charged particle traveling through a dielectric material. a: slow moving particle v <<c; photons destructively interfere with each other and no radiation escapes. b: relativistic particle v=βc; system is asymmetric, a dipole is created. Photons constructively interfere with each other and the radiation escapes. - (Jelley, 1959). 47

3.2 Wavefront of Cherenkov Radiation. Figure a: v<<c destructive interference, no radiation escapes. Figure b: v = c/n, zero intensity predicted. Figure c : v > βc constructive interference, radiation escapes at angle θ_c. Adapted from Zrelov,1970. 48

3.3 An illustration of a γ ray undergoing pair production to generate an electron-positron pair (www.relativitycalculator.com/energy_doppler_shtml) 49

3.4 An illustration of a γ-ray initiated shower (www.dur.ac.uk/∼dph0www4/whyare.php). 50

3.5 An illustration of a hadronic cosmic ray initiated shower (www.phy.cuhk.edu .hk/sure/comments_2011/yung_paper.html). 52

4.1 The arrangement of the VERITAS array prior to the relocation of Telescope 1 (second from the left) in August 2009 (veritas.sao.arizona.edu). 56

4.2 The arrangement of the VERITAS array post relocation of Telescope 1(second from the left) (veritas.sao.arizona.edu). 57

4.3 A comparison of VERITAS' sensitivity to the Crab Nebula before and after the relocation of Telescope 1 and the introduction of an improved mirror-alignment technique. 58

4.4 The hexagonal mirrors and camera focus box on Telescope 2 (veritas.sao.arizona.edu). 59

4.5 Lightcones placed in front of the PMTs (Nagai et al., 2007). 61

4.6 Schematic diagram of the 3 tiered trigger system and the Data Acquisition System (Weinstein et al., 2008). 62

4.7 An example of a BIAS curve used in determining the optimum CFD thresholds. The marker size facilitates error ranges (Weinstein et al., 2008) 64

4.8 Schematic diagram of the LAT (Atwood et al.,2007). 67

4.9 Illustration of the design behind the LAT's tracker, calorimeter and anti-coincidence system (http://fermi.gsfc.nasa.gov/ssc/data/analysis/documentation/Cicerone/Cicerone_Introduction/LAT_overview.html). 68

4.10The LAT ACD design.The 89 plastic scintillator tiles are arranged into an array of 5 x5 on top and 16 for each side. The tiles are overlapped in one dimension to minimize gaps and 2 sets of 4 scintillator fiber ribbons under the tiles also cover gaps (Atwood et al., 2009). 69

4.11Completed 16 module tracker array before integration with the ACD - (Atwood et al., 2009). 71

4.12Schematic diagram of the tracker design. The pair production at point (a) is an ideal conversion and at (b) the tracker can detect 2 particles and track the trajectory. Point (c) demonstrates how the tungsten foils only cover the active areas of the SSDs. At point (d) a "missed hit" is evident, detected in the second layer. The PSF has likely deteriorated significantly. Pair production in the SSD is seen at (e). This lengthens the arms for multiple scattering, multiple hits can highlight this. - (Atwood et al., 2009). 72

4.13A completed tracker module with one sidewall removed (Atwood et al.,2009). 73

4.14Schematic configuration of the LAT calorimeter module. The 96 CsI(Tl) scintillator crystals arranged in 8 layers of 12 with the crystals in adjacent layers rotated by 90° (Atwood et al., 2009). 74

4.15The hierarchal LAT Data Acquisition system (DAQ). The GASU is comprised of the AEM, the GEM, the EBM and the AEM. The TEMs are the interfaces for the tracker and calorimeter modules. At the highest level, there are two EPUs and 1 SIU for onboard data processing and instrument control (Atwood et al., 2009). 75

5.1 An FADC trace of 24 samples of 2ns each with an integration window width of 7 samples - Cogan (2006). 78

5.2 Distribution of the pedestal values recorded for a single pixel for three levels of NSB. No NSB is achieved when the focus box containing the camera closed. Cogan (2006). 79

5.3 Distribution of scaled pedvars for a singe telescope over an observing run of duration 20 minutes. 80

5.4 Distribution of relative gains for a single telescope for a single run. The red lines represent quality cuts. 81

5.5 Distribution of relative gainvars for a single telescope for a single run. The red lines represent quality cuts. 82

5.6 Distribution of T_{offset} values for a single telescope. 83

5.7 Image before cleaning (Ward, 2010) 84

5.8 Image after cleaning (Ward 2010) 85

5.9 Illustration of the Hillas Parameters (Reynolds *et al.* (1993)) 86

5.10Shower direction determination (Valcercel, 2008). 87

5.11Shower core location determination - Valcercel (2008) 88

5.12Mean Scaled Width and Length shower parameters for one run 89

5.13Illustration of the Reflected Region Model - Varcarcel (2008) 91

5.14Illustration of the Ring Background Model (Varcarcel, 2008) 92

5.15Effective collections areas as a function of energy for different zenith angles (Ward, 2010) 93

5.16A schematic diagram of the Fermi LAT simulations, calibration, data processing and high level science analysis (Atwood et al., 2009). 95

5.17Orbit spectra for various background sources. Protons: purple. He : green. electrons: red. Positrons : light blue. Earth albedo neutrons : black. Earth albedo γ rays: dark blue (Atwood et al., 2009). 98

5.18Effective Areas as a function of Energy for normal angles of incidence for the transient (dotted), source (solid) and diffuse class (dashed) (Rando et al., 2009). 100

5.19PSF at normal incidence as a function of energy (www-glast.slac.stanford.edu). 101

5.20Energy resolution at normal incidence as a function of energy (www-glast.slac.stanford.edu). 102

5.21An example of an exposure map using a 10° ROI over a 21 month time interval for the source 1ES 0502+675. 106

6.1 1ES 0502+675 VERITAS wobble theta squared plot to distinguish the source γ-ray signal above the background (red = source, blue = background). 109

6.2 VERITAS 2D significance map centered on the position of 1ES 0502+675 110

6.3 1ES 0502+675 TeV lightcurve in day-long time intervals between September 23^{rd} 2009 and January 8^{th} 2010 indicating no significant variability. 110

6.4 1ES 0502+675 TeV lightcurve in week-long time intervals (as above) indicating no significant variability. 111

6.5 1ES 0502+675 TeV dN/dE spectrum, fit well with a powerlaw. 111

6.6 Initial Fermi LAT 12° TS map before the background sources in the ROI are subtracted, centered on 1ES 0502+675 highlighting high TS sources in the ROI. 114

6.7 Fermi LAT 12° TS after background subtraction centered around 1ES 0502+675, which is also included in the background model. Note the different scales between this and the previous TS map. This is to ensure that after the bright background sources are removed it is possible to see weaker or lower TS sources clearly. 115

6.8 1ES 0502+675 Fermi LAT lightcurve binned in 2 week-long intervals does not suggest significant variability. The VERITAS observation timeline can be seen on the plot. 116

6.9 1ES 0502+675 Fermi LAT lightcurve binned in month-long intervals does suggest variability. The VERITAS observation timeline can be seen on the plot. 116

6.101ES 0502+675 Fermi LAT lightcurve binned in 3 month-long intervals, does not suggest significant variability. The VERITAS observation timeline can be seen on the plot. 117

6.111ES 0502+675 Fermi LAT 10-bin TS versus Energy, showing a peak of $\sim$ 140 TS at 10 GeV followed by a significant dip to $\sim$60 TS at 20 GeV. 117

6.121ES 0502+675 Fermi LAT 10-bin dN/dE spectrum. 118

6.131ES 0502+675 Fermi LAT 10-bin E^2 dN/dE spectrum shown with the best fit powerlaw function. The first point is an upper limit. 118

6.141ES 0806+524 VERITAS theta squared plot which shows the γ-ray signal (red) over the background signal (blue). 119

6.151ES 0806+524 VERITAS 2D significance map. The circles represent the RBM exclusion regions corresponding to the source itself and the star 27Lyn. 120

6.161ES 0806+524 TeV lightcurve binned in day intervals, between November 5^{th} 2007 and March 11^{th} 2011, suggesting no variability. 120

6.171ES 0806+524 TeV lightcurve binned in week intervals, between November 5^{th} 2007 and March 11^{th} 2011, suggesting no variability. 121

6.181ES 0806+524 TeV lightcurve binned in month intervals, between November 5^{th} 2007 and March 11^{th} 2011, suggesting no variability. 121

6.191ES 0806+524 VERITAS TeV dN/dE spectrum and best fit power law. 122

6.201ES 0806+524 12° Fermi LAT TS map before background sources in the ROI are subtracted, highlighting 6 high TS sources in the ROI. 124

6.211ES 0806+524 12° Fermi LAT TS map after background subtraction. Note the different TS scale to ensure that lower TS sources can be seen. The high TS level seen in the left corner is a extragalactic source outside the ROI. 125

6.221ES 0806+524 Fermi LAT lightcurve in 2 week-long intervals, doe not exhibit significant variability. Note the 2 quasi-contemporaneous VERITAS observations. 126

6.231ES 0806+524 Fermi LAT lightcurve in month-long intervals, showing variability. Note the 2 quasi-contemporaneous VERITAS observations. 126

6.241ES 0806+524 Fermi LAT lightcurve in 3 month-long intervals, showing significant variability. Note the 2 quasi-contemporaneous VERITAS observations. 127

6.251ES 0806+524 Fermi LAT TS versus energy in 10 bins. 127

6.261ES 0806+524 Fermi LAT dN/dE spectrum in 10 bins. 128

6.271ES 0806+524 Fermi LAT E^2 dN/dE in 10 bins fit with a powerlaw function. 128

6.281ES 0806+524 E^2dN/dE low-state spectrum of index of -1.92 ± 0.06 with an integral flux (E > 300 MeV) of (7.45 ± 0.62) $\times 10^{-9}$ ph cm^{-2} s^{-1}. 129

6.291ES 0806+524 E^2dN/dE high-state spectrum of index -1.85 ± 0.05 with an integral flux (E > 300 MeV) of (1.56 ± 0.11) $\times 10^{-8}$ ph cm^{-2} s^{-1}. 129

6.301ES 1959+650 VERITAS θ^2 plot showing the signal (red) above the background (blue) 130

6.311ES 1959+650 VERITAS 2D significance map 131

6.321ES 1959+650 TeV Lightcurve in daily intervals, between September 10^{10} 2007 and December 4^{th} 2010. No significant variability is seen. 131

6.331ES 1959+650 TeV Lightcurve in weekly intervals, between September 10^{10} 2007 and December 4^{th} 2010. No significant variability is seen. 132

6.341ES 1959+650 TeV Lightcurve in month intervals, between September 10^{10} 2007 and December 4^{th} 2010. No significant variability is seen. 132

6.351ES 1959+650 VERITAS dN/dE powerlaw spectrum 133

6.361ES 1959+650 Fermi LAT 12° TS map before background sources in the ROI are subtracted highlighting four high TS sources in the ROI 135

6.371ES 1959+650 Fermi LAT 12° TS map after background subtraction. Note the different TS scale. A lower TS scale is required to ensure the lower TS sources in the ROI are seen clearly. 136

6.381ES 1959+650 in 2 week-long bins, showing extreme variability. Note the 2 contemporaneous VERITAS observations. 137

6.391ES 1959+650 in month-long bins. The probability and χ^2/n.d.f values suggest significant variability. Note the 2 contemporaneous VERITAS observations. 137

6.401ES 1959+650 Fermi LAT TS versus energy in 10 bins. 138

6.411ES 1959+650 Fermi LAT dN/dE spectrum in 10 bins. 138

6.421ES 1959+650 Fermi LAT E^2 dN/dE spectrum in 10 bins. 139

6.43W Comae VERITAS θ^2 plot (red = source, blue = blackground). 140

6.44VERITAS 2D significance map showing both W Comae (centre) and 1ES 1218+30.4 (top). 140

6.45W Comae TeV dN/dE spectrum 141

6.46W Comae TeV lightcurve in daily intervals, between January 10^{th} 2008 and April 1^{st} 2011, does not exhibit significant variability. 142

6.47W Comae TeV lightcurve in weekly intervals, between January 10^{th} 2008 and April 1^{st} 2011, demonstrates variability. 142

6.48W Comae TeV lightcurve in monthly intervals, between January 10^{th} 2008 and April 1^{st} 2011, demonstrates variability. 143

6.49Fermi LAT, W Comae 12° TS map before background sources in the ROI are subtracted, highlighting 2 high TS sources in the ROI. 145

6.50Fermi LAT, W Comae 12° TS map after background subtraction. Note the different TS scale. A lower TS scale is required to ensure the lower TS sources in the ROI are seen clearly. 146

6.51W Comae Fermi LAT 2 week-interval lightcurve, showing variability. VERITAS observations are contemporaneous throughout the entire dataset. 147

6.52W Comae Fermi LAT monthly lightcurve showing variability detected. VERITAS observations are contemporaneous throughout the entire dataset. 147

6.53W Comae Fermi LAT 3 month-long interval lightcurve showing no variability. VERITAS observations are contemporaneous throughout the entire dataset. 148

6.54W Comae Fermi LAT TS as a function of energy in 10 bins. 148

6.55W Comae Fermi LAT dN/dE spectrum in 10 bins. 149

6.56W Comae Fermi LAT E ^{2} dN/dE spectrum in 10 bins, fit best by a log parabolic curve. 149

6.573C66A VERITAS θ^2 plot (red = source, blue = background). 150

6.583C66A VERITAS 2D significance map. 151

6.593C66A TeV lightcurve binned in daily intervals timescales, does not suggest variability. 151

6.603C66A TeV lightcurve binned in weekly timescales, does not suggest variability. 152

6.613C66A TeV lightcurve binned in monthly timescales, does not suggest variability. 152

6.623C66A TeV dN/dE spectrum fit by a powerlaw. 153

6.633C66A Fermi LAT 12° TS map before background sources in ROI are subtracted, highlighting 6 high TS source in the ROI. 155

6.643C66A Fermi LAT 12° TS map after background subtraction. Note the different TS scale. A lower TS scale is required to ensure the lower TS sources in the ROI are seen clearly. 156

6.653C66A Fermi LAT 2week-long lightcurve. Apart from a flare in October 2008 there is no significant variability observed. Due to the error bars on 3 of the points the majority of the points appear to be zero, this is not the case. Note the contemporaneous VERITAS observations. 157

6.663C66A Fermi LAT monthly Lightcurve. Apart from a flare in October 2008 there is no significant variability observed. Due to the error bars on 2 of the points the majority of the points appear to be zero, this is not the case. Note the contemporaneous VERITAS observations. 157

6.673C66A Fermi LAT TS as a function of Energy in 10bins. 158

6.683C66A Fermi LAT dN/dE spectrum in 10 bins. 158

6.693C66A Fermi LAT E^2 dN/dE spectrum in 10 bins fit best by a log parabolic function. 159

6.70PKS1424+240 VERITAS θ^2 (red = source, blue = background). 160

6.71PKS 1424+240 VERITAS 2D significance map. 161

6.72PKS 1424+240 TeV spectrum fit best by a powerlaw. 162

6.73PKS 1424+240 TeV lightcurve in 1 day-long time bins. Due to the limited number of observations it is difficult to detect variability. 162

6.74PKS 1424+240 TeV lightcurve in 1 week-long time bins. Due to the limited number of observations it is difficult to detect variability. 163

6.75PKS 1424+140 Fermi LAT 12° TS map before sources in the ROI are background subtracted, highlighting 2 high TS sources in the ROI that need to be included in the background model 164

6.76PKS1424+140 Fermi LAT 12° TS map after background subtraction. Note the different TS scale. A lower TS scale is required to ensure the lower TS sources in the ROI are seen clearly. 165

6.77PKS1424+240 Fermi LAT lightcurve in 2 week bins, showing little variability. Note the contemporaneous VERITAS observations. 166

6.78PKS1424+240 Fermi LAT monthly lightcurve, showing variability. Note the contemporaneous VERITAS observations. 167

6.79PKS1424+240 Fermi LAT lightcurve in 3 month-long time intervals, demonstrating extreme variability. Note the contemporaneous VERITAS observations. 167

6.80PKS 1424+240 Fermi LAT TS as a function of energy in 10 bins 168

6.81PKS 1424+240 Fermi LAT dN/dE spectrum in 10 bins. 168

6.82PKS 1424+240 Fermi LAT E^2 dN/dE spectrum in 10 bins fit best by a log parabolic curve. 169

6.831ES 0502+675 Fermi LAT and de-absorbed VERITAS dN/dE spectra at a redshift of z = 0.3. 170

6.841ES 0502+675 Fermi LAT and de-absorbed VERITAS E^2dN/dE spectra at a redshift of z = 0.3. 171

6.851ES 0806+524 Fermi LAT and de-absorbed VERITAS E^2dN/dE spectra at a redshift of z = 0.138. 171

6.861ES 1959+650 Fermi LAT and de-absorbed VERITAS E^2dN/dE spectra at a redshift of z = 0.047. 172

6.87W Comae Fermi LAT and de-absorbed VERITAS E^2dN/dE spectra at a redshift of z = 0.102. 173

6.883C66A Fermi LAT and de-absorbed VERITAS dN/dE spectra at a redshift of z = 0.3. 173

6.893C66A Fermi LAT and de-absorbed VERITAS E^2dN/dE spectra at a redshift of z = 0.3. 174

6.903C66A Fermi LAT and de-absorbed VERITAS E^2dN/dE spectra at a redshift of z = 0.05. 174

6.91PKS 1424+240 Fermi LAT and de-absorbed VERITAS dN/dE spectra at a redshift of z = 0.6. 175

6.92PKS 1424+ 240 Fermi LAT and de-absorbed VERITAS E^2dN/dE spectra at a redshift of z = 0.6 176

6.931ES 0502+675 multiwavelength E^2 dN/dE spectra including VERITAS and Fermi LAT data with quasi-contemporaneous MDM and Swift XRT data. The data is taken from Acciari et al. (in prep). 177

6.941ES 0502+675 SSC E^2 dN/dE spectra with VERITAS, Fermi LAT, Swift XRT and MDM data. Black = SSC, dashed black = deabsorbed spectrum, Green is the SSC fit. 178

6.951ES 0502+675 SSC + EC E^2 dN/dE spectra with VERITAS, Fermi LAT, Swift XRT and MDM data. Black = SSC, dashed black = deabsorbed spectrum, red = EC, Green is the sum of the SSC+ EC. 179

6.961ES 0806+524 SED with Planck upper limits and Swift XRT data points (Planck Collaboration, 2011) combined with Fermi LAT and VERITAS data points. 180

6.971ES 0806+524 SSC fit to multiwavelength data. Black = SSC, dashed black = deabsorbed spectrum, red = EC, Green is the SSC curve. 181

6.981ES 0806+524 SSC+EC fit to multiwavelength data. Black = SSC, dashed black = deabsorbed spectrum, red = EC, Green is the sum of the SSC + EC. 182

6.991ES 1959+650 multiwavelength data SED including Planck upper limits and Swift UVOT and XRT data points (Planck Collaboration, 2011). 184

6.1001ES 1959+650 SSC fit to multiwavelength data. Black = SSC, dashed black = deabsorbed spectrum, Green = SSC. 184

6.1011ES 1959+650 SSC + EC fit to multiwavelength data. Black = SSC, dashed black = deabsorbed spectrum, red = EC, Green = sum over SSC +EC. 185

6.102W Comae multiwavelength SED with quasi-contemporaneous Planck (data points and upper limits), Swift XRT, Swift UVOT (Planck Collaboration, 2011), Fermi LAT and VERITAS. 186

6.103W Comae SSC fit to multiwavelength data (quasi-contemporaneous Planck (data points and upper limits), Swift XRT, Swift UVOT, Fermi LAT and VERITAS). Black = SSC, dashed black = de-absorbed spectrum, Green = SSC. 187

6.104W Comae SSC + EC fit to multiwavelength data (quasi-contemporaneous Planck (data points and upper limits), Swift XRT, Swift UVOT, Fermi LAT and VERITAS). Black = synchrotron, dashed black = de-absorbed spectrum, red = EC, Green = sum of SSC+EC. 188

6.105C66A multiwavelength SED with quasi-contemporaneous FGASP, MDM, Swift XRT, Swift UVOT (taken from Acciari et al, 2009), Fermi LAT and VERITAS data. 190

6.106C66A SSC fit (z=0.444) to multiwavelength data (quasi-contemporaneous FGASP, MDM, Swift XRT, Swift UVOT, Fermi LAT and VERITAS data). Black = SSC, dashed black = deabsorbed spectrum, red = EC, Green = SSC. 191

6.107C66A SSC + EC fit (z=0.444) to multiwavelength data (quasi-contemporaneous FGASP, MDM, Swift XRT, Swift UVOT, Fermi LAT and VERITAS data). Black = SSC, dashed black = deabsorbed spectrum, red = EC, Green = sum of SSC +EC. 192

6.108C66A SSC fit (z=0.05) to multiwavelength data (quasi-contemporaneous FGASP, MDM, Swift XRT, Swift UVOT, Fermi LAT and VERITAS data). Black = SSC, dashed black = deabsorbed spectrum, red = EC, Green = SSC. 193

6.109C66A SSC + EC fit (z=0.05) to multiwavelength data (quasi-contemporaneous FGASP, MDM, Swift XRT, Swift UVOT, Fermi LAT and VERITAS data). Black = SSC, dashed black = deabsorbed spectrum, red = EC, Green = sum of SSC +EC. 194

6.110PKS 1424+240 multiwavelength SED with quasi-contemporaneous Planck (data= error bars and upper limits=no error bars, Planck Collaboration, 2011), Swift UVOT, Swift XRT(Acciari et al, 2010), Fermi LAT and VERITAS data. 196

6.111PKS 1424+240 SSC fit to multiwavelength data (quasi-contemporaneous Planck (Planck Collaboration, 2011), Swift UVOT, Swift XRT (Acciari et al, 2010), Fermi LAT and VERITAS data). Black = SSC, dashed black = deabsorbed spectrum, Green = SSC. 197

6.112PKS 1424+240 SSC +EC fit to multiwavelength data (quasi-contemporaneous Planck, Swift UVOT, Swift XRT, Fermi LAT and VERITAS data). Black = SSC, dashed black = deabsorbed spectrum, red = EC, Green = sum of SSC+EC. 198

6.113Corresponding γ - γ cross sections weighted with the BLR spectrum are shown by the solid, dotted, dashed and dot-dashed curves, respectively. n_H refers to column density - taken from Poutanen (2011) 200

A.1 Fermi LAT detection of increasing gamma-ray activity of blazars PKS 0537-441 and PKS 0301-243 217

A.2 Fermi LAT observations of increasing gamma-ray activity of blazar 3C279 218

A.3 Fermi LAT detection of a new enhanced gamma-ray emission from the Crab Nebula region 219

A.4 Fermi LAT detection of increased gamma-ray activity from blazar S5 0716+71 220

List of Tables

2.1 AGN characteristics, in comparison to typical galaxies, adapted from Krolik (1999). 16

2.2 AGN properties, adapted from Krolik (1999). 17

2.3 Blazar class differences 19

2.4 Blazar subclass synchrotron frequencies 19

2.5 Selected Blazar Properties 37

4.1 Summary of VERITAS performance 55

4.2 Summary of Lat Instrument Parameters and Estimated Performance (Atwood et al., 2009) 66

5.1 The stages of VEGAS, version v2.3.0, used in the analyses presented in this thesis. 77

5.2 Hillas Parameters 84

5.3 Data Quality Cuts 86

5.4 Mean Scaled Parameters 89

5.5 Wobble 1ES 0502+675 results 90

5.6 RBM 1ES 0502+675 results 91

5.7 Event Classification 99

5.8 Highlights of the LAT point source analysis 103

5.9 Description of the components of the Science Tools 103

5.10Subselection cuts performed on the photon event data file 104

6.1 VERITAS Wobble 1ES 0502+675 results 109

6.2 1ES 0502+675 Fermi LAT Gtlike Unbinned Maximum Likelihood results 113

6.3 VERITAS Wobble 1ES 0806+524 results 119

6.4 1ES 0806+524 Fermi LAT Gtlike Unbinned Maximum Likelihood results 123

6.5 VERITAS Wobble 1ES 1959+650 results 130

6.6 1ES 1959+650 Fermi LAT Gtlike Unbinned Maximum Likelihood results 134

6.7 VERITAS Wobble W Comae results 139

6.8 W Comae Fermi LAT Gtlike Unbinned Maximum Likelihood results 144
6.9 VERITAS Wobble 3C66A results 150
6.103C66A Fermi LAT Gtlike Unbinned Maximum Likelihood results 154
6.11VERITAS Wobble PKS 1424+240 results 160
6.12PKS 1424+240 Fermi LAT Gtlike Unbinned Maximum Likelihood results 166
6.13A comparison of the synchrotron and IC peaks, * denotes sources of uncertain redshift 175
6.14SSC and SSC+EC model fit parameters, 1ES 0502+675 179
6.15SSC and SSC+EC model fit parameters, 1ES 0806+524 181
6.16SSC and SSC+EC model fit parameters, 1ES 1959+650 183
6.17SSC and SSC+EC model fit parameters, W Comae 187
6.18SSC and SSC+EC model fit parameters, 3C66A 189
6.19SSC and SSC+EC model fit parameters, 3C66A 190
6.20SSC and SSC+EC model fit parameters, PKS1424 195
6.21Fermi LAT and VERITAS Detected Flux Variability 202
6.22SSC model fit parameters for each source 204

CHAPTER 1

Introduction

1.1. History of γ-ray astronomy

For close to a century γ-ray astronomy has been the subject of scientific interest. γ-ray radiation is extremely energetic ($>$ 100 keV) emission that is created from the most violent and powerful celestial events that occur in the hottest regions of the universe e.g. supernova explosions, black hole creation. γ-ray radiation is studied to expand our knowledge and improve our understanding of the universe (origins, size and rate of expansion), γ-ray emitting sources and particle acceleration processes. In the early 20th century, scientists marveled over the issue of ionizing radiation levels in the atmosphere. The general assumption was that the level of radiation would decrease with increasing distance into the atmosphere from earth. However, early experiments indicated that this was not the case, that in fact the radiation was increasing. Between 1911 and 1922, Victor Hess measured the radiation in the atmosphere up to 5.3 km above sea level (asl.), with the aid of a balloon. He published that radiation levels did decrease as expected out as far as 1 km but then beyond this, the levels started to increase significantly. From these findings, he hypothesized that there was radiation propagating through our atmosphere from space. In 1925, Robert Andrews Millikan confirmed this theory and in 1936 Hess was awarded the Nobel prize for his work. This radiation became known as cosmic rays. Cosmic rays are highly energetic charge particles, $<$ 1% of which are believed to be γ rays.

Further contributions from Eugene Feenberg and Henry Primakoff in 1948, Sachio Hayakawa and I.B. Hutchinson in 1952 and Philip Morrison in 1958, led to predictions of γ-ray emission from astrophysical processes. This was the beginning of γ-ray observatories. A brief history of γ-ray astronomy over the last five decades is divided into two categories: space-based and ground-based, and discussed below.

1.2. Brief Account of Satellite Experiments

An important limitation in γ-ray astronomy to note is that γ rays are "blocked" by the atmosphere and therefore are not directly detectable on earth. Incident γ rays interact with atmospheric nuclei and convert to other forms. This conversion depends on the energy of the γ ray, e.g. above a few MeV the conversion taking place is pair production. For the purpose of this thesis only pair production satellite telescopes are discussed here, however, lower energy γ-ray interactions with matter are discussed in section 3.2. In order to detect γ rays telescopes were constructed to detect the products of this interaction with matter rather than the γ rays

themselves. An example of this is space-borne, pair production satellites that orbit above the atmosphere so that these limitations are not an issue. The pair production actually occurs within the telescope, the converting material is part of the detector and detection of γ rays can take place. Satellite γ-ray detectors can observe constantly regardless of weather conditions and time of day.

Satellite γ-ray missions began in the 1960s and there have been numerous, very successful missions over the last five decades. Some of the historical milestones of satellite detectors and their contribution to γ -ray astronomy include:

- Explorer XI
- OSO-3
- SAS-2
- COS B
- EGRET (onboard the CGRO satellite)
- Fermi LAT (onboard the Fermi Gamma-ray Space Telescope)

and are described below.

1.2.1. Explorer XI. Launched on the 27^{th} April 1961, NASA's Explorer XI signified the start of satellite γ-ray astronomy and detected the first γ rays from celestial sources. The small cylindrical, solar powered γ-ray detector had dimensions of 20×10 inch and weighed just 32 lbs, with the satellite weighing 80 lbs overall, and it searched for γ rays above 50 MeV. The detector was comprised of crystal scintillators (CsI and NaI), a Lucite Cherenkov counter and a plastic anti-coincidence shield and operated in a scanning mode with a source location accuracy of 5° (Kraushaar et al., 1962). Figure 1.1 is a schematic illustration of the γ-ray detector onboard the satellite. 22 γ-ray events were recorded from nine hours of good quality data from twenty three days of observations. A large portion of the total number of detected events were localized to the galactic plane which prompted more detailed investigations to search for a celestial anisotropy. Although initial results did imply a celestial anisotropy, the further, more detailed analysis of the Explorer XI data did not yield any significant results (Kraushaar et al., 1965). In addition to the detection of twenty two γ rays, the satellite also observed numerous flares and radiation from the Van Allen Belts, before detector failure occured due to power supply difficulties ended the mission in September 1961.

1.2.2. OSO-3. NASA's Third Orbiting Solar Observatory (OSO-3) was launched on the 8^{th} March 1967 and included both an X-ray and a γ-ray detector component. Similar to the γ-ray detector onboard the Explorer XI satellite, the detector was comprised of CsI and NaI scintillators and was designed by MIT to search for γ rays above 50 MeV. The instrument operated continuously for 16 months, detecting a total of 621 γ-ray events. Observations demonstrated a celestial anisotropy with a higher concentration of γ-ray events along the galactic plane. Results also indicated a higher intensity localized at the galactic centre.

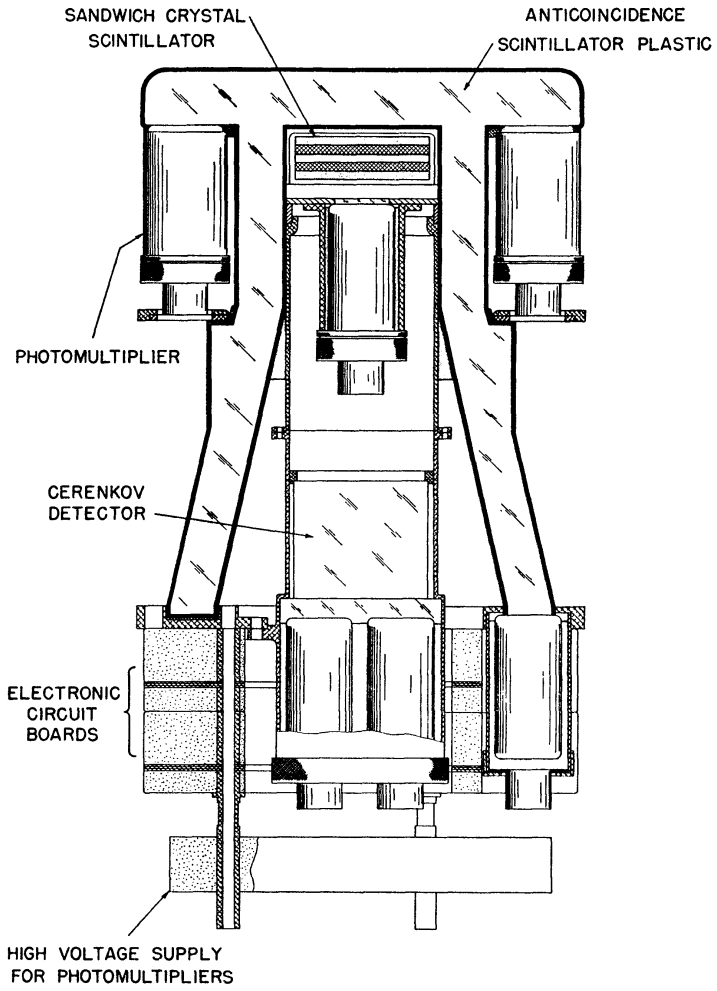

FIGURE 1.1. Schematic drawing of the γ-ray detector onboard NASA's Explorer satellite, taken from Kraushaar et al.,1965.

1.2.3. SAS-2. NASA's Small Astronomy Satellite 2 (SAS-2) mission, launched on the 15^{th} November 1972, was a mission completely dedicated to γ-ray astronomy. The instrument was sensitive to events in the energy range 20 MeV - 1 GeV and carried a single pair production telescope which utilized a 32-level wire spark-chamber system (Fichtel et al., 1975). The satellite is acknowledged as being the first instrument with the ability to distinguish galactic features. Achievements of the mission include the confirmation of a galactic plane anisotropy, the discovery of the diffuse γ-ray background and the detection of γ-ray emission from the Crab, Vela and Geminga pulsars. Despite power failure after six months of operations in June 1973, the mission produced the first detailed maps of the galactic plane, showing a strong correlation between the γ-ray radiation and galactic features. This was achieved through twenty seven pointed observations amounting to approximately a week in duration and covering 55% of the total sky.

1.2.4. COS-B. Another notable mission, following SAS-2, was the γ-ray dedicated satellite COS-B, launched 9^{th} August 1975 into a highly elliptical orbit of ∼100,000 km apogee and ∼ 350 km perigee. Developed by the European Space Agency (ESA), the instrument was sensitive to photons in the energy range 25 MeV - 1 GeV. Originally designed to last two years, the satellite operated successfully for nearly seven years. Among its achievements were the detailed γ-ray observations of the Geminga pulsar and the production of the first complete γ-ray galactic plane sky map. Two catalogs of point sources were released based on the analysis of the COS-B data. The second COS-B catalog is a list of 25 (E > 100 MeV) γ-ray sources, only four of which are associated with previously known sources: Crab and Vela Pulsars, 3C273 and the ρ Oph cloud complex. The catalog is based on 32 month-long pointed observations (Swanenburg et al., 1981). The catalog γ-ray emission sky map is shown in figure 1.2

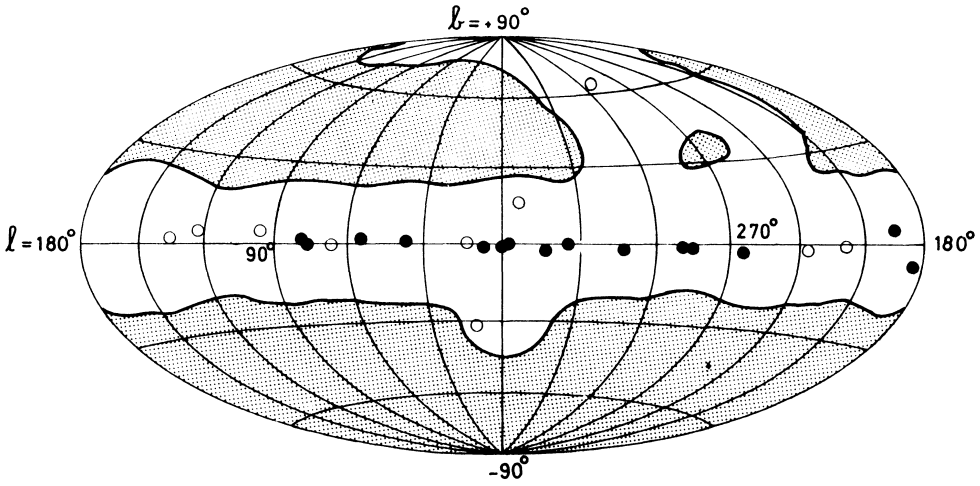

FIGURE 1.2. The second COS-B satellite catalog sky map, displaying 25 detections of γ-ray emitting sources above 100 MeV. The filled circles denote fluxes above 1.3×10^{-6} ph cm^{-2} cm^{-1} and the open circles denote fluxes below this. This flux value is chosen to demonstrate the flux magnitude concentration in the galactic plane. The shaded region indicates unsearched areas - (Swanenberg et al., 1981)

1.2.5. EGRET. The Energetic Gamma Ray Experiment Telescope (EGRET) launched on the 5^{th} April 1991 was one of four instruments onboard NASA's Compton Gamma Ray Observatory (CGRO) satellite.

The telescope was sensitive to photons in the energy range 20 MeV - 30 GeV with a field of view of nearly 1 steradian. The design was based on previous experiments but up to twenty times larger and resembled in particular the SAS-2 and COS B instruments with a wide field of view of 80° in diameter. The effective area was greater than 1000 cm^2 between 100 and 3000 MeV. With an energy resolution of 20 - 25% and an angular resolution (68% containment radius) of 5.5° at 100 MeV decreasing to 0.5° at 5 GeV, EGRET gained an order of magnitude in sensitivity over

its predecessors. Arrival times of incident photons could be recorded within an accuracy of 50 μs (Thompson et al., 1993).

The detector contained a high voltage, gas-filled, spark chamber, on a NaI crystal calorimeter and a plastic scintillator anti-coincidence shield (figure 1.3).

The three other instruments onboard CGRO were the Burst And Transient Source Experiment (BATSE) sensitive in the energy range 0.025 - 2 MeV (Fishman et al., 1994), the Oriented Scintillation Spectrometer Experiment (OSSE) sensitive from 0.05 to 10 MeV (McNaron-Brown et al., 1995) and the imaging COMPton TELescope (COMPTEL) in the energy range 0.07 - 30 MeV (Bloemen H., 1994). The four instruments expanded the CGRO's total energy range from 25 keV to 30 GeV.

The third EGRET catalog includes data recorded between 22^{nd} April 1991 and 3^{rd} October 1995 and contains 271 high-energy (E $>$ 100 MeV) point sources with 170 sources of these unassociated with previously known γ-ray sources at other wavelengths (Hartman et al., 1999). The corresponding sky map is shown in figure 1.4. The achievements of the EGRET mission are numerous and include the first detailed all-sky survey, in-depth studies of individual γ-ray sources, and detection and identification of blazars in addition to monitoring for changes in activity. With the aid of more efficient background rejection models, EGRET produced the first sensitive sky map of the MilkyWay diffuse γ-ray emission.

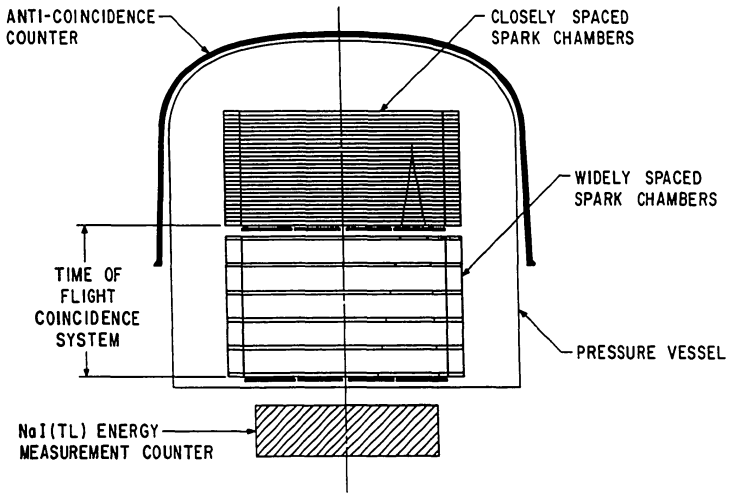

FIGURE 1.3. Schematic diagram of EGRET's spark chamber, calorimeter and anti-coincidence shield (Thompson et al., 1993)

1.2.6. Fermi LAT. The Large Area Telescope (Fermi LAT, also known as LAT) is the primary instrument on-board the Fermi Gamma-ray Space Telescope, formally known as GLAST (Gamma-ray Large Area Space Telescope). The LAT is the successor to EGRET but unlike EGRET, the LAT has a very stable response for absolute, long-term, flux measurements and

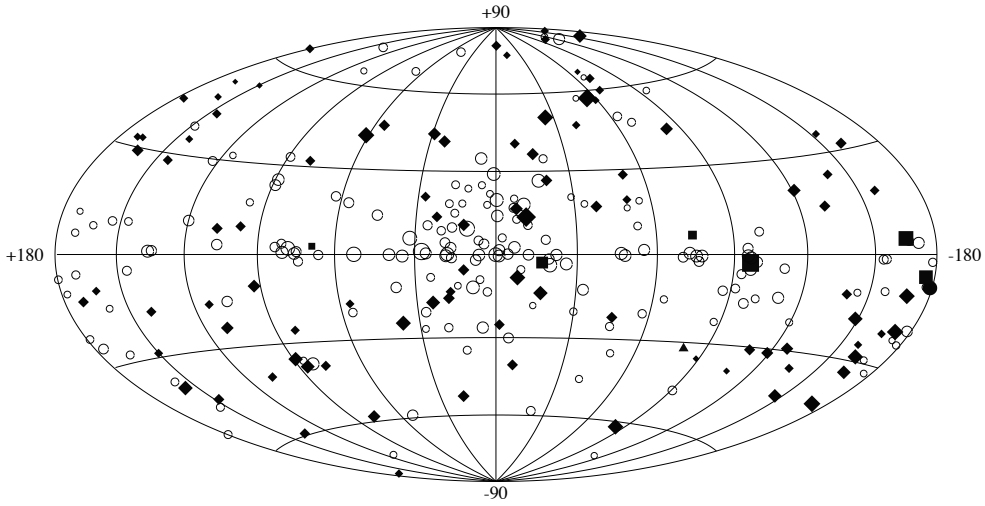

FIGURE 1.4. The third EGRET catalog γ-ray emission sky map, taken from (Hartman et al., 1999). The black diamonds represent AGN with the exception of Cen A, the black squares represent pulsars, the black triangle represents the Large Magellanic Cloud (LMC), the black circle represent solar flares and the open circles represent unidentified EGRET sources.

surveys the entire sky approximately every three hours, allowing for a more uniform exposure and deeper observations of the γ-ray sky. The sensitivity of the LAT is at least one order of magnitude greater than EGRET (Abdo et al., 2009). The first LAT AGN catalog was released in July 2009 and is the result of the first three months of sky-survey observations between August 4^{th} 2008 and November 4^{th} 2008. The observations reveal 132 bright high-latitude $|b| > 10^{\circ}$ sources with a Test Statistic (TS, see section 5.3.4.1) greater than 100 ($\sim 10\ \sigma$). Correlations of the Candidate Gamma-Ray Blazar Survey sources (CGRaBS), Combined Radio All-sky Targeted Eight-GHz Survey (CRATES) and Roma Blazar (BZCat) multifrequency blazar catalogs suggest 106 of the sources are associated with known AGN (Abdo et al., 2009). This 106 bright source list, otherwise known as the LAT Bright AGN Sample (LBAS), contains 58 flat spectrum radio quasars (FSRQs), 42 BL Lac Objects, 4 blazars with unknown classification and 2 radio galaxies (Cen A and NGC1275). Only 33 of these sources were previously detected with EGRET during its lifetime.

Fermi LAT operates an intensive scientific observing program, both extragalactic and galactic, the emphasis of which is on the detection and monitoring of γ-ray emitting sources. The primary objective behind the all-sky survey is to produce an extensive catalog of high energy sources amounting to thousands of detections with a TS greater than 100, during the instrument's lifetime ($\sim$ 5 - 10 years). For blazars in particular, the goals of the scientific observations include the discovery of new (E $>$ 20 MeV) sources, the long-term monitoring of established γ-ray emitting sources and the spectral analysis of individual sources from 20 MeV to 300 GeV. This enables thorough population and variability studies and the search for changes in a source's

activity, in particular increases in flux or "flaring" activity. Variability studies are performed to constrain the size and estimate the location of the emission region. Detailed broadband spectral modeling of the γ-ray emission of blazars provides valuable insights into the mechanics behind particle acceleration, constrains parameters such as Lorentz factor and magnetic field and allows redshifts measurements which are important for the study of the Extragalactic Background Light (EBL).

The capabilities of the LAT also include determining the nature of unidentified sources, localizing point sources to within 0.3 - 2 arcmin and producing spectra of extended sources such as SuperNova Remnants (SNRs), molecular clouds and nearby galaxies. The LAT allows for the rapid detection of GRBs and can measure the diffuse isotropic γ-ray background up into MeV energies. γ-rays detected by the instrument can be used to probe the early universe and cosmic evolution of high energy sources up to a redshift $z \geq 6$, and in the search for Dark Matter. The second instrument onboard the Fermi satellite is the Gamma-ray Burst Monitor (GBM) which is sensitive to photons in the energy range of 8 keV - 40 MeV (Abdo et al., 2009). While the main objective of the GBM is to monitor for GRBs, it can compliment the LAT with regards to observations of blazars.

1.3. Brief Account of Ground Based Experiments

One significant disadvantage of space-borne γ-ray detectors is that the effective areas for pair production and detection are constrained to the size of the detector. By using ground-based telescopes and producing models of extensive air showers, it is possible to expand the effective areas dramatically. Essentially, ground-based detectors use the atmosphere as part of the detector. Pair production occurs in the atmosphere, converting γ rays to electron - positron pairs which propagate through the atmosphere and undergo bremsstrahlung radiation, followed by further pair production. This results in Extensive Air Showers (EASs) which are discussed in more detail in section 3.3 Another advantage is the opportunity to upgrade and perform maintenance on the instrument throughout its lifetime. The development of ground-based instruments can be perceived to be slower in comparison to space-based but it has progressed rapidly over the last two decades.

In 1937, Pavel Alekseyevich Cherenkov discovered faint flashes of blue light from γ-ray radiation from a bottle of water that was bombarded with charged particles (Cherenkov, 1937). This became known as the Cherenkov effect and won Cherenkov a Nobel prize in 1958.

In 1948, Patrick Blackett discussed the possibility that Cherenkov light was a component of the atmosphere, resulting from interactions between cosmic rays and the atmosphere, and would contribute 0.01% of the total night sky light (Blackett, 1948). As this contribution was so small, it was not detectable over the Night Sky Background (NSB) by the instruments and methods at that time. Both the Cherenkov results and the Blackett theory led to the development of ground-based γ-ray detectors, a few of which are described below.

1.3.1. Galbraith and Jelley. In 1953, using an apparatus built from a garbage can, a 60cm diameter mirror and a single PMT, William Galbraith and John Jelley detected what is now known as Cherenkov light pulses from air showers resulting from cosmic rays (Galbraith and Jelley, 1953). The mirror collected the Cherenkov light, reflecting and focusing it on the PMT which recorded the light as an electronic signal. This crude design was the basis for modern ground-based γ-ray detectors.

1.3.2. The Crimean Experiment. The first acknowledged ground-based Cherenkov telescope was overseen by physicist A. E. Chudakov and commissioned by the Lebedev Institute in the Crimea. It consisted of an array of 12 single PMT detectors. Sources were selected as targets for observations based on the predictions of Cocconi (1960). Cocconi predicted that γ rays could be detected from the ground from celestial sources and suggested possible γ-ray emitting sources. The experiment did not detect any γ rays due to the significant charged particle background.

1.3.3. Second Generation of Ground-based Gamma-ray Telescopes. The first official detection of γ rays from a celestial object was reported in 1989 with the detection of the Crab pulsar wind nebula by the Whipple 10m telescope (Weekes et al., 1989). Constructed in 1969, its location at the Fred Lawrence Whipple Observatory (FLWO) on Mount Hopkins in Southern Arizona was chosen because of its dark location (little background light pollution) and generally clear skies. The Imaging Atmospheric Cherenkov Technique (IACT) was first developed by Neil Porter and John Jelly (Porter and Jelley, 1964) and involved capturing Cherenkov light images from γ-ray initiated showers. One advantage of this technique was discrimination of hadronic background through image analysis. Turver and Weekes (Turver and Weekes., 1978) then proposed this technique for the Whipple telescope and in 1982 the telescope was converted to an imaging instrument. It is the pioneering IACT telescope and was still operating successfully as part of a blazar monitoring program until the summer of 2011. The telescope (figure 1.5) is a Davies-Cotton design (Davies and Cotton, 1957) and consists of a 10m diameter optical reflector and a 37 PMT camera, with a field of view of 3.5°.

The telescope also detected a number of blazars including Markarian 421 (Punch et al., 1992), Markarian 501 (Quinn et al., 1995), 1ES 2344+514 (Cantanese et al., 1998), H 1426+428 (Horan et al., 2002) and 1ES 1959+650 (Holder et al., 2003).

1.3.4. Third Generation Ground-based Telescopes. A new family of IACT telescopes followed, based on the design and technique of the Whipple 10m telescope. An example of the third generation was HEGRA (the High Energy Gamma Ray Astronomy) located on the Canary Island of La Palma. The instrument, which operated from 1987, was an array of six identical 8.5 m diameter telescopes that performed for the first time stereoscopic observations (through the overlaying of multiple camera views). Each camera contained 271 PMTs and had a field of view of 4.6° (figure 1.6)

FIGURE 1.5. The Whipple 10m telescope located in Southern Arizona - (www.astro.wisc.edu/ ∼larson/Webpage/Gamma.html)

One notable achievement was the detection of > 16 TeV photons from Markarian 501 (Aharonian et al., 2002). The array was dismantled in September 2002 to make room for its successor MAGIC.

The current γ-ray telescopes still employ a similar construction to the Whipple 10m and include VERITAS in Southern Arizona, H.E.S.S. in Namibia and MAGIC in La Palma.

H.E.S.S. (the High Energy Stereoscopic System) is an array of four 15m diameter reflecting telescopes sensitive to photons in the energy range 100 GeV - 10's of TeV with a 5° field of view (Hofmann et al., 2001). All four telescopes have been in operation since September 2004. In order to lower the energy threshold, the H.E.S.S. collaboration are constructing a fifth larger telescope for the array, to be called H.E.S.S. 2. The reflector will have a diameter of 28 m with a camera of 2048 PMTs and will be located in the center of the array.

Constructed in 2004, MAGIC 1 (Major Atmospheric Gamma-ray Imaging Cherenkov telescope) is located on the former HEGRA site. It is the largest IACT telescope to date with a mirror surface of 236 m^2 (17 m diameter reflector dish). The camera contains 576 PMTs, has a field of view of 3.5° and the telescope is sensitive to photons in the energy range 50 GeV - 30 TeV.

In 2009, MAGIC 2 (with significant upgrades) was constructed 85 m from MAGIC 1 and combined with MAGIC 1 to form an array to expand the energy range of the instrument toward

FIGURE 1.6. A HEGRA γ-ray telescope (www.sciencephoto.com/media/322268/enlarge).

lower energies. The stereoscopic imaging has produced a sensitivity to 0.8% Crab at a low energy threshold of 25 GeV (Aleksić et al., 2011).

VERITAS (the Very Energetic Radiation Imaging Telescope Array System) is an array of four 12m telescopes, located at the Fred Lawrence Whipple Observatory in Southern Arizona. The array has been fully operational since September 2007. Currently, the VERITAS collaboration consists of more than 90 members from 22 institutions in Canada, the U.S.A., Ireland, England and Germany. The array is the successor to the Whipple 10m telescope. The array operates in the energy range of 100 GeV - 30 TeV and is described in more detail in subsequent chapters. VERITAS operates both a galactic and extragalactic science program. The motivations of both programs include discovery and detection of γ-ray emitting sources and long-term monitoring of known γ-ray sources. VERITAS has a growing catalog of γ-ray sources which includes AGN, pulsars, and a starburst galaxy, and also completed a galactic sky survey of the Cygnus Region in November 2009.

1.4. Thesis Outline

For the first time, there is overlap (100 - 300 GeV) in the energy ranges of satellite and ground-based telescopes. This thesis combines two detection methods; the first being detection

when pair production occurs within the telescope, the second is detection involving the atmosphere. Utilizing both detection methods provides a clear picture of the processes taking place between 20 MeV and 30 TeV. Fermi LAT and VERITAS data are analyzed and combined and compared in this thesis to gain and better understanding of γ-ray emitting sources. The outline of the thesis is as follows:

• Chapter 2

This chapter presents a summary of AGN and blazars, describing classification and the unified model, emission processes and models. It provides a discussion of the objectives in this thesis and the motivations behind the source selection.

• Chapter 3

An overview of Cherenkov radiation, pair production and EASs is provided here. γ-ray and hadronic EASs and EASs detection methods are discussed

• Chapter 4

This chapter presents the hardware instrumentation and software of both experiments

• Chapter 5

This is an overview of the analysis procedures of both instruments and covers calibration, background subtraction, source detection and spectral and temporal analyses

• Chapter 6

This chapter presents the results of a comparison study of an extensive dataset which includes detection levels, spectra and lightcurves. The IC emission peaks are constrained and multiwavelength SEDs are constructed and leptonic modeling is performed.

• Chapter 7

A discussion of conclusion and future work is presented.

1.5. My Contributions

Some of my contributions from both the VERITAS array and the Fermi LAT satellite are discussed below

1.5.1. VERITAS. Throughout the duration of my thesis I have participated in short and extended observing shifts on the VERITAS array. This also involved performing a quicklook analysis on a run by run basis, hardware and software operations, telescope maintenance (e.g. mirror alignment as described in section 4.1.1.2). In addition to this, I completed two one month DQM shifts, which included and examining data quality diagnostics and pixel health, and also monitoring trigger rates. I am currently the lead author and analyst for a VERITAS multiwavelength paper on the HBL 1ES 1959+650 with encompasses four years of TeV data (the complete VERITAS data set). The paper will include spectral analysis, variability studies and construction of a multiwavelength SED with leptonic modeling.

1.5.2. Fermi LAT. As an active member of the LAT collaboration, I dedicated one week every 2 - 3 months to the LAT Flare Advocate and Gamma-ray Sky Watcher Program (FA-GSW). This is a quicklook automated science process and is part of the LAT Science Operations. The

program is an all sky survey performed in six hour intervals to search for flux trends, interesting activity and source discoveries. Through extensive analysis I provided detailed daily internal reports and fast notes. In addition to this, I produced Atels, generated ToOs and wrote regularly for the public Fermi Sky Blog. Monitored source list with public lightcurves were also updated weekly. The Atels for which I was lead author/analyst are presented in Appendix A. Atel #2591 (Cannon et al., 2010, figure A.1) announced the Fermi LAT detection of increasing γ-ray activity from sources positionally coincident with the blazars PKS 0537-441 and PKS 0301-243. It provided daily flux levels and encouraged follow-up multiwavelength observations. Atel #2886 (Cannon et al., 2010, figure A.2) highlighted a sharp increase in γ-ray activity from the well known FSRQ 3C279 with both daily and six hour interval analysis results. In April 2011, Fermi LAT detected significant enhanced $>$ 100 MeV emission from the crab nebula region (Buehler, D'Ammando & Cannon, 2011, figure A.3). Preliminary LAT analysis indicated that the LAT had caught the increased emission at the beginning of a flare and was therefore in a position to encourage mutliwavelength observations to capture the activity at all wavelengths for the duration of the flare. Three months later, Atel #3487 (Cannon et al., 2011, figure A.4) reported the detection of a γ-ray flare from the blazar S5 0726+71 with a daily (E $>$100 MeV) flux of more than one order of magnitude greater than its average flux.

In December 2009, a joint Fermi LAT/ VERITAS paper concerning the MeV to TeV detection of blazar 1ES 0502+675 began (Acciari et al., in prep) for which I am the Fermi LAT data analyst and co-auther. This involved detection statistics and the results from both a spectral and temporal analysis. The paper is currently in preparation.

CHAPTER 2

Active Galactic Nuclei

2.1. Introduction

An Active Galactic Nucleus (AGN) is a term used to describe a compact region at the centre of a galaxy that produces more radiation than the remainder of the galaxy combined and where there is evidence of particle acceleration to relativistic speeds. The non-thermal continuum radiation is seen from AGN over twenty decades of the electromagnetic spectrum from radio waves to γ rays. These extreme sources are highly variable and produce luminosities as high as ten thousand times the luminosity of a typical galaxy from a tiny volume, less than 1 pc^3 (Bradley, 1997). AGN also exhibit remarkable optical and UV spectra. In contrast to "normal" galaxies that contain absorption lines in their optical spectra, AGN exhibit emission lines. For decades, AGN have been the subject of observations and studies at wavelengths throughout the entire electromagnetic spectrum to gain insight into the intrinsic properties of the galaxies, the emission processes taking place and the surrounding environment.

2.1.1. The History of AGN Observations. Edward A. Fath of the Lick Observatory, California, performed the first documented observations of AGNs with a 36-inch Crossley reflector. During a spectral study in 1908 of the brightest spiral nebulae (which we now know to be galaxies), Fath noted 6 broad emission lines from the galaxy NGC 1068 (aka Messier Object 77): Hβ, [OII]λ3727, [NeII]λ3869, [OIII]$\lambda\lambda$4363, 4959, 5007 (Fath 1909). Vesto M. Slipher of the Lowell Observatory, Arizona, confirmed this result in 1913 (Slipher, 1917) with a higher resolution spectrum of M77. Slipher also noted the similarity of the emission lines to those seen in planetary nebula and that the lines were resolved with widths of hundreds of km s^{-1} and shifted. The NGC 1068 result was also confirmed by Edwin Hubble in 1926, along with the detection of emission lines from two additional galaxies now known as NGC 4051 and 4151, in his historic study of extragalactic nebulae (Hubble, 1926).

In the 1940s at the Mt. Wilson Observatory in California, American astronomer Carl K. Seyfert undertook pioneering research into the emission from spiral galaxies. In 1943, he published results from a small subset (6 sources) of particularly luminous galaxies, including NGC 1068, 4051 and 4151, whose spectra showed many broadened, high-ionization emission lines (Seyfert, 1943). The hydrogen lines were seen to be broadened up to 8500 km s^{-1}, full width at zero intensity, indicating great speeds. Despite the emission line profiles differing from source to source, it became evident that this characteristic was typical of this subset of AGN. The galaxies

became known as Seyfert galaxies and are the most common type of AGN, which include radio galaxies, quasars, Quasi-Stellar Objects (QSOs), luminous galaxies and field galaxies.

The concept of AGN was first raised in the 1950s by Professor Victor Ambartsumian, a Soviet Armenian scientist. In a report at a Solvay Conference on Physics in Brussels in 1958, he postulated that significant explosions involving the expulsion of large amounts of mass were taking place at the centre of these objects. To allow for this, the objects must contain bodies of huge mass (Ambartsumian, 1998). The theory was met with skepticism. It would be years later before this hypothesis became the accepted theory.

With the identification of emission lines and redshift determination in the case of radio sources 3C273 (Schmidt, 1963) and 3C48 (Greenstein, 1963) it became evident that due to the large distances these highly luminous objects were not stars but instead quasi-stellar radio galaxies (quasars). Through a detailed study of the high-ionization emission lines in NGC 1068, in particular the wide range of ionization mechanisms, Osterbrock and Parker hypothesized that the nuclei of Seyfert galaxies resemble miniature quasars (Osterbrock & Parker, 1965). This was the foundation of the idea that all AGNs are intrinsically the same.

2.1.2. Unified Model. The unified model of AGN proposes that all AGN are fundamentally the same type of object and that the observable properties of AGN depend only on their orientation, in particular the angle with respect to the observer's line of sight (Urry & Padovani, 1995). The non-thermal radiation emitted from radio waves to γ rays is significantly stronger than any emitted thermal radiation. As shown in figure 2.1, the main components of an AGN are accepted as including a super massive black hole, hot accretion disk, dusty torus, both broad and narrow emission-line gas clouds, two relativistic plasma jets and radio lobes, although the presence of jets and lobes appears to be dependent on AGN class.

The nucleus is believed to be powered by accretion of matter from a surrounding hot accretion disk (radius $\sim 10^{12}$ m) onto the super massive black hole (SMBH) of mass 10^8-10^9 $M_\odot$[1] (Weekes, 2003). The accretion disk is surrounded by a dusty optically-thick torus that, depending on orientation, can obscure the view and absorb UV and optical wavelengths. The combination of the build-up of energy and the distortion of the surrounding magnetic fields is thought to be the cause of the formation of the jets, which propel material outwards from the super massive black hole. Two collimated plasma jets perpendicular to the accretion disk, develop opposite each other and aligned with the rotation axis of the SMBH, containing relativistic particles. By spiraling through the surrounding magnetic field, the particles produce synchrotron radiation in the energy range from radio waves to X rays. The processes taking place in the jets are the most energetic and powerful in the AGN. Rapidly moving gas clouds close to ($\sim 10^{14}$ m) the accretion disk are responsible for broad emission lines in the UV and optical spectra, while slower moving colder clouds further out ($\sim 10^{16}$ - 10^{18} m) produce narrower lines (Urry & Padovani, 1996). This broadening is due to the doppler effect. There is also assumed to be a population

[1] $M_\odot$ = mass of the sun, 1.99×10^{30} kg

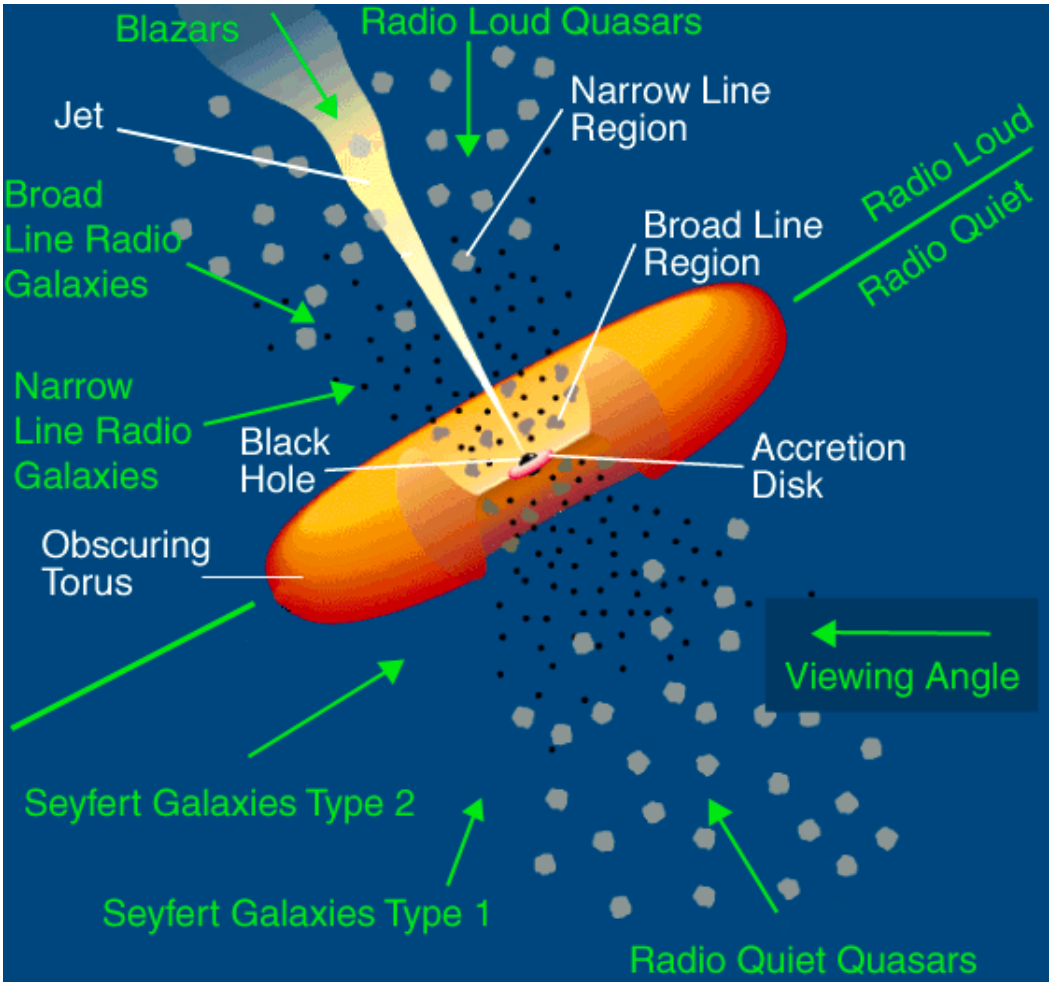

FIGURE 2.1. Illustration of an AGN, highlighting the main components of AGNs and the classification dependent on orientation (http://www.auger.org/news/PRagn/about_AGN.html).

of electrons above and below the accretion disk that emit thermal radiation in the X-ray energy range.

2.1.3. Classification. The classification of AGN (figure 2.2) is based on the observable properties such as the presence of jets, the wavelength of peak the emission, the strengths of emissions lines etc., which are believed to be the result of the orientation of the AGN and not on intrinsic physical differences (Padovani, 1999). The difficulty arises because, although the observable properties are influenced by orientation, there are no set limits for classification, but a continuous distribution exists instead and the distinction is not always clear. Classification is determined from optical spectroscopy, optical morphology, radio properties, variability and peak emission wavelengths (tables 2.1 and 2.2).

TABLE 2.1. AGN characteristics, in comparison to typical galaxies, adapted from Krolik (1999).

Characteristic	Present in AGN	Comments
Small angular size	Most cases if not all	Wavelength dependent
Greater than typical luminosity	Most cases if not all	Lower luminosity AGN are harder to detect due to the large distances
Broadband continuum emission	Most cases	Not always γ-ray detections
Strong emission lines	Most cases	can sometimes be narrow or absent altogether
Variable	Most cases	
Radio emission	Minority of cases	
Strongly variable and polarized	Small minority of cases	

Firstly, AGN can be categorized as either radio-quiet or radio-loud. Radio-quiet AGN, which make up the majority of all AGN (Dermer, 1994), are weak radio emitters, generally do not have jets and are powerful infrared emitters. In contrast, radio-loud AGN (a small subset of all AGN) have evident jets and emit strong radio emission. To date, all AGN detected at TeV energies are radio-loud. The TeV emission is produced by relativistic electrons which are also responsible for the radio emission. Not shown in figure 2.2 is that both the Fanaroff-Riley galaxies (FR1 and FR2) can be broken into Broad-line radio-galaxies (BLRG) and Narrow-line radio-galaxies (NLRG) based on the angle to the observer's line of sight - BLRGs are aligned closer.

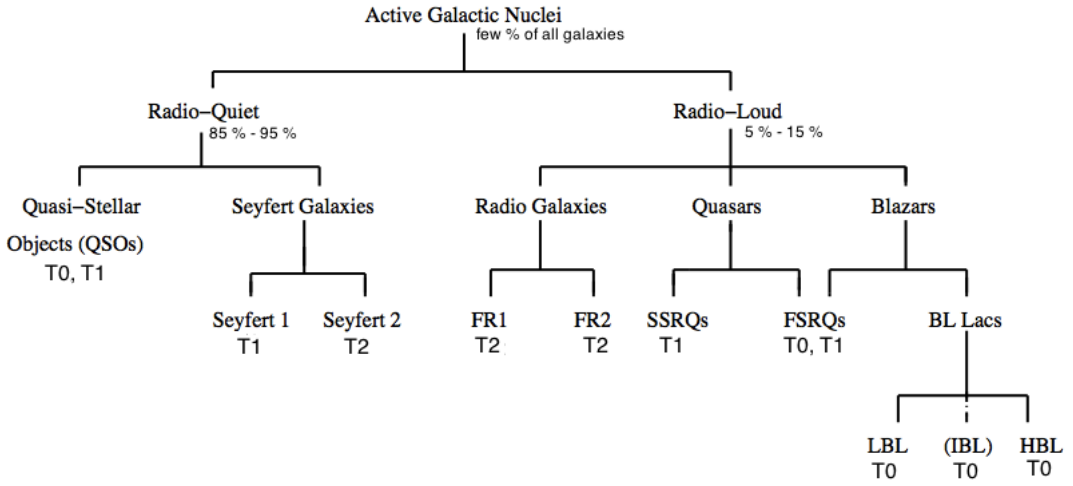

FIGURE 2.2. AGN Classification including types 0, 1 and 2 classification (Adapted from Toner, 2008).

AGN can also be classified based on orientation (figure 2.3). Type 2 AGN are viewed from the side, at right angles to the jet, through the dusty torus which is opaque to broad emission lines, resulting in the observation of only the narrow emission lines and the jets. Examples of Type 2 AGN are Seyfert 2 and narrow-line radio galaxies. As the angle between the observer

TABLE 2.2. AGN properties, adapted from Krolik (1999).

Type	Pointlike	Broadband	Emission Lines	Radio	Variable	Polarized
Radio-loud quasars	Yes	Yes	Both	Yes	Some	Some
Radio-quiet quasars	Yes	Yes	Both	Weak	Weak	Weak
Broad-line radio galaxies	Yes	Yes	Both	Yes	Weak	Weak
Narrow-line radio galaxies	No	yes	Narrow	Yes	yes	No
OVV quasars	Yes	Yes	Both	Yes	Yes	Yes
BL Lac objects	Yes	Yes	Weak/absent	Yes	Yes	Yes
Seyfert type 1	Yes	Yes	Both	Weak	Some	Weak
Seyfert type 2	No	Yes	Narrow	Weak	No	Some

and the jet decreases the core region becomes visible, resulting in both emission line types, the jets and UV thermal radiation being detectable. The AGN is then classed as Type 1. Type 1 AGN are further categorized into core (3C 279) and lobe (3C 207) dominated depending on the location and dominance of the radio emission. Examples of Type 1 include radio-quiet and radio-loud quasars, Seyfert 1 and broad-line radio galaxies. When the jet is aligned at small angles with respect to the observer's line of sight, the AGN is referred to as Type 0 or Blazar. For the purpose of this thesis only the blazar class is described in detail.

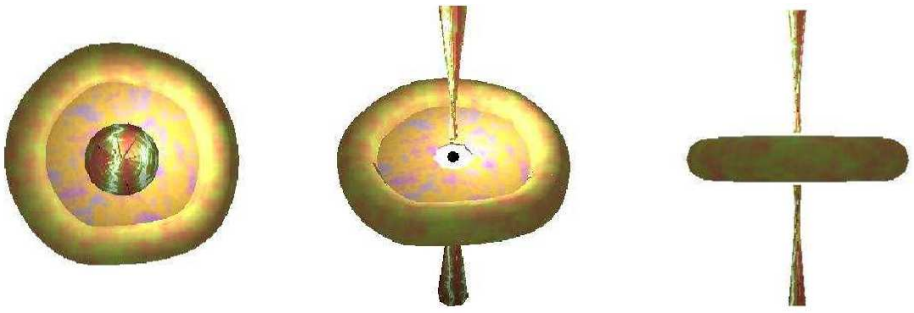

(a) Type 0 (b) Type 1 (c) Type 2

FIGURE 2.3. How AGN classification is influenced by viewing angle (Toner, 2008).

2.2. Blazars

A blazar is an AGN whose jet is aligned with the observer's line of sight. The term blazar, "blazing star", was coined as a joke in 1978 by astronomer Edward Spiegel to unite the two blazar subclasses BL Lacs and Quasars (see below). Due to the small angle with respect to the jet, blazar emission undergoes doppler boosting and superluminal motion and are the most extreme and powerful class of AGN, exhibiting rapid variability and high luminosity with variable polarization.

Blazars emit broadband continuum radiation from radio to γ rays and their Spectral Energy Distributions (SEDs) are characterized by two broad emission peaks. The first peak occurs at

lower energies between radio and X-rays and the emission is generally accepted as being non-thermal synchrotron radiation produced by relativistic electrons in the jet. The higher-energy bump in the γ-ray energy regime is thought to be the result of either leptonic or hadronic processes (figure 2.4).

Blazars are divided into two classes : Flat Spectrum Radio Quasars (FSRQs) and BL Lacs, depending on the presence and strength of emission lines in the optical spectra, optical polarization and the ratio of the X-ray flux to radio flux (table 2.3). There is a continuous sequence from FSRQ to BL Lac, but with overlap and no definite boundaries. FSRQs have strong, clear, distinguishable emission lines in their optical spectra while BL Lacs, named after the prototype source BL Lacerta, exhibit weak or absent emission lines. A blazar is classified as a BL Lac if the equivalent width of the strongest emission line is $< 5\mathring{A}$ and the optical spectrum shows a CaII H/K break ratio < 0.4. This small CAII H/K break ratio ensures that the radiation is predominantly non-thermal (Marcha et al 1996). BL Lacs have more optical flux and optical polarization variability and peak at higher energy. It is generally observed that FSRQs are hosted by more powerful radio galaxies and are more luminous.

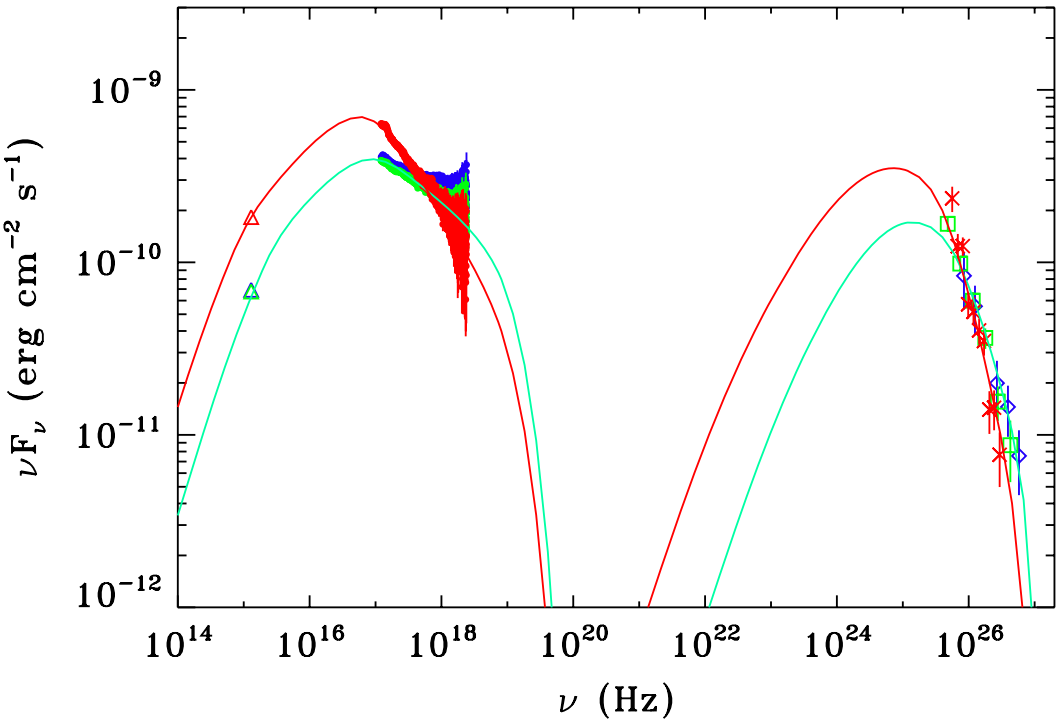

FIGURE 2.4. Multiwavelength SED of the blazar Markarian 421, including XMM-Newton OM (triangles), XMM-Newton EPN (filled circles), MAGIC (squares), Whipple (diamonds) and VERITAS (crosses). SSC model for 2006 data (green) and 2008 data (red) (Acciari et al., 2009).

TABLE 2.3. Blazar class differences

Property	Comments
Emission Lines in Optical Spectra	FSRQs exhibit more emission lines in their optical spectra
Optical Flux Variability	BL Lacs exhibit more variability
Optical Polarization Variability	BL Lacs have more variability in their optical polarization
Higher Energy peak	BLLacs peak higher at higher frequencies
Redshift	FSRQs tend to be at greater distances
Luminosity	FSRQs are in general more luminous

TABLE 2.4. Blazar subclass synchrotron frequencies

Subclass	Peak Frequency Range
LBL	$< 10^{14}$ Hz
IBL	10^{14} - 10^{15} Hz
HBL	$> 10^{15}$ Hz

The energy range of ground-based γ-ray instruments (VERITAS 100 GeV - 30 TeV) is well matched to the energy at which FSRQs and BL Lacs spectra peak. The prototype object BL Lacertae, after first being misidentified as a variable star in 1928, was the first BL Lac discovered (Schmitt, 1968), with observations taken by the Algonquin Radio Observatory 150 ft. telescope. Originally BL Lacs were almost exclusively discovered in radio waves or X-rays and classified as either Radio discovered BL Lacs (RBL) or X-ray discovered BL Lacs (XBL). However, improvements in detectors led to BL Lac detections at optical and γ-ray wavelengths. As BL Lacs exhibit weak optical emission lines, if any, it can be difficult to constrain their redshifts. For example, despite multiwavelength observations and detailed SED modeling, the redshift of BL Lac object PKS 1424+240 has only been constrained to $z < 0.66$ (Acciari et al., 2010).

BL Lacs are further divided into subclasses, based on the frequency at which the synchrotron peak occurs (table 2.4) in the electromagnetic spectrum, into Low frequency BL Lac (LBL), Intermediate frequency BL Lac (IBL) and High frequency BL Lac (HBL). Originally the blazars were classified based on the detection method: Radio BL Lac (RBL) and X-ray BL Lac (XBL). LBLs were typically RBL and HBLs were XBLs. IBLs were introduced into blazar classification as instrumentation became more sensitive to bridge the gap between LBL and HBL.

Observations show that the ratio of the amplitude of the synchrotron peak to the high energy peak is also a function of blazar subclass. FSRQ spectra tend to be dominated by γ-ray emission, having a higher amplitude second peak. In the case of LBLs, both peaks are, on average, similar in amplitude. In contrast, HBLs appear to be more powerful at lower energies with stronger synchrotron peaks. There also appears to be a trend with decreasing observed bolometric luminosity from FSRQs $\rightarrow$ HBLs, known as the "blazar sequence". The concept behind the "blazar sequence" is that the most powerful BL Lac objects and FSRQs (stronger radio sources than BL Lacs) should have relatively small amplitude synchrotron peaks and that as radio power decreases the synchrotron peak amplitude increases (Fossati et al., 1998). In 1998,

the broadband SEDs of three samples of blazars (one FSRQ and two BL Lac) with different radio luminosities (Einstein Slew Survey sample and 1Jy Blazar sample) were studied in detail to confirm this sequence (figure 2.5). However, a study performed by Padovani contradicts this and shows no evidence for an anticorrelation between radio luminosities and synchrotron peak frequency (Padovani, 2007) (figure 2.6). As the theory of the blazar sequence has not been conclusively validated or rejected, studies are ongoing.

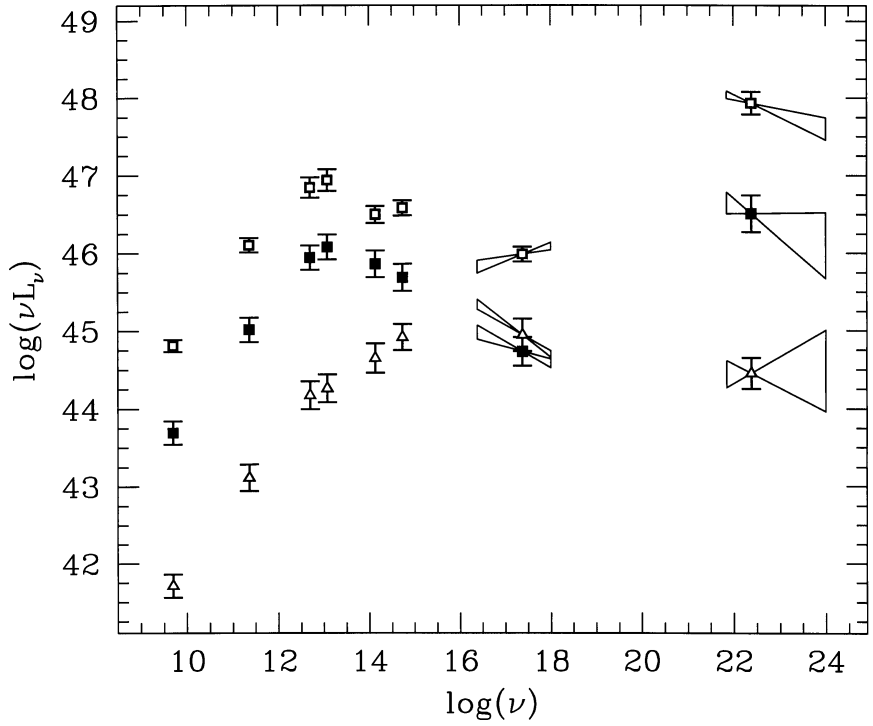

FIGURE 2.5. From top to bottom (referring to radio luminosity) FSRQs (empty boxes), 1 Jy BL Lac sample (filled boxes) and Slew survey BL Lac sample (triangles) - (Fossati et al., 1998).

2.3. Variability

Blazars exhibit extreme flux variability at all wavelengths. The rapid variability, in some cases, is as fast as minutes. For example, γ-ray flux variability on a timescale of 15 minutes has been observed from Markarian 421 (Gaidos et al., 1996), and suggests the γ-ray emitting region is very compact (figure 2.7). Equation 1 can be used to constrain the radius of the emitting region:

$$R \leq \frac{\delta c \Delta t}{1+z} \tag{1}$$

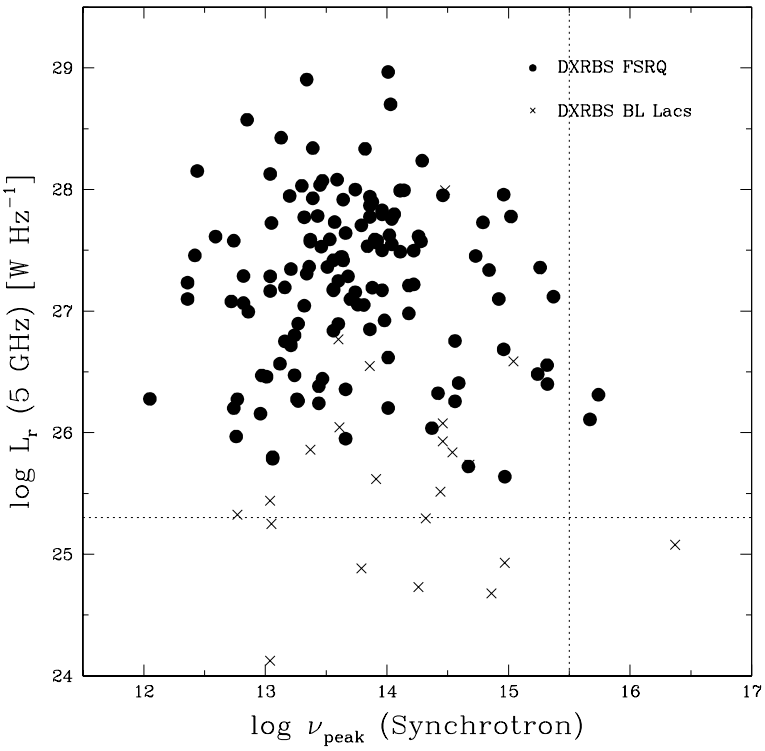

FIGURE 2.6. Radio power at 5 GHz vs. the synchrotron peak frequency for FSRQ (filled points) and BL Lacs (crosses) for the DXRBS sample. The dotted lines denote the two quadrants (top-left and bottom-right) occupied by the sources studied by Fossati et al 1998. (Padovani, 2007).

where R is the radius of the emitting region, δ is the Doppler factor (the ratio of the intrinsic frequency to the frequency the observer sees), Δt is the observed variability timescale, z is the redshift of the galaxy and c is the speed of light.

During periods of significant increases in activity, also known as flaring, the earliest photons correspond to the closest part of emitting region (assumed spherical) to the observer so these photons arrive first. The final photons at this higher energy signify the furthest edge of the emitting region and the time difference is referred to as the variability timescale in equation 1 above. From mulitwavelength SED modeling the doppler factor can be estimated. Assuming a spherical emitting region and a doppler factor of 1, with a redshift of z = 0.031 and a variability timescale of 30 minutes, the radius of the emitting region of Markarian 421 can be constrained to a small value of R $\leq 5.24\times 10^{11}$ m.

2.4. Relativistic Jets

As discussed in section 2.2, blazars are a class of AGN that have a collimated relativistic jet aligned very closely with the observer's line of sight. Some of the most powerful and energetic

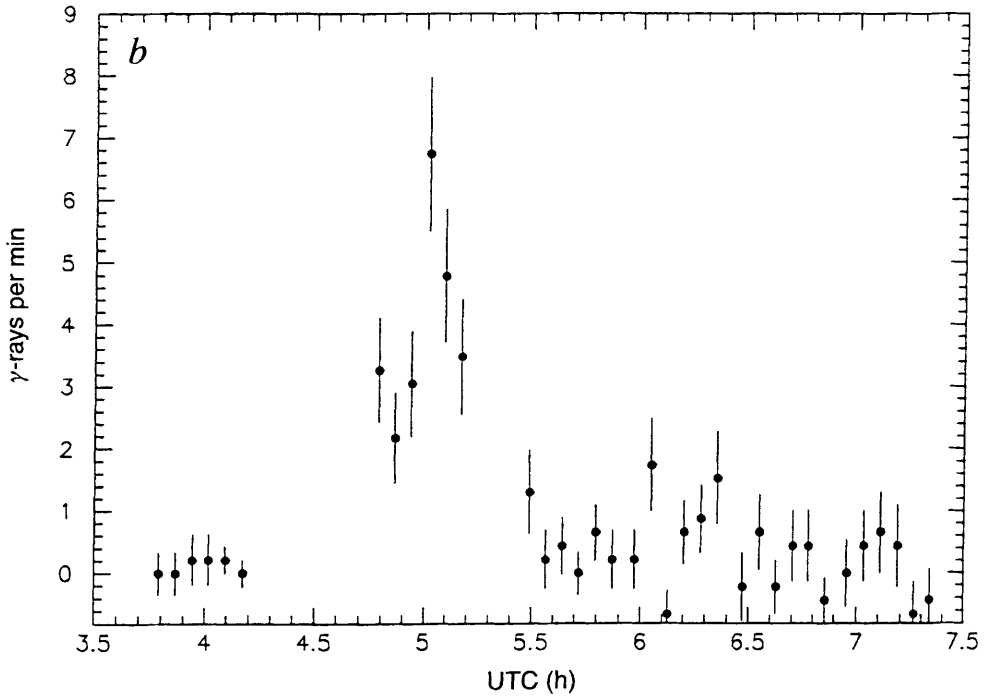

FIGURE 2.7. Whipple 10m lightcurve for Markarian 421 from May 15th 1996, binned in 4.5 minute intervals - (Gaidos et al.,1996)

processes in the universe take place in these jets. The jets are inhomogeneous in nature and are on parsec scales, evident from VLBA radio morphology observations. Blazar observations are crucial to investigating the origin, constitution and function of jets, in addition to understanding the mechanisms behind their formation, acceleration and collimation. It is reasonable to assume the jets are comprised of a combination of electron-positron pairs and proton-electron pairs. Using X-ray blazar observations, Sikora & Madejski (2000) put strong constraints on the composition of the plasma jets. The study demonstrated that using a pure electron-positron model to describe the jet significantly over-predicted the soft X-ray radiation. In comparison, a pure proton-electron model under-predicted the X-ray emission. A widely accepted two-flow model was proposed by Sol et al., (1989) that hypothesized the jets consisted of an inner spine of electron-positron pairs surrounded by a plasma of proton-electron pairs. The population of electron-positron pairs in the ultra-relativistic spine is believed to originate in the innermost part of the accretion disk and can account for the VLBI parsec-scale jet and the observed superluminal motion. In the outer less relativistic surrounding plasma, the particle population is assumed to come from the entire accretion disk and is thought to be responsible for the large kiloparsec-scale jet. Adaptations of this model have proved very successful in subsequent studies. In order for mass to accrete efficiently onto the SMBH, a small percentage of the angular momentum of in-falling material needs to be extracted, resulting in the formation of rotating wind-like outflows. Ejection of

angular momentum is very efficient in AGN due to the magnetic field. The accreted mass rate $\dot{M}_{accretion}$ of $\sim 1\%$ of the total mass is extracted via the jets corresponding to the majority of the angular momentum $\dot{M}_{jet}$ being removed (Spruit, 1996). Acceleration and collimation of the plasmas in this accretion "wind" results in the relativistic jets.

2.4.1. Acceleration. The exact mechanism behind the acceleration of the particles in the accretion wind to relativistic speeds is unknown but 2 possibilities are discussed here:

2.4.1.1. *Magnetic Field-driven Acceleration.* There are 3 types of magnetic field-driven acceleration processes described here:

• Toroidal magnetic field acceleration, also known as the "uncoiling spring" model (Uchida & Shibata, 1985), can describe the initial acceleration of the infalling matter. In short, the rotation of the magnetic field lines emerging from the accretion disk produces an upwards force, similar to a coiled up spring (figure 2.8 (a)). An Alfvén wave develops resulting in an initial acceleration of the plasma. However, the collimation produced is weak and only holds in simulations for one or two rotations.

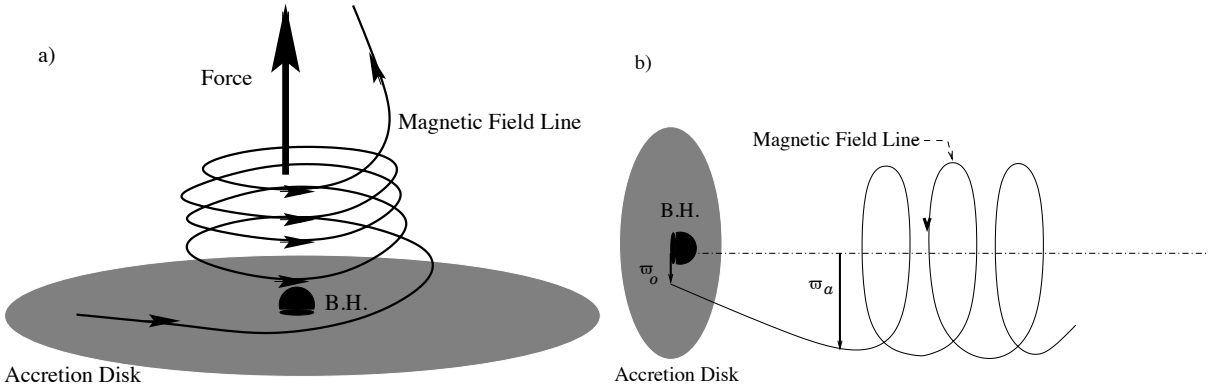

FIGURE 2.8. Illustrations of Toroidal Magnetic Field Acceleration (a) and Magneto-centrifugal acceleration from the accretion disk (b), (Sauty, Tsinganos & Trussoni, 2002)

• Magneto-centrifugal acceleration from the accretion disk employs a combination of centrifugal and a strong poloidal magnetic field (figure 2.8 (b)). This is the most frequently used acceleration model and utilizes classical acceleration mechanisms (Blandford & Payne, 1982). The model assumes the jet plasma consists mainly of proton-electron pairs, as electron-positron pairs would be more difficult to accelerate using this scenario. The subsequent conversion of Poynting energy flux to kinetic energy flux results in acceleration and creates plasma corotation. Although simulations show that the magnetic-centrifugal acceleration from the accretion disk models hold further out than the toroidal magnetic field acceleration models, it is only valid up to the Alfvén radius

(when the magnetic pressure is equal to the ram pressure). In addition to this, an unrealistically high magnetic field is required and an insufficient amount of mass is accreted.
• Magneto-centrifugal acceleration from the BH magnetosphere. This process involves the conversion of Poynting flux to kinetic energy. The differences between this and the previous are the origin of the magnetic field, in this case the BH, and the model is valid is for electron-positron pairs due to sufficient energy from the BH magnetosphere providing enough acceleration for a leptonic jet. Studies show that both mechanisms could be occurring simultaneously (Sol & Pelletier, 1989).

2.4.1.2. *Non-magnetic Field-driven Acceleration.* Two types of non magnetic field driven acceleration are discussed here:
• Radiative acceleration. An example of radiative acceleration is the "Compton Rocket" model. The radiative pressure is produced via annihilation of the electron-positron pair plasma, which in turn accelerates the plasma (O'Dell, 1981). Electron-positron disk wind models suggest the relativistic pressure is a result of dust or line emission. Radiative acceleration models are sufficient to explain radio quiet AGN accretion winds. However, as simulations indicate the maximum outflow speed is $< 50{,}000$ km s^{-1} (Sauty, Tsinganos & Trussoni, 2002), radiation driven acceleration can not completely explain the emission from radio loud AGN. It is reasonable to assume radiatively driven acceleration is taking place but only contributes a small portion to the overall acceleration.
• Thermal acceleration. Thermal acceleration models generally require a hot corona surrounding the accretion disk. Initially used to explain solar winds, thermal acceleration models can be modified to incorporate relativistic outflows as in the case of AGN. The models work efficiently when combined with magneto-centrifugal driven acceleration from the BH magnetosphere models.

2.4.2. Collimation. The mechanism behind the collimation of the relativistic jets is unknown but several possible mechanisms are described here:
• Pressure gradient collimation. Collimation due to pressure, also known as thermal confinement, would occur if the pressure of the surrounding material was higher than the pressure of the outflow, resulting in a pressure gradient (Sauty et al., 2002). In simple terms, the surroundings would pressurize the outflow into a collimated beam. A magnetic field component is also required, as without it the outflow would continue to be externally pressurized until it collapsed onto its rotational axis. A strong magnetic field implies a fast rotation rate. If the rotation rate is fast enough, the centrifugal force should counteract the collapsing pressure.
• Toroidal magnetic field collimation. The concept behind toroidal magnetic field collimation is that the outflows carry electric current that in turn confines the outflow, i.e. not all of the Poynting flux is converted into kinetic energy and the remaining Poynting flux is responsible for

the jet collimations. Spruit (1996) supported this theory through a high resolution polarization study from VLBI observations.

• Poloidal magneto-centrifugal collimation. Poloidal magneto-centrifugal models are sufficient to account for the collimation from the accretion disk out to the Alfvén radius, where magnetic field forces dominate. Beyond the Alfvén radius, the jet becomes super-Alfvén and hydrodynamic forces which do not support collimation dominate. Spruit (1996) provides evidence that supports poloidal magnetic-centrifugal collimation models with magnetic field measurements.

Realistically, the jet collimation is likely the result of a combination of both pressure and magnetic confinement. For example, in a pure magnetic jet, without rotation, where the collimation is solely due to either toroidal or poloidal magnetic field, changes in the surrounding magnetic fields would result in instabilities disrupting the collimation. Similarly, in a pure hydrodynamic flows, hydrodynamic changes would influence the jet.

2.5. Jet Dynamics

Inside the relativistic plasma jets are areas of denser material e.g. shocks or knots containing photons, that travel along the jet at relativistic speeds with bulk (for a mass of photons) Lorentz factor:

$$\Gamma = \frac{1}{\sqrt{1-\beta^2}} \tag{2}$$

where

$$\beta = \frac{v}{c} \tag{3}$$

where v is the velocity at which the knot is traveling. The knots are likely a significant cause of variability. When knots containing photons traveling at a relativistic velocity at a small angle to the observer's line of sight, the photons are beamed in the direction of the observer into a cone of half opening angle

$$\theta = \frac{1}{\Gamma} \tag{4}$$

where Γ is the bulk Lorentz factor described in equation 2. This collimated emission results in superluminal motion, boosted luminosity and increased variability.
The Doppler factor is a measure of Doppler Boosting:

$$\delta = \frac{1}{\Gamma(1-\beta\cos\theta)} \tag{5}$$

Therefore for a continuous jet, the intrinsic luminosity can be inferred from the observed luminosity from the equation

$$L_{obs} = \delta^{2+\alpha} L_{rest} \tag{6}$$

where α is the spectral index of the source and

2.5.1. Superluminal Motion. Superluminal motion is the name given to the "apparent" faster than light motion, v > c. Figure 2.9 is a schematic diagram of how superluminal motion occurs. A source is moving with speed v or θc towards the observer at an angle θ to the observer's line of sight. A pulse of photons is emitted at point A and a time t=0, and a second pulse is emitted at a time ΔT at point B. By this time the source will have travelled $vt_1 \sin\theta$ or $\theta ct_1 \sin\theta$ perpendicular to the observer's line of sight. The time difference between the arrival of the two pulses at the observer is

$$\Delta t_{obs} = \Delta t(1 - \beta \cos\theta) \tag{7}$$

The transverse speed, β_{obs} is then

$$\beta_{obs} = \frac{\beta \sin\theta}{1 - \beta \cos\theta} \tag{8}$$

β_{obs} is at a maximum when cos θ=β, and will be greater than 1 for values of $\beta > 0.7$

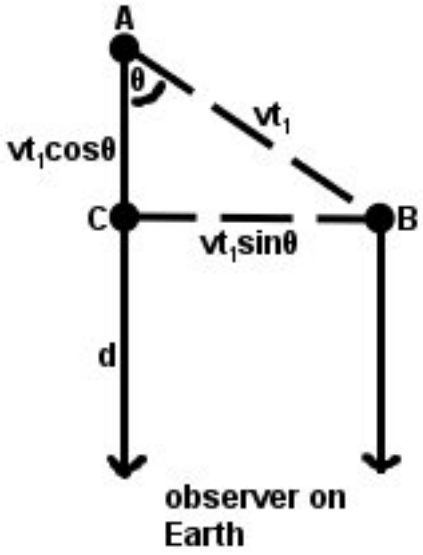

FIGURE 2.9. Illustration of superluminal motion (physicsmadeeasy.wordpress.com/physics-made-easy/cosmology-iii/).

2.6. Synchrotron Radiation

As mentioned before, the lower energy bump of the blazar SED is generally accepted as being synchrotron emission. Synchrotron radiation is the result of accelerating relativistic electrons to very high energies in a curved path through magnetic fields, emitting radiation in the range of radio waves to X rays. The electrons gyrate around the magnetic field direction with gyrofrequency

$$\nu_g = \frac{eB}{2\pi\gamma m_e} \tag{9}$$

where B is the magnetic field strength and γ is the Lorentz factor of an electron. The electron is accelerated towards the centre of the orbit.

Synchrotron emission is extremely collimated and highly polarized in short pulses. It is broadband continuum emission from radio to x-rays and is comprised of overtones of ν_g. The peak frequency is close to the characteristic frequency ν_c given by:

$$\nu_c = \frac{3\gamma^2 eB\sin\alpha}{4\pi m_e} \tag{10}$$

where α is the pitch angle, the scattering angle between ν and the magnetic field direction. The maximum frequency is related to pulse width by

$$w \sim \frac{1}{\Delta t} \tag{11}$$

From this, the spectrum of synchrotron radiation from a given electron (Longair, 2010) is defined as

$$j_{(\nu)} = \frac{\sqrt{3}e^3 B\sin\alpha}{4\pi\varepsilon_0 c m_e} F\left(\frac{\nu}{\nu_C}\right) \tag{12}$$

where F is defined as the function

$$F(x) = x\int_x^\infty K_{\frac{5}{3}}(z)dz \tag{13}$$

with K as the modified Bessel function of order 5/3
The frequency of the radiation emitted depends on the energy of the initial particle. Figures 2.10 and 2.11 show the spectrum of the synchrotron radiation of a single electron with linear axes and logarithmic axes, respectively.

The total power radiated for a single relativistic electron can be expressed by

$$P_s = 2\sigma_T\beta^2\gamma^2 U_B c\sin^2\alpha \tag{14}$$

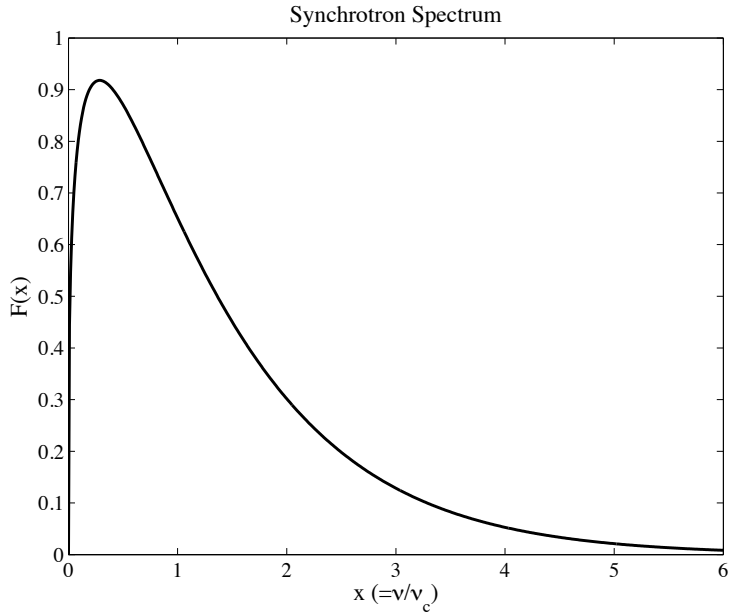

FIGURE 2.10. The spectrum of the synchrotron radiation of a single electron with linear axes.

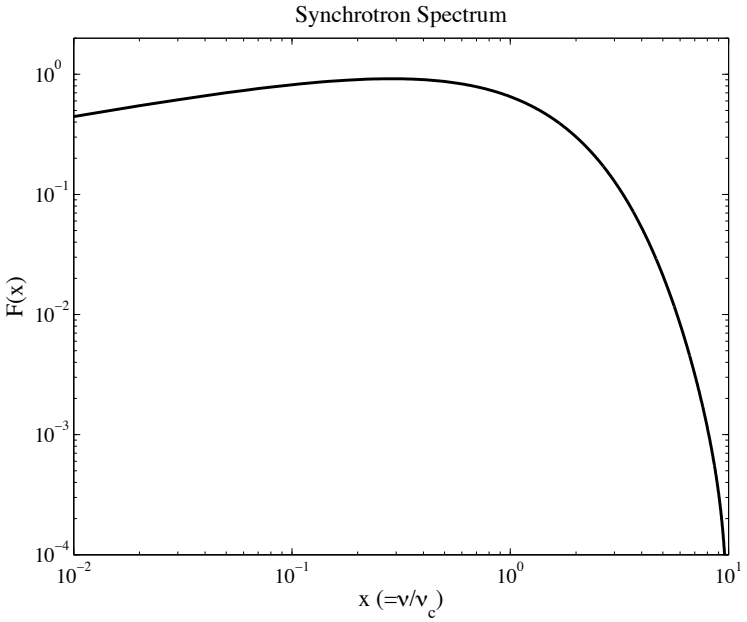

FIGURE 2.11. The spectrum of the synchrotron radiation of a single electron with logarithmic axes.

U_B is the magnetic energy density and the Thompson cross-section of an electron is σ_T.
The relativistic electrons are scattered repeatedly and the distribution of pitch angle eventually becomes random. Averaging over pitch angle :

$$< \beta_\perp >= \frac{\beta^2}{4\pi} \int \sin^2 \alpha d\Omega = \frac{2\beta^2}{3} \tag{15}$$

and $\sin^2\alpha$ becomes 2/3
The total power radiated for a single relativistic electron becomes

$$\frac{dE}{dt} = P_s = \frac{4}{3}\sigma_T \beta^2 \gamma^2 c U_B \tag{16}$$

The characteristic lifetime for an electron ε (Bradt, 2010) for $\beta \approx 1$ and $mc^2 = 8.2 \times 10^{14}$ J

$$\tau = \frac{5.16mc^2}{B^2 U_B} = \frac{5.16}{B^2\gamma} \tag{17}$$

This demonstrates that the highest energy electrons cool quicker.
The electron spectrum can be calculated by convolving the electron emissivity over the electron distribution. The electron distribution function can be expressed in the form

$$N(E) = KE^{-p} \tag{18}$$

The radiation spectrum of the electron distribution is now

$$J(\nu) = \frac{\sqrt{3}e^3 BK}{4\pi\varepsilon c m_e} \left(\frac{3eB}{2\pi\nu m_e^3 c^4} \right)^{\frac{p-1}{2}} a(p) \tag{19}$$

where the constant a depends on the spectral energy index p

$$a(p) = \frac{\sqrt{\pi}}{2} \frac{\Gamma\left(\frac{p}{4} + \frac{19}{12}\right) \Gamma\left(\frac{p}{4} - \frac{1}{12}\right) \Gamma\left(\frac{p}{4} + \frac{5}{4}\right)}{(p+1)\Gamma\left(\frac{p}{4} + \frac{7}{4}\right)} \tag{20}$$

2.6.1. Synchrotron Self Absorption. For every radiative process there is a corresponding absorption process. Synchrotron Self Absorption occurs when synchrotron photons are reabsorbed via interactions with charges in the magnetic field. This happens when the electron temperature exceeds the temperature of the source and the source becomes self-absorbed. Synchrotron Self Absorption significantly changes the source spectrum and needs to be taken account of in SED modeling.

2.7. Leptonic Models of Gamma-Ray Production

The second, higher energy peak in blazar SEDs is believed to be the result of either leptonic or hadronic processes or possibly a combination of both. Due to time constraints, only leptonic models will be used to describe the SED results in this thesis.

Leptonic models involve the process of Inverse Compton (IC) scattering of a relativistic electron with a soft photon. After an initial collision with an electron, the soft photon is accelerated to a higher energy (figure 2.12).

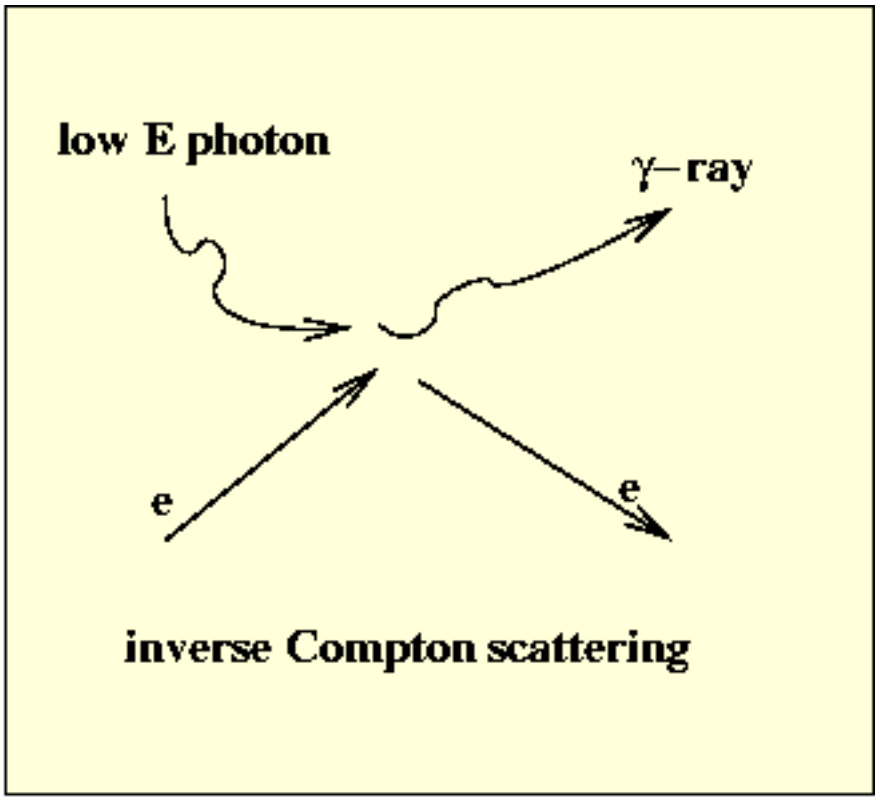

FIGURE 2.12. An illustration of Inverse Compton scattering of a low energy photon up to γ-ray energies (www.cv.nrao.edu).

The cross section for inverse Compton scattering depends on the incoming photon energy in the electron's rest frame

$$E'_{ph} = \gamma E_{ph}(1 + \beta \cos\theta) \tag{21}$$

where γ is the electron Lorentz factor, E_{ph} is the photon energy in the observer's frame and θ is the angle of collision between the electron and photon.
For $E_{ph} \leq m_e c^2$, elastic scattering is occurring and in the Thomson regime. For $E_{ph} \geq m_e c^2$, inelastic scattering is occurring in the Klein-Nishina regime.

To derive the inverse Compton scattering equations we start with the non-relativistic case (Thomson regime) and transform to the relativistic case. In the rest frame of the electron, the Poynting flux can be defined as

$$\overrightarrow{S} = \frac{c}{4\pi}\overrightarrow{E} \times \overrightarrow{H} \tag{22}$$

The scattered radiation has power

$$P = |\overrightarrow{S}|\delta_T \tag{23}$$

and can be written as

$$P = \delta_T c U_{rad} \tag{24}$$

where U_{rad} is the energy density of the incident radiation. When considering relativistic electrons, the Thomson scattering formula is only valid in the electron's rest frame

$$P' = \delta_T c U'_{rad} \tag{25}$$

In order to transform to the observer's frame. let P=P$'$

$$P = \delta_T c U'_{rad} \tag{26}$$

From equation 5, concerning the relativistic Doppler factor, the frequency in the electron's rest frame can be written as

$$\nu' = \nu[\gamma(1 + \beta\cos\theta)] \tag{27}$$

The photon number in the electron's rest frame can be described by

$$N = N[\gamma(1 + \beta\cos\theta)] \tag{28}$$

In the observers frame U_{rad}=Nhν. Similarly in the electron's rest frame

$$U'_{rad} = N'h\nu' = N[\gamma(1 + \beta\cos\theta)]h\nu[\gamma(1 + \beta\cos\theta)] = U_{rad}[\gamma(1 + \beta\cos\theta)]^2 \tag{29}$$

It is evident that the transformation between energy density $U_{rad}{}'$ and U_{rad} depends on the collision angle θ between the incident photon and electron directions. Integrating in all directions of the observer's frame yields

$$U'_{rad} = \frac{U_{rad}}{4\pi} \int_{\phi=0}^{2\pi} \int_{\theta=0}^{\pi} [\gamma(1 + \beta \cos\theta)]^2 \sin\theta d\theta d\phi \tag{30}$$

where ϕ is the azimuthal angle around the x-axis. The energy density in the electron's rest frame is therefore

$$U'_{rad} = U_{rad} \left(\frac{4\gamma^2}{3} - \frac{1}{3}\gamma^2(1 - \beta^2) \right) \tag{31}$$

As γ^2(1-β^2)=1, the energy density in the electron's rest frame can now be written as

$$U'_{rad} = U_{rad} \frac{4(\gamma^2 - 1/4)}{3} \tag{32}$$

The total power radiated after inverse Compton scattering, in the electron's rest frame is now

$$P = \frac{4}{3}\delta_T c U_{rad}(\gamma^2 - \frac{1}{4}) \tag{33}$$

By subtracting the initial power and replacing γ^2-1 with $\beta^2\gamma^2$, the net power radiated from inverse Compton scattering is

$$P_{IC} = \frac{4}{3}\sigma_T c \beta^2 \gamma^2 U_{rad} \tag{34}$$

The ratio of inverse Compton to synchrotron radiation losses is given by:

$$\frac{P_{IC}}{P_S} = \frac{U_{rad}}{U_B} \tag{35}$$

2.7.1. Klein-Nishina Limit. The scattering process is inelastic, resulting in the electron receiving a large recoil, losing most of its energy and an increase in energy for the photon. When the energy of the incident photon is greater that $m_e c^2$ the cross-section decreases along with the rate of collisions. By multiplying the rate of collisions by the average energy per collision the power radiated can be defined as

$$P_{IC} = \frac{3}{8}\delta_T m_e^2 c^5 \int d\varepsilon \frac{\eta(\varepsilon)}{\varepsilon} \left[\log \frac{2\gamma_\varepsilon}{m_e c^2} + \frac{1}{2} \right] \tag{36}$$

One result is the scattered photon spectrum will be steeper than in the Thomson scattering regime.

Though leptonic models agree on the process of inverse Compton scattering, they differ on the origin of the population of photons.

2.7.2. Synchrotron Self Compton. In the Synchrotron Self Compton (SSC) model, the population of photons involved in the inverse Compton scattering process is the synchrotron radiation population. A population of relativistic electrons is accelerated through magnetic

fields and produces synchrotron radiation photons. The synchrotron photons then collide with the original population of relativistic electrons and are inverse Compton scattered to higher energies - "Self Comptonization". The first SSC model was published in 1969 (Ginzburg and Syrovatskii, 1969) and subsequent models have been developed over the years to incorporate emission processes in the relativistic jet and multiple emission regions. A one-zone SSC model that assumes the synchrotron radiation and inverse Compton scattering occur in the same region is applied to multiwavelength SEDs in this thesis. The region (possibly a knot or shock) travels along the jet at a relativistic velocity (v=βc) through a magnetic field of strength B with a radius R and exhibits a variability timescales t_{var}

SSC accounts for the observed correlation in X-ray and γ-ray variability while orphan γ-ray flares contradict the model. Multiwavelength SED modeling suggests that SSC models work well for HBLs but not as well for FSRQs.

2.7.3. External Compton. In contrast to the SSC model, the population of seed photons that are inverse Compton scattered are surrounding external photons. This external photon population could enter the jet directly from the accretion disk or dusty torus. Another explanation (Ghisellini et al., 1996) is that the jet or accretion disk heats the broadline region resulting in synchrotron photons being reflected back into the jet. In External Compton (EC) models, the magnetic field strength is predicted to be significantly lower in order for the energy density of the external photons to be higher than the synchrotron radiation photons. With the launch of Fermi in June 2008 and the increase in the rate of discovery of FSRQs and LBLs producing γ rays, EC and hybrid SSC+EC models are becoming more popular as theories to describe blazar SEDs.

2.7.4. One-zone SSC and SSC+EC model. The one-zone SED model used in this thesis is from Krawczynski et al., (2004). The model assumes a spherical emitting region of radius R and uniform magnetic field B, moving towards the observer at an angle θ with doppler factor δ, and bulk Lorentz factor Γ. The emission population is assumed to be filled with an homogeneous non-thermal electron population described by a broken power law with break energy: p=2 $<$ break energy $>$ p=3. It models the synchrotron and inverse Compton correcting for synchrotron self-absorption and EBL absorption (Franceschini et al., 2008). The model also includes the option to incorporate external seed photons acting as a SSC+EC model: The input parameters are

- redshift
- bulk Lorentz factor of the emitting volume
- angle to the observer's line of sight
- magnetic field strength
- electron energy density
- minimum and maximum electron energy

• electron energy(peak in νF_ν at the break of the powerlaw between the minimum and maximum energies
• differential spectral index between the minimum energy and the break energy
• differential spectral index between the break energy and the maximum energy
• mass of the black hole
• accretion rate in solar masses per unit time
• height of emitting volume above the accretion disk in schwarzschild radii

The mass of the black hole and the accretion rate determine the density of the seed photons necessary for EC emission to occur. The electron spectrum, assumed to be from 10^4 to $10^{27.5}$ Hz, the synchrotron spectrum between 10^4 and 10^{15} Hz, the SSC spectrum between 10^{18} and $10^{27.5}$ Hz and the EC spectrum between 10^{12} and $10^{27.5}$ Hz are calculated based on the above parameters. The SSC and EC components are summed to determine the overall IC spectrum.

The fitting process involves assuming a redshift value, a doppler factor and upper limits on magnetic field strength B (e.g. $\Gamma < 50$, B < 1G) based on previously published results. The individual parameters are adjusted until the combined SSC and EC (if applicable) represent the shape and amplitude of the data. The model parameters are then compared with expected results to see if they are consistent. For example, the radius of the emitting zone can be estimated from equation 1 if a short-term variability timescale is known.

For pure SSC, δ and B can be calculated if the frequency of both peak (ν_s and ν_{IC}) and the luminosities (L_s and L_{IC}) are known

$$B\delta^3 \simeq (1+z)\sqrt{\frac{2L_s^2}{L_c t_{var}^2 c^3}} \tag{37}$$

or

$$B\delta \simeq (1+z)\frac{\nu_s^2}{3.7\times 10^6 \nu_{IC}} \tag{38}$$

When an EC component is included B can be estimated equations 37 and 38 from

$$B = \left(3.6\times 10^8 \Gamma \frac{\nu_s \nu_{o,15}}{\nu_{IC}}\right) \tag{39}$$

where $\nu_{o,15}$ is the flux at 10^{15} Hz.

2.8. Hadronic Models

In hadronic models, protons are accelerated in the jet due to material falling inwards onto a SMBH from the accretion disk. The protons then interact and produce γ rays. One requirement is that the protons must be energetic enough ($> 10^{16}$ eV) to undergo pion production. Hadronic models generally require a larger magnetic field strength than leptonic models. There are two accepted hadronic models:

• high-energy proton interacting with either a γ_{soft} or another proton
• direct synchrotron radiation
The first model involves two possible interactions resulting in pion decay, pion cascades or a combination of both.

$$p + p \rightarrow \pi^0 + hadronic\ debris \tag{40}$$

$$p + p \rightarrow \pi^{\pm} + hadronic\ debris \tag{41}$$

$$p + \gamma_{soft} \rightarrow p + \pi^0 + hadronic\ debris \tag{42}$$

$$p + \gamma_{soft} \rightarrow n + \pi^{\pm} + hadronic\ debris \tag{43}$$

If the original proton has a sufficiently high energy, this could result in pion decay producing two hard γ rays.

$$\pi^0 \rightarrow 2\gamma_{hard} \tag{44}$$

The charged pions could decay to produce pion cascades

$$\pi^{\pm} \rightarrow \mu^{\pm} + \upsilon_{\mu} \tag{45}$$

which further cascades to produce neutrinos, electrons and positrons via pair production and eventually γ rays via bremsstrahlung radiation:

$$\mu^{\pm} \rightarrow e^{\pm} + \upsilon_e + \upsilon_{\mu} \tag{46}$$

$$e^{\pm} \rightarrow e^{\pm} + \gamma_{hard} \tag{47}$$

In the second hadronic model as demonstrated in a study of Markarian 501 (Aharonian et al, 2000), very high energy ($> 10^{19}$ eV) protons undergo synchrotron radiation. This would require a large magnetic field strength of 30 - 100 G, considerably higher than in the leptonic models. Hadronic models can be validated if cosmic rays with emission greater than 10^{20}eV are detected from blazars or from detailed multiwavelength SED modeling (The Hillas condition in pure leptonic models prohibits this). If validated, the theory behind hadronic models would significantly help explain the origin of charged cosmic rays.

2.9. Motivation

This thesis presents a detailed comparison study of an extensive dataset of a subset of two BL Lac classes : IBLs and HBLs. These subclasses were chosen based on the position of the Inverse Compton peaks in their spectra which coincides with the sensitivity ranges of the GeV and TeV instruments. The study consists of a selection of 6 northern hemisphere sources: 3 IBLS (the complete VERITAS IBL collection to date) and 3 HBLs (table 2.5). The criteria for source selection was a detection of at least 5 σ (or TS $>$ 25) with both the Fermi LAT satellite and the VERITAS array, in addition to another detection at lower energies. SED modeling is performed on simultaneous Fermi LAT and VERITAS data, accompanied by contemporaneous radio to X-ray data where available. Archival data, when relevant, is also included.
The main objectives of this study were to:
• generate detailed source spectra and lightcurves
• constrain the inverse Compton peak using MeV - TeV data for the first time
• constrain redshifts for sources of uncertain redshifts
• construct multiwavelength spectral energy distributions
• perform SED modeling and compare SSC to SSC +EC fits
• examine for blazar subclass properties

2.9.1. 1ES 1959+650. 1ES 1959+650 is a low-redshift (z = 0.048) X-ray selected HBL known to exhibit extreme flaring. It was originally suggested as a TeV radiation emitter by (Stecker, DeJager & Salamon, 1996) based on its close distance and the theory that XBLs are TeV sources. The study used the 3rd EGRET catalog source information and an SSC model, and predicted that 1ES 1959+650 would be the third strongest TeV blazar after Markarian 421 and Markarian 501. The HBL was first seen at TeV energies at a 3.9σ level by the Seven Telescope Array in Utah after 57 hours of observations (Nishiyama et al., 1999). From May to July 2002, the Whipple 10m telescope with 39 hours of data, detected the source and noted the high flux activity, up to 5 times the Crab Nebula flux, with a variability timescale on the order of 7 hours (figure 2.13). This flaring activity was only seen at TeV energies and not in the radio to X-ray energy regime and were christened “Orphan” flares. Orphan flares imply a second population of photons suggesting an EC component.

Despite this, 1ES 1959+650 is generally fit well with both the leptonic SSC and leptonic-hadronic hybrid model at lower energies (figure 2.14).

2.9.2. 1ES 0806+524. 1ES 0806+524 is a relatively weak TeV emitting HBL with a moderate redshift of z =0.138. The source was identified as a BL Lac in 1996 after radio observations by the Green Bank 19m telescope and Einstein Slew Survey X-ray observations (Schachter et al., 1993). It was predicted to be a TeV emitter due to the presence of relativistic electrons and seed photons evident from the EGRET detection (Costamante & Ghisellini, 2002). The first TeV detection (6.3σ) of 1ES 0806+524 was obtained by VERITAS between November 2006 and

TABLE 2.5. Selected Blazar Properties

Name	Type	RA	Dec	z	GeV Discovery	GeV Publication	TeV Discovery	TeV Publications
1ES 1959+650	HBL	19:59:59.9	+65 08 55	0.048	EGRET	Hartman et al., 1999	Telescope Array	Nishiyama et al., 1999
1ES 0806+524	HBL	08:09:59	+52 19 20	0.138			VERITAS	Acciari et al., 2009
1ES 0502+675	HBL	05:07:56.2	+67 37 24	0.231 (uncertain)	Fermi LAT	Abdo et al., 2009	VERITAS	
W Comae	IBL	12:21:31.7	+28 13 59	0.102	EGRET	Hartman et al., 1999	VERITAS	Acciari et al., 2008
PKS 1424+240	IBL	14:27:00	+23 47 40	< 0.66	Fermi LAT	Abdo et al., 2009	VERITAS	Acciari et al., 2010
3C66A	IBL	02:22:41.6	+43 02 35.5	0.444, uncertain	EGRET	Hartman et al., 1999	Crimea	Neshpor et al., 1998

RA and Dec coordinates are J2000 epoch coordinates

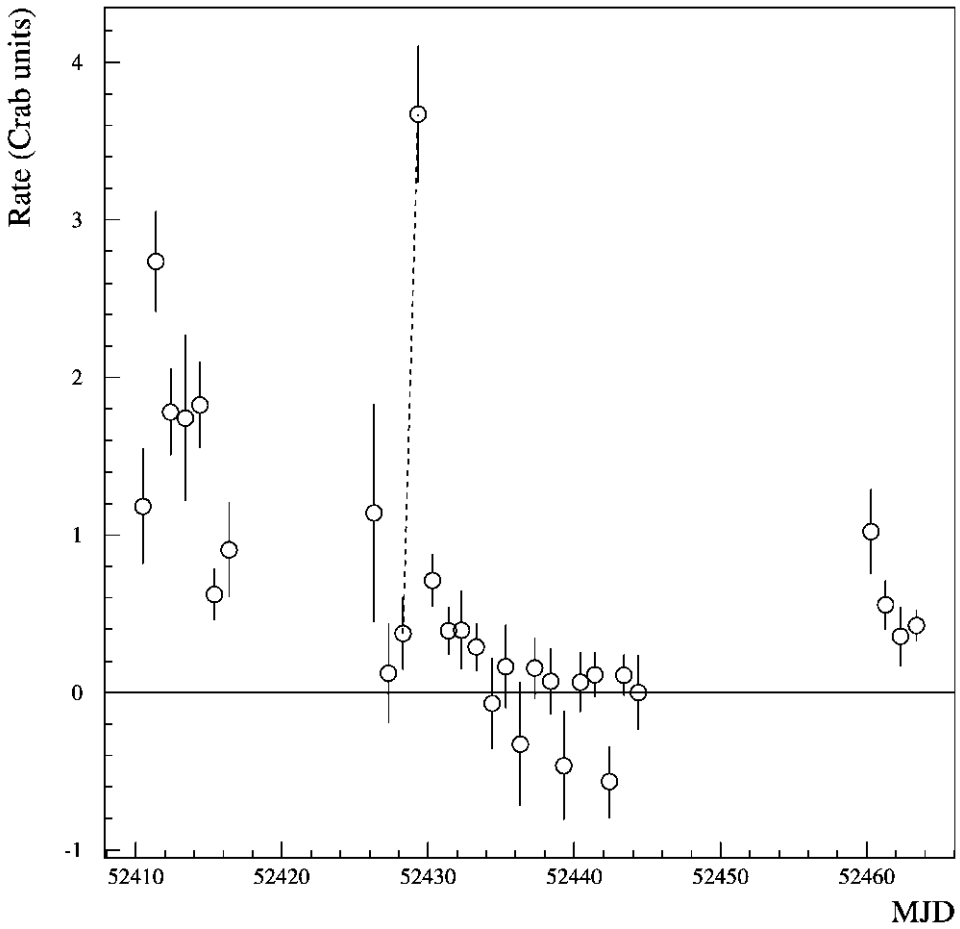

FIGURE 2.13. Daily average Whipple 10m lightcurve for 1ES 1959+650 for May - July 2002, with rate displayed in Crab units. The dashed line corresponds to the quickest flux change, indicating a variability timescale on the order of 7 hours (Holder et al., 2003)

April 2008. The observations showed little or no evidence for variability in monthly timescales with a χ-squared probability of being constant of 0.24 (figure 2.15).

Spectral analysis produced a TeV power law source spectrum of spectral index $\Gamma = 3.6 \pm 1.0_{stat} \pm 0.4_{sys}$ and an integral flux above 300 GeV of $(2.2 \pm 0.5_{stat} \pm 0.4_{sys}) \times 10^{-12}$ ph cm^{-2} s^{-1}, corresponding to 1.8% of the Crab Nebula flux. Modeling of a non-contemporaneous multiwavelength SED (figure 2.16) indicates an SSC model including an (Franceschini et al, 2008) EBL absorption component provided the best fit. Note there is no contemporaneous MeV - GeV data.

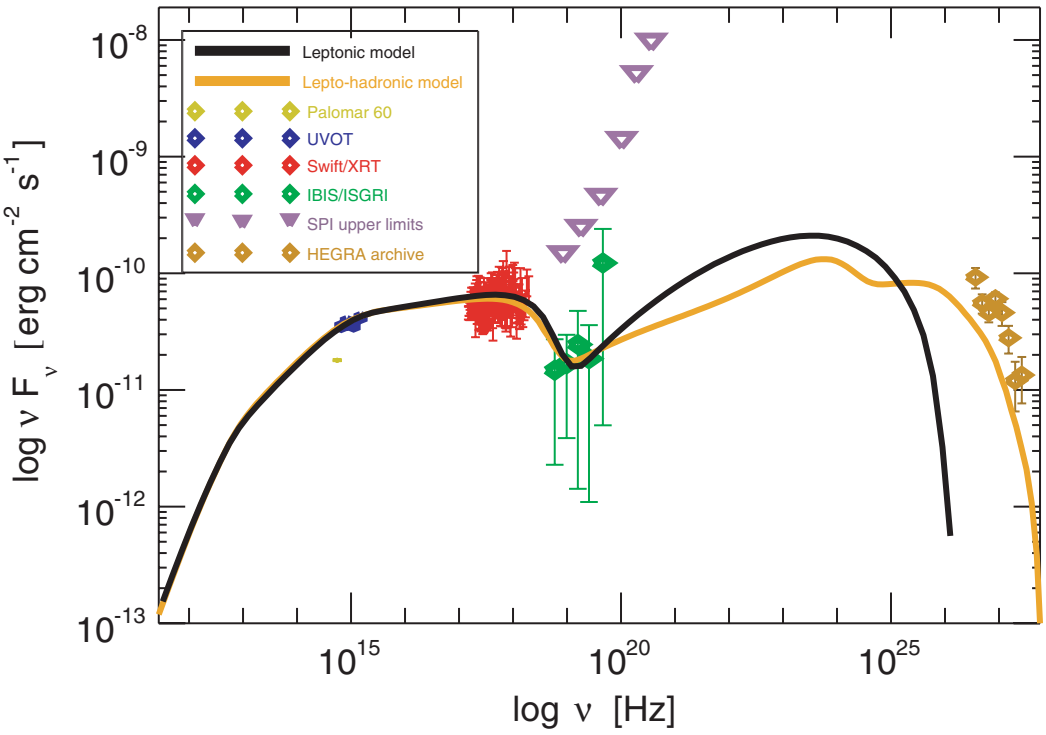

FIGURE 2.14. Multiwavelength SED of 1ES 1959+650 using November - December 2007 data, with the addition of 2002 HEGRA data. (Bottacini et al, 2010)

2.9.3. 1ES 0502+675. 1ES 0502+675 is a HBL with unknown redshift. 13 hours of VERITAS observations, between 23^{rd} September 2009 and 16^{th} November 2009 yield a detection of $> 6\sigma$ significance. The integrated flux about 350 GeV is approximately 4% of the Crab Nebula flux. The VERITAS observations were motivated by the flux and energy spectrum reported in the Fermi LAT Bright Source List for the same source (Abdo et al., 2009). Extrapolation of the LAT spectrum up to higher energies suggested that 1ES 0502+675 would be a TeV γ-ray emitter. The original redshift estimation of z = 0.341 (E. Perlman, private communication, 2009) indicates that this is one of the most distant BL Lacs detected at TeV energies.

2.9.4. W Comae. Also known as ON 231, W Comae is an IBL with moderate redshift (z = 0.102) and was the first IBL to be detected at TeV energies. The BL Lac was first discovered in radio waves (Brown, 1971) and then in X-rays by the Einstein Imaging Proportional Counter in June 1980 (Worrall & Wilkes, 1990). W Comae has been a target for TeV instruments for years for two reasons. The first is an exceptional optical outburst that occurred between April and May 1998. Rapid variability on timescales of hours was recorded (Massaro et al., 1999). Correlations between flux activity in both spectral peaks are crucial for distinguishing between

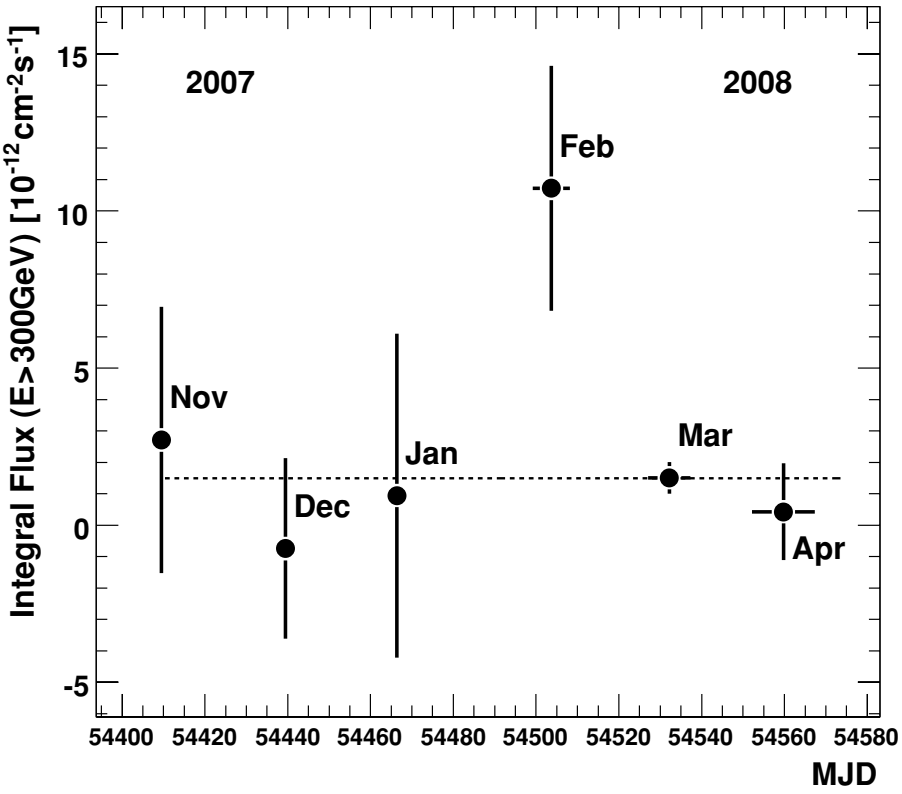

FIGURE 2.15. Lightcurve in months bins in units of integral flux about 300 GeV from 1ES 0806+524 observations. A Chi-squared probability of being constant yields a value of 0.24, indicating little to no variability (Acciari et al., 2009).

leptonic models, e.g. a pure one zone SSC model would see similar activity in both SED peaks. The second reason is the exceptionally hard EGRET spectrum ($\Gamma = 1.73 \pm 0.18$) with no sign of spectral cutoff.

VERITAS discovered TeV γ-ray emission from W Comae from observations between January 2008 and April 2008. A 4-day flare in March contributes at least 70% to the overall detection (Acciari et al., 2008). An integral flux above 200 GeV equivalent to $\sim 9\%$ of the Crab Nebula flux was recorded on two days of the flare (figure 2.17).

Including quasi-simultaneous Swift X-ray observations demonstrates than a linear X-ray/γ-ray flux correlation is unlikely for that particular flare, suggesting a significant EC emission. The multiwavelength SED is described by a one zone SSC model with the addition of an EC component (figure 2.18). Although a purely SSC model also fits the flux data points well, it yields unrealistically an low magnetic field strength.

Another stronger flare (approximately 3 times brighter) with similar results was observed by VERITAS between June 7^{th} and 8^{th} 2008 (Acciari et al., 2009). Note here the lack of MeV - GeV data

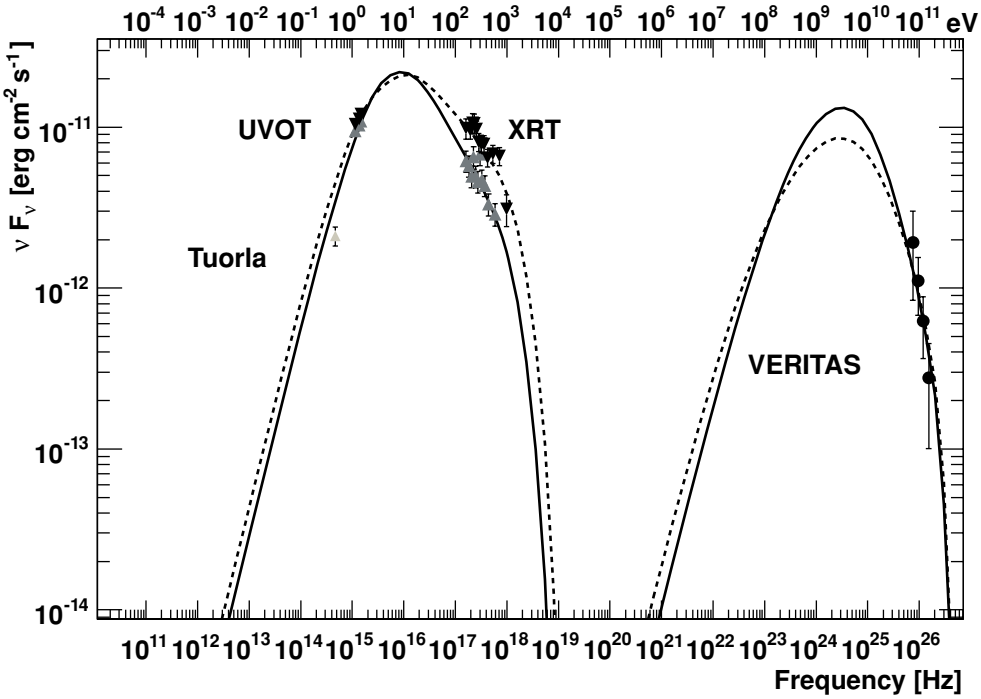

FIGURE 2.16. Broadband multiwavelength SED of 1ES 0806+524. The Swift data was taken on two separate days: grey points - 8th March 2008 and black points - 12th March 2008. The solid (March 8th) and dashed (March 12th) lines are the SSC fits to the data (Acciari et al., 2009).

2.9.5. PKS1424+240. PKS 1424+241, with an unknown redshift, was the first VHE source found with the help of Fermi LAT. Like 1ES 0502+675, the VERITAS observations were also motivated by a hard Fermi spectrum, $\Gamma_{FermiLAT}$ =1.73 $\pm$ 0.07$_{stat}$ $\pm$ 0.05$_{sys}$ (Abdo et al., 2009). By extrapolating up from GeV energies, taking into account various EBL models and accompanied by broadband SED modeling, the redshift was constrained to z $<$ 0.66 with a 95% confidence level. The SED is fit well by an improved version of a leptonic one-zone SSC model (Boettcher & Chiang, 2002), containing an EBL absorption model (Franceschini et al, 2008). However above z $\sim$ 0.2, the predicted TeV spectrum becomes increasingly steep compared to the observed VERITAS spectrum. Including an EC component results in an even steeper VHE spectrum (Acciari et al., 2010). This indicates that the photons in both peaks are produced by the same source, i.e. with little or no contribution from external photons. As the source could in fact be classified as a HBL due to the position of the synchrotron peak (Padovani & Giommi, 1996), this could be a characteristic of this sub- class of blazar (figure 2.19).

2.9.6. 3C66A. 3C66A is an IBL that exhibits variability on the timescale of hours during periods of flaring.

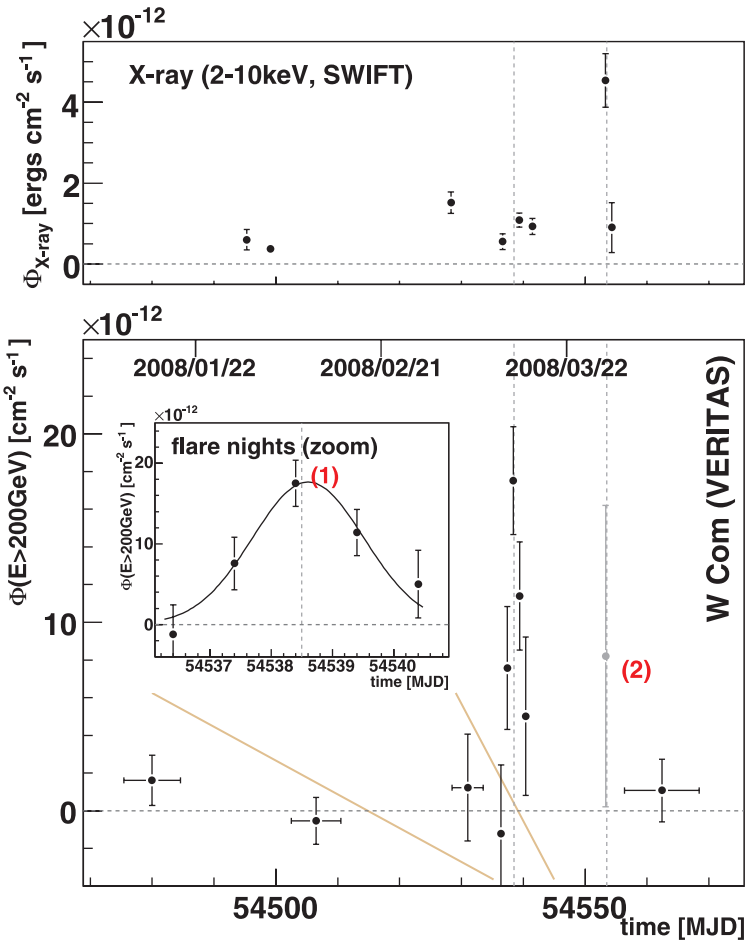

FIGURE 2.17. W Comae lightcurves. Bottom panel: Integrated flux above 200 GeV. Each data point is a 3 week period of observations, except for the period of flaring around MJD 54538, which is binned nightly. Top panel: Quasi-simultaneous Swift X-ray data (Acciari et al., 2008).

Mackay (1971) demonstrated that the radio source 3C66 was actually composed of two separate sources, separated by 0.11° : a compact source 3C66A and a resolved radio galaxy 3C66B. There is also a pulsar, PSR J0218+4232, nearby (figure 2.20). The redshift of z = 0.444 was measured using the one emission line, MgII, in the optical spectrum, making the measurement unreliable. Multiwavelength SED modeling helps to constrain the redshift further.

3C66A is the first source to have been caught by GeV and TeV instruments during a flare ($\sim$ 6% of the Crab Nebula flux above 200 GeV). In October 2008, both Fermi LAT and VERITAS detected 3C66A in a flaring state. A broadband SED was produced with the addition of simultaneous radio to X-ray data: F-Gamma, GASP-WEBT, PAIRITEL, MDM, ATOM, Swift

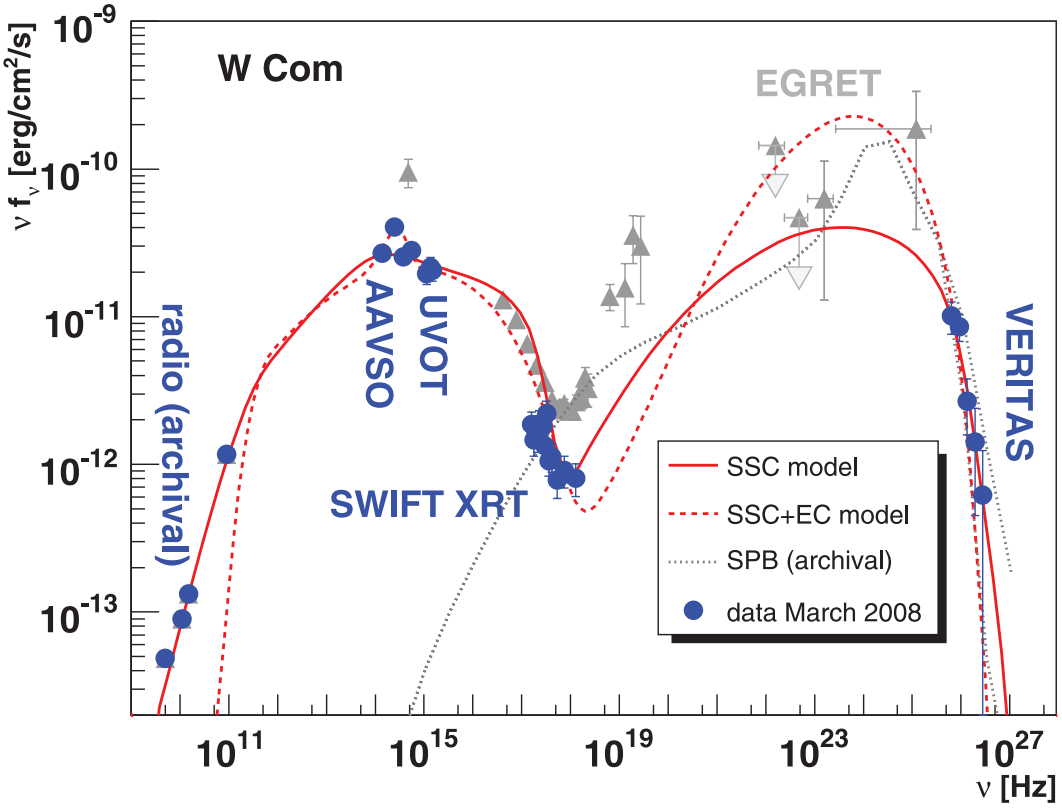

FIGURE 2.18. Quasi-simultaneous multiwavelength observations SED for W Comae. The EGRET, optical and X-ray data are archival and shown in grey (Acciari et al., 2008).

and Chandra (figure 2.21). Similar to the case of W Comae, while a purely SSC model fits the quiescent data well, the addition of an EC component is needed to fit the intra-night variability (the pure SSC model yields too high an emitting volume radius). The EC photons are believed to come from external near-infrared radiation.

In addition to constraining the SED model parameters, the multiwavelength lightcurves demonstrate a flux correlation in both the optical and γ-ray energy ranges (figure 2.22).

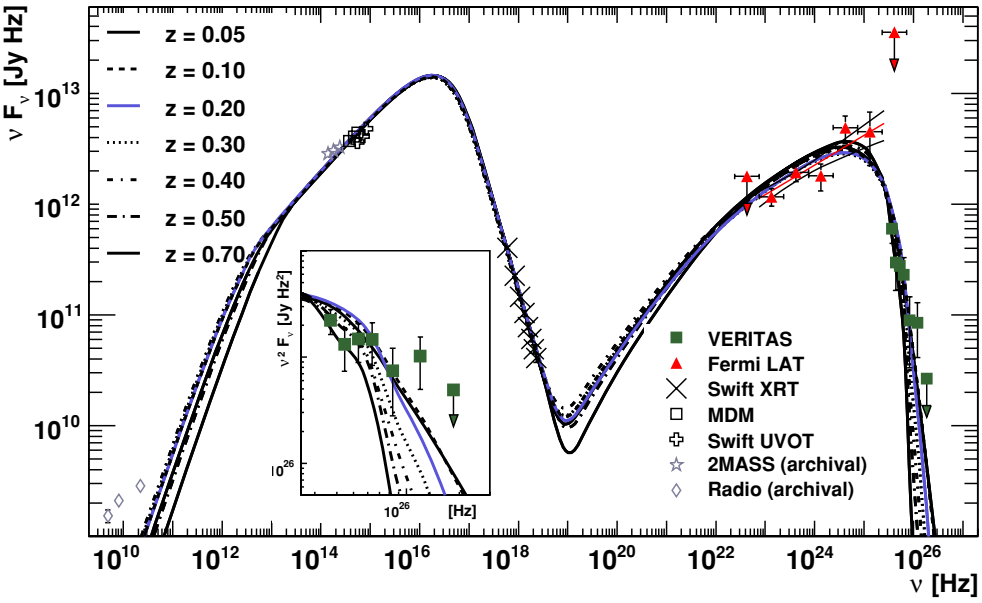

FIGURE 2.19. Multiwavelength observations SED of PKS1424+240. The lines represent different SSC model fits as a function of redshift. The zoomed in area is the υF_υ VERITAS spectrum. The Fermi LAT upper limits correspond to TS < 25, with a 95% confidence level (Acciari et al., 2010).

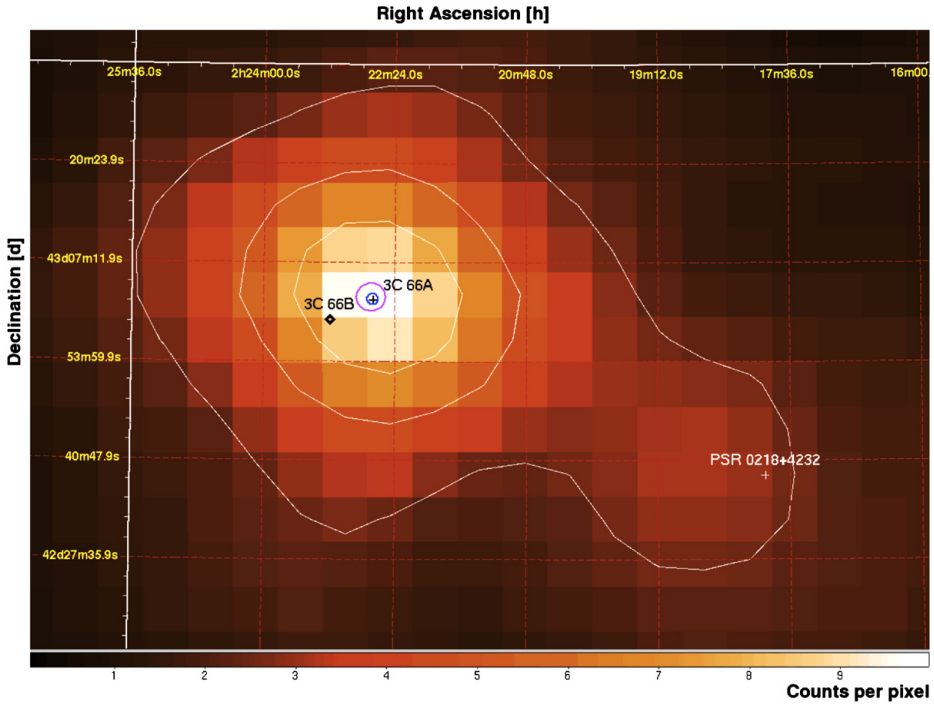

FIGURE 2.20. Smoothed Fermi LAT counts map for the 3C66A region, E > 100 MeV, between September 2008 and December 2008. The magenta circle represents the VERITAS 3C66A location, the blue circle corresponds to the 95% error radius of the LAT position (Abdo et al., 2011).

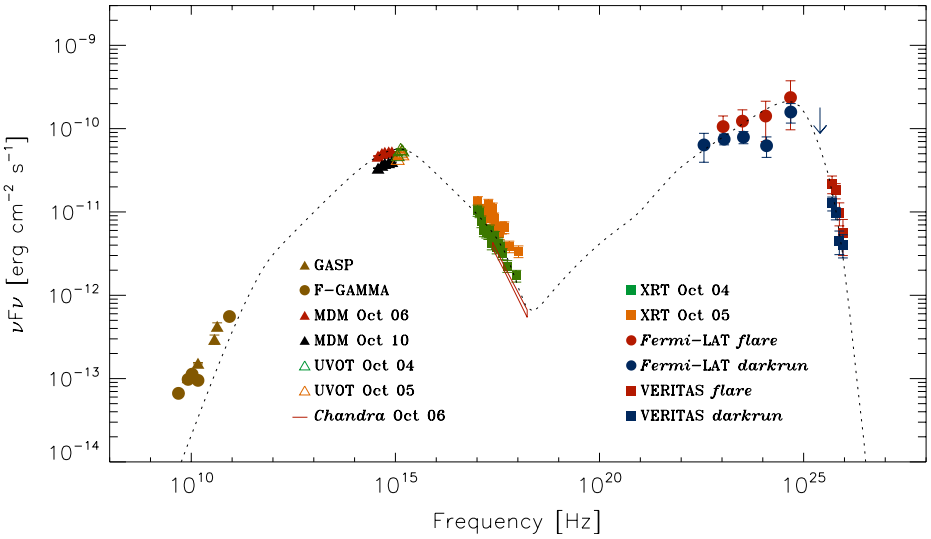

FIGURE 2.21. Broadband 3C66A SED during the October 2008 flare. The fit is a SSC+EC model, EBL absorption corrected with a redshift of z = 0.3 (Abdo et al, 2011).

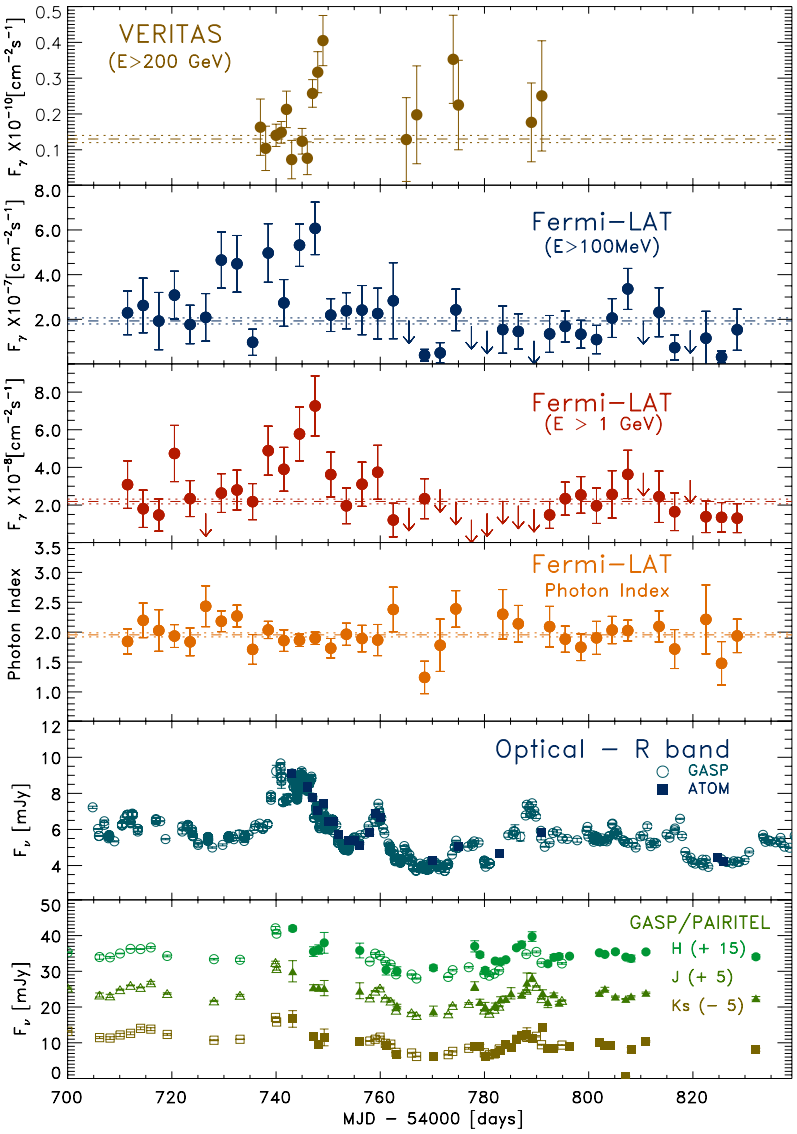

FIGURE 2.22. 3C66A multiwavelength lightcurves for the period 22nd August 2008 to 31st December 2002, including the October 2008 flare. The dashed and dotted lines correspond to the average 2007 and 2008 data respectively. The VERITAS data is binned nightly and the Fermi LAT data is divided up into 3 day bins (Abdo et al., 2011).

CHAPTER 3

Cherenkov Radiation and its Detection from Extensive Air Showers

3.1. Cherenkov Radiation

Cherenkov radiation occurs when charged particles move through a dielectric material at close to relativistic speeds with $\beta > 1/n$, where n is the refractive index of the medium. Cherenkov radiation will only be emitted if the velocity is greater than c/n. As a charged particle travels through the medium it distorts the electromagnetic (em) field, and adjacent atoms become polarized. The atoms then rapidly return to the equilibrium after the em field distortion has passed and a pulse of radiation is emitted. Whether or not this radiation escapes is dependent on the level of em field distortion caused by the particle's velocity. For relatively slow velocities (v << c), the system remains symmetric, the emitted photons destructively interfere with each other canceling each other out and no radiation escapes. For relativistic velocities v = βc, where $\beta > 1/n$ and n is the refractive index of the medium. The em field distortion is traveling through the medium more slowly than the particle, the system is radially asymmetric and a dipole is generated. The photons interfere with each other constructively, the radiation is intensified and escapes (figures 3.1 (a) and (b)).

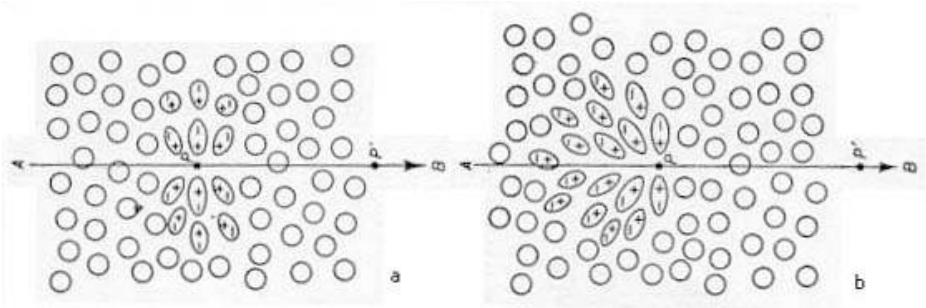

FIGURE 3.1. Illustration of the electromagnetic field distortion caused by a charged particle traveling through a dielectric material. a: slow moving particle v <<c; photons destructively interfere with each other and no radiation escapes. b: relativistic particle v=βc; system is asymmetric, a dipole is created. Photons constructively interfere with each other and the radiation escapes. - (Jelley, 1959).

The angle of the radiation to the trajectory of the original particle (figure 3.2) is related to the particle's velocity by

$$\cos\theta = \frac{1}{\beta n} \tag{48}$$

The maximum angle, 0.8° above sea level (asl.), will occur for v=c.
By letting θ=0°, it is possible to determine the particle velocity and therefore the minimum particle energy for scenarios where Cherenkov radiation is produced:

$$E_{min} = \frac{m_0 c^2}{\sqrt{1 - 1/n^2}} \tag{49}$$

where m_0 is the particle's rest mass.

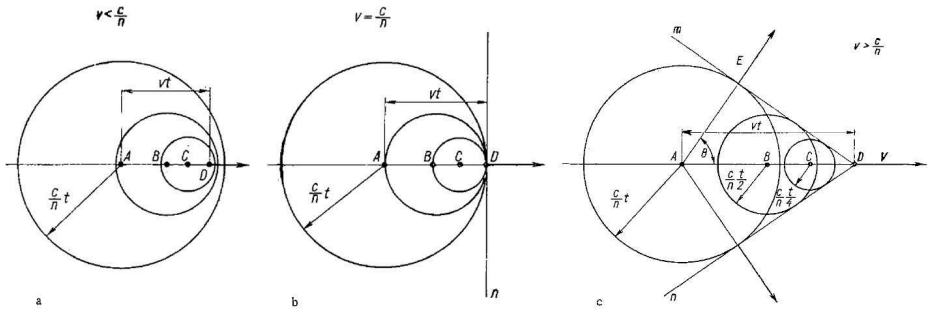

FIGURE 3.2. Wavefront of Cherenkov Radiation. Figure a: v<<c destructive interference, no radiation escapes. Figure b: v = c/n, zero intensity predicted. Figure c : v > βc constructive interference, radiation escapes at angle θ_c. Adapted from Zrelov,1970.

An example of this is an electron asl. (N=1.00029). The minimum relativistic energy required to produce Cherenkov radiation is ∼21 MeV.
The energy, dE, radiated per unit path length dl is given (in eV cm^{-1}) by

$$\frac{dE}{dl} = 4\pi^2 \frac{ze^2}{c} \int_{\beta n>1} (1 - \frac{1}{\beta^2 n(\lambda)^2})\omega d\omega \tag{50}$$

where ze is the charge of the particle and ω is the angular frequency.
From this, the number of photons emitted by an electron or a positron between λ_1 and λ_2 can be calculated as

$$N = 2\pi z^2 \alpha l (\frac{1}{\lambda_1} - \frac{1}{\lambda_2})(1 - \frac{1}{\beta^2 n(\lambda)^2}) \tag{51}$$

where α = fine structure constant 1/137 (Jelley, 1959).

Both equations show a λ^{-2} dependency suggesting that more intense Cherenkov radiation is produced at higher frequencies. However at higher frequencies, the refractive index falls below 1 and the conditions for Cherenkov radiation do not hold. Cherenkov radiation peaks in the UV region of the em spectrum.

3.2. Gamma-ray interactions with matter

There are three widely accepted absorption mechanisms for γ rays with matter and depend on the energy of the incident γ ray. The first is the photoelectric effect and occurs below 50 keV. The incident γ-ray or X-ray interacts with an atomic electron and transfers energy to it and ejecting the electron from the atom.

Compton Scattering is the principal interaction mechanism between 100 keV and 10 MeV. The incident γ ray interacts with an atomic electron, transferring energy to it and is then beamed as a lower energy γ ray. As the energy of the γ ray increases, into the Fermi LAT and VERITAS (the two instruments involved in this thesis) energy range, the probability of γ-ray absorption due to the photoelectric effect or Compton scattering decrease.

The third type of matter interaction is pair production. As mentioned previously, γ rays above a MeV interact with atmospheric nuclei and pair produce to generate secondary particles. The secondary particles involved here are an electron-positron pair (figure 3.3).

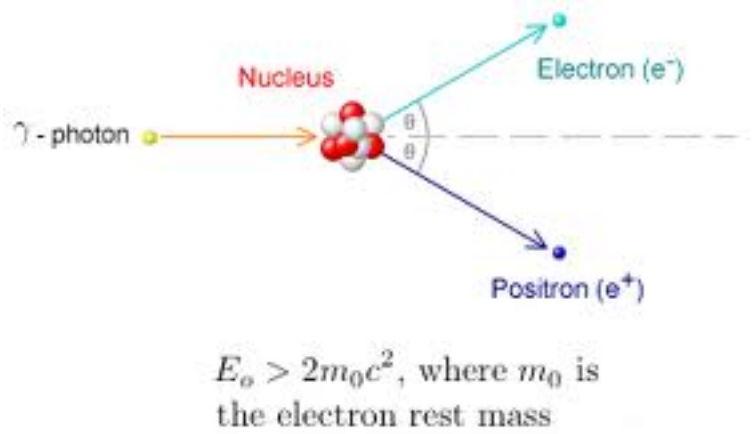

FIGURE 3.3. An illustration of a γ ray undergoing pair production to generate an electron-positron pair (www.relativitycalculator.com/energy_doppler_shtml)

The minimum energy required for pair production to occur is ∼1.02 MeV ($E=2m_ec^2$), the electron and positron rest energies.

3.2.1. Bremsstrahlung. Bremsstrahlung ("breaking radiation") is the emission from a charged particle as a result of scattering in an electric field. It occurs when the particle's energy is significantly larger than its rest energy. The particle is decelerated over a very short distance emitting radiation.

3.3. Extensive Air Showers

Extensive Air Showers (EASs) are the results of cascades of secondary ionized particles and em radiation from cosmic rays in the atmosphere. Two types that are described here are γ-ray initiated EASs and hadronic cosmic ray initiated EASs. EASs generally start tens of km asl. with the number of particles increasing exponentially as the shower propagates downwards through the atmosphere. The primary energy is divided between the secondary particles whose energies are then divided between their secondary particles and this pattern continues through the shower development. Only a small percentage of the total number of particles involved in the shower actually reach the ground.

3.3.1. γ-ray initiated air showers. A γ ray initiated shower occurs when an initial γ ray with an energy of E $\geq$ 1.02 MeV in the earth's atmosphere interacts with an atmospheric nucleus at a height 10 - 30 km asl. and pair produces generating an electron-positron pair. The electron and positron are Coulomb scattered and continue to propagate through the atmosphere. They each emit a secondary γ ray via bremsstrahlung within one radiation length (37.7 g cm^{-2}). The secondary γ rays are lower in energy than the original.

$$\gamma_{original} \rightarrow e^+ + e^- + \gamma + \gamma \tag{52}$$

The secondary γ rays then undergo pair production within 1 radiation length and the process continues. The number of particles grows exponentially and the average particle energy decreases exponentially. This is known as the Heitler model (figure 3.4 is a illustration of this).

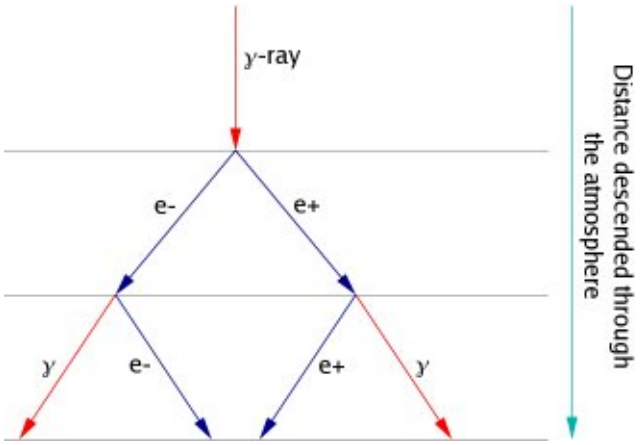

FIGURE 3.4. An illustration of a γ-ray initiated shower (www.dur.ac.uk/∼dph0www4/whyare.php).

The cascade continues until the minimum energy required to create new particles is no longer met. This is the critical energy (E$_c$ $\sim$ 81 MeV) where the energy loss per unit length by bremsstrahlung

is equal to that by ionization and the shower begins to die out and is calculated from (Berger and Seltzer, 1964) :

$$E_c = \frac{800MeV}{Z + 1.2} \tag{53}$$

where Z is atomic number ($Z_{Nitrogen} = 7$)
This point in the shower's development is referred to as the shower maximum. As the shower height and number of particles are dependent on the energy of the original γ ray it is possible to determine the shower maximum. For example a 1 TeV γ ray that initiates a shower at 25 km asl. has a shower maximum at 8 km asl and a total number of particles involved of $\sim$ 1200.

3.3.2. Hadronic cosmic ray initiated air showers. Typically a cosmic ray proton will interact with an atmospheric proton resulting in 3 pions (1 neutral and 2 charged) and other light particles or debris.

$$pr_{cosmic\ ray} + pr_{atmospheric} \rightarrow \pi^0 + \pi^+\pi^- + light\ particles \tag{54}$$

The 3 pions make up 90% of the total resultants. The neutral pion will decay into a γ-ray pair which will result in a γ-ray initiated shower and the charged pions decay into muons. Before the muons decay, they interact with atmospheric nuclei and can decay to produce electron and neutrinos. The muons can travel to the ground or decay into electrons and neutrinos (figure 3.5). Hadronic initiated showers have a higher number of particles than γ-ray initiated showers and develop closer to the ground and have more of a lateral spread.

3.4. Detection

Below is a rough calculation of the photon density per Cherenkov flash based on velocity, shower maximum and the estimated number of particles per shower. The calculation does not take into account changes in refractive index as a function of altitude and neglects absorption processes.

At an altitude of 10 km (typical GeV shower maximum), the refractive index of the atmosphere is n=1.000096. It can be assumed that v=c and β=1 for the majority of the shower (the velocity decreases at the shower edges and when the shower starts to die out). The angle of the wavefront of the radiation can be approximated to $\theta \sim 0.8°$. For a shower maximum of 10 km, a Cherenkov light pool on the ground of radius of 140 m can be expected. From equation 51, the number of photons emitted per path length can be estimated to N $\sim 2.8 \times 10^4$ ph integrated over the wavelength range 200 nm to 600 nm. If the total number of particles per shower is assumed to be 1000 and by taking into account the total area on the ground covered by the light pool for the Cherenkov shower the photon density can be estimated to be 500 ph m^{-2}.

A more in-depth calculation can be performed by generating Monte Carlo simulations. Assuming a uniform light pool at a height of 2300 m (VERITAS' altitude) for showers in the energy

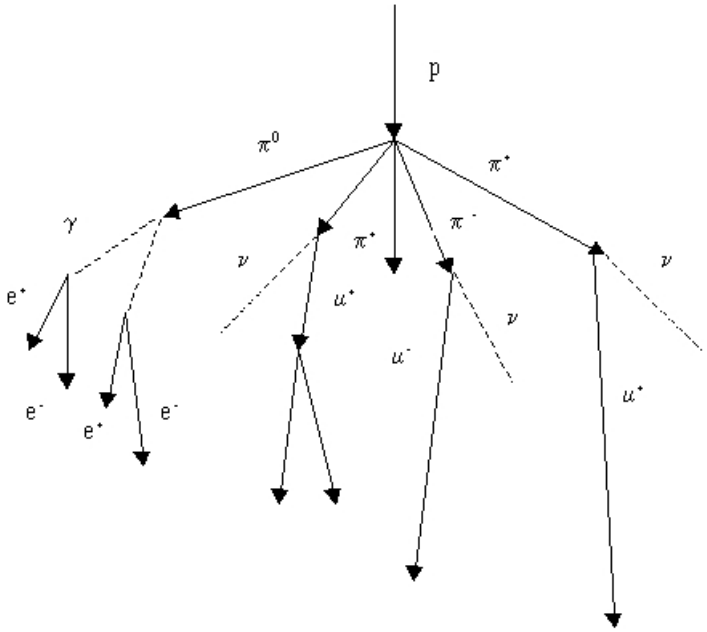

FIGURE 3.5. An illustration of a hadronic cosmic ray initiated shower (www.phy.cuhk.edu .hk/sure/comments_2011/yung_paper.html).

range of 100 GeV to 1 TeV, the photon density per shower can be constrained to 10 - 100 ph m^{-2} (Weekes, 2003).

3.5. Atmospheric Cherenkov Telescopes

As mentioned above, a typical value for Cherenkov photon density is 10 - 100 ph m^{-2} e.g. for a $\sim$ 4ns flash. This is a relatively small number in comparison to the measured NSB flux of $\sim 10^{12}$ ph s^{-1} sr^{-1} which can be problematic. For an accurate measurement, the telescope needs to be located within the light pool. Atmospheric Cherenkov Telescopes (ACTs) operate by collecting and focussing the Cherenkov light. A Cherenkov light pool of radius $\sim$ 140 m corresponds to a possible collection area of $\sim 6 \times 10^4$ m^2.

The total signal recorded for a single PhotoMultipler Tube (PMT) is defined (Weekes, 2003) as

$$S = \int_{\lambda_1}^{\lambda_2} C(\lambda)\eta(\lambda)A \, d\lambda \tag{55}$$

where C(λ) is the Cherenkov photon flux between λ_1 and λ_2, $\eta(\lambda)$ is the response curve of the PMT and A is the collection area of the reflector

$$C(\lambda) = kE(\lambda)T(\lambda) \tag{56}$$

where E(λ) is the shower Cherenkov emission spectrum, T(λ) is the atmospheric transmission and k is a constant depending on the number of particles in the shower (Weekes, 2003)
The total NSB flux can be determined from

$$B = \int_{\lambda_2}^{\lambda_2} B(\lambda)\eta(\lambda)\tau A\Omega d\lambda \tag{57}$$

where B(λ) is the NSB spectrum, τ is the integration window length (time) and Ω is the solid angle on the sky.
Combining equations 55 and 57, it is possible to calculate the signal-to-noise ratio, assuming the number of background photons follow a Poisson distribution, from

$$\frac{S}{N} = \frac{S}{\sqrt{B}} = \int_{\lambda_1}^{\lambda_2} C(\lambda)\sqrt{\frac{\eta(\lambda)A}{\Omega B(\lambda)\tau}} \tag{58}$$

It is evident from this that the signal-to-noise ratio is inversely proportional to the integration window length and the solid angle and proportional to the collection area. The minimum detectable Cherenkov light flash is inversely proportional to τ and the minimum energy threshold of a detectable γ ray can therefore be estimated from

$$E_{threshold} \propto \sqrt{\frac{B(\lambda)\Omega\tau}{\eta(\lambda)A}} \tag{59}$$

The energy threshold increases with integration time.

3.6. Imaging Atmospheric Cherenkov Technique

The Cherenkov light is collected by a spherical or a parabolic optical reflector which focusses it onto a PMT camera. To increase the amount of light collected large reflectors are used (e.g. VERITAS : 12 m diameter reflector). The higher the resolution the better the image quality, thereby making characterization of the image easier and more accurate. The effective area is determined by the zenith angle of the source during the observations, the quantum efficiency of the detector and the energies of the γ rays detected. These parameters are taken into account during Monte Carlo simulations to generate Effective Area tables required for spectral analysis.

The ACTs alone, without any modification, cannot distinguish between γ-ray initiated air showers and hadronic cosmic ray initiated showers. Less than 1 % of cosmic rays are γ-rays while 99% are hadronic. One method of distinguishing the two is image analysis, paying particular attention to the lateral and longitudinal development of the shower.

Distinguishing γ-ray initiated showers from hadronic cosmic ray initiated showers is achieved through analysis and characterization the angular shape and orientation. As discussed in section 3.3.2, hadron showers occur closer to the ground and have a larger lateral spread in particles, while γ-ray shower images are more compact and regular in shape. As the telescope is pointed

towards the target γ-ray producing source, the major axis of the image will point to the source location and the image will be more elliptical than that of a hadron shower.

By employing an array of Cherenkov telescopes during the observations (VERITAS is an array of 4) the efficiency of the observatory is increased significantly. Having simultaneous images for the same shower light pool means higher quality image analysis and characterization to improve hadron shower discrimination. Intersection of the major axes of each image make it possible to trace backwards to the γ-ray origin location and to trace forwards to the shower core location on the ground. Stereoscopic observations also help prevent accidental triggering (i.e. local muons detected in 1 or 2 telescopes only) which lowers deadtime and means the array can detect lower energy showers. It sharpens angular resolution to an accuracy of $\sim 0.1^{\circ}$ at 1 TeV (Ward, 2010) and improves the efficiency of calculations of the impact distance from the telescopes required to determine the energy of the original γ-ray. Stereoscopic observations are described in more detail in section 5.2.6.

CHAPTER 4

VERITAS and Fermi LAT Instrument Description

4.1. The VERITAS array

VERITAS is an array of four 12 m Imaging Atmospheric Cherenkov Technique (IACT) telescopes located at the base-camp of the Fred Lawrence Whipple Observatory (1275m asl.) in southern Arizona, USA. The array is the successor to the pioneering Whipple 10m (IACT) telescope which first detected the Crab Pulsar Wind Nebula, the first TeV source, in 1989 (Weekes et al., 1989). The reflector telescopes are of Davies Cotton design and each consists of 350 mirrors. Cherenkov light from extensive air showers is captured by a 499-pixel photomultiplier tube camera located in the focal plane of each telescope, each having a 3.5° field of view adequate for both point and diffuse source observations. The array has been fully operational since September 2007, with its first light ceremony the previous April, and is currently the most sensitive TeV ground-based IACT instrument. At present, the VERITAS collaboration consists of more than 90 members from 22 institutions in Canada, USA, Ireland, England and Germany. This chapter outlines the optical, mechanical and electronic components of the array and also provides a description of stereoscopic imaging and the data acquisition system. Table 4.1 is an outline of VERITAS' performance.

4.1.1. Telescope Design, Mirrors and Alignment. Each telescope is positioned to form a general parallelogram shape with sides of length 85 m, 35 m, 85 m, and 109 m, providing a baseline of 100 m (Weekes et al., 2008). Originally telescopes 1 and 4 were situated closer to each other (figure 4.1). In August 2009, to expand the collection area of the array, telescope 1 was relocated (figure 4.2). This, along with a more efficient mirror alignment technique, was part of a recent upgrade to the array. The results of this upgrade are better image definition and increased flux sensitivity, almost halving the time needed to detect a 1% Crab Nebula source at the 5σ level (figure 4.3). Further upgrades, including improvements to the array-level trigger, atmospheric monitoring, camera PMTs and slew speed are due to take place in the near future.

TABLE 4.1. Summary of VERITAS performance

Parameter	Value or Range
Energy Range	100 GeV - 30 TeV
Field of view	3.5°
Energy Resolution	20%
Angular Resolution	0.1° at 1 TeV

The array performs stereoscopic observations, using the intersection of the major axes of the image to determine shower core location.

FIGURE 4.1. The arrangement of the VERITAS array prior to the relocation of Telescope 1 (second from the left) in August 2009 (veritas.sao.arizona.edu).

4.1.1.1. *Telescope Design and Mirrors.* The reflector is supported by a custom-designed, Optical Support Structure (OSS), which is in turn supported by a commercial altitude-over-azimuth positioner manufactured for precision rotation. This and motion controlling software ensure the tracking errors remain less than 0.01°. At present, the maximum slew speed is 1° s^{-1} (Holder et al., 2006).

Due to the constraining factors including manufacture and maintenance costs, a Davies Cotton design was used (Maiseev et al., 2004). The optics of each telescope consists of 350 identical spherical mirrors (figure 4.4), strategically placed so that the individual focal points intersect, creating an overall spherical reflector. This is more effective and manageable in terms of maintenance than the use of a single 12m diameter mirror. Each mirror is glass, hexagonal in shape, (11.5 ± 1.0) mm thick, (60.96 ± 0.3) cm wide and has a radius of curvature of (24 ± 1.0) mm. The area of a single mirror facet is 0.322 m^2 yielding a total reflector area of $\sim$ 110 m^2. The large focal length F=12m and f-number of f/1.0 is used in order to reduce aberrations due to off-axis mirrors. For comparison the f-number for the Whipple 10m telescope is f/0.7. However, one disadvantage of the Davies Cotton design is that the reflector is anisochronous. This creates a time spread of approximately 4 ns in the light arriving at the focal point which fortunately is similar in value to the time spread in light from Cherenkov showers.

FIGURE 4.2. The arrangement of the VERITAS array post relocation of Telescope 1(second from the left) (veritas.sao.arizona.edu).

The mirror facets undergo cleaning, aluminization and anodization once an observing season on-site. To ensure the upkeep of the telescopes and that a degradation in the optics is not seen throughout the year, these processes are done in rotation, usually 6 mirrors at a time. The mirrors are first washed with a phosphate-free mild detergent to remove surface dirt and dried upright. A 180 nm thick layer of Al is deposited on the front side of the mirror facet followed by an electrolytic passivation process to increase the natural oxide layer. The benefits include increased corrosion resistance and surface hardness; important weather proofing for what can be harsh desert conditions. Anodized aluminization also aids in avoiding UV light absorption in the glass and the mirrors can be washed as needed. The reflectivity at 320 nm, ideal to capture Cherekov emission, is $> 90\%$ and ≥ 85 % between 280 nm and 450 nm (Roache et al., 2008). On average, a 3% decrease in reflectivity is seen each year at 320 nm.

4.1.1.2. *Mirror Alignment.* Each mirror is mounted on 3 adjustable screws (used in the alignment process or for minor adjustments) on a triangular frame attached to the OSS. Mirror alignment is crucial to ensuring the separate mirrors act as a single spherical reflector and for maintaining an adequately small point spread function (PSF), and takes place when needed once a year. The PSF is an indicator of how the array responds to a point source, and is calculated by measuring the full width half maximum (FWHM) of a 2D gaussian fit to the distribution of light from a star, or in the case of alignment, a laser placed at the centre of curvature, focused on the focal plane. At present, the PSF of the VERITAS array is calculated to be 0.6°.

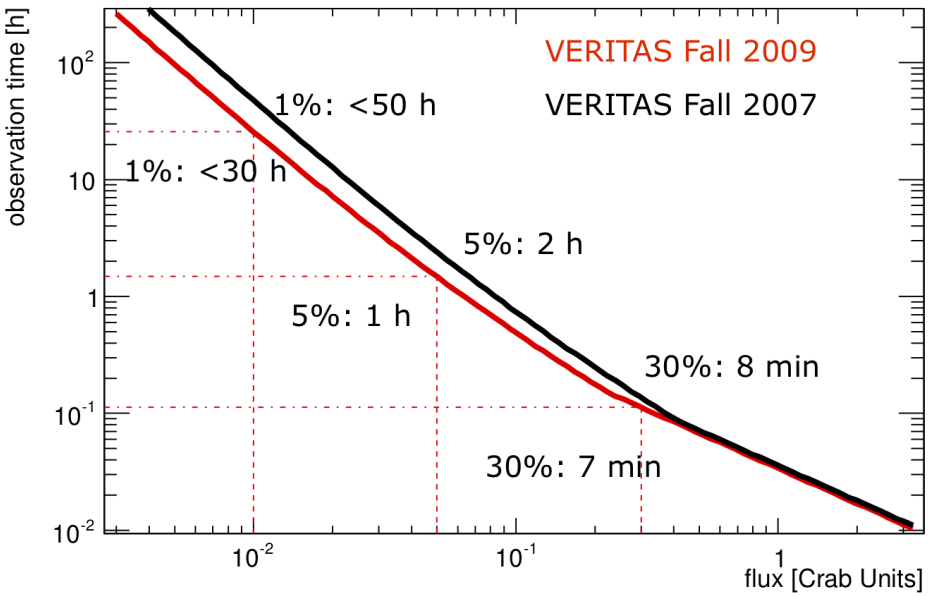

FIGURE 4.3. A comparison of VERITAS' sensitivity to the Crab Nebula before and after the relocation of Telescope 1 and the introduction of an improved mirror-alignment technique.

At stow, performed separately yearly and repeated for each individual mirror, a laser (helium-neon) is placed at the centre of curvature and then reflected back onto a CCD camera. A correctly aligned mirror will reflect the laser back along its original path. The corrections needed in order to overlap both beams are calculated and the mirrors are adjusted accordingly by means of the adjustable screws and the mirror is aligned. However, one flaw in this alignment method is that the mirrors are aligned for the stow position. Due to the weight and flexing of the OSS, the PSF generally increases with elevation. As the majority of the observations are performed above an elevation $> 50°$ for maximum light collection and reduced atmospheric effects, an alignment method is required that can be performed at stow but is sufficient for high elevation observations. One simple method that has proved useful, known as "bias measurements", involves misaligning the mirrors by a previously calculated offset at stow, so that the mirrors are actually aligned correctly for observations. These misalignments or "bias offsets" are measured by attaching lasers to each mirror (usually 6 at a time) and projecting the image onto the screen placed at the focal plane of the telescope that is captured by CCD camera. The telescope is then moved to a high elevation e.g. 65° (to account for the maximum focus distortion from elevation), and the image of the laser is taken again. The difference in the PSF of both images is used to calculate the "bias misalignment offset". The mirror is offset accordingly and classified as aligned.

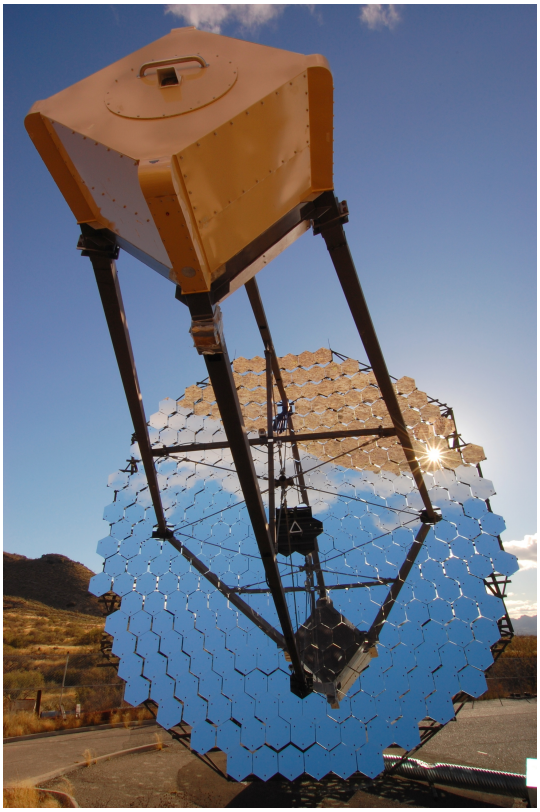

FIGURE 4.4. The hexagonal mirrors and camera focus box on Telescope 2 (veritas.sao.arizona.edu).

4.1.2. Camera. After reflection, photons are collected by a PhotoMultiplier Tube (PMT) camera enclosed in a 1.8 m × 1.8 m focus box located at the focal plane of each telescope. A remote-controlled, rolling shutter acts as a camera lid making the focus box both sunlight- and waterproof when closed. The focus box also houses a temperature sensor to protect against overheating and a humidity sensor to reduce the risk of arcing when the High Voltage (HV) is switched on. Arcing occurs when the humidity exceeds the upper limit, and electrical discharge between the PMTs occurs due to the increase in conductivity. Other components of the focus box include signal preamplifier (section 4.1.2.3) and current monitor boards (section 4.1.2.5). Enclosing electronics in the focus box allows real-time monitoring of the PMT currents and weather conditions.

4.1.2.1. *Photo-Multiplier Tubes.* PMTs play an important role in many areas of physics, such as particle, nuclear, medical and, in particular, astronomy. The numerous benefits of using PMT detectors in γ-ray telescopes include high gain, low noise, high-frequency response, large collection area and their relative low cost. These vacuum tubes are very efficient; in instances of comparably low flux, individual photons can still be detected. The incoming Cherenkov photon strikes the photocathode (a metal component of the PMT) and produces a photoelectron as a

consequence of the photoelectric effect. The Quantum Efficiency (QE) of a PMT is the percentage of photons striking the photocathode material that releases a photo-electron. The electron is then directed by the focusing electrode and accelerated past a series of increasingly positive dynodes. As the electron strikes the emissive material of the dynodes, low energy electrons are emitted and are themselves accelerated towards the second dynode which is held at a larger potential than the first. This series continues and a cascade of electrons is produced, collecting at the anode where the total charge produces a current pulse.

The VERITAS camera contains 499 29 mm diameter, 10 gain stage, Photonic XP2970/02 PMTs with a quantum efficiency of 20 - 25% at 320 nm (relevant for Cherenkov images). They are operated at a gain of $\sim 2 \times 10^5$ when at a HV of 850 V because of their fast rise time of $\sim$1.9 ns. This model of PMT is extremely sensitive in the UV/Blue region of the electromagnetic spectrum where the peak of Cherenkov emission is located and the night sky background is at a minimum, allowing Cherenkov photons to be detected. The PMTs are capable of resolving the fast, weak Cherenkov flashes ($\sim$4 - 6 ns). The camera has a total field of view of 3.5° with 0.15° pixel spacing. This is sufficient for both point and diffuse source observations.

4.1.2.2. *Lightcones.* Hexagonal tiling (allows precise position adjustment and focal plane tilting) of circular PMTs produces gaps or dead-space between the PMTs, where photons are lost. To compensate for this, a light concentrator plate of moulded plastic hollow lightcones is placed in front of the PMTs (figure 4.5). The lightcones are an adapted version of Winston cones with a hexagonal shaped entrance evolving to a Winston cone (Winston, 1970). The cones are coated with Al with a SiO_2 protective overlayer to increase reflectivity, $>$ 90% above 320 nm (Nagai et al., 2007). Photon collection efficiency is increased from 55% to 75% (Jordan et al., 2004) as light is "bounced" off the reflective surfaces of the cone until it reaches the PMT. The hexagonal shaped entrance of each cone also constrains the field of view of the PMTs by limiting their acceptance angle to the solid angle subtended by the telescope so that the majority of light collected has been reflected from the 12m reflector and is not night-sky background.

4.1.2.3. *Preamps.* At the base of each PMT is a low noise signal pre-amplifier that boosts the charged pulse produced by a photon striking the photocathode. This is done to distinguish it from noise generated when the signal is transmitted through 45 m of RG-59 coaxial cable to the FADCs in the nearby electronics trailer and consequently improves the signal-to-noise ratio. At the normal operating HV (1000 HV), the 300 MHz bandwidth aids in reproducing Cherenkov pulse shapes with a fast rise-time of 2.5 ns. The signal amplification factor of 6.6 produces a pulse height of 2.4 mV and outputs a range of 0 to 2.2 V which matches the required range of 0 to 1.65 V by the Flash-ADCs (FADCs) (Nagai et al., 2007). The preamplifiers allow the PMTs to be operated at a lower HV if/when needed for example, during moonlight observations (up to 60% moon) A lower HV prohibits the anode current increasing to a point that would cause potential damage to the PMTs.

4.1.2.4. *HV.* Each telescope possesses 2 HV crates to supply the PMTs located in the telescopes electronics trailer. The first crate, CAEN model 1527, contains 8 HV modules and the

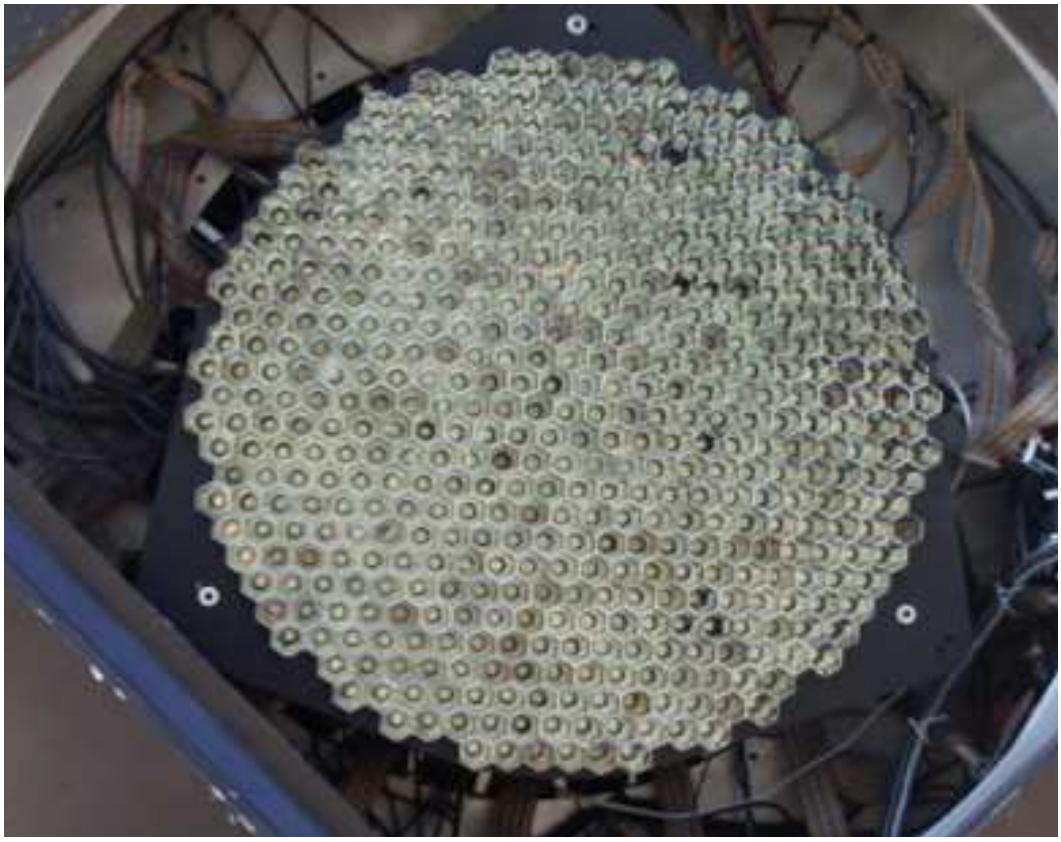

FIGURE 4.5. Lightcones placed in front of the PMTs (Nagai et al., 2007).

second CAEN model 2527 holds 3, with each module connected to an assembly of 48 adjacent channels (arranged in 6 groups of 8). High Voltages are adjusted individually for each PMT in the range 800 - 1000 V up to an upper limit of 1500 V, with the objective of yielding a PMT gain of $\sim$2 x 10^5. Each PMT is read out via ethernet from the VERITAS offline database to a custom designed program that sets and controls the HV values. This program can control the HV values to an accuracy within 1 volt allowing a precise gain setting. It utilizes the current monitor to identify PMTs that exceed a preset anode current threshold and then reduces the HV accordingly or in certain cases, turn the tube off. This is known as HV suppression and it prevents potential damage to the light sensitive PMTs, thereby prolonging the PMT lifespan.

4.1.2.5. *Current Monitor.* A custom-designed current monitor is located inside the focal box and provides a real-time monitoring system for the PMT anode currents. When the anode current in a pixel exceeds a pre-determined value (e.g. 15 mA), the observer is provided with live diagnostics and the HV in that pixel is automatically reduced or turned off completely. This excessive current can be caused by bright stars/transient sources (generally if this is the case, an increase in anode current will also be seen in the surrounding pixels) or by human activity on or near the array site such as vehicle headlights or helicopters. The hardware for the current monitor

inside the focus box includes 16 FPGA-controlled circuit boards with each board consisting of 32 input channels that are connected to the FADCs (in each telescope electronics trailer) at 50 MHz. Each channel can transmit current and temperature and humidity sensor readings. On average, the gain in each PMT decreases by ∼1%/C° with increasing temperature. A fan cooling system is used and is routinely switched on 90 minutes before observations are due to commence to ensure adequate cooling. At present, the maximum operating camera temperature is preset to 45°C. The predetermined operating humidity threshold for the VERITAS telescopes is 80%. Above this humidity arcing is observed which can cause damage to the PMTs.

4.1.3. Trigger System. It is important to detect photons from Extensive Air Showers (EASs) but reject NSB and also noise fluctuations in the channels, through filter algorithms run in real time during observations. This is achieved through a 3-tiered trigger system: Single pixel (L1) trigger, Pattern or Telescope (L2) trigger and Array level (L3) trigger (figure 4.6).

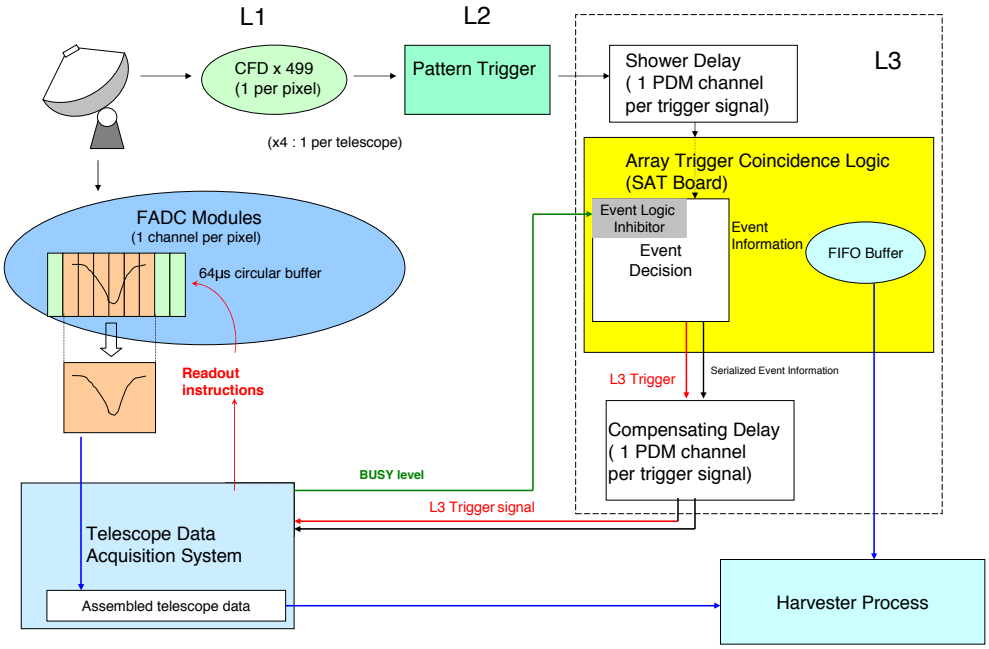

FIGURE 4.6. Schematic diagram of the 3 tiered trigger system and the Data Acquisition System (Weinstein et al., 2008).

4.1.3.1. *L1 pixel trigger.* The L1 trigger utilizes Constant Fraction Discriminators (CFDs) on FADC boards and threshold limits. CFDs solve problems such as pulses of different amplitudes not crossing the threshold at the same time (Vassiliev et al., 2003). CFD thresholds can be adjusted for each individual pixel. A typical operating CFD threshold is ∼50 mV. This corresponds to 4-5 photoelectrons. Other typical CFD operating parameters include an output pulse

of 10 ns and also a rate-feedback (RFB) loop at 60 mV/MHz (Weinstein et al., 2008) to increase the threshold as noise rises. When the PMT pulse exceeds a preset limit (mV) an output logic pulse (with typical widths 4-25 ns) is created and sent to the FADC boards. A programmable delay of up to 6 ns is introduced to the system to compensate for timing differences in the channels (PMTs). The pulse is then divided into 3 signals. One signal is transferred to a simple threshold discriminator while signals 2 (which is time delayed and inverted) and 3 (attenuated) are sent to a zero crossing discriminator. Signals 2 and 3 are combined to calculate the zero crossing point (the point where the signals cancel each other). At this point the logic signal is produced. The threshold discriminator and zero crossing discriminator outputs are combined to generate the level 1 (L1) trigger signal.

4.1.3.2. *L2 pattern trigger.* A PMT that has crossed a preset threshold and triggered on an L1 level is not sufficient to reduce the data and perform background rejection as both noise and NSB can heat up pixels. EAS photons will form an image which will heat up adjacent pixels. The L1 trigger signal is transmitted to an L1 dedicated computer which divides the camera into 19 clusters of 59 pixels to search for patterns. These clusters are arranged to overlap each other and utilize pre-programmed memory chips to recognize patterns (Bradbury et al., 2002). Within a preset time window, patches of adjacent L1 triggered pixels are examined to look for spatial and temporal patterns. The typical L2 trigger pattern is at least 3 adjacent PMTs within a 6 ns window (Weinstein et al., 2008). When specifying a predetermined time width a balance is needed between being wide enough to facilitate Cherenkov light front spread times ($\sim$ 4 ns) and being narrow enough to avoid false triggering.

4.1.3.3. *L3 array trigger.* At low energies in particular the L3 array trigger plays an important role in rejecting local muons which are relativistic and mimic Cherenkov showers. Fortunately, local (occurring close to the telescope) muons will create an EAS-like image in a single telescope only. An L3 array level trigger, which requires signals from more than one telescope, will effectively reject the muon and essentially perform adequate muon background rejection. This discriminates a large fraction of L2 pattern triggers which in turn takes the bulk of the reliance off the CFD thresholds. The CFD thresholds can thus be lowered which increases the sensitivity of the array at low energies. A substantial amount ($\sim$ 60 - 75%) of the L2 rate per telescope is reduced by the L3 trigger. L2 triggers are sent to the L3 system from each telescope via custom-designed Digital Asynchronous Transceiver (DAT) modules. Further information regarding the DAT modules can be found in White et al. (2008). The L3 system examines the L2 trigger signals with a predetermined coincidence window (10-250 μs), produces event numbers and monitors dead-time. For an L3 rate of 150 Hz, the corresponding dead-time would be $\sim$7%. When the L3 trigger criteria is met the shower data for each telescope is read out from the FADCs.

4.1.3.4. *BIAS Curves.* One of the observing tasks is to strike a balance between lowering the instruments' CFDs triggering thresholds to increase sensitivity at low energies and increasing the thresholds to reduce dead-time. The optimum CFD threshold (which is the same for all

telescopes) is determined through a BIAS Curve. Towards lower energies, the background is significantly dominated by fluctuations in the NSB and by local muons while at higher energies the background is dominated by cosmic rays. With the array directed towards a dark patch of sky, a calibration run is taken with the CFD threshold set to a large value (to collect events) and decreased gradually over the course of the run. L2/L3 triggers signals are plotted as a function of the L1 CFD threshold (figure 4.7). The steep slope of the curve represents NSB triggers and the flatter section represents cosmic-ray shower triggers. Where the graph levels out is an optimal value for the CFD for the CFD threshold. This procedure is performed at the beginning of each season and throughout is needed (i.e. upgrades, changes to array, etc.).

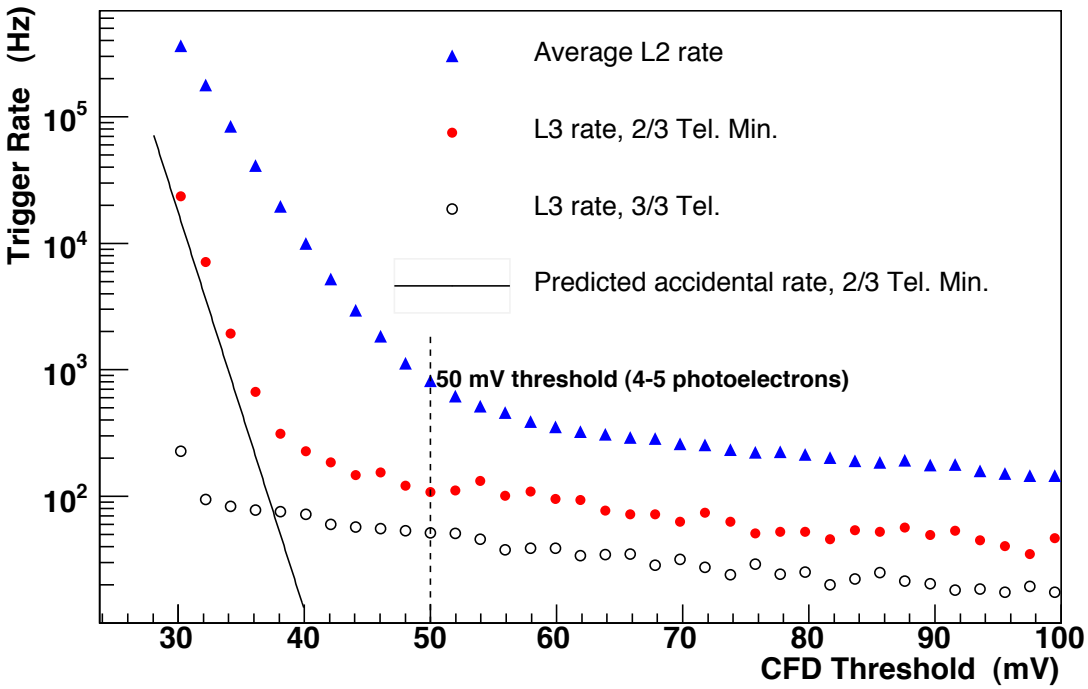

FIGURE 4.7. An example of a BIAS curve used in determining the optimum CFD thresholds. The marker size facilitates error ranges (Weinstein et al., 2008)

4.1.4. Telescope Data Acquisition system. When the L3 trigger criteria is met, data processing takes place in a Data Acquisition (DAQ) chain. The first stage of the DAQ chain takes place in the 500 MHz flash-ADC (FADC) boards. The signal in each PMT undergoes amplification and is transferred to a corresponding channel in the FADC board for digitization at a rate of 500 MHz (Rebillot et al., 2008). The FADCs can measure voltages to within an accuracy of 2 ns, which decreases the integration window for each event, minimizing the signal to

noise ratio. The high temporal resolution means the timing information used in characterization of the showers and shape information is maintained for offline data analysis.

In each telescope there are five Virtual Machine Environment (VME) crates, four to hold the FADC boards and a crate-level clock trigger module and one that contains the Global Positioning System (GPS) clock and the array-level clock trigger module. The VME Data Acquisition (VDAQ) initializes the system, providing the VME crates with the FADC and CFD hardware information which is stored in the offline database, which is accessible by the analysis software and waits for L3 triggers. The VDAQ is also the interface between the VME system and the Event Builder as described below. The L3 trigger signal is sent to the array-level clock trigger board which distributes the signal to the crate-level clock trigger boards. An array-level busy signal is sent back to the L3 system to ensure no additional L3 trigger signals are sent. The VDAQ read outs the digitized FADC channels and transfers this data, along with time stamp information, to the Event Builder computer via a Scalable Coherent Interface (SCI) link at a rate of 50 MB s^{-1}.

The Event Builder receives the events in fragments. For each event, after all the fragments arrive from the crates, the complete event is constructed. The events are written to disk and then transferred to the Harvester computer where the individual events are collected and assembled in a single array events file of VERITAS Bank Format (VBF). The events are arranged by event number and the files are compressed to a few GB per file. Each file corresponds to one run (typically $\sim$ 20 minutes) and this is the starting point for the offline data analysis.

While events are being collected and assembled, the database continues to record all the observation settings and changes with everything from CFD thresholds and trigger information to observing conditions and environmental monitoring information e.g. the weather. This diagnostic information plays an important role in offline analysis.

4.2. The Fermi LAT satellite

The Large Area Telescope (Fermi LAT, also known as LAT) is the primary instrument on-board NASA's Fermi Gamma-ray Space Telescope, formerly known as GLAST (Gamma-ray Large Area Space Telescope).

It is a pair conversion, high-energy γ-ray imaging telescope in the energy range of 20 MeV - 300 GeV (Atwood et al., 2009). The high energy range of the LAT intersects with the low energy range of the IACTs so, for the first time there is an energy overlap between space- and ground-based telescopes allowing continuous spectra between 20 MeV and 30 TeV. This enables more detailed spectral modeling and is thus beneficial in constraining model parameters. The LAT (figure 4.9) consists of a segmented anti-coincidence system (to reject cosmic rays), a precision tracker and a calorimeter (to calculate the direction and energy of the γ-ray) along with a data acquisition system and a programmable trigger, each of which is described individually in sections 3.1 - 3.3. The dimensions of the LAT instrument are 1.8 m $\times$ 1.8 m $\times$ 0.72 m with a mass of 2789 kg. The power required for operation is 650 W and there are no consumables on-board.

TABLE 4.2. Summary of Lat Instrument Parameters and Estimated Performance (Atwood et al., 2009)

Parameter	Value or Range
Energy Range	20 MeV - 300 GeV
Effective area at normal incidence	9,500 cm^2
Energy resolution (equivalent Gaussian 1σ):	
100 MeV-1 GeV (on-axis)	9% - 15%
1GeV-10 GeV (on-axis)	8% - 9%
>10 GeV (> 60° incidence)	≤6%
Single photon angular resolution (space angle)	
on-axis, 68% containment radius:	
>10 GeV	≤0.15°
1 GeV	0.6°
100 MeV	3.5°
on axis, 95% containment radius	$< 3 \times \theta_{68\%}$
off-axis containment radius at 55%	< 1.7 × on-axis value
Field of View (FoV)	2.4 sr
Timing accuracy	< 10 μs
Event readout time (deadtime)	26.5 μs
GRB location accuracy onboard	$< 10'$
GRB notification time to spacecraft	< 5 s
Point source location determination	$< 0.5'$
Point source sensitivity (>100 MeV)	3×10^{-9} ph cm^{-2} s^{-1}

The energy resolution at the highest energy is better than 10% and the angular resolution (68% containment) is 0.1°. Table 4.2 has a complete account of performance parameters.

4.2.1. LAT Instrumentation. The LAT is a pair-conversion telescope that consists of a precision converter-tracker, calorimeter, an anti-coincidence system and uses a programmable trigger and data acquisition system (figure 4.8). It is made of a 4 × 4 array of 37 × 66 cm^2 towers supported by a low mass Aluminum grid structure. Each tower contains a silicon-strip tracker, calorimeter and DAQ module. The array is surrounded by a segmented anticoincidence shield, sensitive to charged particles. This thin, plastic detector is the first line of defense in background rejection. Incoming γ rays will pass freely through it while cosmic rays will cause a flash of light enabling the LAT to distinguish between them. The γ ray then continues to the converter-tracker (figure 4.9). Lastly, the system is wrapped in a multilayer "blanket" to provide thermal insulation and protection from debris. For a γ-ray trigger there must be no signal in the anticoincidence shield, the trajectory of the resultant e^+e^- pair must be reconstructed and a realistic measurement in the calorimeter must be made. The LAT is self-triggered and when triggered, all relevant information from the three subsystems is read out to the DAQ and onboard data processing begins. This reduces the size of the data being transmitted to the ground through a process of background rejection. The LAT is not powered by consumables and any heat produced by the overall system is transferred to radiators via heat pipes.

4.2.1.1. *AntiCoincidence Detector.* The primary objective of the ACD is charged particle background rejection. γ rays should penetrate freely while background particles will cause a

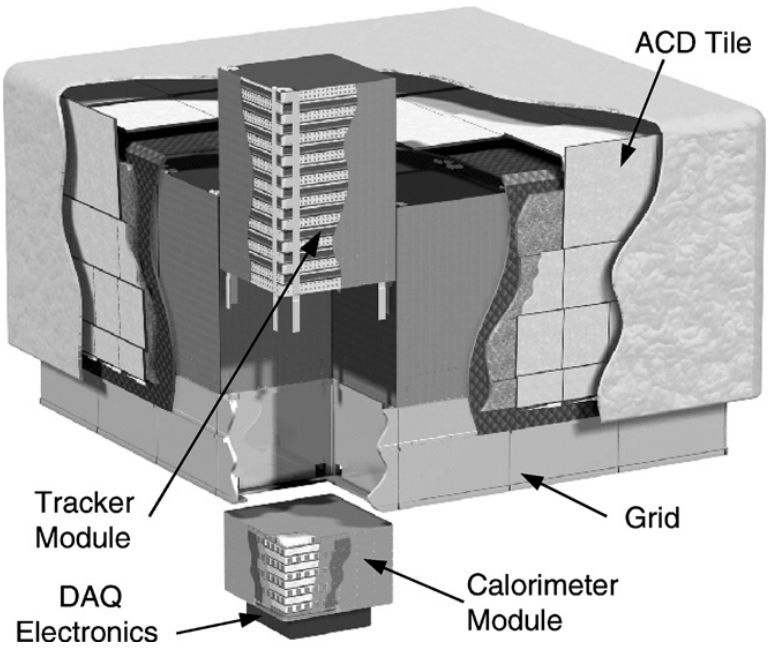

FIGURE 4.8. Schematic diagram of the LAT (Atwood et al.,2007).

flash of light due to an interaction between the highly ionizing, heavy nuclei in the cosmic rays and the ACD, and are discarded. The initial charged particle background rejection is performed using an onboard threshold of 0.45 MIP. Offline ground analysis also provides a threshold of 0.30 MIP (Minimum Ionizing Particle). The LAT requires a high rejection efficiency for charged particles, at least 0.997 efficiency (Atwood et al., 2009). In order to measure γ rays up to the desired 300 GeV, a large calorimeter of mass 1800 kg is required. The size of the calorimeter means a large ACD which increases the Backsplash Effect. The Backsplash Effect occurs when isotropically distributed secondary particles created from pair production in the tracker Compton scatter in the ACD, react with the ACD shield and the entire shower is vetoed. Evidence for this was seen in EGRET data; the detection efficiency deteriorated by a factor of 2 when increasing in energy from 1 GeV to 10 GeV. To keep the process of self-vetoing to a minimum of 20%, the ACD is segmented into 89 plastic scintillator tiles. The scintillator tiles are arranged in a 5×5 array on the top and 16 tiles on each side (figure 4.10). The segmentation significantly reduces the possible area of the ACD where backsplash vetoing can occur (Moiseev et al., 2004).

The advantages of using plastic scintillator tiles include efficiency and reliability, plastic tiles are inexpensive and have been used successfully in various space applications. Wavelength shifting fibers (WLS) embedded in each tile collect the scintillated light. The uniform light collection efficiency for each tile is $\sim 95\%$. However, this decreases to $> 75\%$ for the tile edges (1 - 2 cm on each side) (Atwood et al., 2009). To compensate for this, and maintain an overall

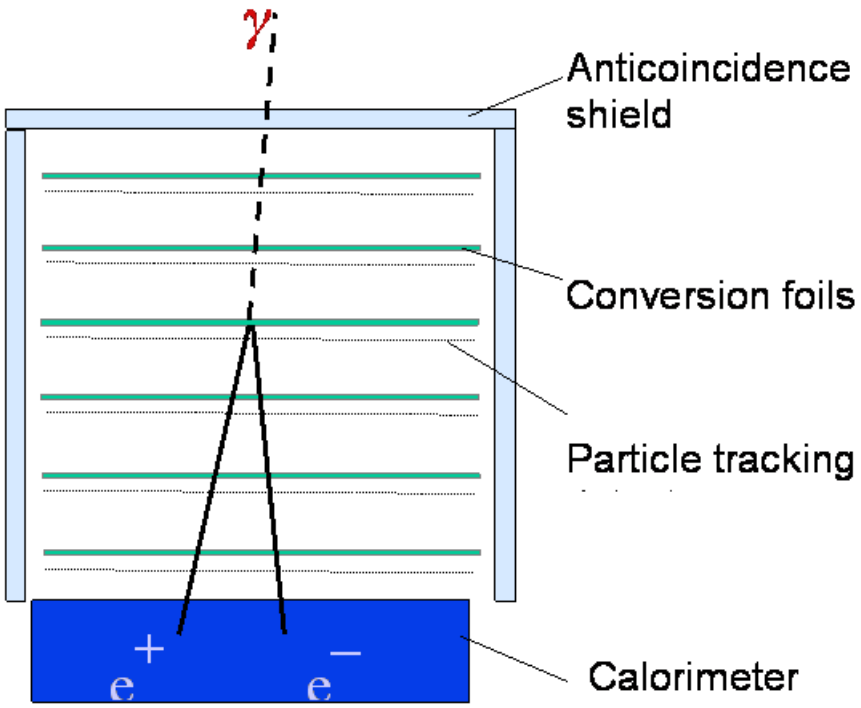

FIGURE 4.9. Illustration of the design behind the LAT's tracker, calorimeter and anti-coincidence system (http://fermi.gsfc.nasa.gov/ssc/data/analysis/documentation/Cicerone/ Cicerone_Introduction/LAT_overview.html).

efficiency of $> 90\%$, the tiles are overlapped in one dimension to minimize these gaps, and in the other dimension scintillating fiber ribbons are use to cover them. Through clear fibers scintillated light is transferred to the electronics, which include 2 PMTs, stored in the bottom of the ACD. The electronics contain 216 channels divided up into 12 groups of 8, each group on a single circuit board, completely independent from each other and connected to the LAT central electronics (Moiseev et al., 2007). The PMTs are powered by a high voltage supply. The ACD is then completely surrounded by a low mass micrometeoroid shield, of density 0.39 g cm^{-2}, to provide protection from micrometeoroids and other debris.

4.2.1.2. *Tracker.* The tracker is the primary detector onboard the LAT, responsible for reconstructing the trajectories of the e^-e^+ pair resulting from pair production and is an array of 4×4 modules (figure 4.11). Each tracker module holds 18 tracking planes. The first 16 are interleaved with high Z, tungsten converter foil (Atwood et al., 2007). The idea behind the process taking place in the converter foils is simple: a γ-ray continues from the ACD into the tracker, reacts with an atom in one of the thin converter foils and pair produces to create an e^-e^+ pair. The e^- and e^+ proceed through the tracker creating ions. The main components of the position-sensitive tracking module are single sided Silicon Strip Detectors (SSDs). SSD

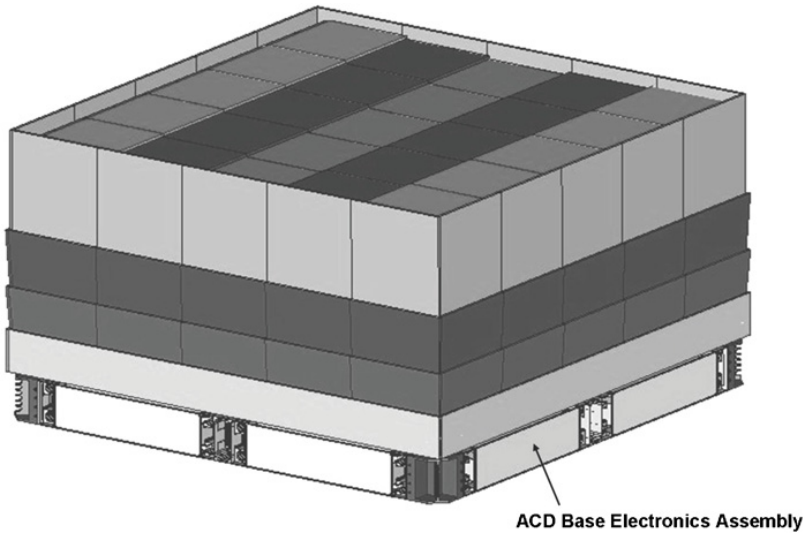

FIGURE 4.10. The LAT ACD design.The 89 plastic scintillator tiles are arranged into an array of 5 x5 on top and 16 for each side. The tiles are overlapped in one dimension to minimize gaps and 2 sets of 4 scintillator fiber ribbons under the tiles also cover gaps (Atwood et al., 2009).

were selected because of their high quality. The bad channel rates of the SSD are $< 0.01\%$ and the average total leakage current is $\sim$ 110 nA (Atwood et al., 2009). The AC-coupled SSDs are 384.56 μm wide with dimensions 8.95 $\times$ 8.95 cm^2 x 400 μm thickness, with an inactive area layer of 1 mm wide. It is important to note here that e^-e^+ pairs produced on the conversion foils that proceed through the inactive area of the SSD are not recorded and are known as "missed hits" or missed detections. At 100 MeV, missing a detection immediately after conversion can result in deterioration of a factor of 2 in resolution creating large tails in the PSF (figure 4.12). To minimize the effects of the inactive regions the tungsten foils only cover the active areas of the SSDs. One of the responsibilities of the tracker is to strike a balance between a small PSF at low energies and a large effective area at high energies. At low energies to achieve a small PSF ($\sim$1/E), thin conversion foils are used. At higher energies to achieve a large effective area, more converter material is required. To compensate for this, the tracker is divided up into 2 regions: the "front" region of the first 12 tracking planes and the "back" region of the next 4 planes. The front region utilizes thin tungsten foils, each of radiation length 0.03 to reduce the PSF at low energies. The back region planes are significantly thicker at a radiation length each of 0.18 in order to increase the effective area for detection at high energies at the expense of angular resolution and also off-axis response. Angular resolution deteriorates by a factor of 2 at 1 GeV. However both simulations and operations show a balance of the LAT's sensitivity to point sources between the front and back sections.

The readout system of the tracker is built around two Application Specific Integrated Circuits (ASICs); a 64-channel amplifier-discriminator chip and a digital readout controller. One of the designs behind the readout system is essentially damage control; to minimize the effects for single layer/cables failure, which at present is the loss of at most 64 channels. When triggered, each amplifier-discriminator registers a 0 (miss) or a 1(hit) to ensure that just the information required for effective tracking is readout and little calibration is needed. The system can continue to trigger on events during the readout of digital counts reducing the deadtime and sustaining a noise occupancy (fraction of channels that stores a noise hit) of 10^{-2} (Atwood et al., 2009). When all tracker layers in a module are considered, the noise in the system becomes negligible and the trigger efficiency approaches 100%.

To guard against attempts to track paths from electromagnetic showers initiated in the calorimeter, time-over-threshold (TOT) of each layer is calculated. Because the charge deposited from such paths is quite large the TOT can distinguish γ-ray events from background events.

The tracker and conversion planes are supported by 19 3 cm thick low-mass carbon-composite trays surrounded by carbon-composite walls (figure 4.13). Because carbon is both thermally conductive and thermally stable, the surrounding walls transfer heat to the base of the tracker array. Along with housing the tracker-converter planes and front end electronics, the bottom trays include the mechanical and thermal connections to the Aluminum grid structure and the top trays support readout cables and mechanical lifting apparatuses.

4.2.1.3. *Calorimeter.* The calorimeter has two main objectives: to calculate the energy deposited from the tracker resulting from pair production and to image the electromagnetic shower development resulting from the e^-e^+ pair. Each calorimeter module (16 in total) is comprised of an array of 8 $\times$ 12, with the dimensions of each crystal being 27 cm $\times$ 2.0 cm $\times$ 32.6 cm (Grove et al., in prep.). The size of the crystals was selected based on the CsI radiation length of 1.86 cm and the Moliere's radius (a constant which describes the interaction properties of a material based on radiation length and atomic length) of 3.8 cm. The crystals are isolated from each other to reduce cross-talk, allow realistic spatial imaging of the shower and accurate reconstruction of its trajectory. Each module is strategically placed perpendicular to surrounding modules (Carlson et al., 1996) and the total vertical depth is 8.6 radiation lengths (figure 4.14).

Each CsI crystal reads out 2 discrete coordinates of the position of the energy deposition in the crystal, along with a more precise coordinate obtained from a light yield asymmetry profile. Two PIN photodiodes are connected to each of 2 ends of the crystal to measure the difference in light and thus determine an energy deposition position. The first photodiode, the larger of the two, has an area of 147 mm^2 and covers the energy range 2 MeV - 1.6 GeV. The smaller photodiode has an area of 2.5 mm^2 and covers the energy range 100 MeV - 70 GeV. In addition to this, each crystal has a pre-amplifier and front end electronics. Both readout signals go through a preamplifier, a shaper and then a pair of Track and Hold circuits. The best energy measurement is then transferred to an Analog to Digital Converter. The position resolution can range from a few mm at low energies to a fraction of a mm at higher energies.

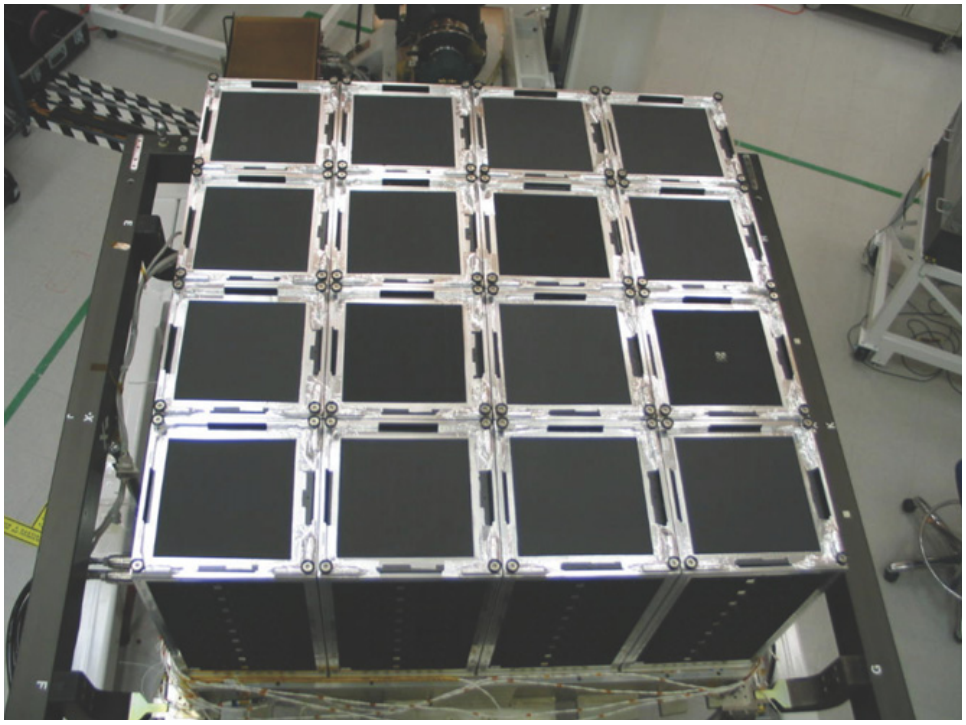

FIGURE 4.11. Completed 16 module tracker array before integration with the ACD - (Atwood et al., 2009).

4.2.2. Data Acquisition System. The LAT's Data Acquisition system (DAQ) is responsible for collecting the recorded data from the ACD, tracker and calorimeter, triggering for multilevel events and performing onboard data processing with background rejection. This significantly reduces the size of the data downlinked form the instrument to ground. Another task performed by the DAQ is preliminary onboard data analysis to detect transients.

The DAQ is hierarchically structured with a four tier architecture (figure 4.15). At the lowest level, each conversion tracker and calorimeter module is linked to a Tower Electronics Module (TEM). TEM triggers are directly dependent on the tracker and calorimeter triggers. The TEM also provides event buffering for smooth event readout and is the interface to the Event Builder Module (EBM). The EBM combines events readout by the TEM and ACD Electronics Module (AEM) and produces complete instrument events which are then transferred to the Event Processor Units (EPUs). The AEM is the equivalent to the TEM for the ACD. Both the EBM and AEM are components of the overall instrument Global-trigger/ACD- Module/Signal distribution Unit (GASU), which is controlled by onboard trigger software. In addition to the EBM and AEM, the GASU also comprises of a Global-Trigger Electronics Module (GEM) and the Command Response Unit (CRU). The GEM produces decision signals based on the TEM and ACD triggers while the CRU is responsible for the DAQ clock signal and also sends and receives commands. There are two EPUs onboard for data processing. This level of data processing

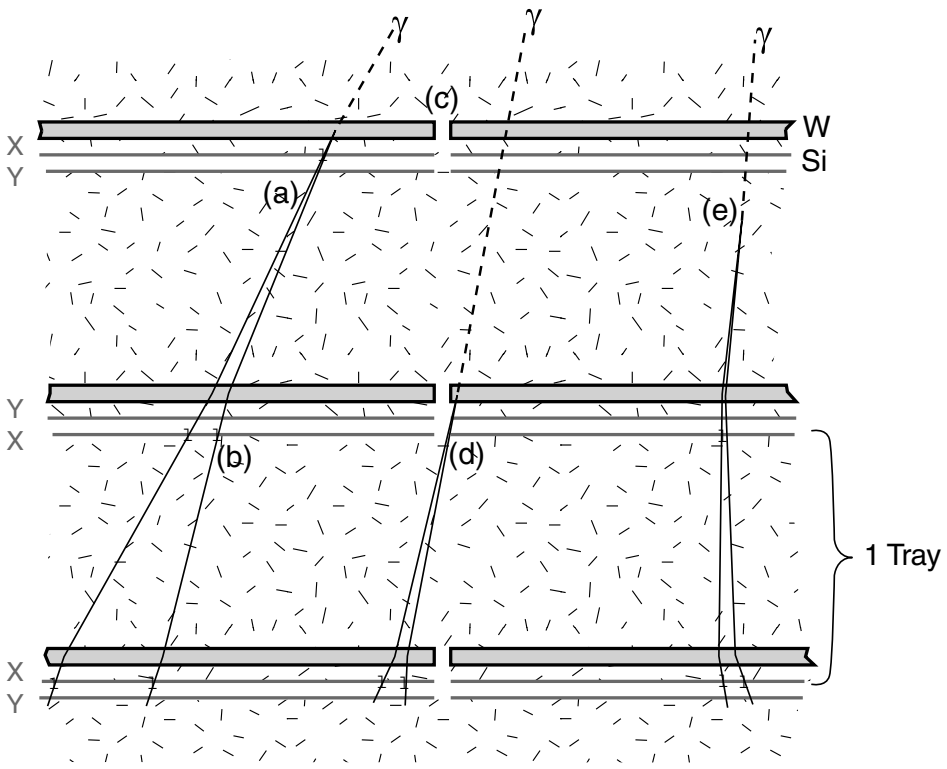

FIGURE 4.12. Schematic diagram of the tracker design. The pair production at point (a) is an ideal conversion and at (b) the tracker can detect 2 particles and track the trajectory. Point (c) demonstrates how the tungsten foils only cover the active areas of the SSDs. At point (d) a "missed hit" is evident, detected in the second layer. The PSF has likely deteriorated significantly. Pair production in the SSD is seen at (e). This lengthens the arms for multiple scattering, multiple hits can highlight this. - (Atwood et al., 2009).

involves using filter algorithms to reduce the event rate from 2-4 kHz to ∼400 Hz (Atwood et al., 2009) and also downlinks the data. The event rate is reduced by charged particle background rejection thereby increasing the γ-ray event rate in relation to the total event rate. The highest level of the DAQ architecture is the Spacecraft Interface Unit (SIU) which controls the LAT instrument itself. Both the EPUs and SIU use a RAD 750 Compact PCI processor operating at 115.5 MHz, which provides 80-90 MIPs, and are controlled by the LAT's flight software. A final component of the DAQ is the Power Distribution Unit (PDU) which supplies DC current to the GASU and EPUs and monitors the instrument's temperature and voltage.

4.2.3. Programmable Trigger. The LAT's instrument-level event trigger system begins in the tracker and calorimeter modules. A tracker module can generate a trigger request signal if a channel/plane exceeds a preset threshold. The trigger request is sent to the TEM associated with that particular module. If the trigger is verified by the TEM, the trigger request is then

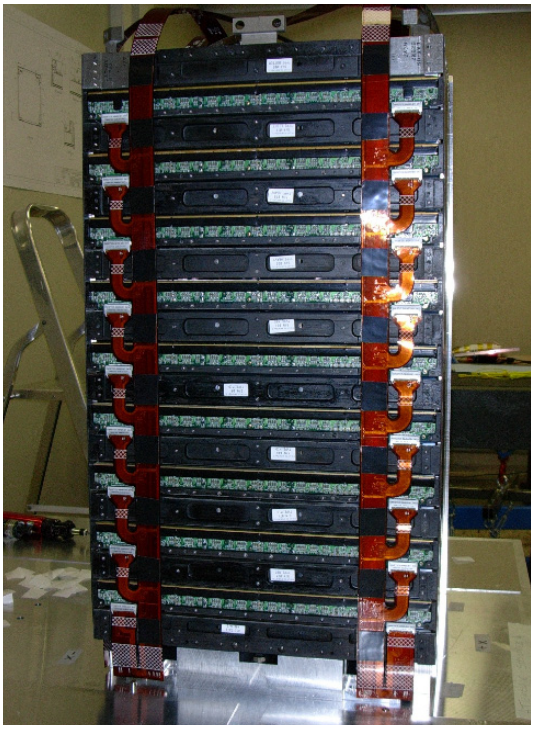

FIGURE 4.13. A completed tracker module with one sidewall removed (Atwood et al.,2009).

transmitted to the GEM. Typically the TEMs' trigger condition criteria request prompts from 3 planes. A calorimeter module can also generate a trigger request signal if the predetermined low or high energy thresholds are reached for a given crystal. A trigger accept message (TAM) signal is then sent by the GEM to the AEM and each TEM if the TEM trigger request meets the instrument-level trigger standards within a preset trigger window width. There are no delays in this stage of the system. In response to the TAM, the TEM transmits a trigger acknowledge (TACK) signal to the tracker and calorimeter front ends, and the AEM sends the signal to the ACD. This initiates a complete readout of the tracker, calorimeter and ACD system e.g. location of detection with regards to layers in the tracker module, the TOT for every layer in each tracker module, calorimeter channel pulse heights, ACD statistics, etc. ACD statistics include discriminated signals due to BackSplash self vetoing and charge particle background rejection discrimination of cosmic rays. The trigger information is then sent from the GEM to the EBM where complete LAT events are constructed, this is the final stage of the triggering process. The GEM also records the overall system deadtimes to the event data. A typical instrument deadtime for this stage of the system is $\sim$26.50 μs while the deadtimes recorded in the TACK signal stage range from 2.3 - 2.4 μs (Atwood et al., 2009). The GEM can also be triggered on non-detection inputs for calibration or diagnostics. An example of this is when a

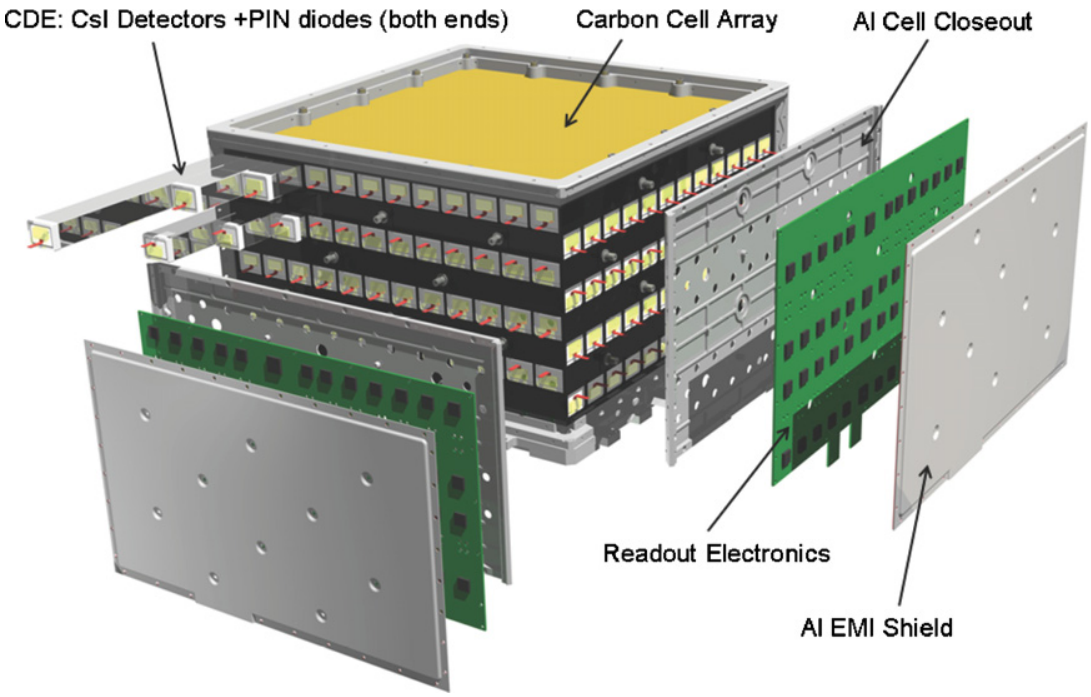

FIGURE 4.14. Schematic configuration of the LAT calorimeter module. The 96 CsI(Tl) scintillator crystals arranged in 8 layers of 12 with the crystals in adjacent layers rotated by 90° (Atwood et al., 2009).

GPS spacecraft clock signal is transmitted to the GEM, to investigate if the time measurement for an individual event is accurate.

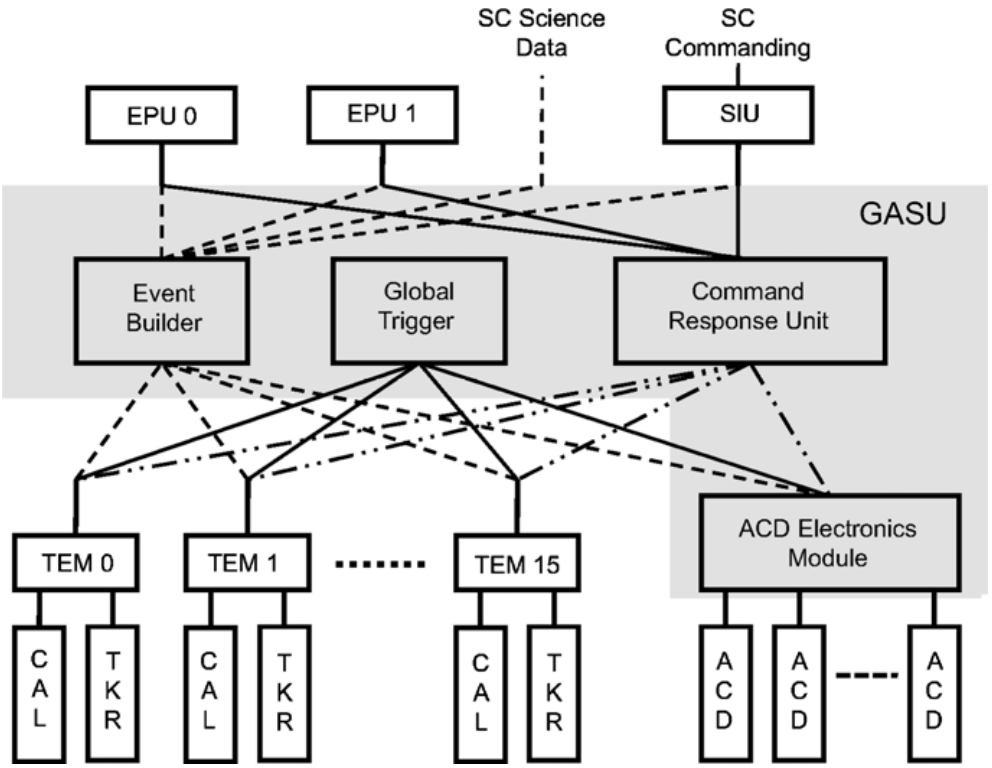

FIGURE 4.15. The hierarchal LAT Data Acquisition system (DAQ). The GASU is comprised of the AEM, the GEM, the EBM and the AEM. The TEMs are the interfaces for the tracker and calorimeter modules. At the highest level, there are two EPUs and 1 SIU for onboard data processing and instrument control (Atwood et al., 2009).

CHAPTER 5

Data Analysis

5.1. Introduction

This chapter presents an outline of the point source analysis procedures for both the VERITAS telescope array and the Fermi LAT satellite. While both analyses focus on source detection and localization, significance estimation, integral flux and flux rates determination, spectral analysis and variability studies, the analysis packages and methodologies differ. For VERITAS, the calibration, NSB and charged particle background rejections, γ-ray shower reconstruction and analysis take place within the offline VEGAS analysis software. In contrast to this, the Fermi LAT analysis is divided between on-board calibration, level-1 charged particle background rejection and shower reconstruction at the Fermi Instrument Science Operations Center (ISOC), and high-level γ-ray analysis with the offline Fermi science tools.

5.2. VERITAS

The primary aim of the VERITAS analysis package is to identify γ-ray signals above background. There are five main steps in the analysis of VERITAS data:

- Calibration calculation involving pedestal subtraction, relative gain flatfielding and timing corrections
- Calibration application to the raw data
- Image cleaning and parameterization to identify pixels with potential Cherenkov signals and to distinguish between γ-ray and hadronic showers
- Shower reconstruction to determine the shower origin and core location
- Results extraction to generate spectra, lightcurves and 2D images

The software package used in this thesis is VEGAS (the VERITAS Gamma-ray Analysis Suite), version v230. Table 5.1 presents an outline of the various stages of the VEGAS software. A summary of each stage in the analysis chain is given below.

5.2.1. FADC traces. An FADC trace is the name given to the voltage profile of the digitized pulse of photoelectrons produced when a photon strikes a PMT. The trace is digitized into a 48 ns window of 24 samples. The FADC trace contains total charge information and the arrival time at each pixel.The charge or amplitude of digital counts (DC) of the FADC trace for each photon is proportional to the number of photoelectrons generated.

This signal includes a significant amount of NSB that have durations of only 8 - 10 ns. To compensate for this and to limit the amount of NSB, an integration window is used to capture

TABLE 5.1. The stages of VEGAS, version v2.3.0, used in the analyses presented in this thesis.

Stage	Function
1	Calibration Calculation
2	Calibration Application
	Image Cleaning
	Hillas Parameterization
4.2	Quality Selection Cuts
	Energy Reconstruction
	Shower Origin and Core Reconstruction
6	Results Extractor
	Mean Scaled Parameter cuts
	θ^2 cut
	Flux an Significance determination
	Spectral Analysis

the Cherenkov signal. The standard point source integration window width used is 7 samples. This means the FADC trace accommodates several integration windows (figure 5.1) . This FADC trace has 24 samples, and the integration window width is seven samples. The start of the first window starts randomly at the second sample, covering samples 2 to 9. The second window covers 9 to 16 and the third window covers samples 16 to 23. The fourth window starts at sample 23 and wraps around to the beginning and includes samples 0 to 5.

5.2.2. Raw data productions. The inputs to the analysis chain are VERITAS Bank Format (VBF) files. Each VBF file is a separate ($\sim$ 20 minutes) observing run containing event information (e.g. trigger details) and also contains pedestal, gain flatfielding and timing discrepancy information required in the camera calibration stage described below. Additional longer term information (e.g. pointing corrections) is stored in the VERITAS offline database which is accessible by the analysis chain.

5.2.3. Calibration Calculation. The first stage of the analysis process is to calculate the precise calibration corrections required for each camera. This process involves calculations for FADC injected pedestal subtraction, relative gain flatfielding and timing offsets corrections.

5.2.3.1. *Pedestals.* In order to characterize a Cherenkov image, it is necessary to obtain an accurate representation of the NSB which is evident during observations as fluctuating Direct Current (DC). The output PMT signals are "AC Coupled", using a high-pass filter to remove the DC component, thereby repositioning the fluctuating signal around the zero mark before being transferred to the FADCs for digitization. As the FADCs can only digitize the negative polarity of the PMTs, positive NSB fluctuations can not be identified, making generating an accurate NSB distribution representation difficult. To compensate for this, a fixed ($\sim$ 16 DC) artificial offset (a pedestal) is injected into the PMT signal in order to shift the entire oscillating signal into one polarity for digitization. In order to get an accurate picture of the NSB, the camera is covered/pointed to a dark patch of sky and the FADC's are read out, with an event rate of 1 - 3 Hz (Cogan, 2006). The resulting signals, which are not expected to contain Cherenkov pulses,

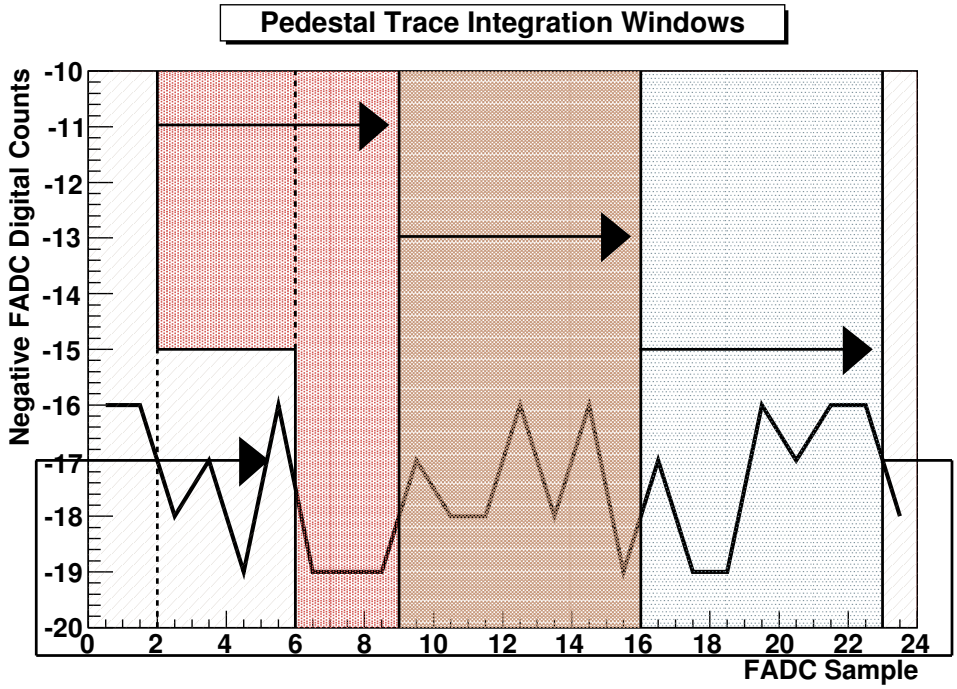

FIGURE 5.1. An FADC trace of 24 samples of 2ns each with an integration window width of 7 samples - Cogan (2006).

are read-out in a forced-trigger mode and are known as "pedestal events". Each pedestal event samples the NSB per pixel and an accurate NSB distribution can be created. For a given pixel, a distribution of pedestal events for an observing run is generated (figure 5.2).

The greater the NSB, the wider the pedestal distribution. The RMS value of the pedestal distribution is defined as the "pedvar". The pedvar for a given channel is dependent on the NSB and is not constant throughout an observing run (> twenty minutes) as NSB fluctuates and is recalculated every three minutes. This time interval was selected as it is large enough to collect adequate statistics but also small enough for NSB changes to be assumed negligible. Scaled pedvar is a term that describes the pedvar of each pixel relative to the average of the camera and is also recalculated every three minutes. Scaled pedvar is used to identify bad pixels as it takes the camera average into account (figure 5.3)

$$scaled\ pedvar = \frac{pedvar - mean\ camera\ pedvar}{\delta_{pedvar}} \tag{60}$$

where δ_{pedvar} is the standard deviation of the mean camera pedvar.
The pedvar is used to distinguish pixels that are not consistent with the camera average. The pixels may be poorly operating pixels or experiencing a large signal due to NSB or the presence

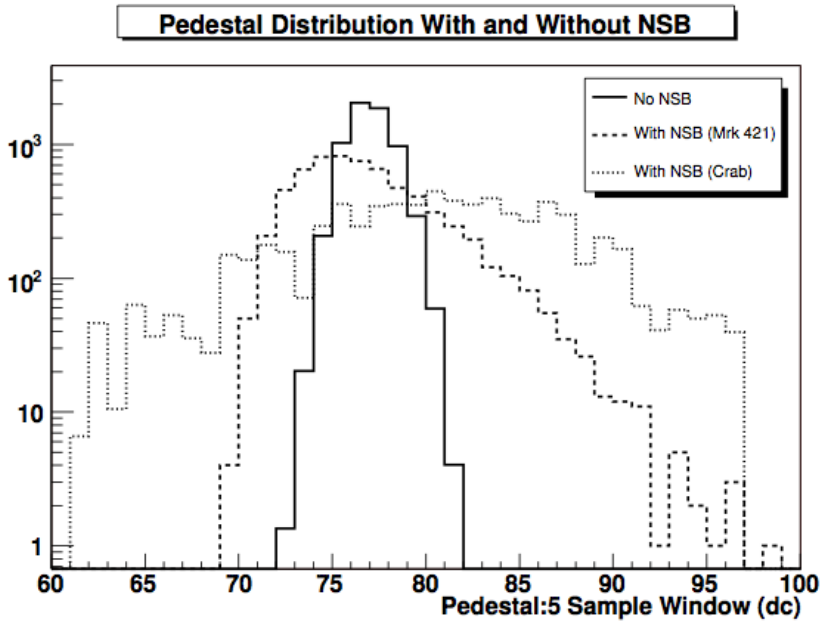

FIGURE 5.2. Distribution of the pedestal values recorded for a single pixel for three levels of NSB. No NSB is achieved when the focus box containing the camera closed. Cogan (2006).

of a Cherenkov pulse. Using relative pedvar cuts of -2.5 and 4, performed in the second stage of the analysis chain, it is possible to exclude PMTs not consistent with the camera average from the analysis chain.

5.2.3.2. *Relative Gain Flatfielding.* For each telescope it is crucial that PMT responses across the camera are uniform to avoid Cherenkov shower images being distorted. The gain in each PMT is dependent exponentially on the high voltage applied to it by a factor of $\sim$7.5.[1]

$$Gain = HV^{7.5} \tag{61}$$

However, due to the subtle differences in the PMTs as a result of the combination of damage/aging and manufacturing processes, the same voltage applied to each PMT will not yield the same gain. The consequence of this is that the charge measured across the camera is not uniform, distorting images. A "flatfielding" process of adjusting the HV applied to each PMT (to aid in equalizing the gains) is performed at the beginning of each observing season but gain differences (due to humidity, dirt, aging of the PMTS) are also see on a nightly basis so an offline procedure known as "relative gain flatfielding" is performed. Nitrogen laser calibration runs, at equal intensity and at a frequency of 10 Hz, are used to measure the relative gains required for flatfielding. The laser utilizes an opal diffuser positioned on the optical axis of each telescope to

[1]Photonis product specification datasheet

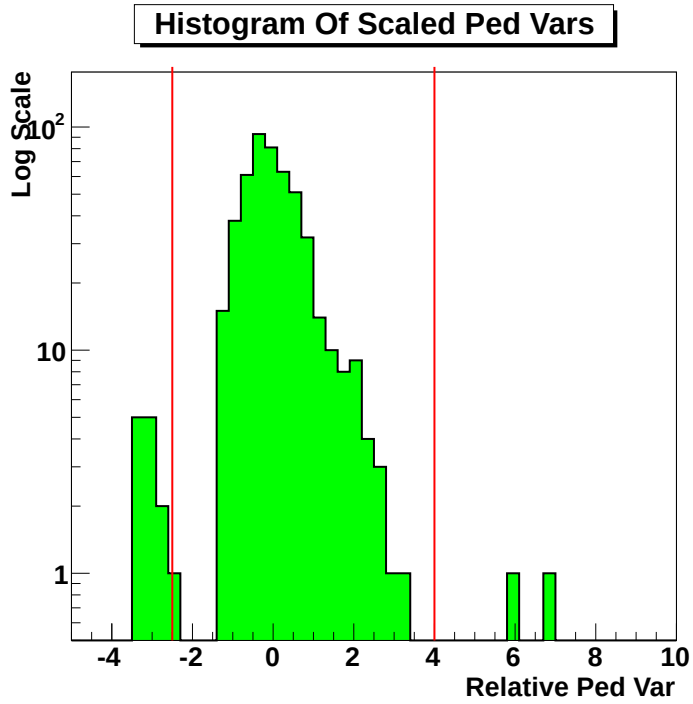

FIGURE 5.3. Distribution of scaled pedvars for a singe telescope over an observing run of duration 20 minutes.

illuminate the PMTs with uniform flashes. In November 2009, VERITAS introduced a low cost, compact LED flasher with a similar rate and intensity to the laser, which gradually replaced the laser. The PMT signal is read out with no adjustments to the pixel status (e.g. current) and without any pixel suppression. For each laser flash, the FADC trace is recorded in each pixel and the average charge across the camera is calculated. The relative charge statistics for each pixel for the duration of the calibration run is generated.

The mean of this distribution is referred to as the relative gain while the standard deviation from the mean is known as the relative gainvar. The relative gain is used in the relative gain flatfielding of the camera, to scale the charge measured across the camera (figure 5.4). The relative gainvar is used to identify poorly operating pixels. A generally accepted range of values for relative gainvars is between 0.05 and 0.4. Outside of these values, the PMT is classified as "bad" and its statistics are excluded from the analysis during stage 2 (figure 5.5). In addition to monitoring gains, laser calibration runs are used to monitor for dead pixels and other problems.

5.2.3.3. *Relative Timing Offsets.* Due to differences in FADC clock times, the 4 FADC crates in each telescope read out their channels at different times. To compensate for these timing discrepancies, a copy of the L2 trigger signal is stored in a designated channel in each crate. During the offline analysis, using one of the L2 signals as a reference, the L2 traces are compared

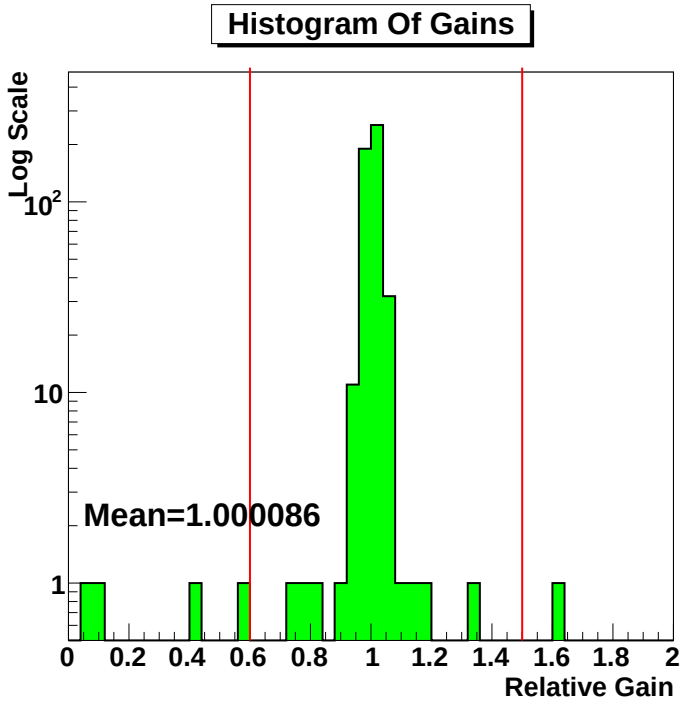

FIGURE 5.4. Distribution of relative gains for a single telescope for a single run. The red lines represent quality cuts.

and aligned. The timing adjustments required for each signal are then applied to each crate's PMT traces.

To calculate the charge produced by a Cherenkov signal in an FADC trace an integration window is placed at the position of the pulse. This is based on the logic that a uniform light produces FADC traces that match up temporally. However a spread in the arrival times of the Cherenkov pulses is observed due to various influencing factors such as the above mentioned cable length differences and general delays in the FADC electronics. As increasing the integration window size will also increase the background in the signal, one option is to reposition the integration window on the average trace arrival time. Measuring timing offsets is required here. The laser calibration run is also used in the timing measurements. The trace arrival time (T_{zero}) is the time taken for the trace to reach half its maximum value. T_{zero} is measured for each pixel for a given event and the average arrival time for the camera for an event is calculated from

$$T_{event} = \frac{1}{n}\sum_{i=1}^{n} T_{zero} \tag{62}$$

where n is the number of pixels.

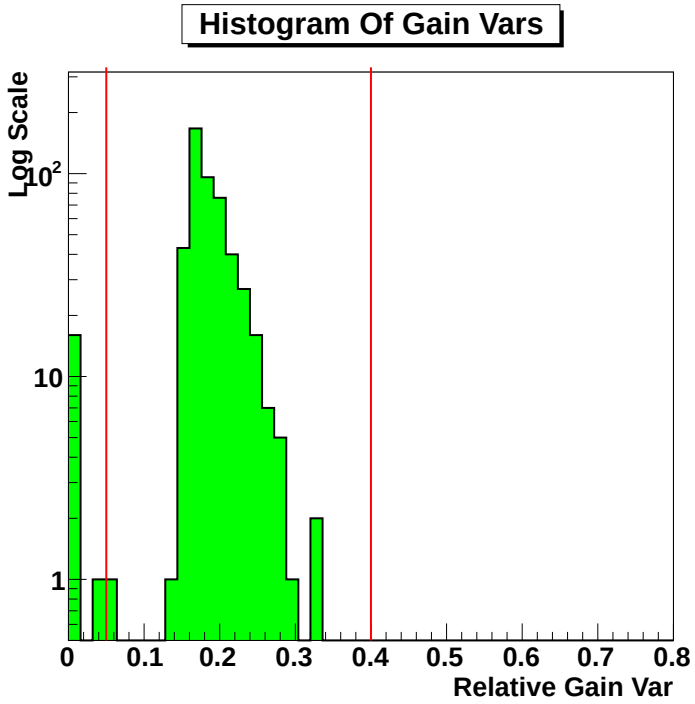

FIGURE 5.5. Distribution of relative gainvars for a single telescope for a single run. The red lines represent quality cuts.

The difference between the two values is recorded for each pixel.

$$\Delta T_i = T_{zero\ i} - T_{event} \tag{63}$$

This process is repeated for a number of events (m) and a distribution for each pixel is generated. The mean of this distribution is referred to as the timing offset (T_{offset}) for that pixel.

$$T_{offset\ i} = \frac{1}{m}\sum_{j=0}^{m} \Delta\ T_{i\ j} \tag{64}$$

Each pixel will be adjusted by its calculated (T_{offset}) value during the calibration application stage of the analysis, for the entire night's data. For each channel, the T_{offset} correction is applied and the FADC traces then match up temporally. This enables a smaller sized integration window to be used, decreasing background and increasing sensitivity (figure 5.6).

5.2.4. Calibration Application. Once the charges in each PMT are measured for an image, all the previously calculated calibration parameters can be applied to them. The calculated timing offsets are applied to each channel to temporally match up the FADC traces. For each pixel, the measured pedestal is subtracted from the calculated relative charge per event and the pixel is relative gain adjusted as part of the flatfielding processes. Relative pedvar and gainvar

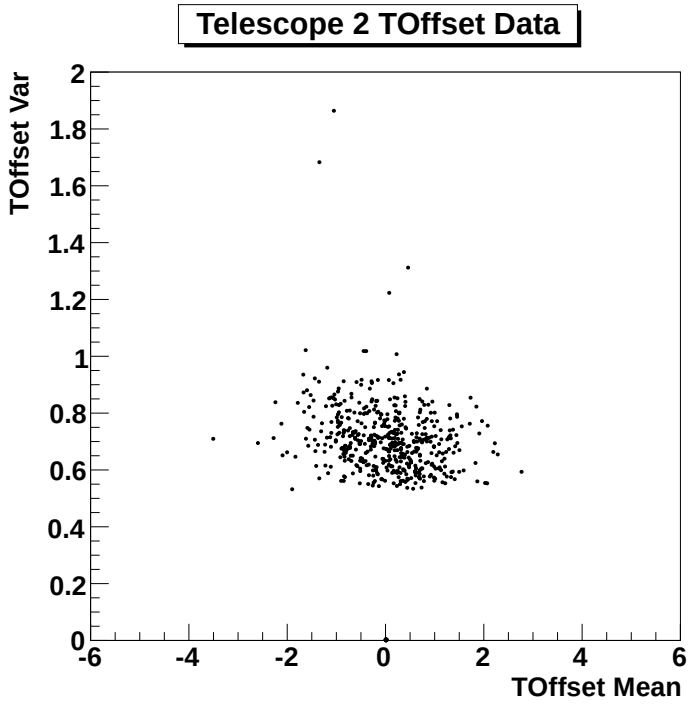

FIGURE 5.6. Distribution of T_{offset} values for a single telescope.

cuts to remove poorly operating pixels are performed here. The data is now ready for image cleaning and parameterization.

5.2.5. Image Cleaning and Parameterization.

5.2.5.1. *Image Cleaning.* This stage of the analysis is dedicated to identifying potential Cherenkov signals and performing background rejection. It is probable that a large portion of the camera pixels at this point contain just NSB which can be removed with the identification and exclusion of these pixels while keeping the pixels that show evidence of Cherenkov light. A pixel is classified as a "picture" pixel if its measured charge is more than five times greater than the pixel pedvar while the criteria for a "boundary" pixel includes both that it is adjacent to a "picture" pixel and that its measured charge is at least 2.5 times the pedvar value. Both categories of pixels define the image and are retained for image parameterization and shower reconstruction. Single, isolated pixels that surpass either threshold are set to zero and are effectively removed from the image (figures 5.7 and 5.8).

5.2.5.2. *Image Parameterization.* Image parameterization is the next step after image cleaning in the analysis chain and is the basis for hadron image discrimination. For parameterization of an image in a single telescope, the Hillas (1985b) moment-analysis parameters are the most effective. Parameterization of generated 3D Monte Carlo simulations provides a range of values for each of the parameters described in table 5.2 and figure 5.9. The first order moments find the

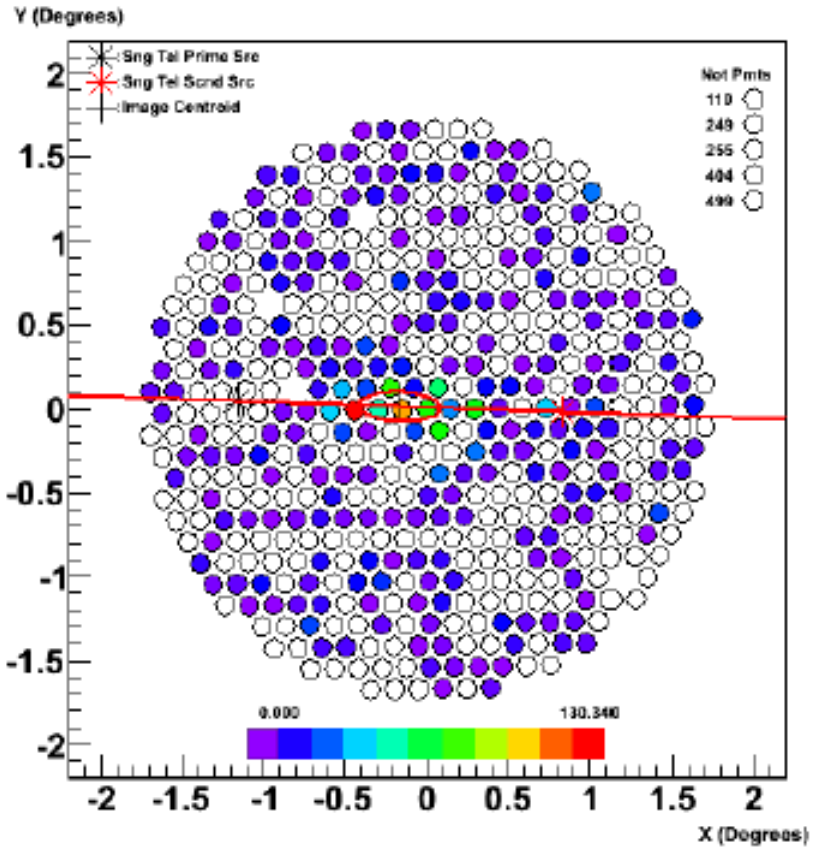

FIGURE 5.7. Image before cleaning (Ward, 2010)

TABLE 5.2. Hillas Parameters

Parameter	Description
Size (dc)	Total integrated charge in all image pixels; the total light measured for the image
Distance	Distance from the image centroid to the centre of the FOV
Width	R.M.S. spread of light perpendicular to the major axis of the image ellipse
Length	R.M.S. spread of light parallel to the major axis of the image ellipse
Alpha	Angle between the image ellipse major axis and a line from the image centroid to the center of the field of view

image centroid, the primary axis of which is responsible for estimating the position and orientation. A set of of second order moments applied to the image then enable the width and length to be calculated, which characterize the longitudinal and lateral development of the shower. For an image to be considered a γ-ray image the following parameters must be within a specified range: Distance, Width, Length and Size.

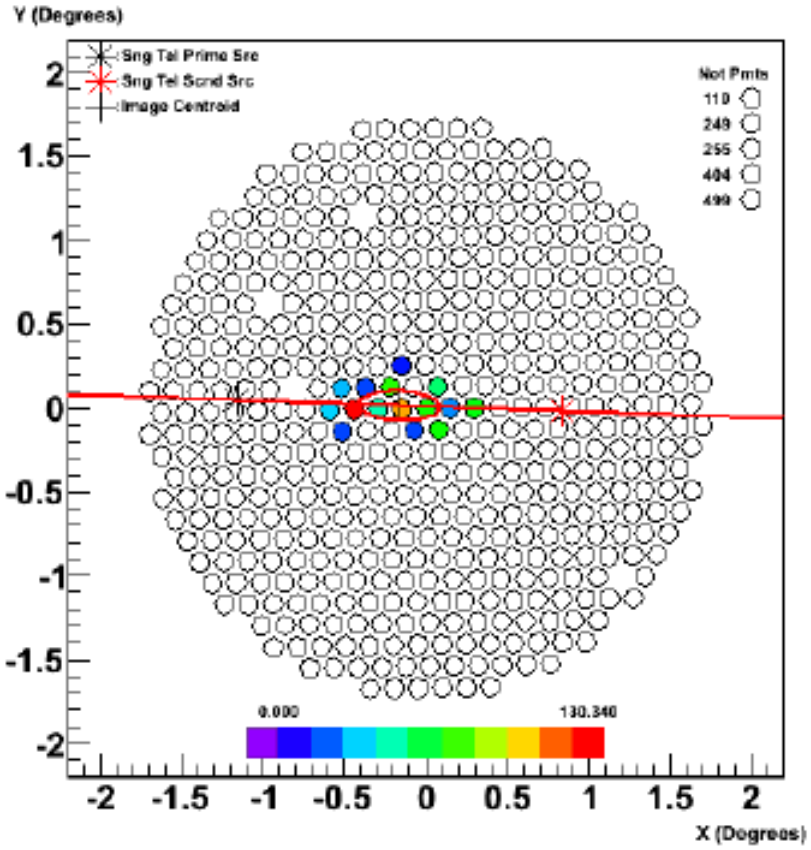

FIGURE 5.8. Image after cleaning (Ward 2010)

5.2.6. Shower Reconstruction. Hillas parameterization, with the addition of stereoscopic multi-telescope observations, increases the efficiency of both hadronic image discrimination and shower reconstruction. Using the intersection of the major axes of the γ-ray shower image in multiple cameras, it is possible to constrain the arrival direction of the γ ray. The energy is estimated with the application of Monte Carlo shower simulations. Data Quality Monitoring is also performed at this stage through a system of quality selection cuts described in section 5.2.6.1, to ensure the events are adequate for accurate shower reconstruction.

5.2.6.1. *Data quality for shower reconstruction.* Data quality selection performed on the images comprises of three principal cuts: minimum size (total integral charge in dc in the image PMTs), maximum distance between the image centre and the centre of the field of view (measured in degrees) and the minimum number of pixels that contain the image. The combination of these cuts ensure good quality images. The values of the cuts are selected based on the calculated photon index for the spectrum of the source being observed (table 5.3). The minimum size cut (a crude energy cut) is important as there is difficulty involved in accurately reconstructing small

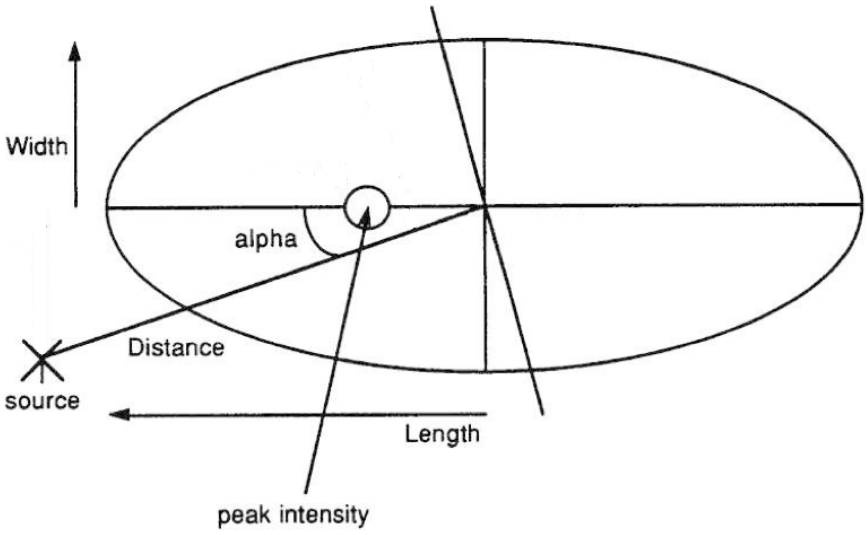

FIGURE 5.9. Illustration of the Hillas Parameters (Reynolds *et al.* (1993))

TABLE 5.3. Data Quality Cuts

Cuts	Soft	Medium	Hard
Photon Index	-4	-2.4	-2
Lower Size (dc)	200	600	1000
Upper Distance (m)	2.0	1.43	1.43
Minimum Ntubes	5	5	5

or faint images. The maximum distance cut removes images close to the camera edge which can be truncated and distorted. With faint or distorted images, Hillas Parameterization becomes unreliable. An example of this is an underestimated size measurement of an image at the camera edge making realistic shower reconstruction problematic. Unfortunately at lower energies γ-ray images are fainter which decreases the array's sensitivity at the lower end of the array's energy range.

5.2.6.2. *Shower Direction and Core Location Determination.* It is difficult with a single telescope to estimate where along the trajectory of the major axis the shower originated. It is possible to estimate the direction the shower is coming from the intersection of at least two camera images axes with the camera views superimposed (figure 5.10). Using multiple images (stereoscopic imaging) decreases the uncertainty on the intersection and further constrains the shower core origin location.

To determine the energy of the γ-ray shower, the core location on the ground is calculated. Major axes are reconstructed out of the camera towards the ground (figure 5.11). Note here, the camera views are not superimposed. For more than two telescopes, it is not probable that a

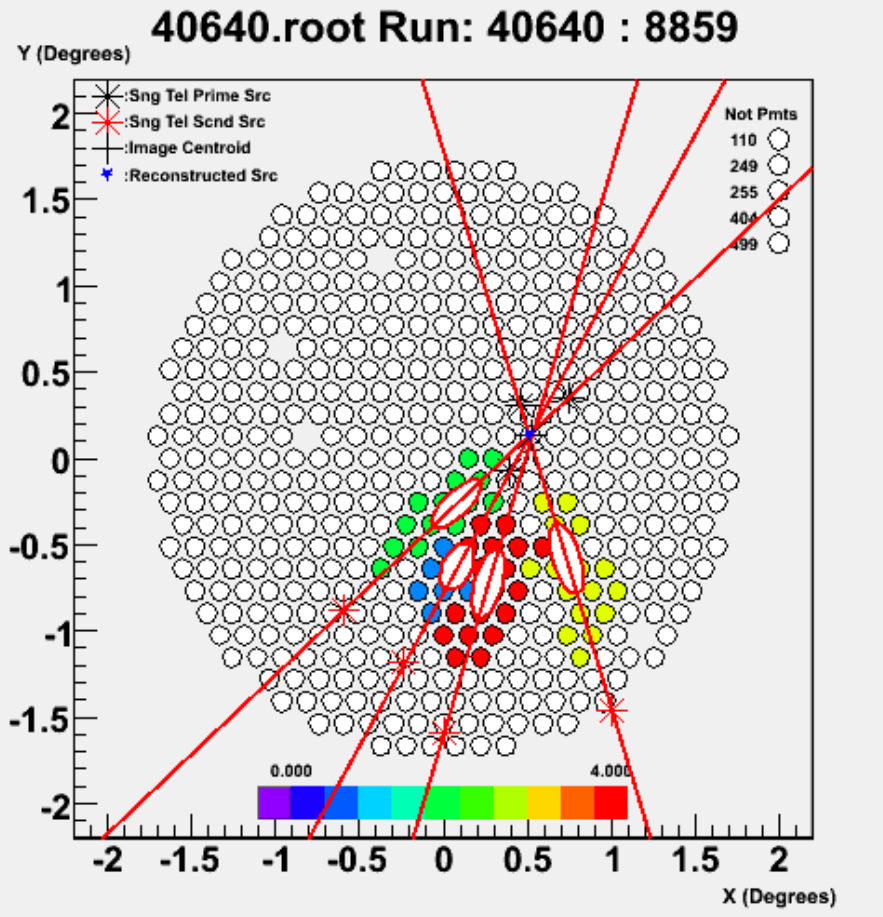

FIGURE 5.10. Shower direction determination (Valcercel, 2008).

perfect intersection producing a single point will occur. It is necessary to calculate the impact distances (the minimum angular distance from each telescope to the shower core location in the array plane) as the telescopes closest to the shower core will have brighter images than those further away. Currently the shower core location resolution for the array is $\sim$ 7.5 m (Krawczynski et al., 2007). Because the impact distance varies for each telescope, the distance values are weighted and the shower core distance is determined. Accurately reconstructing the shower origin location improves energy and angular resolution. Angular resolution is defined as the 68% containment radius and is currently 0.15°.

5.2.7. Mean Scaled Parameters. As mentioned above, the Hillas parameterization (in particular width and length) enables hadron shower images to be discriminated based on their shapes. One limitation however is that the shape of the image depends on a number of factors such as impact distance, elevation, zenith angle, etc. Because of this it is difficult to infer the energy of a shower from the Hillas parameters alone. Thousands of γ-ray showers are simulated

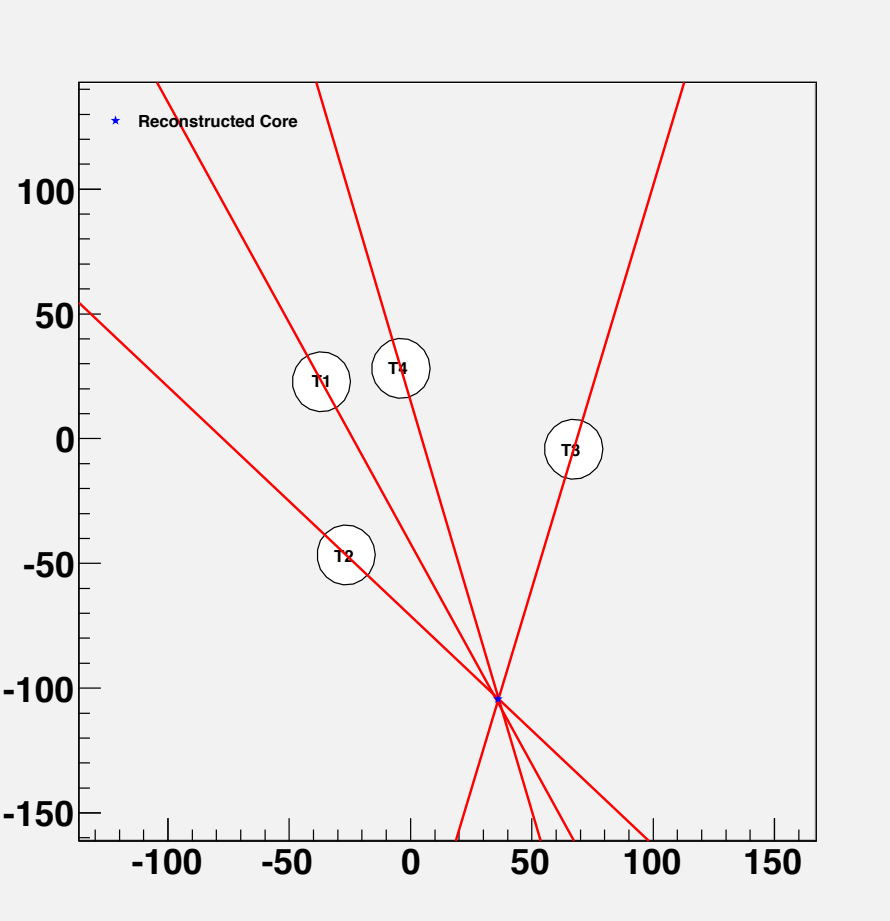

FIGURE 5.11. Shower core location determination - Valcercel (2008)

for various observational properties such as zenith angle and NSB, and are propagated through detector simulations and offline analysis to produce "lookup" tables containing Hillas parameter, size and impact distance values for comparison with the actual events detected so that the energy can be estimated. For an event at distance D with size S, mean scaled parameters (length and width) are calculated and provide excellent cuts for distinguishing γ-ray images from cosmic-ray background. The Scaled Length is defined as

$$SL = \frac{L(S,D)}{L_{sim}(S,D)} \tag{65}$$

where L(S,D) is the measured image length and L_{sim}(S,D) is the length for a simulated event with the same size and impact distance from the lookup tables. The Scaled Width is calculated similarly.

TABLE 5.4. Mean Scaled Parameters

Mean Scaled Parameter	Soft	Medium	Hard
MSL	0.05 - 1.15	0.05 - 1.28	0.05 - 1.28
MSW	0.05 - 0.13	0.05 - 1.08	0.05 - 1.08

From these values the Mean Scaled Length (MSL) and Width (MSW) values are calculated for the array by

$$MSL = \frac{1}{N_{telecope}} \sum_{i=0}^{N_{telescope}-1} SL \tag{66}$$

Optimal MSL and MSW cuts can be determined from photon index of the source being analysed and can significantly reduce background signal (table **??** and figure 5.12).

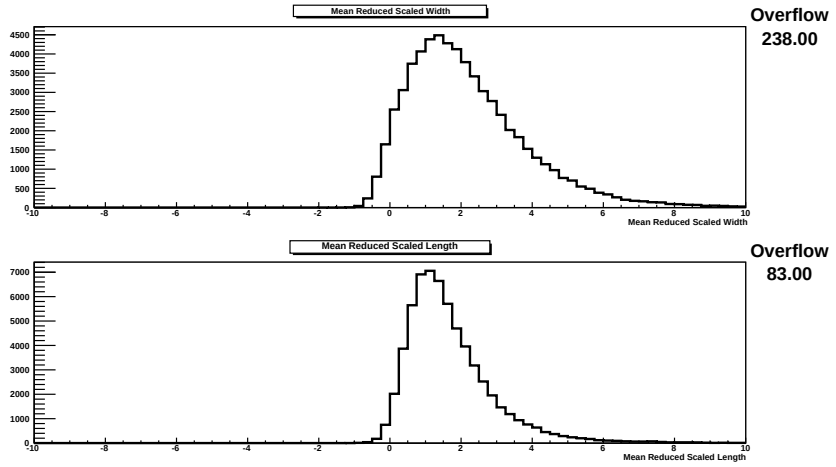

FIGURE 5.12. Mean Scaled Width and Length shower parameters for one run

A θ^2 cut (θ is the angular radius around the source being analyzed) can also be applied here to limit background. This aids in background rejection and limits the events detected to events from the particular source.

5.2.8. Energy Calculation. The original energy of the γ ray can be determined from size and impact distance values combined with simulation tables, in this case energy lookup tables. From simulations of various sizes, impact distances, zenith angle etc., it is possible to estimate the energy via comparison with the actual event. Energy resolution (accuracy) is $\sim$20%.

5.2.9. Background Models. It is necessary to create an accurate representation of the background in order to represent the source γ-ray events or ON events that surpass the hardware triggers and software cuts to calculate the excess events required for flux estimation and spectral analysis. The number of excess events is calculated from the equation

TABLE 5.5. Wobble 1ES 0502+675 results

Total On Events	4.49e3
Total Off Events	3.33e4
Total Exposure Time	1.73e3
Alpha	0.111, 0.0909
Significance σ	12.1
γ-ray Rate (min^{-1})	0.47 $\pm$ 0.04
Background Rate (min^{-1})	2.13

$$N_{excess} = N_{on} - \alpha N_{off} \tag{67}$$

where α is the normalization factor between the two regions. There are two methods explained below, of modeling the background and also of determining this α value.

5.2.9.1. *Reflected Region Model.* The Region Background Model, as illustrated in figure 5.13 uses an OFF region of the same size and angular distance from the centre of the field of view of the camera as the ON region. The OFF region is observed with the same exposure time during the same observation which means the camera acceptance is equal. The alpha α value can be determined from

$$\alpha = \frac{1}{n} \tag{68}$$

where n is the number of background regions. This model is only relevant in wobble mode and for source of known position. During wobble observations, the source is offset by a distance of 0.5° in north, south, east and west directions from the centre of the field of view of the camera. Ideally, an equal number of north, south, east and west observations are achieved and an accurate representation of the background is produced (Fomin et al., 1994). As many as 11 OFF regions can be used as long as the regions are at a large enough distance from the ON region to prevent cross contamination of γ-rays. The larger the number of OFF regions used, the better the background estimation. The data used in the analyses of this thesis were all taken in wobble mode.

5.2.9.2. *Ring Background Model.* This model is more frequently used in sky surveys or in situations where the exact source location is unknown. The Off region is an annulus positioned around the On region (figure 5.14). Due to the difference in size, the camera acceptance for both regions differs and the calculation of alpha becomes more complicated.

Tables 5.5 and 5.6 are wobble and RBM analyses for the blazar 1EA 0502+675 which agree very well (note the differences in ON and OFF counts die to the difference in background).

5.2.10. Significance Calculation. Once the background region is accounted for and the number of excess events is calculated, the next step is determining whether there is a significant detection. If N_{excess} is negative, one can assume there is no signal present. When N_{excess} is

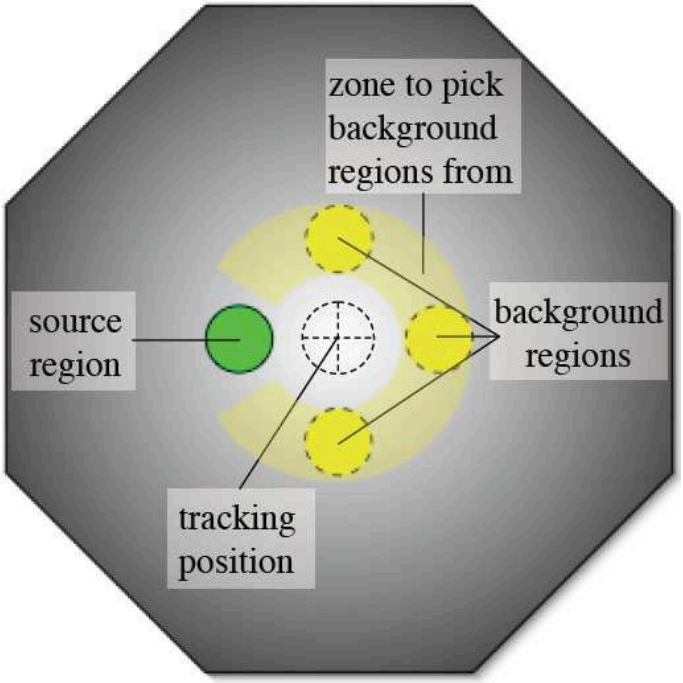

FIGURE 5.13. Illustration of the Reflected Region Model - Varcarcel (2008)

TABLE 5.6. RBM 1ES 0502+675 results

Parameter	Source Location
RA (deg)	76.9846
Dec (deg)	67.6233
ON Counts	4552
OFF Counts	55078
EXCESS Counts	785.25
Alpha parameter	0.0678448
SIGNIFICANCE σ	12.00
EXPOSURE (min)	1728.07
Integral acc.	0.05
RATE (γ-ray min^{-1})	0.45 ± 0.04
Background RATE (Bg min^{-1})	2.16 ± 0.01

positive, the questions arise as to whether the significance is high enough for a detection or if an upper limit should be calculated. The significance of the excess counts (defined as the number of standard deviations from zero) is calculated from Li and Ma (1983) equation 17.

$$S = \sqrt{-2ln\lambda} = \sqrt{2}\sqrt{N_{on}ln(\frac{1+\alpha}{\alpha})(\frac{N_{on}}{N_{on}+N_{off}}) + N_{off}ln(1+\alpha)(\frac{N_{off}}{N_{on}+N_{off}})} \tag{69}$$

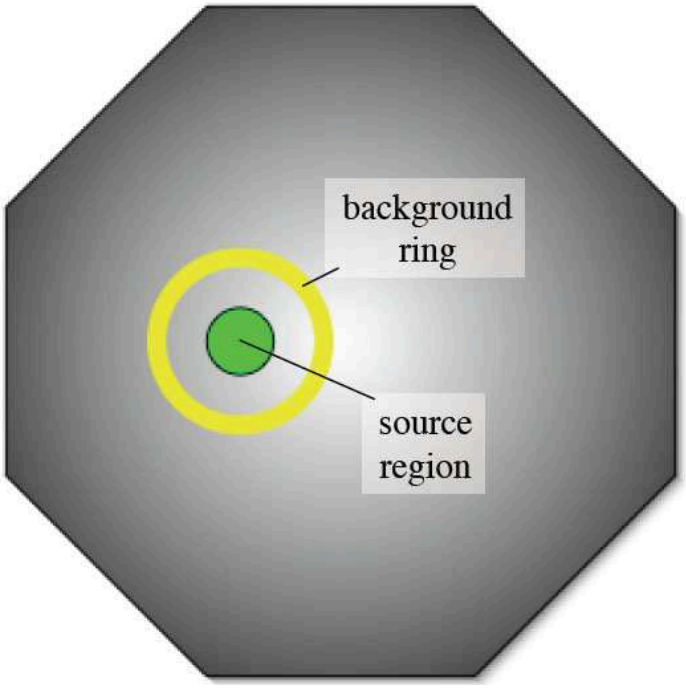

FIGURE 5.14. Illustration of the Ring Background Model (Varcarcel, 2008)

If the significance is low it can be assumed that the signal is due to random fluctuations or the background signal. The detection threshold is 5 σ for a new γ-ray source.

5.2.11. Spectral Analysis. Livetime is the total observational time minus the recorded deadtime. Deadtime is a delay occurring during event or trigger readout. The differential energy, spectrum is dN/dE vs E, defined as the number of photons detected as a function of area, effective area of the array for various energies and livetime during the observation.

$$\frac{dFlux_\gamma}{dE} = \left(\frac{1}{t_{livetime}A(E)}\right)\left(\frac{dN_\gamma}{dE}\right) \tag{70}$$

Effective Area tables (the effective collection areas) are generated from simulation events (γ rays for all photon indexes) and depend on a number of factors: energy E, azimuth, zenith, noise, the angular distance measured from the centre of the field of view to the source being observed, the number of simulated events over a preset area and the number of simulated events that trigger the array and pass all selections/cuts. γ rays are simulated and are then passed through detector simulations, and noise and background are added. The simulations are then analyzed as normal and the collection areas are generated (figure 5.15).

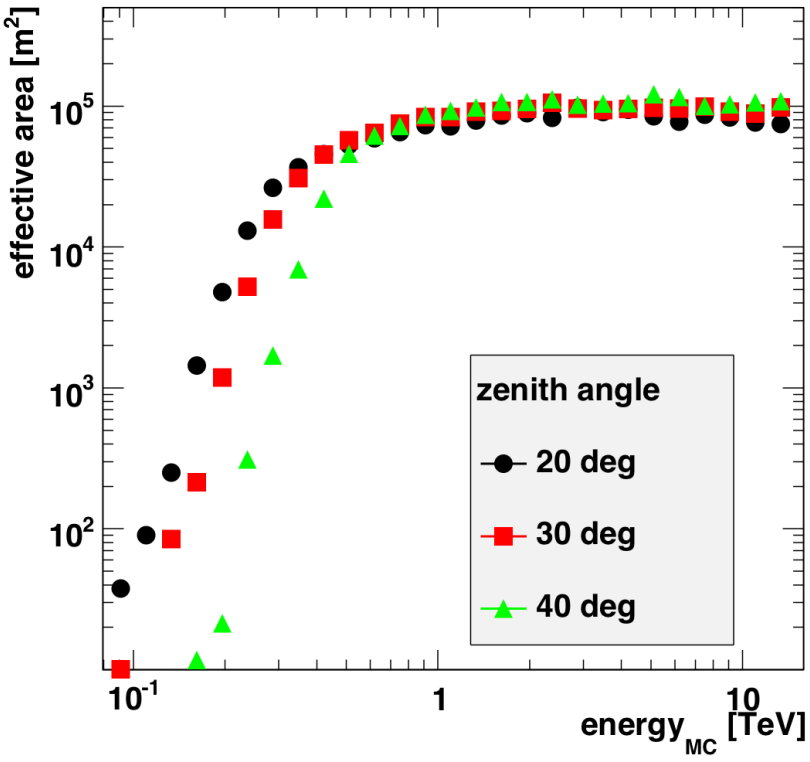

FIGURE 5.15. Effective collections areas as a function of energy for different zenith angles (Ward, 2010)

As the energy of each γ ray has been calculated, the ON and OFF regions are binned into user-specified energy bins, and the differential flux for each bin is calculated. A powerlaw is then fit to the data:

$$\frac{dN}{dE} = F_o \times 10^{-12} \left(\frac{E}{1TeV} \right)^{-\Gamma} \tag{71}$$

where F_o is the normalization factor at 1 TeV and Γ is the spectral index.

5.2.12. Lightcurves. Similarly to spectral analysis, temporal analysis involves binning the data set, but in this case the data set is divided up into different time bins and the integral flux about an energy threshold is calculated for each bin.
A simple χ^2 test determines if the source is constant or variable and can highlight periods of interesting activity.

5.3. Fermi LAT

In contrast to VERITAS, a significant portion of the Fermi data analysis is performed through automated processing at the Fermi ISOC which is comprised of level 1 event reconstruction, background rejection, event classification and level-1 data preparation. This leaves the data Science Tools (the official Fermi LAT analysis package) to concentrate solely on high-level analysis of γ rays. While VERITAS' small field of view means the array's primary aim is to identify γ-ray signals over background, in the case of Fermi LAT, with a much larger field of view an additional objective is to assign γ rays to individual sources. A description of the Fermi LAT analysis chain is given below. For the purposes of the Fermi LAT section an event is defined as a charged particle.

5.3.1. Calibration. In addition to prelaunch, testing calibration is performed on-board. On-orbit calibration is responsible for

- synchronizing trigger signals and optimization of latching data delays caused by rise-time slewing effects
- determining the detector threshold and gains
- evaluating of the SAA influence and its perimeter
- livetime and deadtime calculations
- alignments, both instrument and instrument components
- hardware and software filters

On-board calibration is performed by 2 methods: dedicated and continuous (Abdo et al., 2009). Dedicated calibration (e.g. SAA perimeter evaluation, which is carried-out yearly) is not compatible with data-taking operations and monitors the electronics' responses to known stimuli. Continuous calibration with compatible with science data-taking and calibrates the electronics with known inputs (e.g. calorimeter pedestals) and generally monitors the performance of the LAT, causing minimal deadtime.

5.3.2. ISCO Automated Processing. The LAT event data is downlinked to the Instrument Science Operations Center (ISOC) in 1.5 GB data sets every two orbits, where automated processing takes place. The data is then processed using a java application server, and batch processors at SLAC at Stanford to enable parallel processing with a programmable delay incorporated to ensure that all the data is available before recombination takes place. The 1.5 GB downlinked dataset can be processed in less than two hours using 100 computer cores (Atwood et al., 2009). As the data is only downlinked every 3 hours there is no bottleneck in processing. Automated processing increases the size of the downlinked data file to a substantial 30 GB. Event information from the Anti-Coincidence Detector (ACD), tracker and calorimeter are combined. An event is classified as either a source γ ray or a background γ ray with arrival direction calculated, trajectory and energy reconstructed. The arrival time is recorded, which is necessary for temporal studies. The LAT instrument performance from the onboard calibration is also downloaded and included in both the event analysis and long-term instrument monitoring

(figure 5.16). The main objective of the automated processing is to perform event reconstruction (track and event), background rejection and event classification.

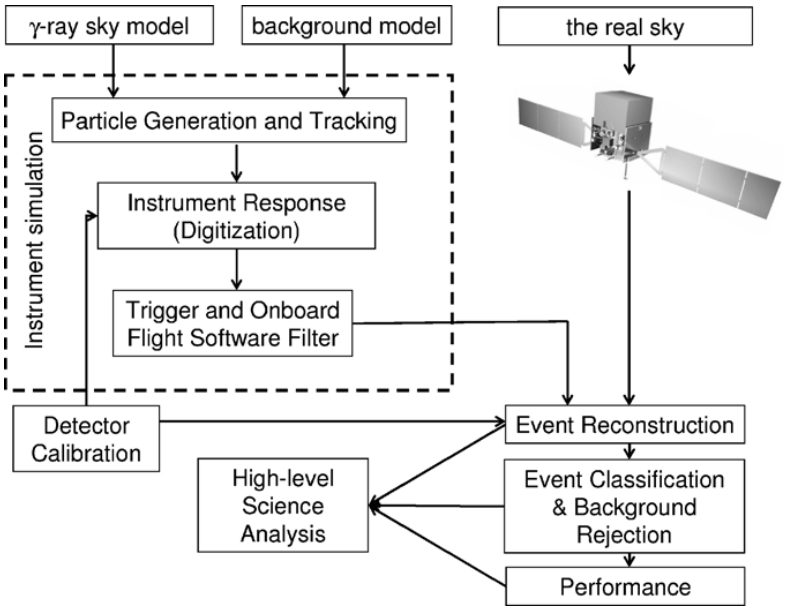

FIGURE 5.16. A schematic diagram of the Fermi LAT simulations, calibration, data processing and high level science analysis (Atwood et al., 2009).

5.3.2.1. *Track Reconstruction.* The adjacent silicon strip detectors in a tracker module are grouped together. From each group, the precise location of an event in the x, y and z planes is determined. Uncertainties arise in the projection path after the initial hit when more than 1 particle produces a "hit" in a detector plane within a small time interval. This is resolved if more than one tracker module is involved. When the hit is confined to one module, the uncertainties can be reduced to ∼10% when the calorimeter information (energy and location) is used. The principal process taking place at this stage is the reconstruction of a trajectory essential for determining the original location of the γ ray. This can be achieved through two track generation algorithms described here. The possible trajectory is then compared with the instrument's readout sensors and is either accepted or rejected.

• Calorimeter-Seeded Pattern Recognition

The Calorimeter-Seeded Pattern Recognition (CSPR) algorithm utilizes the centroid and the shower axis of the energy deposited in the calorimeter and is based on the assumption that the centroid lies on the trajectory. Provided the energy is deposited in the calorimeter, after the first hit a linear projection of the possible track is made. A search cone is produced in the subsequent layer where the next hit is expected and searched for. The search cone radius incorporates the possible scattering caused by the energies of the particles and the material in the tracker planes. If a hit is recorded, the process is weighted and repeated for a third layer. At least two layers

containing hits are required at present for adequate track reconstruction. The process continues until a realistic trajectory is created (based on the initial hit and the energy deposited in the calorimeter). A fit is performed on the trajectory, incorporating a modified version of Kalman fitting (Frühwirth et al, 2000), to determine the track quality which is influenced by the number of layers with hits and the number of layers with gaps. The greater the number of layers with recorded hits the higher the quality parameter. The process is repeated starting with the second hit and the third and so on. The best quality track (e.g. the straightest) is selected and the other possible tracks are discarded.

•Blind Search Pattern Recognition

In the Blind Search Pattern Recognition (BSPR) algorithm the measurement of the energy deposited in the calorimeter is not required. The procedure is the same as with CSPR but without estimating the energy of the trajectory using measurements from the calorimeter. Instead, a minimum energy of 30 MeV is assumed and the trajectory uncertainties due to multiple scattering are calculated (Atwood et al., 2009). Hypothesized tracks can share a hit if the hit is the first for one of the tracks. The best track is selected (as described above) and is used to estimate the percentage of energy deposited in the calorimeter. The estimated energy is then used in the Kalman fitting process. The next step combines the best track with the other tracks into vertex-pairs one by one. The second track is chosen by looping over all the hypothesized tracks and selecting the second best by means of the quality parameter. One requirement is that the distance between the two tracks is less than 6 mm. The process is repeated for the "next" second best track to create a selection of vertex-pairs.

In scenarios where a large percentage of energy is seen as γ rays due to Bremsstrahlung radiation, the trajectories can be deflected far from the original shower axis. Including calorimeter energy information (specifically the centroid location) compensates for this and enables the amount of energy left behind in the tracker to be calculated. The energy combined with the best track or best vertex can place an even better constraint on the incident γ-ray direction.

5.3.2.2. *Event Reconstruction.* Event reconstruction is performed using measurements taken in the calorimeter. The event signal is first digitized followed by gain flatfielding and pedestal adjustments calculated through onboard calibrations. The calorimeter provides the energy recorded and also the location in each calorimeter crystal. The results are combined to produce an overall energy and shower direction. Both the track reconstruction methods can estimate the energy that is expected to be deposited in the calorimeter thereby determining what percentage of energy is lost (e.g. through leakage). In energy reconstruction, it is important to take into account the significant percentage of energy that does not leave the tracker. For adequate energy reconstruction it is required that this value is estimated and added to the total calorimeter energy measured. An example of this is at $\sim$100 MeV the percentage of energy deposited in the tracker module can be as high as 50% (Atwood et al., 2009).

At present there are three different algorithms used in energy reconstruction:

1) Shower Profile (SP) Fit. The main emphasis is placed on a 3D fit to the shower development to calculate the energy of the event. It is most effective above ∼1 GeV where the percentage of energy left behind in the tracker is small relative to the energy deposited in the calorimeter (including energy lost due to leakage out of the calorimeter).

2) Maximum Likelihood (LK) method. This method performs a 3D fit to parameterized shower development profiles to estimate the energy lost due to leakage out of the sides and back of the calorimeter. The energy estimation takes into account the number of hits in the tracker and the energy deposited in the last hit layer before the event proceeded into the calorimeter. This method is also most efficient above ∼1 GeV but also for angles of incidence of the incoming γ ray $< \sim 60°$.

3) Parametric Correction (PC). As the name suggests this is a parameterized shower model that allows for corrections due to energy deposited in the tracker and missing due to gap layers, and energy lost due to leakage in the calorimeter. This is the only algorithm to extend over the entire energy range and is used for all events, whether it is by itself or in conjunction with SP, LK or both. Therefore, there are technically four algorithm methods for energy reconstruction: PC+LF+SP, PC+LF,PC+SP and PC. If more than one energy estimating method is available, the best one is selected using Classification Trees (CTs). Classification trees are hierarchical algorithms used to predict behaviour or responses and can be displayed graphically (Breiman et al., 1994).

Now that the event energy is estimated, track reconstruction is performed again and both the best tracks and track vertices are weighted by the total event energy.

Both track and energy reconstruction described below make use of trainable CTs generated probabilities. A CT will select the most appropriate energy reconstruction method from the four mentioned above. Similarly for track reconstruction, a CT will determine for a particular event whether CSPR or BSPR is best.

5.3.2.3. *Event Classification with Background Rejection.* It is extremely beneficial that background rejection is performed onboard in order to significantly reduce the size of the downlinked data and also the deadtime of the instrument. At present the signal to noise ratio in the downlinked data is 1:300. A background model was developed (table 5.7 is an example of the particles present in the model) to limit the background triggering and increase the efficiency of the onboard filtering. This model is only valid outside of the South Atlantic Anomaly but accounts for Earth albedo γ rays.

The spectra of the particles to be vetoed are generated from the flux values taken from previous experiments (AMS, BESS, NINA etc.) integrated over solid angle and are averaged over an orbit (figure 5.17). The effect of geomagnetic cutoff (the minimum energy for a particle to each the top of the atmosphere) is seen at 3 GeV for protons and electrons.

Event classification is principally based on the efficiency of the background rejection. In addition to this background model, background rejection via the ACD is performed. For γ-ray showers that develop in the calorimeter, the trajectory is traced backwards, and the ACD tiles

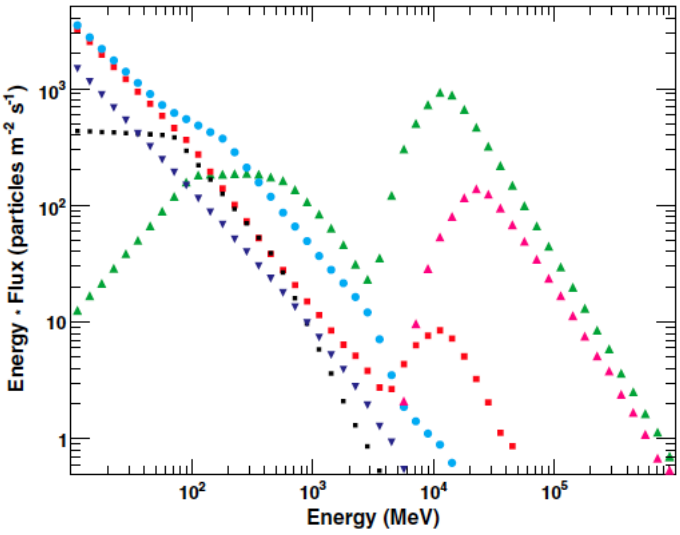

FIGURE 5.17. Orbit spectra for various background sources. Protons: purple. He : green. electrons: red. Positrons : light blue. Earth albedo neutrons : black. Earth albedo γ rays: dark blue (Atwood et al., 2009).

the track points to are vetoed. As the trajectory reconstruction, and therefore the pointing to the ACD tiles, is energy dependent the amount and position of the tiles used in the vetoing process can differ. At lower energies, due to multiple scattering, nearby tiles close to the search cone of the reconstructed track are used in vetoing, while at higher energies, where there is less scattering and the search cone radius is smaller, generally only one ACD tile is required. Another strong indicator of background is the presence of additional unassociated hits in the vicinity of the reconstructed track (unlikely to be tracks from pair production). The properties of the γ-ray electromagnetic shower itself also aid in background identification. From simulations of the longitudinal and transverse development in the calorimeter, the reconstructed trajectory quality parameter and how well it matches the energy centroid in the calorimeter, etc., can distinguish between it and a background shower.

5.3.2.4. *Event Classes.* The rate of background rejection is used to distinguish between the event classes (table 5.7). The transient class (class 0) has the loosest background cuts and is used for the analysis of transient (i.e. short timescales) sources. The source class (class 1) was originally used in the study of localized source but due to improvements it is now the diffuse class (class 2) that is recommended for individual sources. The dataclean (class 3) is used in the analysis of diffuse emission and also as a cross check for individual source analysis (particularly if the source is faint or if >20 GeV photons are predicted. The dataclean event class has the highest level of background rejection. Classes 2 and 3 were used in the analyses for this thesis.

Background events that make it through the on-board filter system and background cuts are classified into 2 types: Irreducible background (which accounts for ∼60% of the residual

TABLE 5.7. Event Classification

Event Class	Type	Description
0	Transient	Maxmium effective area, maximum background rate
1	Source	The previous event class for point source analysis
2	Diffuse	Use in point source analysis
3	Dataclean	Smallest PSF, use in diffuse emission and in faint point source analysis

background above ∼100 MeV, Atwood et al., 2009) occurs when a charged background particle interacts with a passive material outside or just within (∼1 mm) the ACD, and a γ ray is produced in the field of view. There is no method of discriminating against the γ ray at this stage. Reducible background is background that in principle should have been identified and rejected, but due to the instrument's design or performance, the event made it through. An example of this is background events that proceed through gaps in the ACD. However reducible events can easily be identified by comparing fluxes measured with and without vertices. A non-vertex sample will contain ∼10 times the background events of a vertex sample.

Both the event classification and background rejection methods (in particular the background model) are continuously evolving as data levels increase and more simulations and data analysis are performed.

5.3.3. Automated Science Processing. The data now is known as level-1 (isolated, reconstructed γ rays) and is the input to the high-level science analysis. The event data is publicly available to download from the Fermi Science Support Center (FSSC) approximately 3-4 hours after it is initially downlinked to the ISOC for analysis. Automated Science Processing (ASP) takes place for every downlink, and both on a daily and weekly basis. An unbinned Likelihood analysis (explained below) is performed to search for interesting or increased activity from known sources and for discoveries of previously unknown sources. Through a weekly, public sky blog [2]

Fermi Gamma-ray Sky group provides up-to-date, relevant information on the γ-ray sky. This, in addition to published Atels (Astronomer's Telegram), with at least one a week, alerts the multiwavelength communities to targets that warrant observations.

5.3.3.1. *Performance of the LAT.* The performance of the LAT is determined by:

- LAT instrument design
- Simulations
- Track reconstruction algorithm efficiency
- Event reconstruction algorithm efficiency
- Background rejection efficiency
- Event classification efficiency

Instrument Response Functions (IRFs) describe the performance of the instrument which is dependent on various parameters including the energy of the photon and the incidence angle of the measurement. The LAT IRFs are determined using Monte Carlo γ-ray simulations. The

[2] http://fermisky.blogspot.com

current instrument response functions being used are Pass6 version11 and they characterize the detector effective area, point spread function and energy dispersion (figures 5.18 5.19 5.20)

Effective areas for normally incident photons ($\theta < 25°$) are plotted as a function of energy for the 3 event classes : transient, source and diffuse (the P6_V11 IRFs plots were generated before the addition of the Dataclean event class). The effective areas are averaged over all azimuthal angles and the plot is smoothed (Rando et al., 2009). The Point Spread Function (psf) is expressed as a function of energy for both the 68% and 95% containment radius for photons at normal incidence and Energy Resolution is also expressed as a function of energy (for the 68% containment radius and normal incidence).

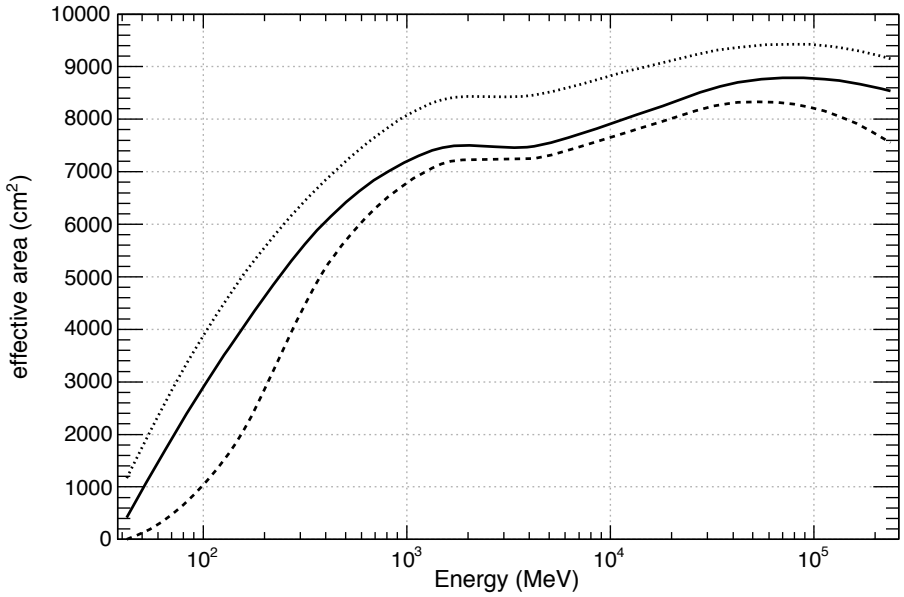

FIGURE 5.18. Effective Areas as a function of Energy for normal angles of incidence for the transient (dotted), source (solid) and diffuse class (dashed) (Rando et al., 2009).

5.3.4. Unbinned Maximum Likelihood Analysis. Source detection, flux determination and spectral analysis are performed using an unbinned Maximum Likelihood Analysis (MLA) method. Binned analysis, which can be used for deep exposures of complex regions e.g. the Galactic centre, is not a component of this work and is therefore not described. To perform likelihood analysis on a source, a model is hypothesized based on previously published results and simulations. The Likelihood, L, is the probability of matching an input model (source +background) to the actual event data being analyzed, where the most realistic model will yield the highest probability.

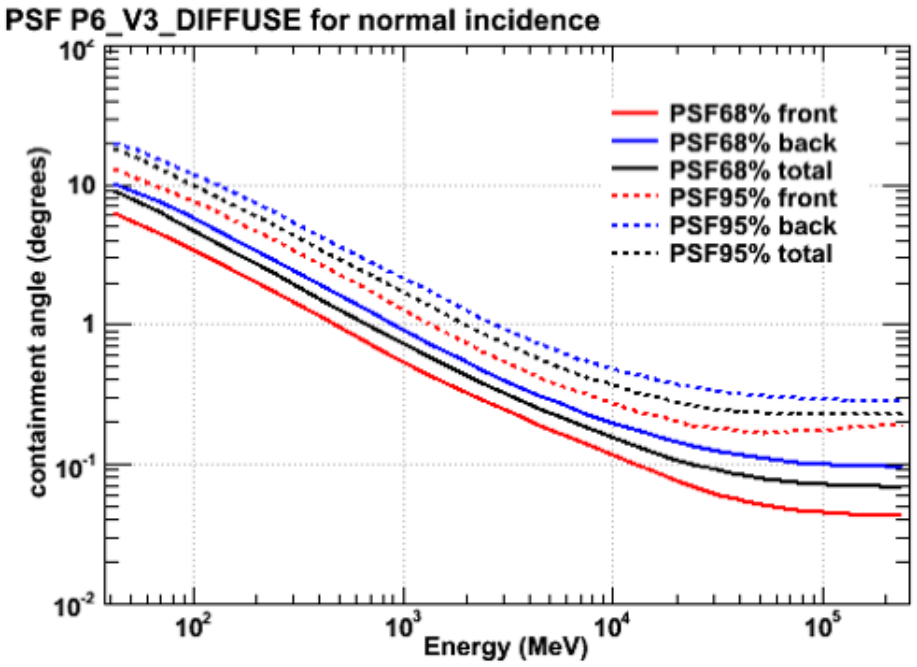

FIGURE 5.19. PSF at normal incidence as a function of energy (www-glast.slac.stanford.edu).

$$L = exp[-N_{exp}]\pi_i \frac{M_i^{n\_i}}{n\_i!} \tag{72}$$

where the expected number of counts in the ith bin is m_i (the model). The probability of detecting n_i counts in the ith bin is $m_i{}^{n\_i}/n\_i!$ This depends on the data and the product of exp[-m_i]. N_{exp} is the exponential of the minus of the sum of m_i.

The process involves varying the model parameters and performing multiple likelihood iterations until a maximum likelihood is reached. After each iteration, L is calculated, followed by the calculation of its logarithm and the free parameters are computed and adjusted. Iterations continue until the Δlog(L) is minimized (i.e. the input model converges) and the maximum likelihood is found.

As each input model source is being fitted simultaneously, optimizers are employed to increase efficiency. The optimizer used in this analysis is NEWMINUIT, a conservative optimizer that produces reliable results and uncertainties. The fit tolerance (the fractional change in log-Likelihood) is set at 1e-5.

Each model includes:

- the RA and Dec (J2000 epoch) coordinates of the source being analyzed
- the coordinates of other sources in the Region Of Interest (ROI) (24 months source list)

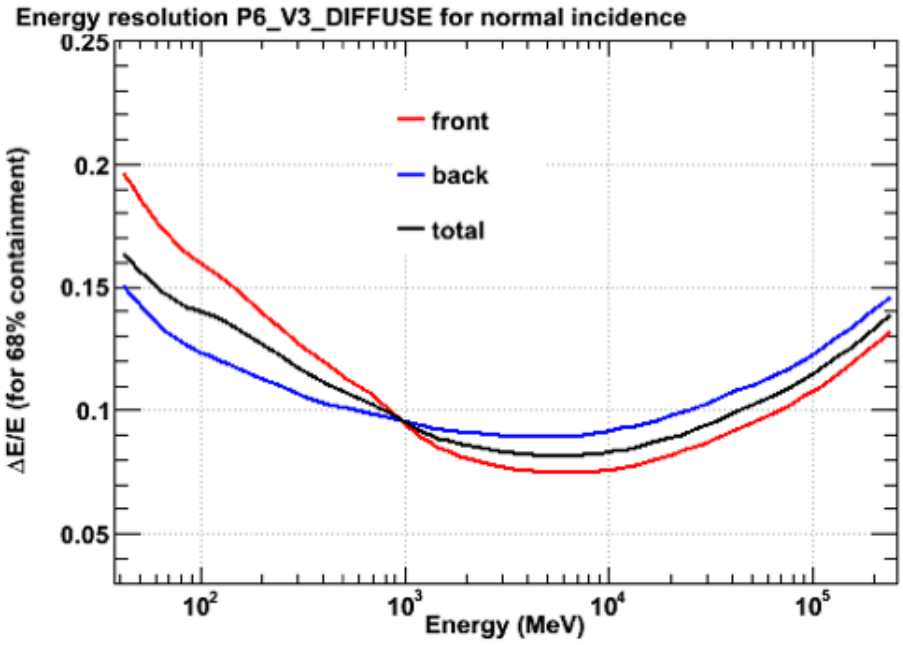

FIGURE 5.20. Energy resolution at normal incidence as a function of energy (www-glast.slac.stanford.edu).

• the coordinates of additional source in the ROI (achieved through exploration of detailed TS maps
• estimates or determinations of the flux and photon index for each source
• a model of the galactic diffuse emission region; gll_iem_v02_P6_V11_DIFFUSE.fit
• the corresponding model of the extragalactic diffuse emission regions; isotropic_v02_P6_V11_DIFFUSE.txt

The galactic diffuse emission model incorporates the distribution of interstellar gas in Galactocentric rings by using H I and HII and spectral lines studies. The model also has an inverse Compton emssion component produced by GALPROP (Vladimirov et al., 2011). The corresponding isotropic model includes the extragalactic ($>$ 30 degrees latitude) diffuse γ rays and the residual cosmic rays.
As χ^2 = -2lnL, χ^2 will demonstrate goodness of fit.

5.3.4.1. *TS.* The Test Statistic (TS) is defined as

$$TS = -2ln(\frac{L_{max,0}}{L_{max,1}}) \tag{73}$$

where is $L_{max,0}$ is the null hypothesis with no additional sources in the source model and $L_{max,1}$ is the maximum likelihood hypothesis. TS increases as a function of $L_{max,1}$ therefore

TABLE 5.8. Highlights of the LAT point source analysis

Analysis method	Unbinned Maximum Likelihood
Science Tools version	v9r23p1
IRFs	P6_V3_DIFFUSE
Background source model	LAT24 month source list
Galactic diffuse emission model	gll_iem_v02.fit
Extragalactic diffuse emission model	isotropic_iem_v02.txt

TABLE 5.9. Description of the components of the Science Tools

Analysis tool	Description
gtselect	perform subselection of the event data based on ROI, energy, time and zenith angle
gtmktime	create GTIs, apply SAA cut
gtbin	produce counts map
gtltcube, gtexpmap	generate livetime cube and create an exposure map
gtlike	run a maximum Likelihood analysis with an input model
gttsmap	generate test statistics maps to explore the ROI for additional sources and also for accurate description of the source itself

increasing the likelihood parameter will naturally increase the TS of the source (Mattox et al., 1996).

5.3.5. Analysis data products. As mentioned above the data is available for download from the FSSC webpage [3] where the ROI, energy range and time range can be specified. The data is downloaded in two data types. The photon Data files (PH00.fits) contain the recorded events for the corresponding region of interest selected and energy and arrival times for each event. The Spacecraft File (SC00.fits) provides details regarding the LAT's pointing during the time period specified, in 30 second intervals and describes the LAT's position and orientation as a function of time. Extended Data files can also be downloaded but are more useful in terms of extended source emission and are not described in this thesis For the analyses of the sources of this thesis a ROI of 10° was used. No energy or time cuts are applied at this stage.

Tables 5.8 and 5.9 provide summaries of the different analysis tools involved in the Fermi software and a brief outline of the analysis.

5.3.6. Data Subselection. The first stage of the analysis consists of making subselections of the event data based on ROI, energy range, time range and maximum zenith angle cuts. Table 5.10 provides an outline of the subselections used in this thesis. For point source analysis, only diffuse and dataclean event classes are used as they include events that have the highest probability of being a photon and the background rate is low relative to the transient and source classes. A value of 105° is used to filter out the Earth's limb albedo γ rays. A lower energy limit of 300 MeV is used; below this the response of the detector is not well defined and effective areas decrease.

[3] http://fermi.gsfc.nasa.gov/ssc/data/

TABLE 5.10. Subselection cuts performed on the photon event data file

Parameter	value
Analysis	point
ROI	10°
eclsmin*	3
eclsmax*	4
Energy range	300 MeV - 100 GeV
Time Range	differs per analysis
Zenith	105°
Rocking angle	52 °

*eclsmin and eclsmax are the min and max event class used

5.3.7. Good Time Intervals. In this step of the analysis the Good Time Intervals (GTIs) are calculated. GTIs are defined as the spacecraft file time intervals over which the data pass both the ROI and zenith angle cuts. A GTI is the time interval that the data is considered valid. The process involves using the spacecraft file to create a list of GTIs, when the spacecraft orientation is within acceptable rocking angles and there are no software updates or onboard calibrations taking place. This list is then compared with the actual GTIs seen in the data and any GTIs not present in the list are removed. A rocking angle of 52 degrees, between the source and the LAT z-axis, is also used to exclude events acquired when passing through the South Atlantic Anomaly.

5.3.8. Counts Maps. To achieve a clean visualization of the extracted region and to identify possible sources for the likelihood model, preliminary counts maps are produced for the ROI used. Axis size and image scale are adjusted to suit the particular analysis and the projection method used is AIT (Advanced Imaging Technology), an equatorial adaption of the zenith equal areas projection method and is the most commonly used all-sky projection method (Calabreatta & Greisen, 2002).

5.3.9. Exposure Maps. The likelihood analysis requires that an exposure map (area × time) is created. The map is an integral of the total instrument response over the ROI specified. This step is repeated for every energy range (spectral analysis) and time range (lightcurve generation) and is generated using the events file and a livetime cube (figure 5.21). As the response is dependent on photon energy, the exposure function can then be used to determine the expected number of events from a given set of coordinates. For this thesis, the radius of the exposure map was set to be 10° larger than the ROI used for the events file to ensure that any photons from sources outside the ROI are accounted for.

One component of the exposure map is a livetime cube which covers the entire sky. The livetime cube is essentially a HealPix (Hierarchical Equal Area isoLatitude Pixelization of the sphere) table of integrated livetime as a function of inclination between the source being observed and the LAT z-axis plane. The number of events detected from a source depends on the time

taken for observations for a given position and a given inclination angle. Generation of a livetime cube requires the timing and orientation information found in the spacecraft file.

5.3.10. Gtlike Likelihood Analysis. For the first likelihood iteration, the sources' integral and index parameters are left free to fluctuate. The gtlike science tool is run and the parameter values are computed. The input parameters are then modified based on the likelihood results. At this stage generally only the parameters of the source being analyzed and the parameters of the sources within 1° radius are left free (to compensate for possible overlapping PSFs). The RA and Dec coordinate parameters are fixed for the entire process. With the final iteration of the gtlike tool TS value, flux and index values and the number of photons are obtained for the source for the given energy and time range.

5.3.10.1. *Spectral and Temporal Analysis.* The above unbinned likelihood analysis is performed for different energy ranges and the results are combined and fitted with the fixed photon index obtained from the original full energy range likelihood analysis. Similarly for temporal studies or in the production of lightcurves the analysis is performed for different time bins. A general rule of thumb for this analysis is no less than 20 photons per energy/time bin in order to achieve a detection for each bin to ensure accurate fitting.

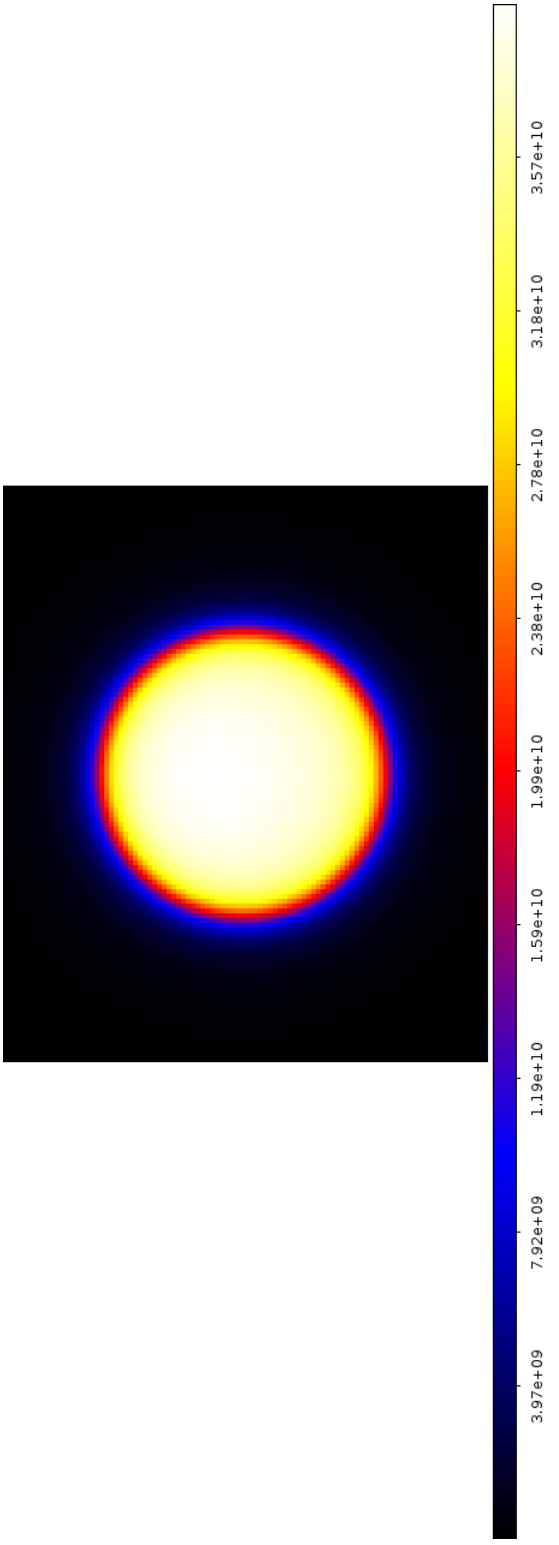

FIGURE 5.21. An example of an exposure map using a 10° ROI over a 21 month time interval for the source 1ES 0502+675.

CHAPTER 6

Results

6.1. Introduction

This chapter presents the detailed analysis and results of extensive data sets of a subset of objects from two of the blazar subclasses: Intermediate frequency Bl Lac objects (IBLs) and High frequency Bl Lac objects (HBLs). 3 HBLs (1ES 0502+675, 1ES 0806+524 and 1ES 1959+650) and 3 IBLs (W Comae, 3C66A and PKS 1424+240) were selected as described previously. Results were then interpreted and compared to look for blazar subclass characteristics. Fermi LAT and VERITAS data analyses for each source were performed to generate detailed γ-ray spectra and lightcurves to investigate variability. Time-averaged spectra were used for both instruments to combine the quasi-simultaneous continuous Fermi LAT observations with spread out VERITAS snapshots, and also to ensure activity states typical of each source were used, necessary for adequate SED modeling. The main objective was to constrain the Inverse Compton (IC) peak using MeV - TeV data. The majority of the sources do not have previously published Fermi LAT results, which for the first time constrains the rising of the IC emission curve. In addition to this, another aim was to model the radio to γ-ray Spectral Energy Distribution SED in order to shed light on intrinsic source properties, surrounding environments and particle acceleration processes. Multiwavelength SEDs were constructed and modeled by both SSC and SSC+EC processes and the modeled parameters were then compared to look for correlations between model parameters and blazar subclass. The results are summarized and interpreted below.

6.2. Data Analysis

6.2.1. VERITAS Data Analysis. All the analyses were performed with VEGAS version 2.3 as described in section 5.2. All good quality data from April 2007 to May 2011 were used. The criteria for quality data selection for the above sources included: good weather (clear to very light cloud) and steady L3 rates, based on the internal observer elog entries and the examination of the Data Quality Monitoring (DQM) files for each run. Depending on previously published TeV spectra or in the case of 1ES 0502+675 (no previous TeV publications), several iterations were made over the spectral analysis to constrain the index, the sources were categorized into soft or medium spectrum cuts analysis and the appropriate background rejection cuts were applied. Wobble and RBM analyses were run to to compare background models, and temporal analysis was performed to investigate variability. Time-averaged spectra were used as the VERITAS observations for all six sources were spread out over the Fermi LAT analysis period. The wobble

and RBM analyses for all six sources were in good agreement with each other and therefore only the wobble results are presented here. The 2D significance maps were generated from the RBM analysis. The data were then divided into pre- and post- Telescope 1 relocation and further divided into subsamples based on the time of year for spectral analysis: Winter (November to April), summer (May to October). This was done to compensate for the change in effective areas due to the movement of T1 and for differences in the winter and summer atmospheres (VERITAS internal note). The minimum significance for a spectral data point in each bin is set at 1σ with a minimum excess of 2 counts. Below this, an upper limit is generated. The subsamples were then combined and an overall spectrum was generated for each source using the VEGAS macro *CombineMultipleStage6Results.C*. Lightcurves were generated in day, week and month long time intervals to test for variability. A detection level of 1 σ was required in each time bin to create a data point. Upper limits were not included in the lightcurves as they did not constrain the straight line fit, to test for variability, applied to the data.

6.2.2. Fermi Data Analysis. All quality-accepted Fermi LAT data taken in survey mode between the 8^{th} of August 2008 and the 16^{th} of May 2011 was analyzed with Science Tools version v9r23p1. The data selection criteria included: zenith angle $< 105°$, ROI $= 10°$ and an energy range of 300 MeV to 100 GeV. Above this energy range, the statistics for the instrument response function aren't well known. Unbinned analysis was performed with the P6_V11_DIFFUSE Instrument Response Functions (IRFs).

The background was estimated using the Gll_iem_v02_P6_V11_DIFFUSE.fit galactic model and the Isotropic_iem_v02_P6_V11_DIFFUSE.txt extragalactic model, with the addition of sources from the preliminary 24 month catalog gll_psc_24month_v2.fit (second version).

As the VERITAS observations were either taken sporadically over the course of 4 years (as in the case of 1ES 1959+650) or in a semi-continuous way (e.g. W Comae), time averaged spectra for both Fermi and VERITAS were used for multiwavlength analysis. The macro *LikeSED.py* was used to divide the data set into 10 energy bins for spectral analysis. The minimum detection level in each bin was set to a TS of 9 ($\sim 3\sigma$). Below this, an upper limit was obtained instead of a data point. The lightcurves were produced with the macros *BALM.py*, with the minimum detection required for a data point set at a TS of 9. The x axis is in units of Mission Elapsed Time (MET) which is the number of seconds since the reference time of January 1^{st} 2001. Upper limits were not included in the lightcurves as they did not constrain the test for variability, applied to the data.

6.3. 1ES 0502+675

1ES 0502+675 is a HBL detected from radio to γ-ray energies with an unknown redshift (Acciari et al., 2009). The VERITAS and Fermi LAT analysis results are described below.

6.3.1. VERITAS analysis. The soft TeV spectrum HBL 1ES 0502+675 was observed between 23^{rd} September 2009 and 8^{th} January 2010 with VERITAS after being identified as a TeV candidate based on the flux and TS quoted in the three month Fermi LAT Bright Source List (Abdo et al., 2009). The total livetime of the data set was calculated to be 28.83 hours. A wobble analysis yielded a γ-ray event rate of 0.47 ± 0.04 γ's min^{-1} resulting in a detection of $\sim$ 12.1 σ. The wobble results are shown in table 6.1, and the detection is clearly evident in the θ^2 plot and significance maps as shown in figures 6.1 and 6.2. No significant variability is detected (figures 6.3 and 6.4) in this short timeframe.

The spectrum (figure 6.5) is fit well, χ^2/n.d.f $= 8.35/4$, by a powerlaw of $(7.68 \pm 2.11)\times10^{-7}$ $\left(\frac{E}{1TeV}\right)^{-3.811\pm0.282}$ with an integral flux (E $>$ 1 TeV) of $(1.89 \pm 0.72)\times10^{-8}$ ph m^{-2}s^{-1}.

TABLE 6.1. VERITAS Wobble 1ES 0502+675 results

Total On Events	4.49×10^3
Total Off Events	3.33×10^4
Total Exposure Time (min)	1.73×10^3
Alpha	0.111, 0.0909
Significance (σ)	12.1
γ-ray Rate (min^{-1})	0.47 ± 0.04
Background Rate (min^{-1})	2.13

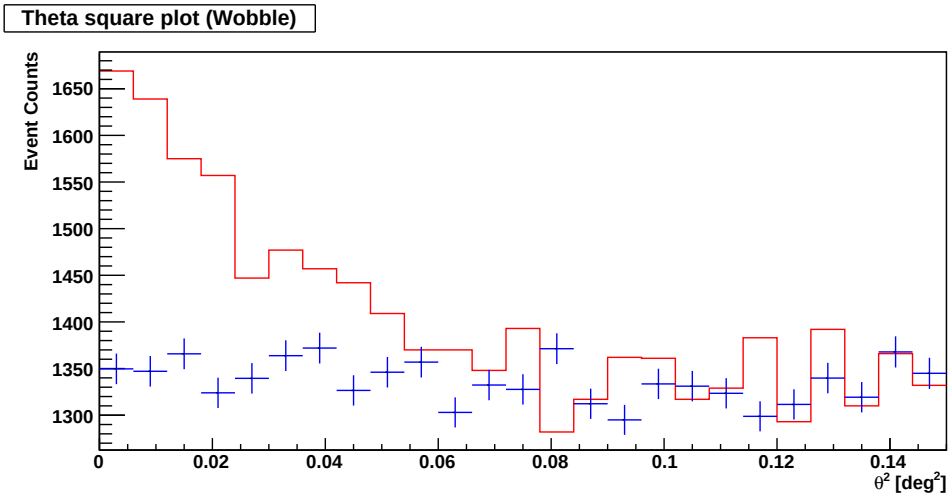

FIGURE 6.1. 1ES 0502+675 VERITAS wobble theta squared plot to distinguish the source γ-ray signal above the background (red = source, blue = background).

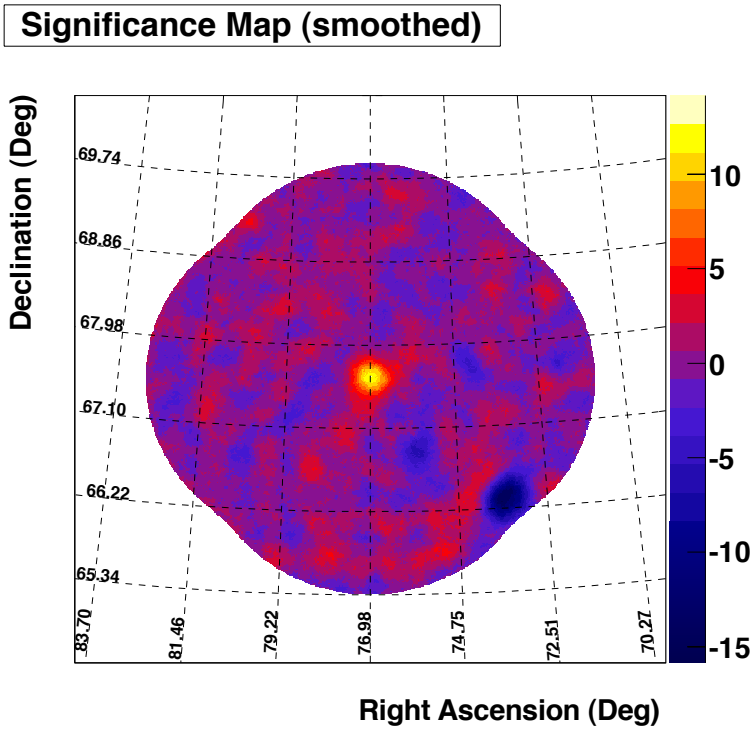

FIGURE 6.2. VERITAS 2D significance map centered on the position of 1ES 0502+675

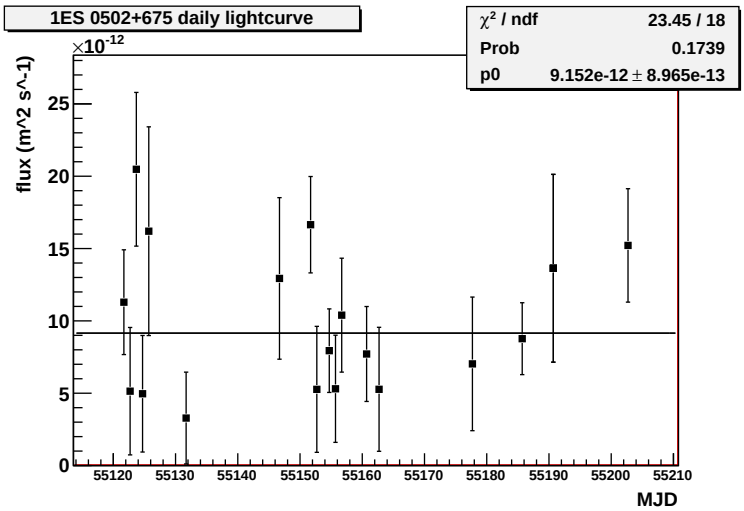

FIGURE 6.3. 1ES 0502+675 TeV lightcurve in day-long time intervals between September 23^{rd} 2009 and January 8^{th} 2010 indicating no significant variability.

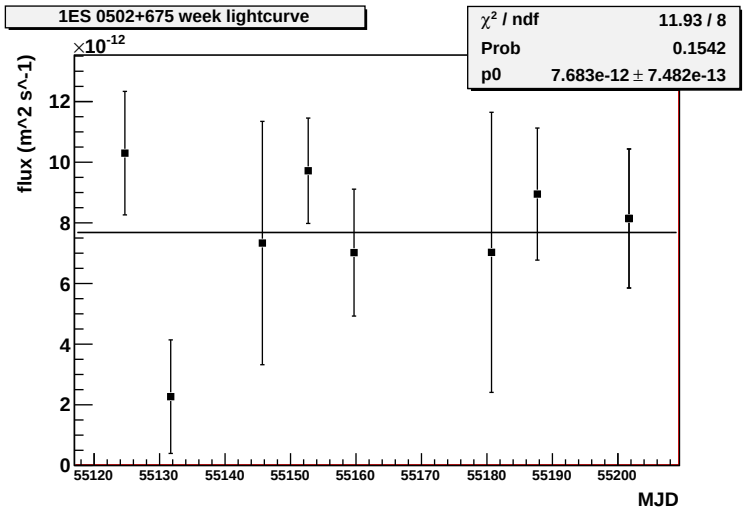

FIGURE 6.4. 1ES 0502+675 TeV lightcurve in week-long time intervals (as above) indicating no significant variability.

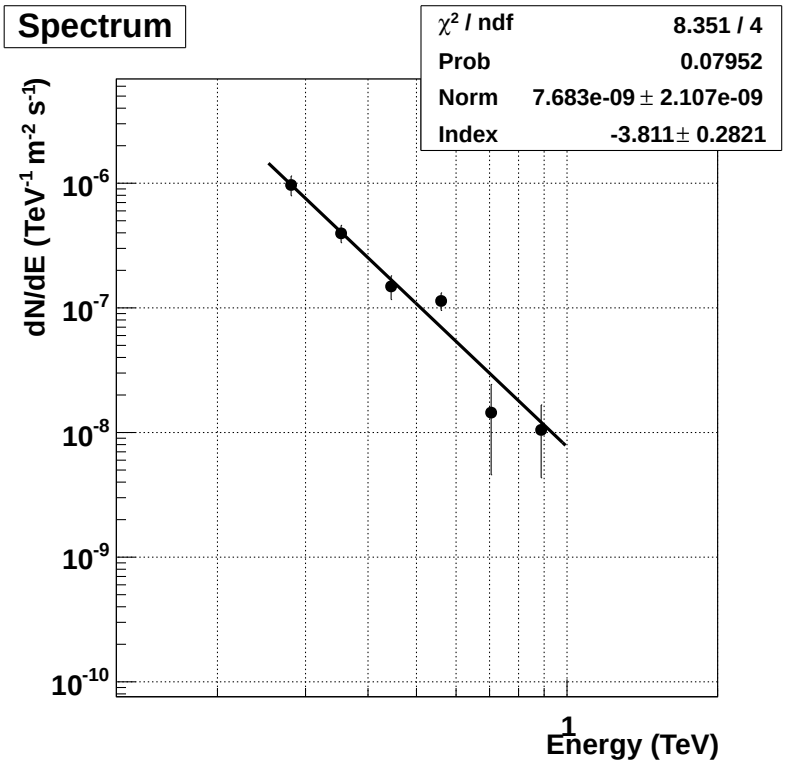

FIGURE 6.5. 1ES 0502+675 TeV dN/dE spectrum, fit well with a powerlaw.

6.3.2. Fermi analysis. 1ES 0502+675 is detected from the complete Fermi LAT data set at a TS of $\sim$ 732. Figure 6.6 shows the TS maps for the 12° radius around 1ES 0502+675 with 1ES 0502+675 included in the background model. Apart from 1ES 0502+675 and the diffuse extragalactic and extragalactic models there is no background subtraction performed yet, highlighting the bright sources in the field of view. After several TS map iterations including both the 24 month catalog and additional sources, the background is left relatively flat (figure 6.7. Six additional sources were required in order to achieve this. Six high energy ($>$ 1GeV) photons were detected from a 1° radius around the source location; 214 GeV, 179 GeV, 152 GeV, 120 GeV, 112 GeV and 110 GeV, indicating a near overlap between the Fermi Lat and VERITAS spectra, highly beneficial for constraining the IC peak.

An unbinned Maximum Likelihood analysis was performed generating index, flux , TS, Npred (number of expected photons) and angular distance (°) from 1ES 0502+675 for each source in the ROI (table 6.2). The integral flux (E $>$ 300MeV) calculated for 1ES 0502+675 is (5.63 $\pm$ 0.61)$\times 10^{-9}$ ph cm^{-1} s^{-1} at a TS of 731.89 ($\sim$ 27 σ).

The data set was binned biweekly, monthly and tri-monthly to search for variability. The source does not exhibit significant variability on timescales of biweekly (χ^2/n.d.f = 42.52/30 with a probability of 0.06453 of being at a constant flux) and monthly (χ^2/n.d.f = 72.72/19 with a probability of 3.229×10^{-8}) time intervals (figures 6.8 and 6.9). The three month lightcurve (figure 6.10) also does not suggest variability with χ^2/n.d.f of 24.34/8 and a probability of constant flux of 0.002009. TS as a function of energy (figure 6.11) indicates that the flux is at its highest at $\sim$ 10 GeV and demonstrates a dip at $\sim$ 20 GeV. This spectral dip is discussed in section 6.11. The counts map, dN/dE as a function of energy is shown in figure 6.12. The E^2 dN/dE spectrum is shown in figure 6.13.

TABLE 6.2. 1ES 0502+675 Fermi LAT Gtlike Unbinned Maximum Likelihood results

Source	Index	Flux (ph cm^{-2} s^{-1})	TS	Npred	ROI Distance (°)
1ES 0502+675	-1.53 ± 0.06	(5.63 ± 0.61)×10^{-9}	731.78	325.65	0
1FGL J0334.3+6536	-2.18 ± 0.14	(5.64 ± 1.37)×10^{-9}	73.02	230.58	9.43
1FGL J0505.9+6121	-2.11 ± 0.14	(4.28 ± 0.98)×10^{-9}	68.08	219.79	6.33
1FGL J0515.2+7325	-2.05 ± 0.18	(2.38 ± 0.70)×10^{-9}	54.13	127.16	6.31
1FGL J0527.6+6646	-2.13 ± 0.19	(2.21± 0.71)×10^{-9}	38.36	117.46	2.05
1FGL J0533.9+6758	-2.18 ± 0.1	(5.68 ± 0.79)×10^{-9}	144.92	300.93	2.49
1FGL J0545.6+6022	-2.18 ± 0.13	(4.84 ± 0.83)×10^{-9}	97.84	231.81	8.38
1FGL J0639.9+7325	-2.61 ± 0.13	(7.05 ± 0.92)×10^{-9}	130.30	260.89	9.51
24M0499	-2.23 ± 0.11	(6.70 ± 1.10)×10^{-9}	96.00	350.30	4.90
24M0527	-1.80 ± 0.23	(1.46±- 0.80)×10^{-9}	36.52	78.94	6.13
24M0705	-1.99 ± 0.13	(5.38 ± 1.13)×10^{-9}	99.35	149.40	9.93
24M0836	-2.97 ± 0.25	(5.31 ± 0.87)×10^{-10}	56.49	235.58	8.56
AS1	-2.96 ± 0.27	(4.06 ± 0.81)×10^{-9}	38.73	197.30	5.67
AS2	-3.23 ± 0.36	(3.77 ± 0.77)×10^{-9}	34.66	160.36	8.65
AS3	-2.29 ± 0.22	(3.12 ± 1.02)×10^{-9}	35.21	162.69	3.04
AS4	-2.30 ± 0.25	(2.67 ± 0.80)×10^{-9}	31.11	138.28	6.10
AS5	-2.29 ± 0.27	(3.64 ± 0.78)×10^{-9}	49.89	186.95	4.65
AS6	-2.43 ± 0.19	(3.38 ± 0.81)×10^{-9}	50.33	171.50	7.06

AS=Additional Source

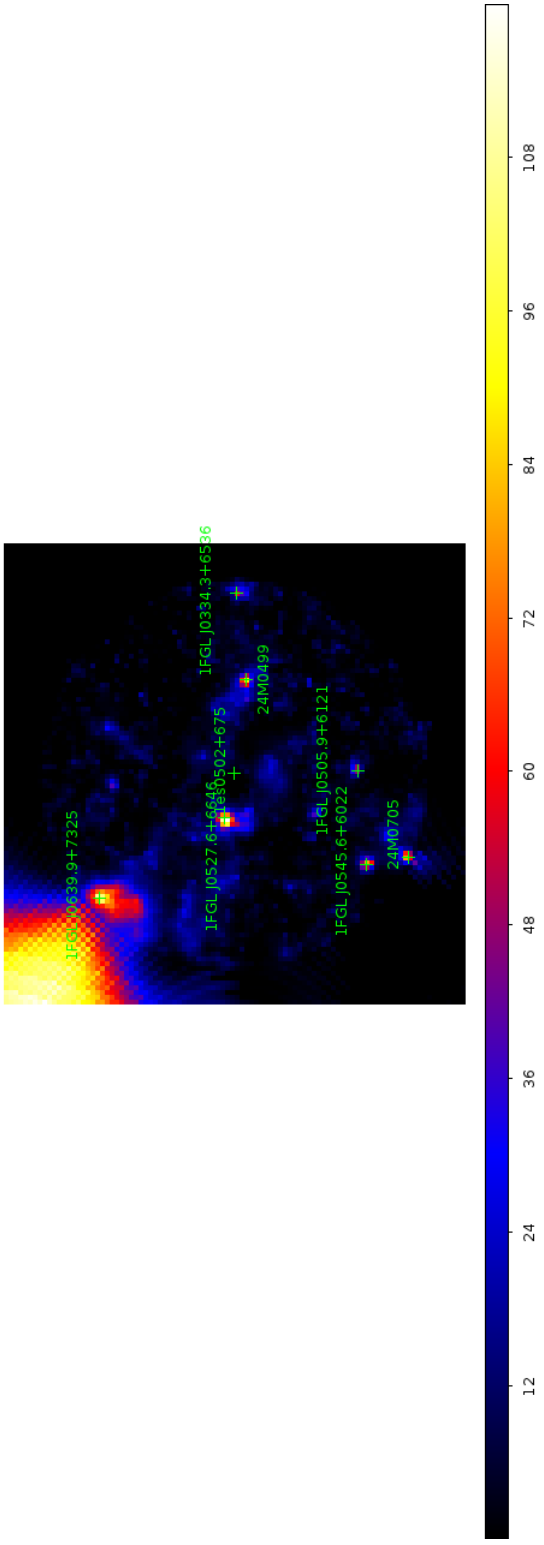

FIGURE 6.6. Initial Fermi LAT 12° TS map before the background sources in the ROI are subtracted, centered on 1ES 0502+675 highlighting high TS sources in the ROI.

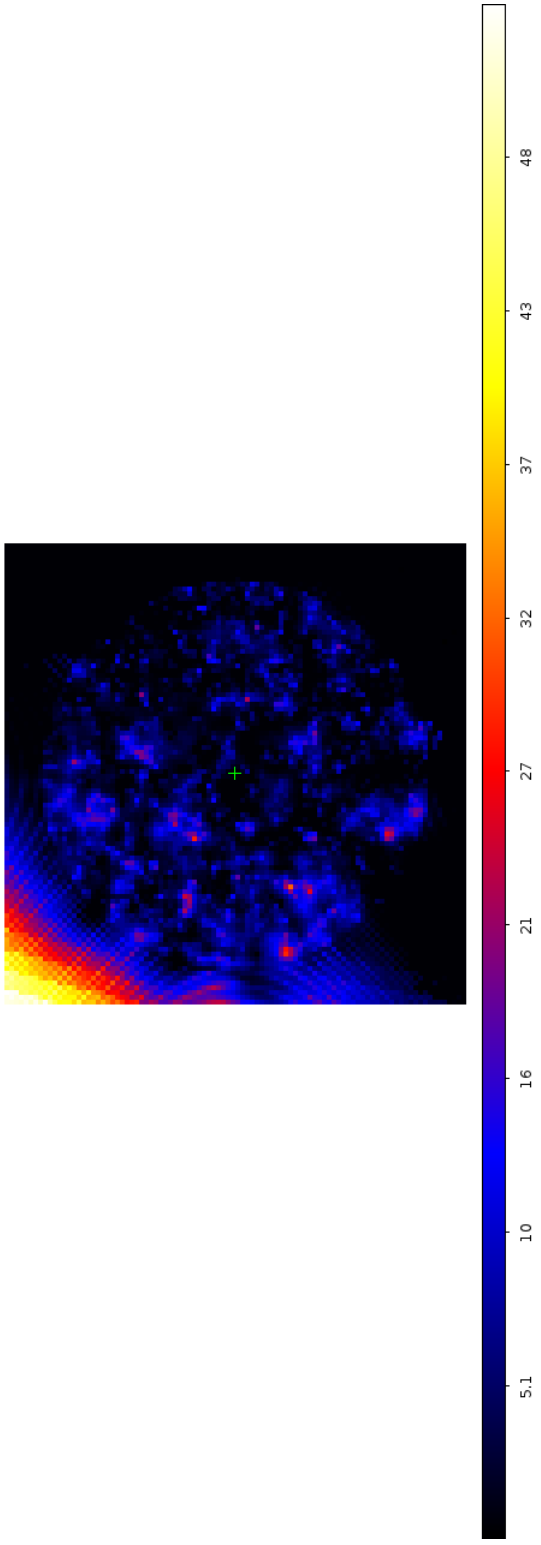

FIGURE 6.7. Fermi LAT 12° TS after background subtraction centered around 1ES 0502+675, which is also included in the background model. Note the different scales between this and the previous TS map. This is to ensure that after the bright background sources are removed it is possible to see weaker or lower TS sources clearly.

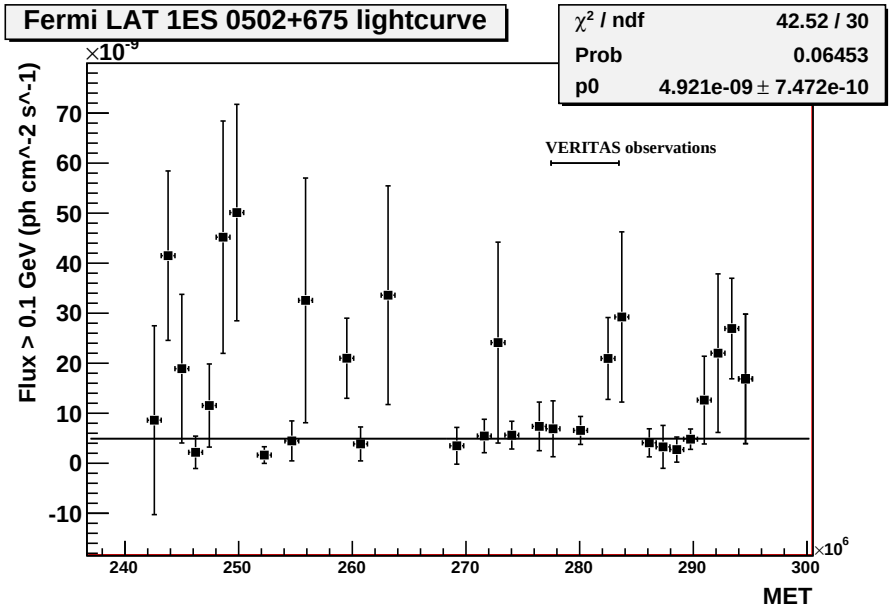

FIGURE 6.8. 1ES 0502+675 Fermi LAT lightcurve binned in 2 week-long intervals does not suggest significant variability. The VERITAS observation timeline can be seen on the plot.

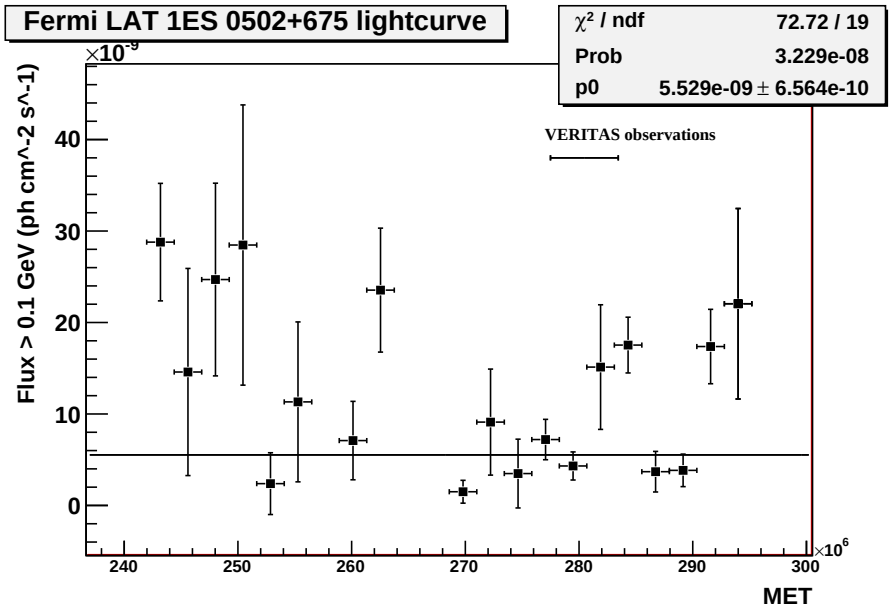

FIGURE 6.9. 1ES 0502+675 Fermi LAT lightcurve binned in month-long intervals does suggest variability. The VERITAS observation timeline can be seen on the plot.

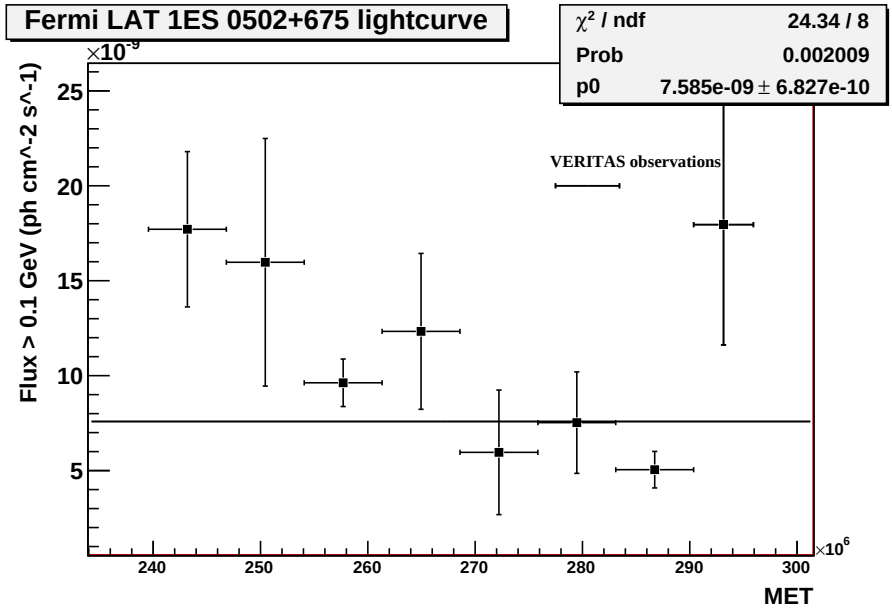

FIGURE 6.10. 1ES 0502+675 Fermi LAT lightcurve binned in 3 month-long intervals, does not suggest significant variability. The VERITAS observation timeline can be seen on the plot.

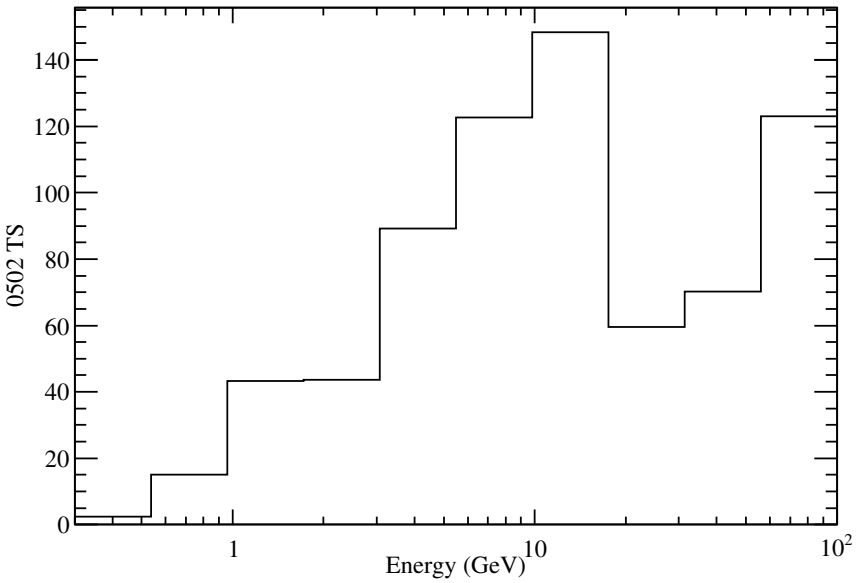

FIGURE 6.11. 1ES 0502+675 Fermi LAT 10-bin TS versus Energy, showing a peak of $\sim$ 140 TS at 10 GeV followed by a significant dip to $\sim$60 TS at 20 GeV.

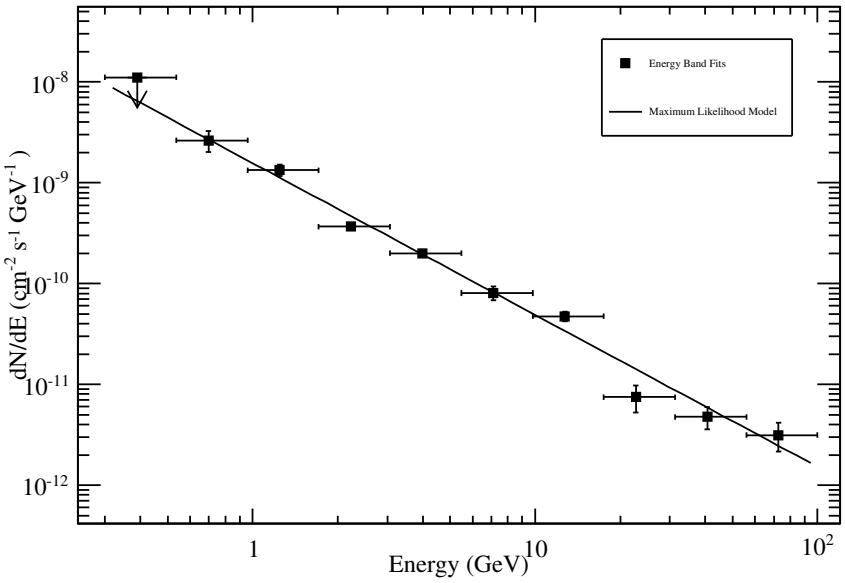

FIGURE 6.12. 1ES 0502+675 Fermi LAT 10-bin dN/dE spectrum.

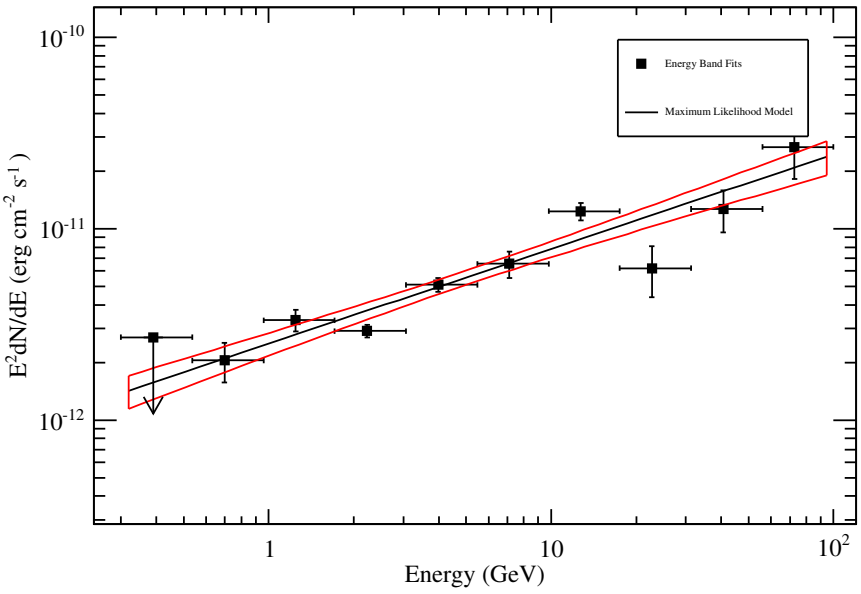

FIGURE 6.13. 1ES 0502+675 Fermi LAT 10-bin E^2 dN/dE spectrum shown with the best fit powerlaw function. The first point is an upper limit.

6.4. 1ES 0806+524

1ES 0806+524 is a HBL detected by both VERITAS and Fermi LAT and analysis results are described below.

6.4.1. VERITAS analysis. 1ES 0806+524, a medium TeV spectrum source HBL, was observed between November 5^{th} 2007 and March 11^{th} 2011 with a total livetime of $\sim$ 46.5 hours. A wobble analysis produced a 6.35σ excess with a γ-ray rate of 0.08 ± 0.01 γ's min^{-1}. The excess events can be seen in the θ^2 plot (figure 6.14). The wobble results are shown in table 6.3. Both the detection and a 4.9 magnitude star, 27Lyn, can be seen clearly in the 2D significance maps (figure 6.15). There is also a 6.8 magnitude star named SAO26716 located in the field of view. The spectrum is best fit by a powerlaw of $(1.099\pm1.159)\times10^{-9}$ $\left(\frac{E}{1TeV}\right)^{-4.14\pm0.92}$ with χ^2/n.d.f = 1.898/2 and a 0.38 probably of a straight line fit (figure 6.19). These results are consistent with previously published VERITAS subset results (Acciari et al., 2009). The integral flux ($>$ 1 TeV) is $(4.41 \pm 0.89)\times10^{-9}$ m^{-2}s^{-1}. No significant variability is seen on day, week and month timescales (figures 6.16, 6.17, 6.18).

TABLE 6.3. VERITAS Wobble 1ES 0806+524 results

	2007-2008	2008-2009	2010-2011	Total
Total On Events	888	51	296	1235
Total Off Events	7.37×10^3	355	2.07×10^3	9.79×10^3
Total Exposure Time (min)	2.31×10^3	35.79	442	2.78×10^3
Significance (σ)	4.4	0.67	5.19	6.35
γ-ray Rate (γ's min^{-1})	0.057 $\pm$ 0.013	0.134 $\pm$ 0.211	0.192 $\pm$ 0.0404	0.08 $\pm$ 0.01
Background Rate (γ's min^{-1})	0.328	1.29	0.478	0.364

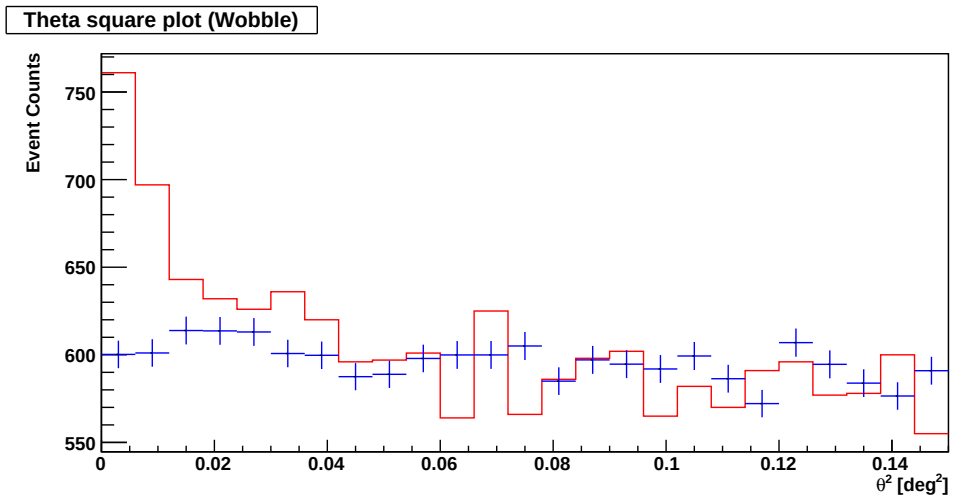

FIGURE 6.14. 1ES 0806+524 VERITAS theta squared plot which shows the γ-ray signal (red) over the background signal (blue).

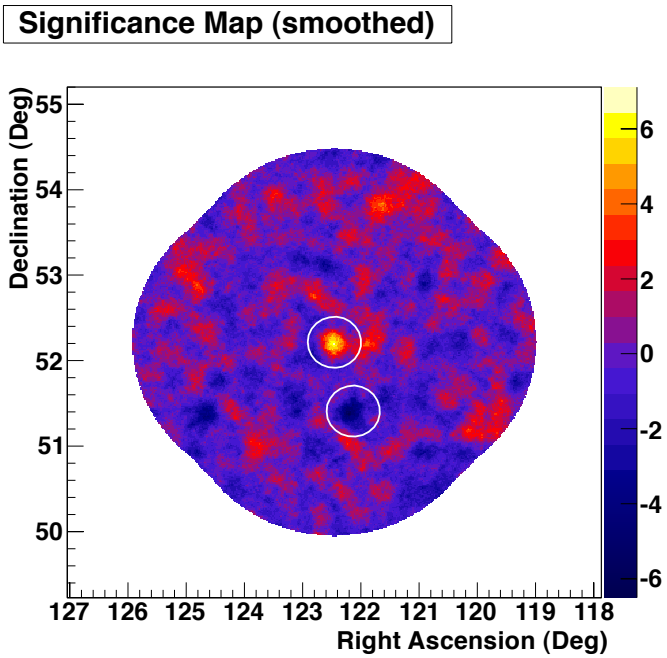

FIGURE 6.15. 1ES 0806+524 VERITAS 2D significance map. The circles represent the RBM exclusion regions corresponding to the source itself and the star 27Lyn.

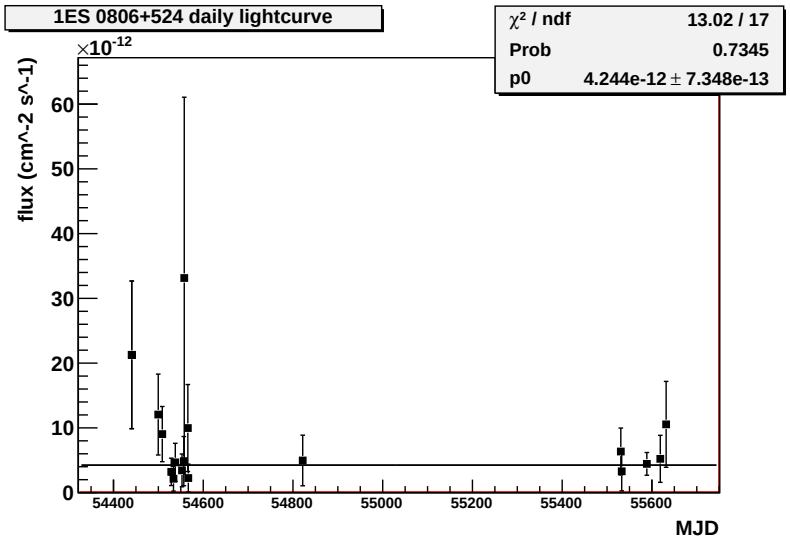

FIGURE 6.16. 1ES 0806+524 TeV lightcurve binned in day intervals, between November 5^{th} 2007 and March 11^{th} 2011, suggesting no variability.

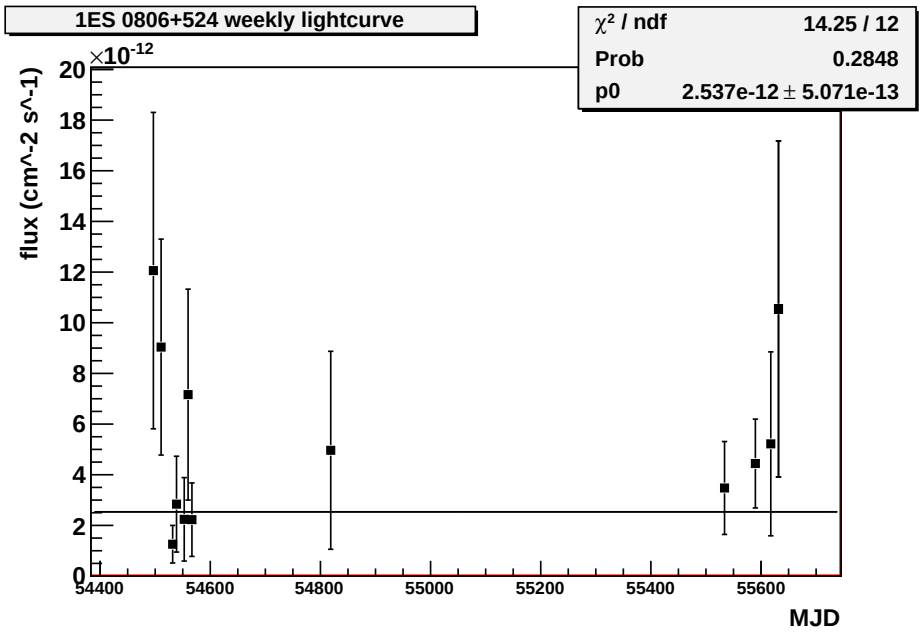

FIGURE 6.17. 1ES 0806+524 TeV lightcurve binned in week intervals, between November 5^{th} 2007 and March 11^{th} 2011, suggesting no variability.

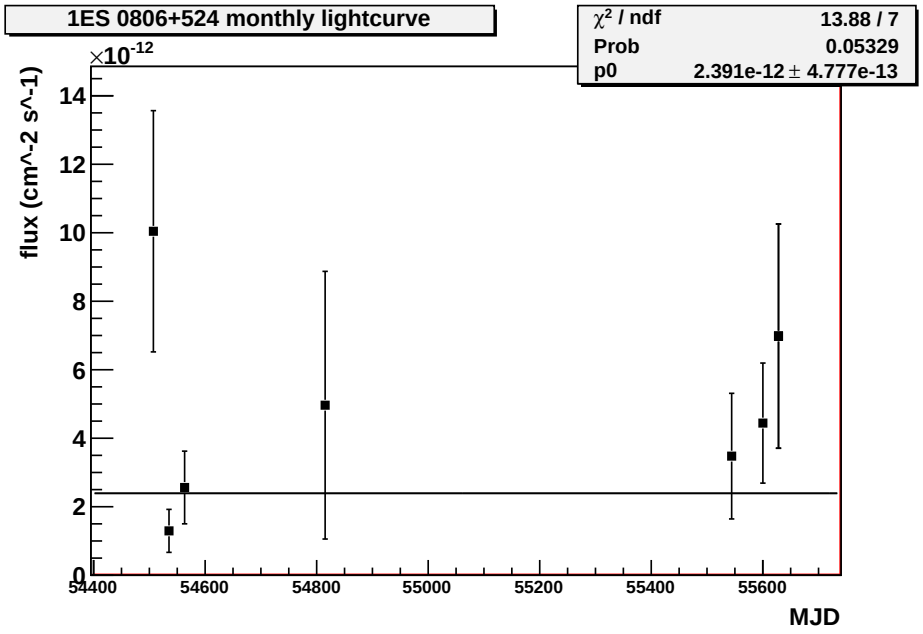

FIGURE 6.18. 1ES 0806+524 TeV lightcurve binned in month intervals, between November 5^{th} 2007 and March 11^{th} 2011, suggesting no variability.

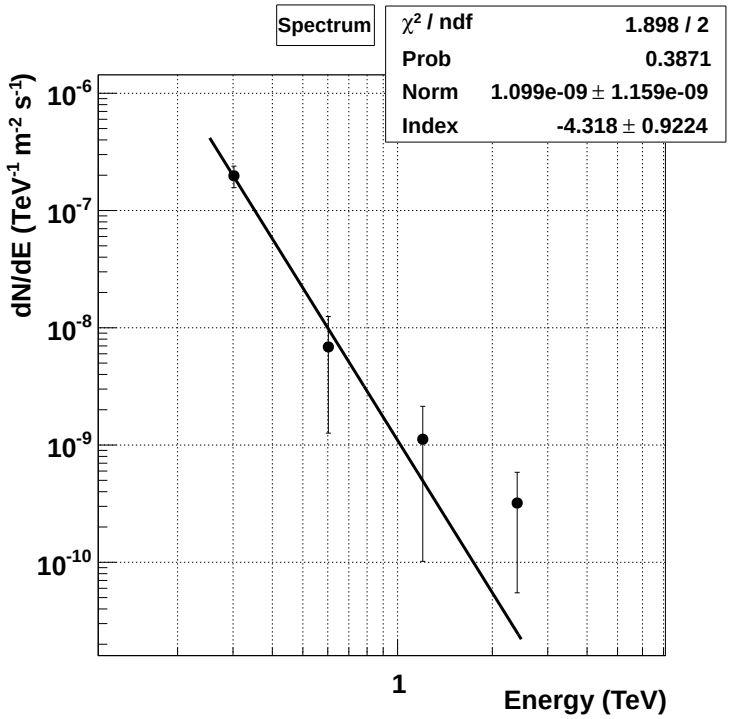

FIGURE 6.19. 1ES 0806+524 VERITAS TeV dN/dE spectrum and best fit power law.

6.4.2. Fermi analysis. 1ES 0806+675 is detected with a flux (> 300 MeV) of (1.02 ± 0.06) × 10^{-8} ph cm^{-2} s^{-1} at a TS of 1221.66, equivalent to a significance of $\sim 35\sigma$. Figures 6.20 and 6.21 show the background before the addition of other γ-ray sources in the ROI and after 1ES 0806+524 is included in the background model. There are eleven "unknown source" or TS bumps required in the model in order to generate a flat background. Table 6.4 give a list of these sources, in addition to the Unbinned Maximum Likelihood analysis results for each source. Three high energy (> 100 GeV) photons were detected within 1° of the source location from the dataset; 171 GeV, 114 GeV and 100 GeV. The lightcurves (figures 6.22, 6.23, 6.24) clearly show that the source is variable on weekly, monthly and three monthly timescales and at a higher flux in the last third of the dataset. The dataset is divided into ten equal bins for spectral analysis. The TS as a function of energy (figure 6.25) exhibits a high peak at $\sim$ 2 GeV with a dip between 7 and 30 GeV. The dN/dE spectrum is shown in figure 6.26 and is fit best by a powerlaw with an index of -1.89 ± 0.04.

The E^2 dN/dE spectrum with the $\sim$ 10 GeV dip as mentioned above being very prominent is seen in figure 6.27. To test, if this dip is a function of flux or activity the dataset was divided into two subsets: before July 30^{th} 2010 and after (low and high state), and the Unbinned Maximum Likelihood and spectral analyses were run again. As the flux increases (in the second half of the data set), the dip shifts significantly to higher energies, see figures 6.28 and 6.29.

TABLE 6.4. 1ES 0806+524 Fermi LAT Gtlike Unbinned Maximum Likelihood results

Source	Index	Flux (ph cm^{-2} s^{-1})	TS	Npred	ROI Distance $^{\circ}$
1ES 0806+675	-1.89 +/- 0.04	$(1.02 \pm 0.06)\times10^{-8}$	1221.66	787.46	0.00
1FGL J0712.7+5033	-2.16 ± 0.07	$(6.39 \pm 0.57)\times10^{-9}$	309.69	409.68	9.06
1FGL J0742.2+5443	-2.36 ± 0.03	$(2.53 \pm 0.08)\times10^{-8}$	2477.25	1860.54	4.70
1FGL J0752.8+5353	-1.98 ± 0.07	$(4.03 \pm 0.47)\times10^{-9}$	242.32	309.22	2.96
1FGL J0800.5+4407	-2.68 ± 0.14	$(4.20 \pm 0.55)\times10^{-9}$	94.84	265.20	8.43
1FGL J0806.2+6148	-2.94 ± 0.10	$(8.53 \pm 0.69)\times10^{-9}$	233.16	450.104	9.35
1FGL J0816.7+5739	-2.15 ± 0.09	$(4.08 \pm 0.49)\times10^{-9}$	174.55	308.13	5.42
1FGL J0818.2+4222	-2.15 ± 0.04	$(2.85 \pm 0.13)\times10^{-8}$	1493.72	945.99	10.02
1FGL J0825.0+5555	-2.92 ± 0.12	$(2.88 \pm 0.61)\times10^{-9}$	133.71	413.72	4.22
1FGL J0844.0+5314	-2.34 ± 0.09	$(4.29 \pm 0.48)\times10^{-9}$	188.52	312.58	5.233
1FGL J0849.9+4852	-2.35 ± 0.05	$(1.15 \pm 0.06)\times10^{-8}$	821.76	801.63	7.22
1FGL J0920.9+4127	-0.91 ± 0.06	$(5.00 \pm 0.69)\times10^{-6}$	186.03	869.52	13.99
24M0955	-2.51 ± 0.12	$(4.12 \pm 0.54)\times10^{-9}$	98.31	291.89	5.92
24M0996	-2.54 ± 0.13	$(3.99 \pm 0.55)\times10^{-9}$	90.66	261.36	8.16
24M1013	-2.18 ± 0.08	$(5.08 \pm 0.52)\times10^{-9}$	250.31	372.70	4.56
24M1080	-2.48 ± 0.10	$(5.03 \pm 0.54)\times10^{-9}$	196.38	285.22	9.25
AS1	-2.56 ± 0.18	$(2.33 \pm 0.49)\times10^{-9}$	38.37	163.17	7.10
AS2	-2.59 ± 0.17	$(2.70 \pm 0.51)\times10^{-9}$	44.46	194.68	1.50
AS3	-2.64 ± 0.16	$(2.82 \pm 0.51)\times10^{-9}$	58.88	196.98	4.73
AS4	-2.77 ± 0.20	$(2.38 \pm 0.45)\times10^{-9}$	44.67	151.61	8.48
AS5	-3.30 ± 0.30	$(2.53 \pm 0.51)\times10^{-9}$	31.67	162.96	6.99
AS6	-2.77 ± 0.21	$(2.13 \pm 0.47)\times10^{-9}$	33.05	140.13	8.20
AS7	-2.52 ± 0.10	$(5.35 \pm 0.53)\times10^{-9}$	195.40	376.07	6.29
AS8	-3.04 ± 0.18	$(3.77 \pm 0.57)\times10^{-9}$	55.93	258.83	2.66
AS9	-3.34 ± 0.24	$(3.73 \pm 0.53)\times10^{-9}$	70.87	209.36	8.95
AS10	-2.88 ± 0.20	$(3.24 \pm 0.53)\times10^{-9}$	51.32	224.03	3.77
AS11	-2.74 ± 0.22	$(2.07 \pm 0.48)\times10^{-9}$	34.73	133.56	8.05

AS = Additional Source

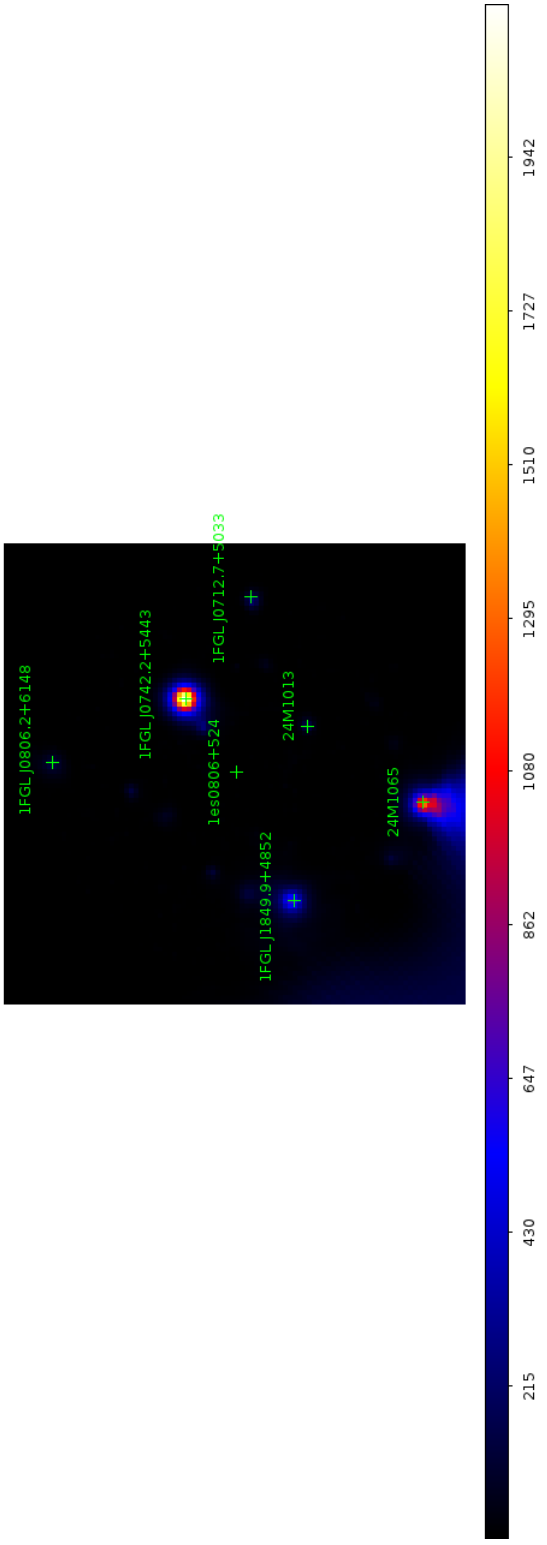

FIGURE 6.20. 1ES 0806+524 12° Fermi LAT TS map before background sources in the ROI are subtracted, highlighting 6 high TS sources in the ROI.

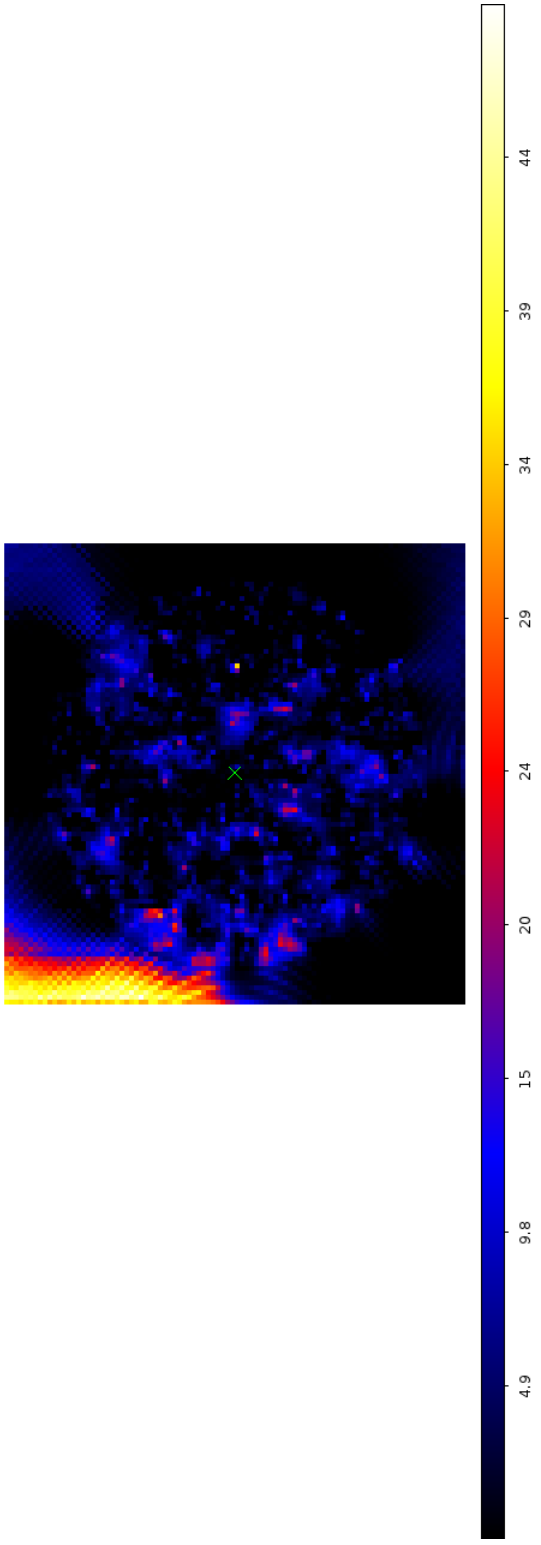

FIGURE 6.21. 1ES 0806+524 12° Fermi LAT TS map after background subtraction. Note the different TS scale to ensure that lower TS sources can be seen. The high TS level seen in the left corner is a extragalactic source outside the ROI.

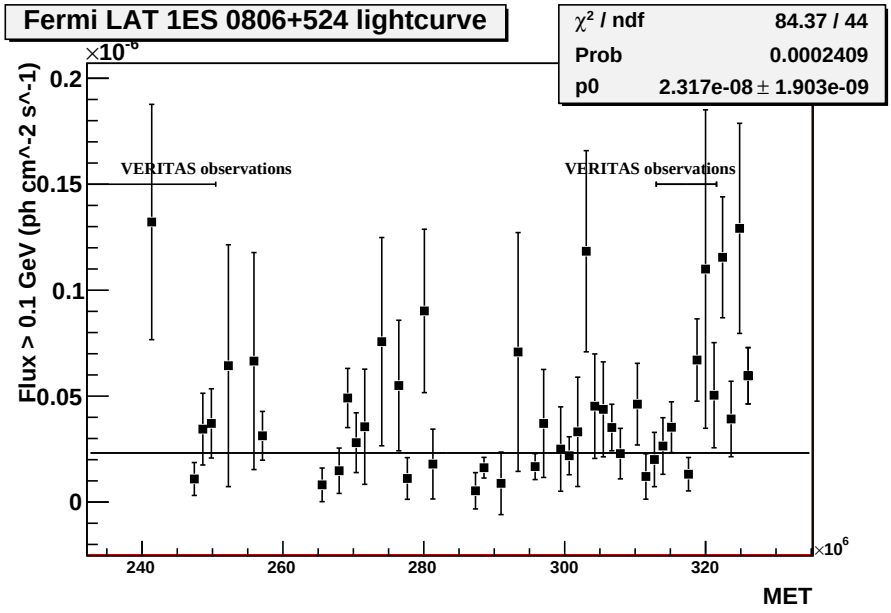

FIGURE 6.22. 1ES 0806+524 Fermi LAT lightcurve in 2 week-long intervals, doe not exhibit significant variability. Note the 2 quasi-contemporaneous VERITAS observations.

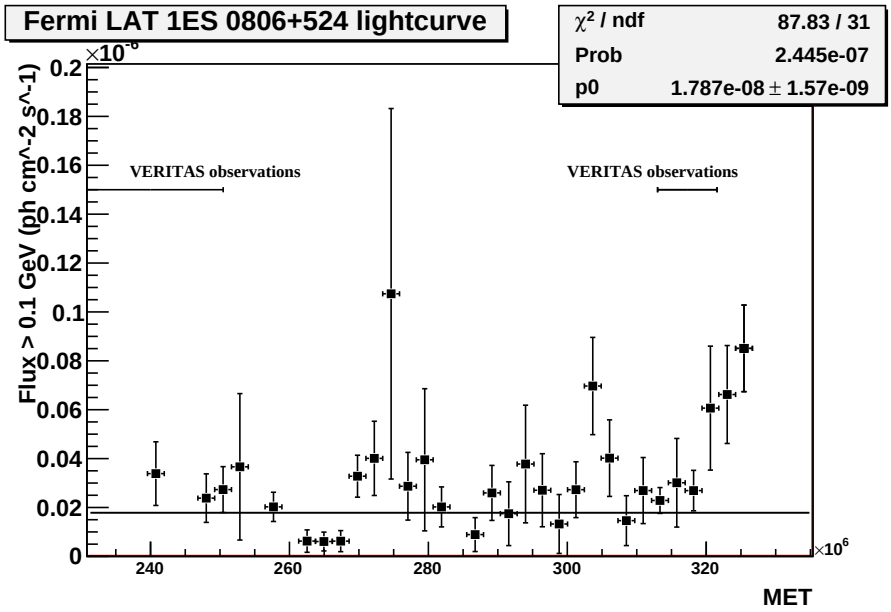

FIGURE 6.23. 1ES 0806+524 Fermi LAT lightcurve in month-long intervals, showing variability. Note the 2 quasi-contemporaneous VERITAS observations.

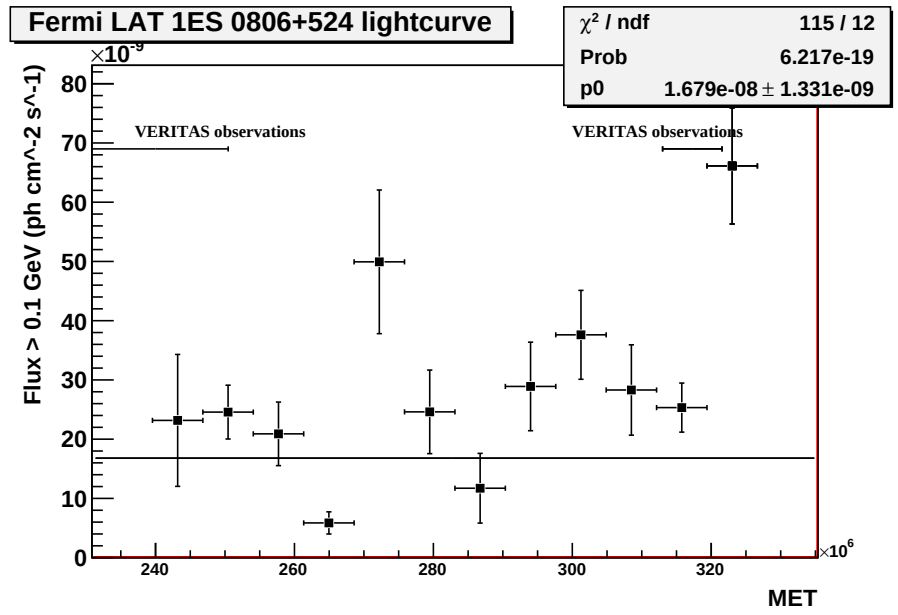

FIGURE 6.24. 1ES 0806+524 Fermi LAT lightcurve in 3 month-long intervals, showing significant variability. Note the 2 quasi-contemporaneous VERITAS observations.

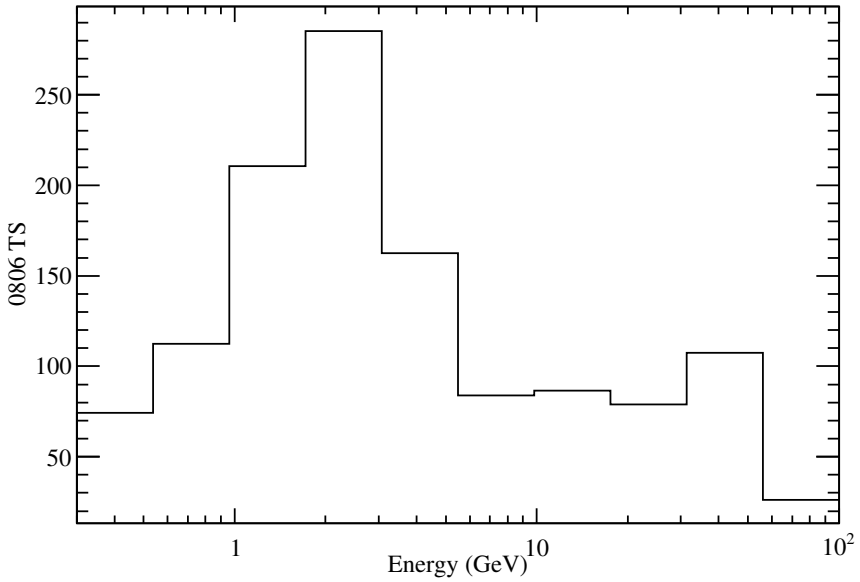

FIGURE 6.25. 1ES 0806+524 Fermi LAT TS versus energy in 10 bins.

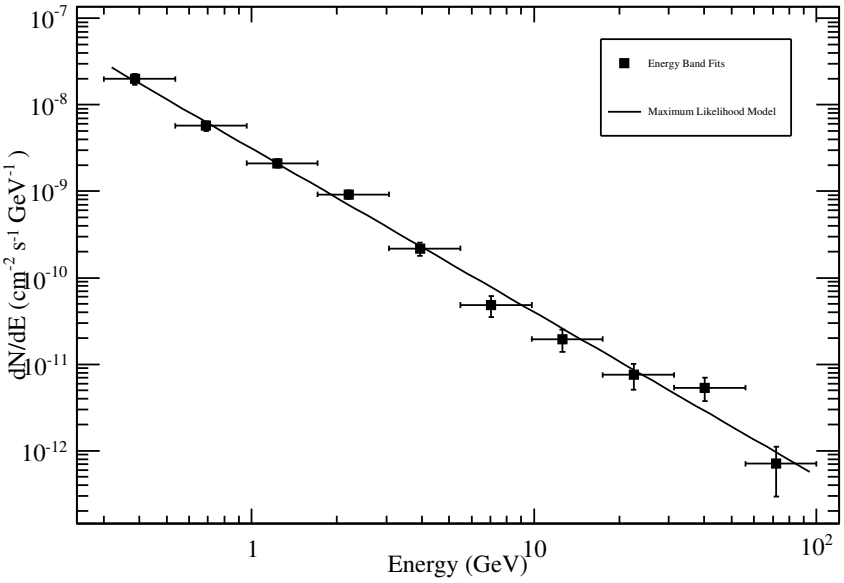

FIGURE 6.26. 1ES 0806+524 Fermi LAT dN/dE spectrum in 10 bins.

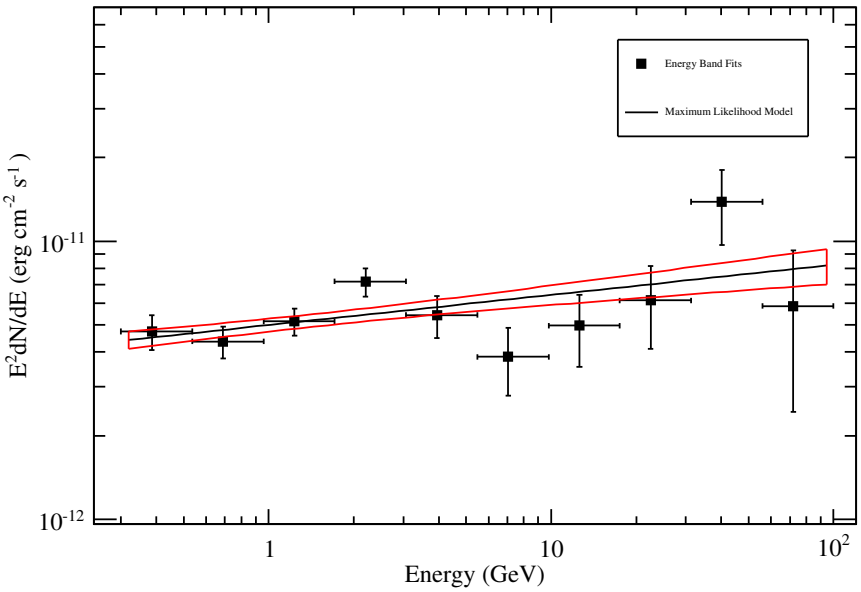

FIGURE 6.27. 1ES 0806+524 Fermi LAT E^2 dN/dE in 10 bins fit with a powerlaw function.

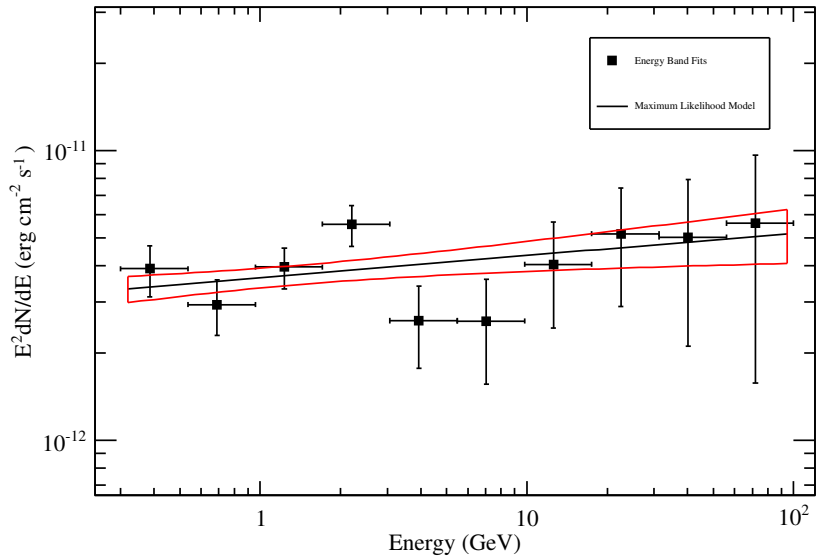

FIGURE 6.28. 1ES 0806+524 E^2dN/dE low-state spectrum of index of -1.92 ± 0.06 with an integral flux (E > 300 MeV) of (7.45 ± 0.62) $\times 10^{-9}$ ph cm^{-2} s^{-1}.

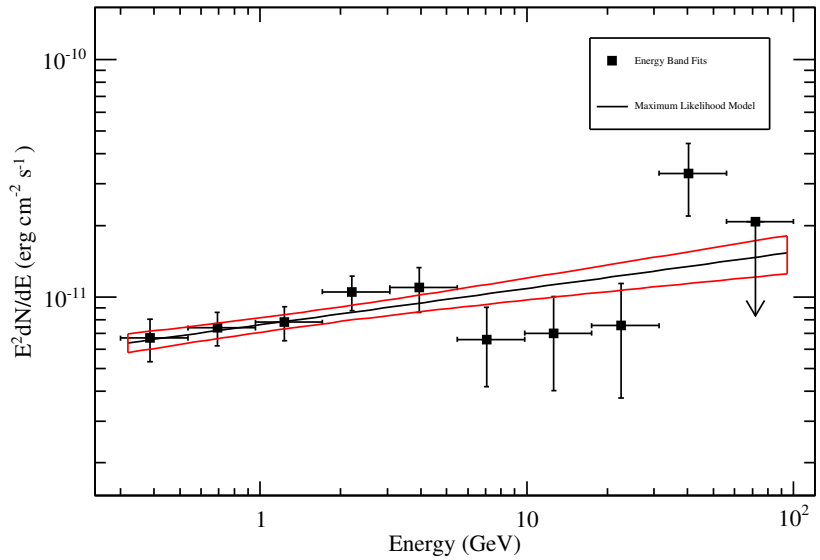

FIGURE 6.29. 1ES 0806+524 E^2dN/dE high-state spectrum of index -1.85 ± 0.05 with an integral flux (E > 300 MeV) of (1.56 ± 0.11) $\times 10^{-8}$ ph cm^{-2} s^{-1}.

6.5. 1ES 1959+650

1ES 1959+650 is a HBL detected by both VERITAS and Fermi LAT and analysis results are described below.

6.5.1. VERITAS analysis. 1ES 1959+650 is a medium TeV spectrum source analysis HBL that VERITAS observed sporadically between September 10^{th} 2007 and December 4^{th} 2010 with a total livetime of $\sim$ 6 hours. A wobble analysis (table 6.5) produced a 13.33σ excess with a γ-ray rate of 0.50 $\pm$ 0.05 γ's min^{-1}. The excess events can be seen in the θ^2 plot, figure 6.30. 1ES 1959+650 can be seen in the 2D significance map (figure 6.31). The spectrum is best fitted by a powerlaw of $(6.33 \pm 1.36)\times10^{-8}$ $\left(\frac{E}{1TeV}\right)^{-1.998\pm0.432}$ with χ^2/n.d.f = 4.271/1 and a 0.04 probably of a straight line fit (figure 6.35). The integral flux ($>$ 1 TeV) is $(3.49 \pm 0.44)\times10^{-8}$ m^{-2}s^{-1}. The day, week and month-long lightcurves (figures 6.32, 6.33 and 6.34) show a marginal increase in flux in December 2010.

TABLE 6.5. VERITAS Wobble 1ES 1959+650 results

	2007-2008	2008-2009	2010-2011	Total
Total On Events	58	69	146	273
Total Off Events	274	397	431	1318
Total Exposure Time (min)	95.58	118.91	126.87	341.36
Significance (σ)	5.32	4.60	12.1591	13.33
γ-ray Rate (γ's min^{-1})	0.35 +/- 0.08	0.28 $\pm$ 0.7	0.84 $\pm$ 0.10	0.50 $\pm$ 0.5
Background Rate (γ's min^{-1})	0.26	0.30	0.31	0.30

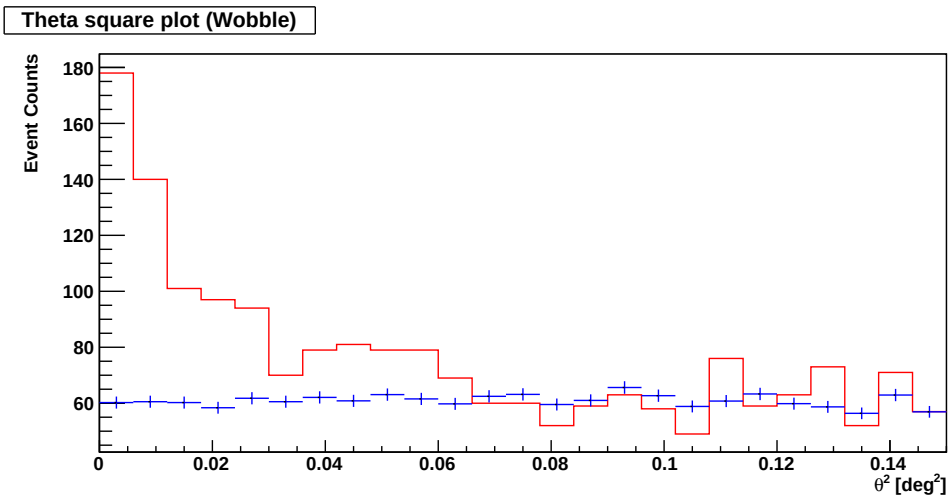

FIGURE 6.30. 1ES 1959+650 VERITAS θ^2 plot showing the signal (red) above the background (blue)

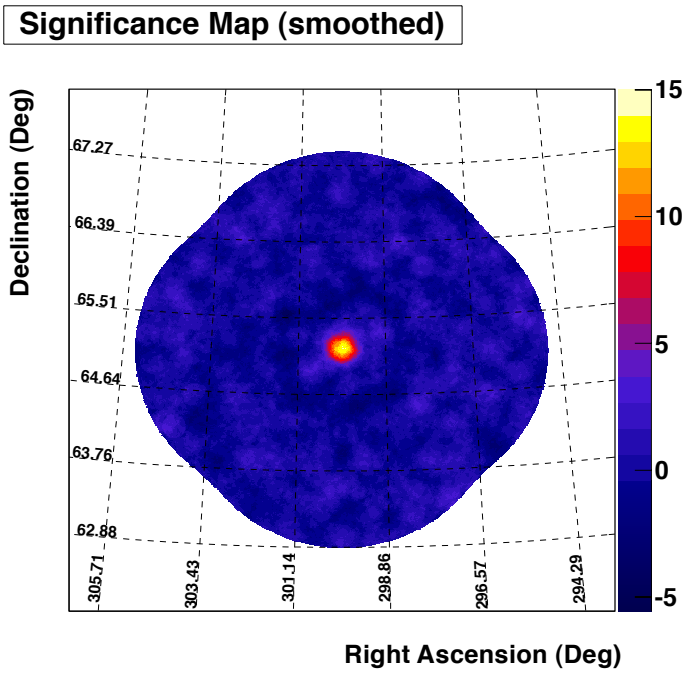

FIGURE 6.31. 1ES 1959+650 VERITAS 2D significance map

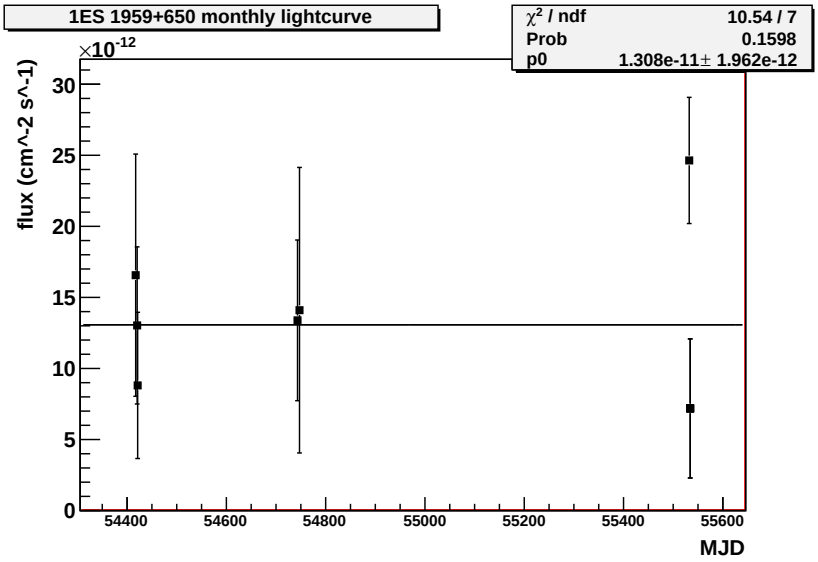

FIGURE 6.32. 1ES 1959+650 TeV Lightcurve in daily intervals, between September 10^{10} 2007 and December 4^{th} 2010. No significant variability is seen.

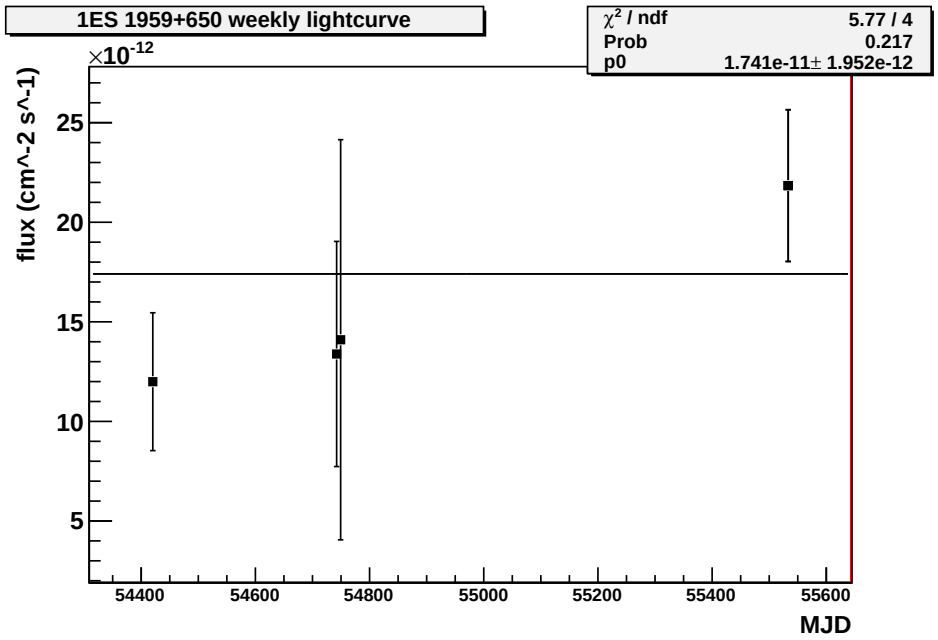

FIGURE 6.33. 1ES 1959+650 TeV Lightcurve in weekly intervals, between September 10^{10} 2007 and December 4^{th} 2010. No significant variability is seen.

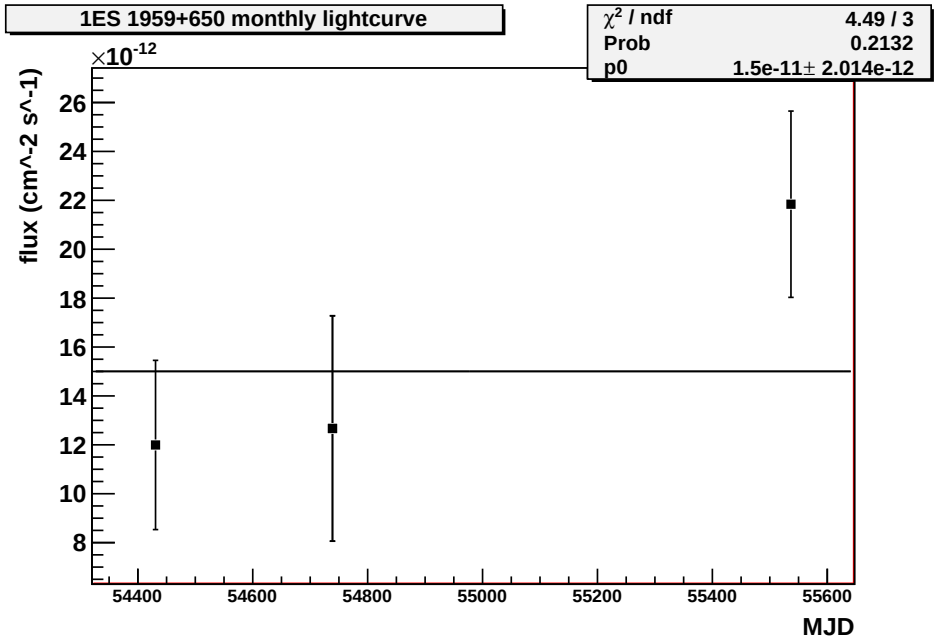

FIGURE 6.34. 1ES 1959+650 TeV Lightcurve in month intervals, between September 10^{10} 2007 and December 4^{th} 2010. No significant variability is seen.

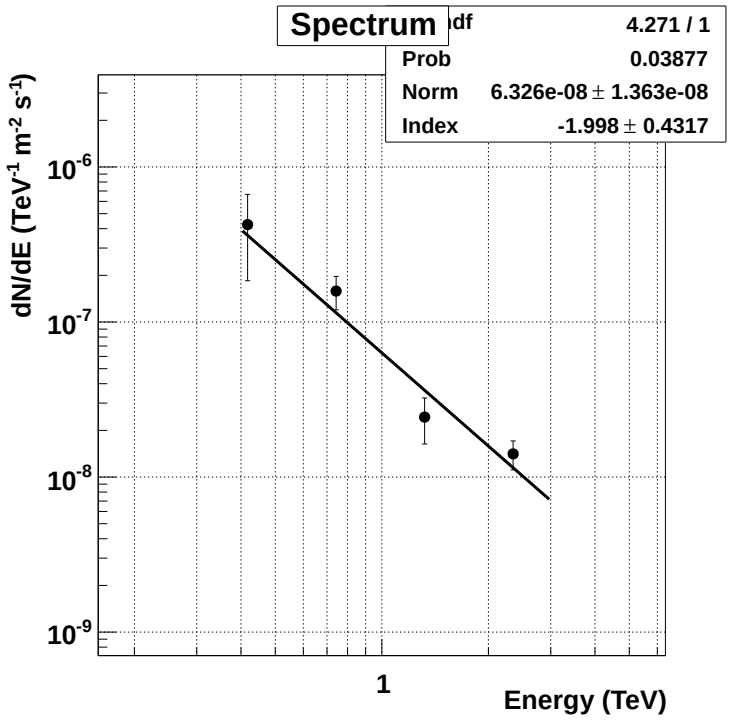

FIGURE 6.35. 1ES 1959+650 VERITAS dN/dE powerlaw spectrum

6.5.2. Fermi. 1ES 1959+650 is detected with a flux (> 300 MeV) of $(1.88 \pm 0.06) \times 10^{-8}$ ph cm^{-2} s^{-1} at a TS of 2312.53, equivalent to a significance of $\sim 48\sigma$. Figures 6.36 and 6.37 show the background before and after the addition of other γ-ray sources in the ROI. There are sixteen "unknown source" or TS bumps required in the model in order to generate a flat background. Table 6.6 gives a list of these sources, in addition to the Unbinned Maximum Likelihood analysis results for each source. Six high energy (> 100 GeV) photons were detected within 1° of the source location from the dataset: 244 GeV, 198 GeV, 167 GeV, 157 GeV, 120 GeV and 103 GeV.

Though difficult to see ongoing variability in the weekly timescale lightcurve (figure 6.38), the monthly timescale lightcurve (figure 6.39) clearly shows variability with increased flux in the first $\sim$ six months of the dataset. The TS as a function of energy (figure 6.40) exhibits a high peak at ~ 2 GeV and the dN/dE spectrum is shown in figure 6.41 and is fit best by a powerlaw with an index of -1.95 $\pm$ 0.06. The E^2 dN/dE spectrum is shown in figure 6.42.

TABLE 6.6. 1ES 1959+650 Fermi LAT Gtlike Unbinned Maximum Likelihood results

Source	Index	Flux (ph cm^{-2} s^{-1})	TS	Npred	ROI Distance
1ES 1959+650	-1.95 ± 0.01	$(1.88 \pm 0.06)\times10^{-8}$	2312.53	1643.21	0.00
1FGL J1849.3+6705	-2.31 ± 0.01	$(2.86 \pm 0.07)\times10^{-8}$	3455.45	2321.59	7.37
1FGL J1926.8+6153	-1.86 ± 0.03	$(6.27 \pm 0.42)\times10^{-9}$	612.37	545.31	4.90
1FGL J1941.6+7214	-2.67 ± 0.05	$(6.54 \pm 0.06)\times10^{-9}$	139.29	518.23	7.37
1FGL J2001.9+7040	-2.16 ± 0.05	$(3.75 \pm 0.46)\times10^{-9}$	111.61	320.68	5.55
1FGL J2004.8 +7004	-2.02 ± 0.04	$(4.46 \pm 0.45)\times10^{-9}$	189.41	388.25	4.90
1FGL J2009.1+7228	-2.32 ± 0.04	$(7.93 \pm 0.57)\times10^{-9}$	265.18	651.25	7.38
1FGL J2038.1+6552	-2.13 ± 0.06	$(2.95 \pm 0.43)\times10^{-9}$	66.01	252.31	3.86
24M2257	-2.56 ± 0.06	$(7.06 \pm 0.73)\times10^{-9}$	123	269.48	10.02
24M2418	-2.44 ± 0.04	$(7.92 \pm 0.56)\times10^{-9}$	303.39	640.41	5.31
24M2707	-2.19 ± 0.05	$(5.19 \pm 0.64)\times10^{-9}$	100.80	315.59	9.60
PSR J1836+5925	-1.79 ± 0.02	$(4.00 \pm 0.15)\times10^{-7}$	1917.11	2224.99	11.21
AS1	-3.00 ± 0.07	$(7.10 \pm 0.70)\times10^{-9}$	104.72	566.21	1.30
AS2	-2.85 ± 0.11	$(2.66 \pm 0.45)\times10^{-9}$	35.02	210.61	4.73
AS3	-2.85 ± 0.08	$(4.41 \pm 0.62)\times10^{-9}$	63.66	327.21	8.40
AS4	-2.28 ± 0.08	$(2.65 \pm 0.41)\times10^{-9}$	60.27	221.53	2.09
AS5	-2.71 ± 0.08	$(4.73 \pm 0.89)\times10^{-9}$	52.35	343.92	8.72
AS6	-2.59 ± 0.09	$(2.80 \pm 0.43)\times10^{-9}$	45.82	207.45	8.17
AS7	-1.93 ± 0.06	$(2.10 \pm 0.36)\times10^{-9}$	64.21	182.31	4.29
AS8	-1.91 ±0.08	$(1.37 \pm 0.34)\times10^{-9}$	36.66	115.92	7.89
AS9	-2.35 ± 0.07	$(3.53 \pm 0.52)\times10^{-9}$	48.49	291.73	6.66
AS10	-2.95 ± 0.08	$(4.21 \pm 0.51)\times10^{-9}$	72.03	325.49	7.24
AS11	-2.56 ± 0.09	$(2.97 \pm 0.49)\times10^{-9}$	41.92	245.24	4.07
AS12	-2.75 ± 0.10	$(3.28 \pm 0.49)\times10^{-9}$	43.09	266.21	2.15
AS13	-2.76 ± 0.08	$(4.18 \pm 0.55)\times10^{-9}$	65.61	315.48	8.09
AS14	-2.52 ± 0.09	$(3.78 \pm 0.62)\times10^{-9}$	40.63	303.35	7.39
AS15	-2.97 ± 0.10	$(3.71 \pm 0.54)\times10^{-9}$	48.35	293.10	5.81
AS16	-4.13 ± 0.17	$(2.99 \pm 0.54)\times10^{-9}$	31.39	194.27	8.58

AS = Additional Source

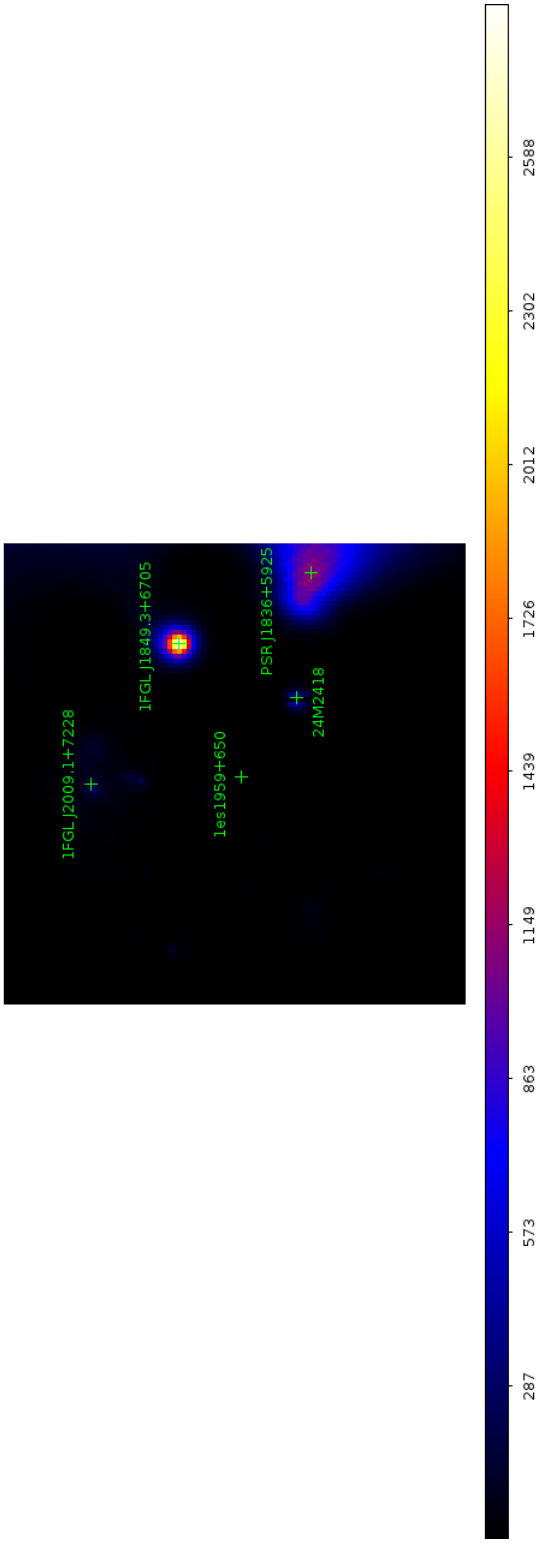

FIGURE 6.36. 1ES 1959+650 Fermi LAT 12° TS map before background sources in the ROI are subtracted highlighting four high TS sources in the ROI

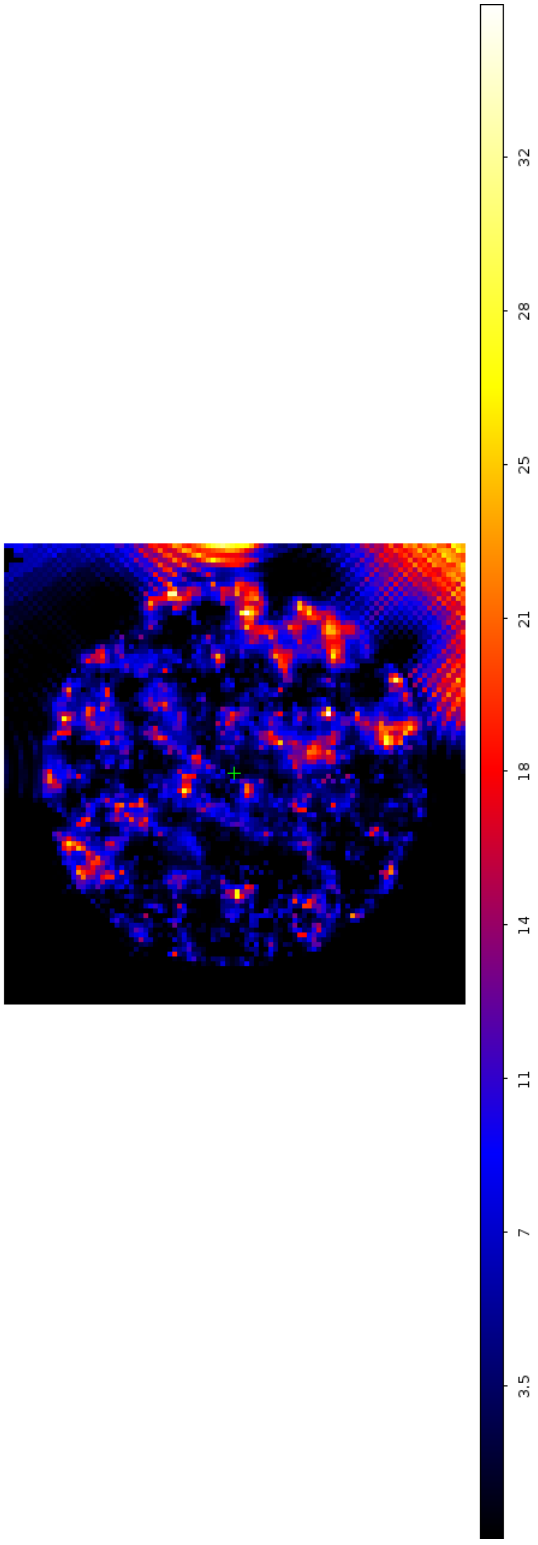

FIGURE 6.37. 1ES 1959+650 Fermi LAT 12° TS map after background subtraction. Note the different TS scale. A lower TS scale is required to ensure the lower TS sources in the ROI are seen clearly.

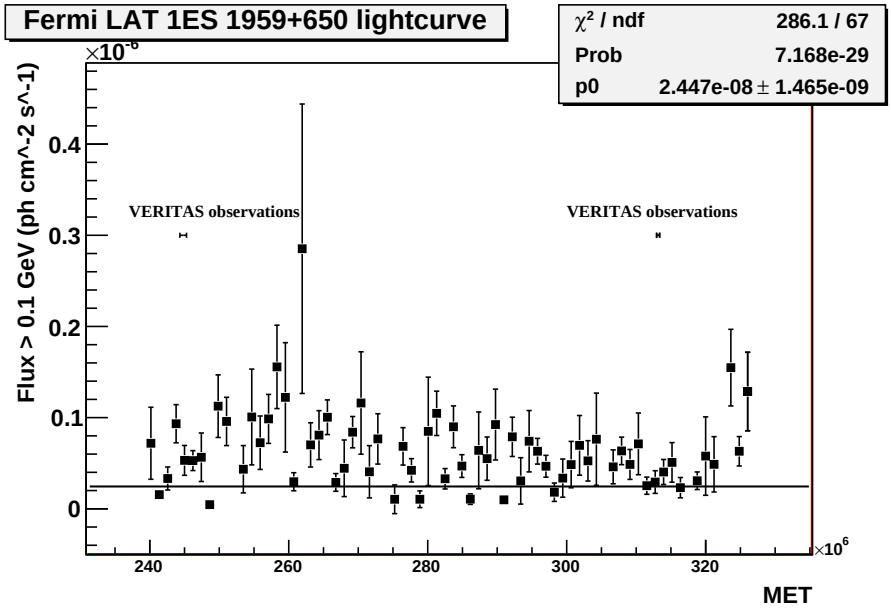

FIGURE 6.38. 1ES 1959+650 in 2 week-long bins, showing extreme variability. Note the 2 contemporaneous VERITAS observations.

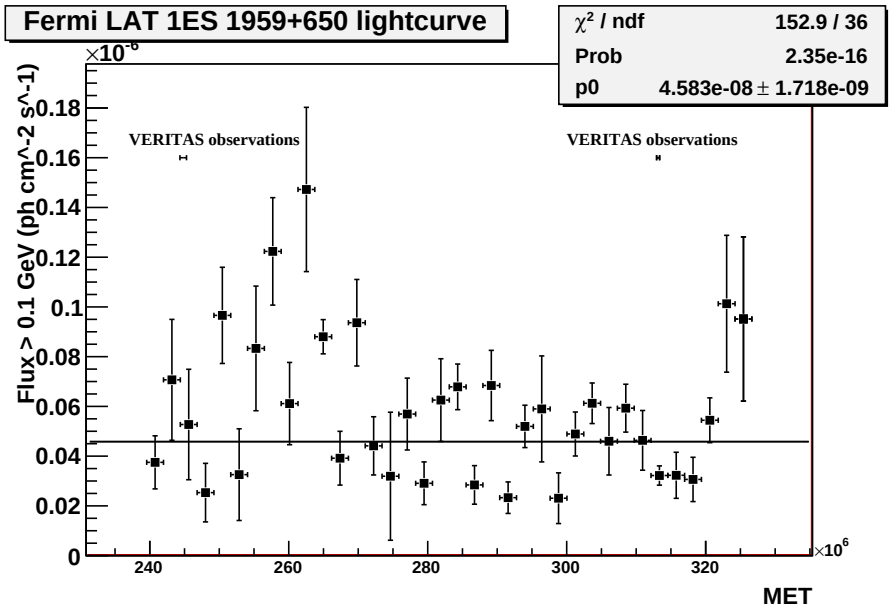

FIGURE 6.39. 1ES 1959+650 in month-long bins. The probability and χ^2/n.d.f values suggest significant variability. Note the 2 contemporaneous VERITAS observations.

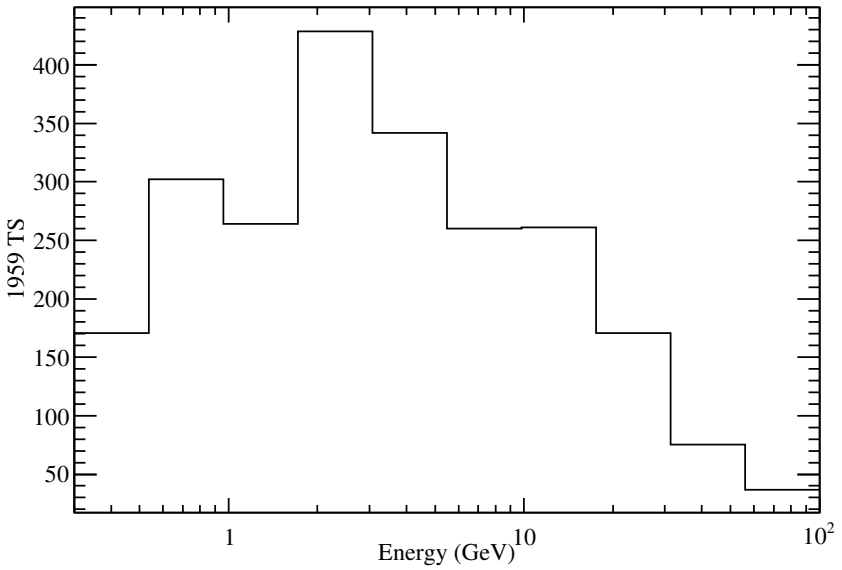

FIGURE 6.40. 1ES 1959+650 Fermi LAT TS versus energy in 10 bins.

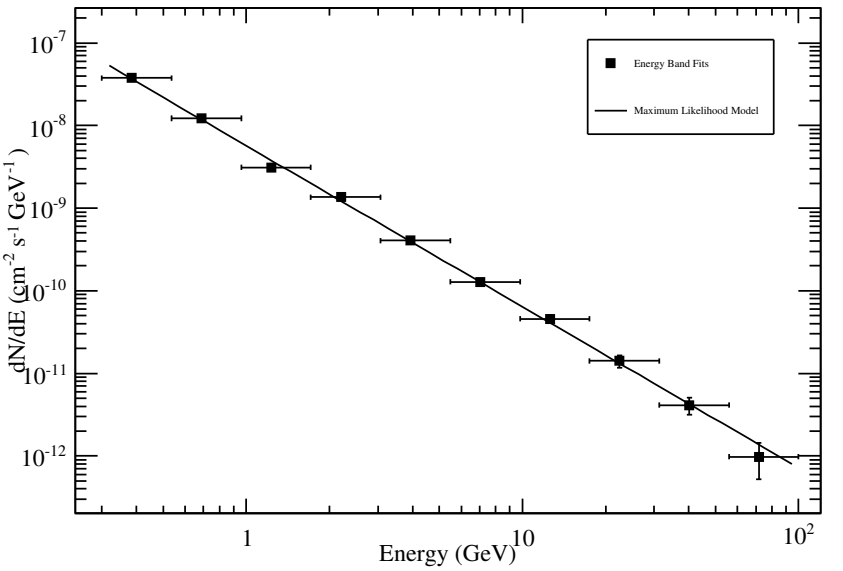

FIGURE 6.41. 1ES 1959+650 Fermi LAT dN/dE spectrum in 10 bins.

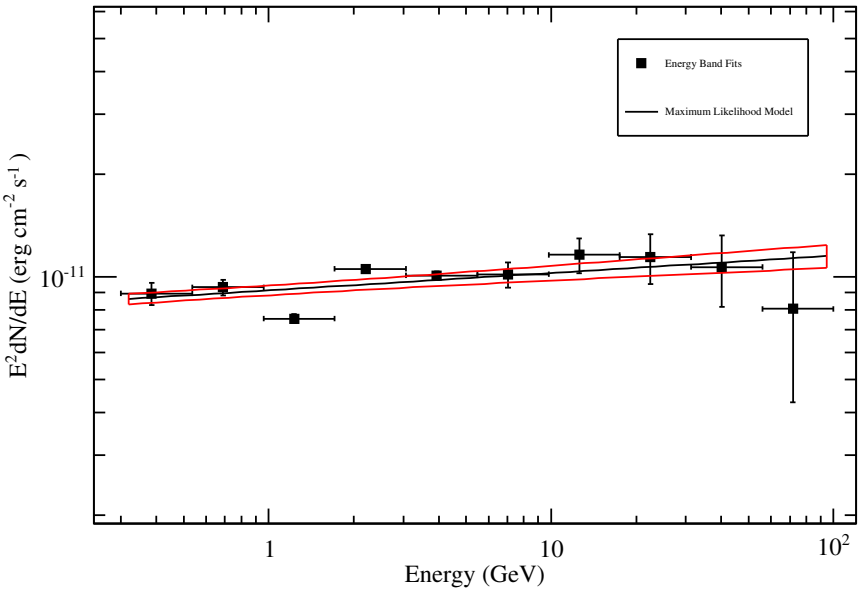

FIGURE 6.42. 1ES 1959+650 Fermi LAT E^2 dN/dE spectrum in 10 bins.

6.6. W Comae

W Comae is an IBL detected by Fermi LAT and VERITAS as described below.

6.6.1. VERITAS analysis. WComae, a medium TeV spectrum source analysis IBL, has been observed extensively between January 10^{th} 2008 and April 1^{st} 2011 with a total livetime of $\sim$ 62 hours. A wobble analysis (table 6.7) produced a 10.57σ detection with a γ-ray rate of 0.12 $\pm$ 0.01 γs min^{-1}. The excess events can be seen in the θ^2 plot (figure 6.43). Both W Comae and another blazar 1ES 1218+30.4 can be seen clearly in the 2D significance maps (figure 6.44). The spectrum is best fit by a powerlaw of $(1.73 \pm 0.38)\times10^{-7}$ $\left(\frac{E}{1TeV}\right)^{-3.34\pm0.27}$ with χ^2/n.d.f = 1.406/3 and a 0.70 probably of a straight line fit (figure 6.45). The integral flux ($>$ 1 TeV) is $(8.87 \pm 1.25)\times10^{-9}$ m^{-2}s^{-1}. While the daily lightcurve does not show variability (probability of 0.003 of being of constant flux, figure 6.46) the weekly and monthly lightcurves (figures 6.47 and 6.48) do with probabilities of being constant of 2.11×10^{-5} and 3.19 $\times10^{-6}$, respectively.

TABLE 6.7. VERITAS Wobble W Comae results

	2007-2008	2008-2009	2009-2010	2010-2011	total
Total On Events	1.26×10^3	166	253	318	2×10^3
Total Off Events	1.14×10^4	1.43×10^3	2.27×10^3	2.58×10^3	1.53×10^4
Total Exposure Time (min)	2.40×10^3	3.36×10^2	4.01×10^4	5.47×10^2	3.70×10^3
Significance (σ)	8.94	2.75	4.18	3.09	10.57
γ-ray Rate (γ's min^{-1})	0.13 $\pm$ 0.02	0.10 $\pm$ 0.04	0.16 $\pm$ 0.04	0.10 $\pm$ 0.03	0.12 $\pm$ 0.01
Background Rate (γ's min^{-1})	0.40	0.39	0.47	0.48	0.42

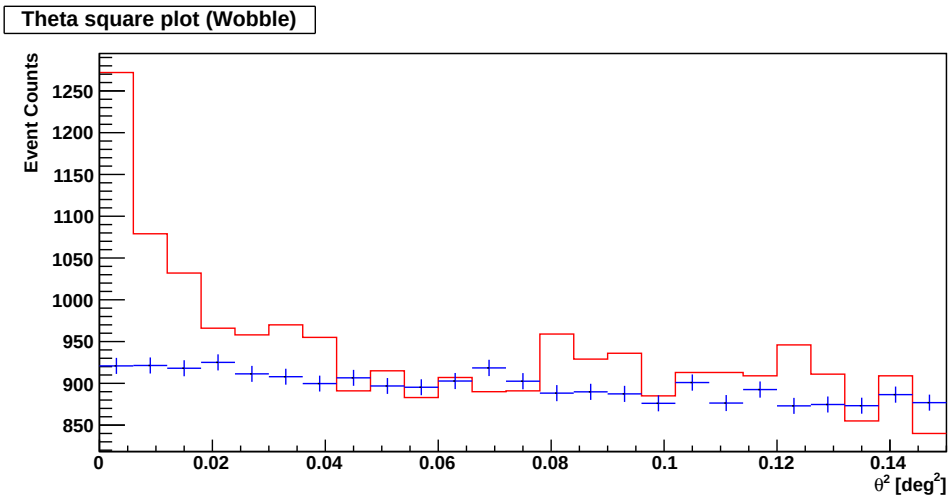

FIGURE 6.43. W Comae VERITAS θ^2 plot (red = source, blue = blackground).

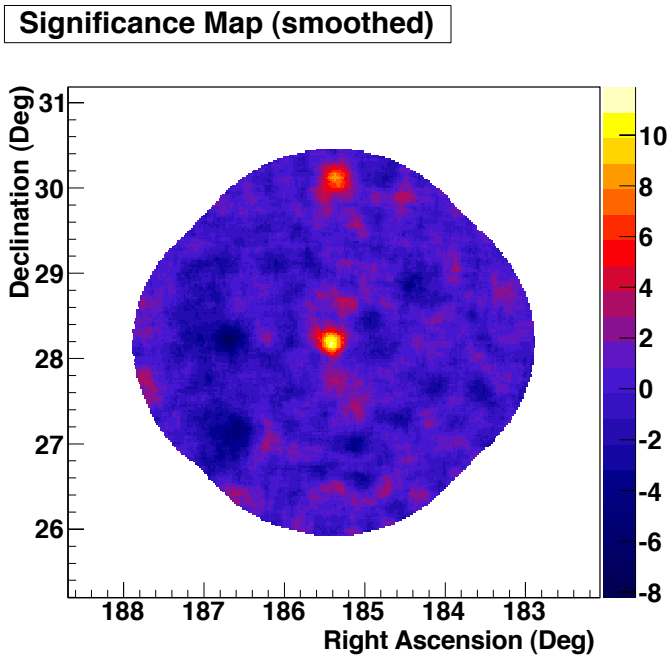

FIGURE 6.44. VERITAS 2D significance map showing both W Comae (centre) and 1ES 1218+30.4 (top).

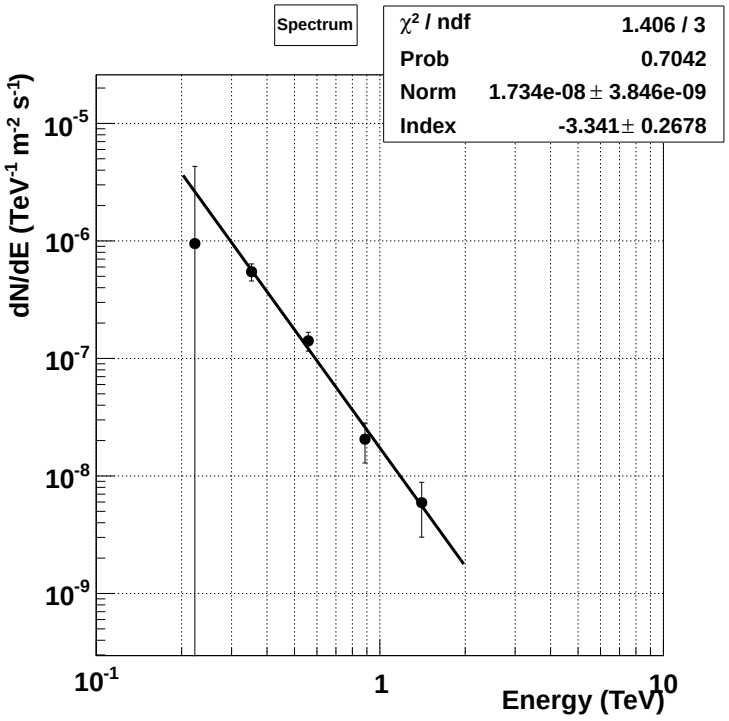

FIGURE 6.45. W Comae TeV dN/dE spectrum

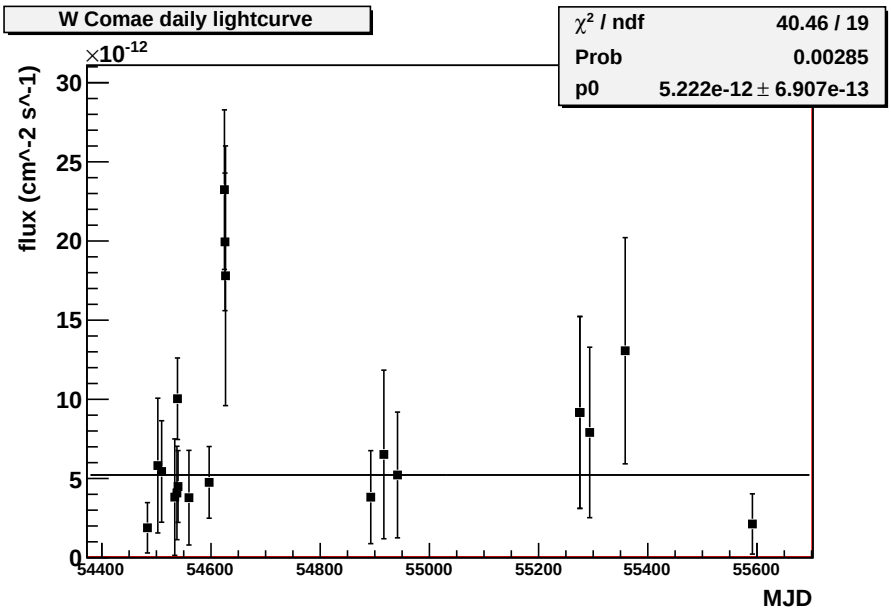

FIGURE 6.46. W Comae TeV lightcurve in daily intervals, between January 10^{th} 2008 and April 1^{st} 2011, does not exhibit significant variability.

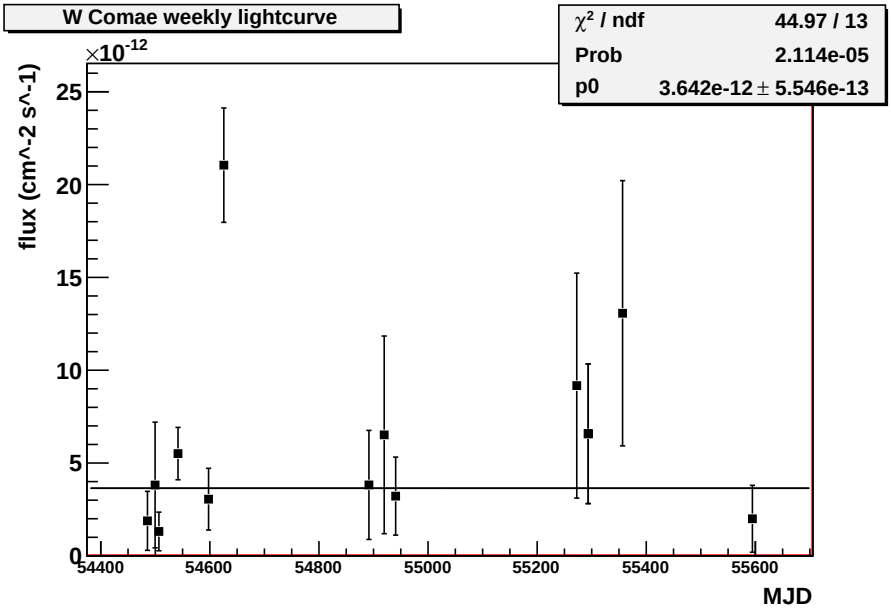

FIGURE 6.47. W Comae TeV lightcurve in weekly intervals, between January 10^{th} 2008 and April 1^{st} 2011, demonstrates variability.

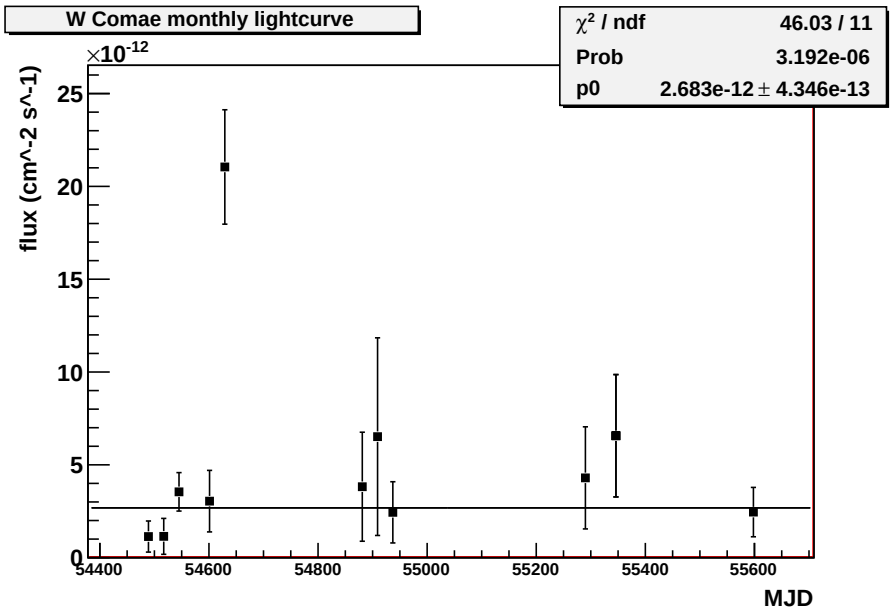

FIGURE 6.48. W Comae TeV lightcurve in monthly intervals, between January 10^{th} 2008 and April 1^{st} 2011, demonstrates variability.

6.6.2. Fermi analysis. WComae is detected with a flux (> 300 MeV) of $(2.64 \pm 0.08) \times 10^{-8}$ ph cm^{-2} s^{-1} and an dN/dE spectral index of -2.05 $\pm$ 0.02 at a TS of 1378.46, equivalent to a significance of $\sim 37\sigma$. Figures 6.49 and 6.50 show the background before the addition of other γ-ray sources in the ROI and after. There are no "unknown source" or TS bumps required in the model in order to generate a flat background. Table 6.8 give a list of the 24 month catalog sources, in addition to the Unbinned Maximum Likelihood analysis results for each source. There were no (> 100 GeV) photons were detected within 1° of the source location throughout the dataset.

The lightcurves (figures 6.51 , 6.52 and 6.53) clearly show variability on biweekly, monthly and three monthly timescales and at a higher flux in the last third of the dataset. The dataset is divided into ten equal bins for spectral analysis. The TS as a function of energy (figure 6.54) exhibits a high peak at ~ 1 GeV. The dN/dE spectrum is shown in figure 6.55.

The E^2 dNdE spectrum is best fit by a log parabolic curve demonstrating the the peak of the IC bump at ~ 4 GeV with a severe dip between 10 GeV (figure 6.56).

TABLE 6.8. W Comae Fermi LAT Gtlike Unbinned Maximum Likelihood results

Source	Index	Flux (ph cm^{-2} s^{-1})	TS	Npred	ROI Distance (°)
W Comae	-2.05 ± 0.02	$(2.64 \pm 0.08)\times10^{-8}$	1378.46	713.08	0.00
1FGL J1150.2+2419	-2.35 ± 0.05	$(6.49 \pm 0.55)\times10^{-9}$	122.21	160.75	8.02
1FGL J1159.4+2814	-2.38 ± 0.02	$(2.78 \pm 0.09)\times10^{-8}$	1161.68	715.45	4.93
1FGL J1217.7+3007	-1.99 ± 0.02	$(2.18 \pm 0.08)\times10^{-8}$	991.58	589.26	2.05
1FGL J1220.2+3432	-1.98 ± 0.08	$(1.71 \pm 0.20)\times10^{-9}$	32.84	45.26	6.34
1FGL J1221.3+3008	-1.69 ± 0.03	$(7.92 \pm 0.51)\times10^{-9}$	354.84	223.65	1.95
1FGL J1224.7+2121	-2.56 ± 0.03	$(1.93 \pm 0.08)\times10^{-8}$	582.62	483.84	6.90
1FGL J1226.0+2954	-2.16 ± 0.05	$(4.88 \pm 0.50)\times10^{-9}$	89.83	129.41	1.94
1FGL J1230.4+2520	-2.23 ± 0.05	$(5.25 \pm 0.48)\times10^{-9}$	98.90	139.09	3.51
1FGL J1231.6+2850	-1.96 ± 0.03	$(1.08 \pm 0.06)\times10^{-8}$	437.66	294.88	2.32
1FGL J1243.1+3627	-1.81 ± 0.03	$(6.16 \pm 0.45)\times10^{-9}$	274.22	138.60	9.41
1FGL J1254.4+2209	-2.12 ± 0.07	$(2.85 \pm 0.04)\times10^{-9}$	42.35	55.50	9.61
1FGL J1303.0+2433	-2.21 ± 0.03	$(1.65 \pm 1.00)\times10^{-9}$	322.46	214.94	9.98
1FGL J1310.6+3222	-1.78 ± 0.25	$(7.46 \pm 1.94)\times10^{-8}$	25.12	110.86	11.39
24M1505	-1.91 ± 0.06	$(2.18 \pm 0.32)\times10^{-9}$	51.39	60.09	3.69

AS = Additional Source

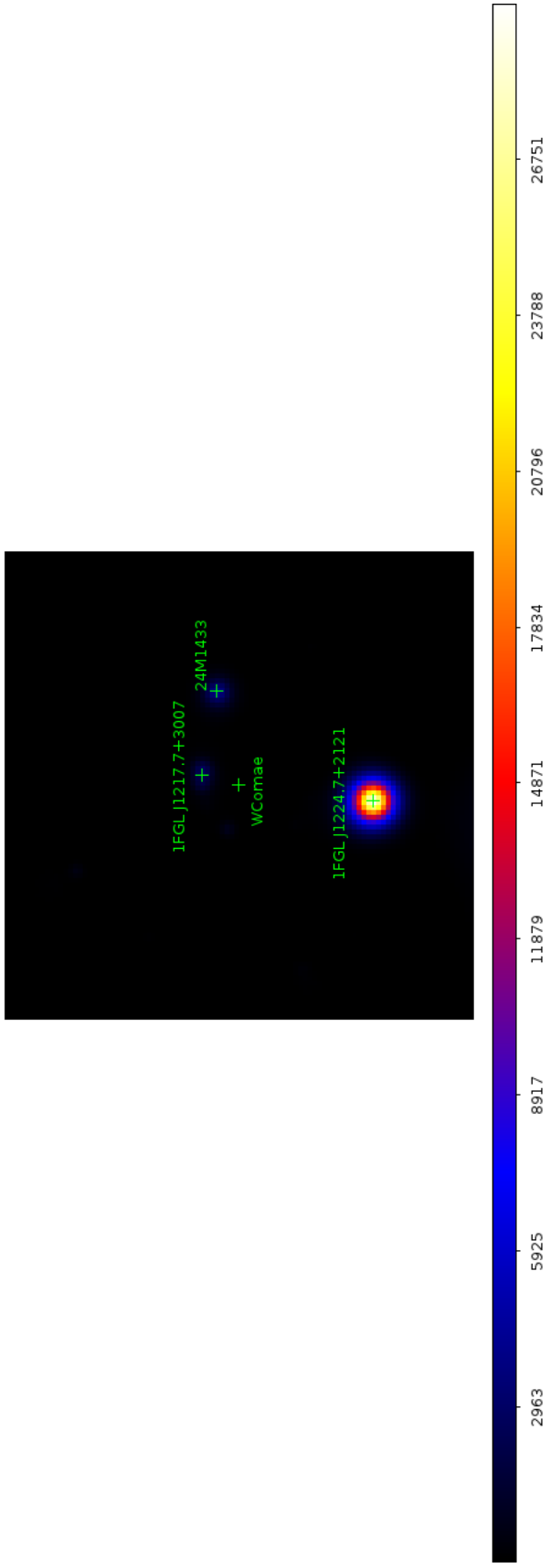

FIGURE 6.49. Fermi LAT, W Comae 12° TS map before background sources in the ROI are subtracted, highlighting 2 high TS sources in the ROI.

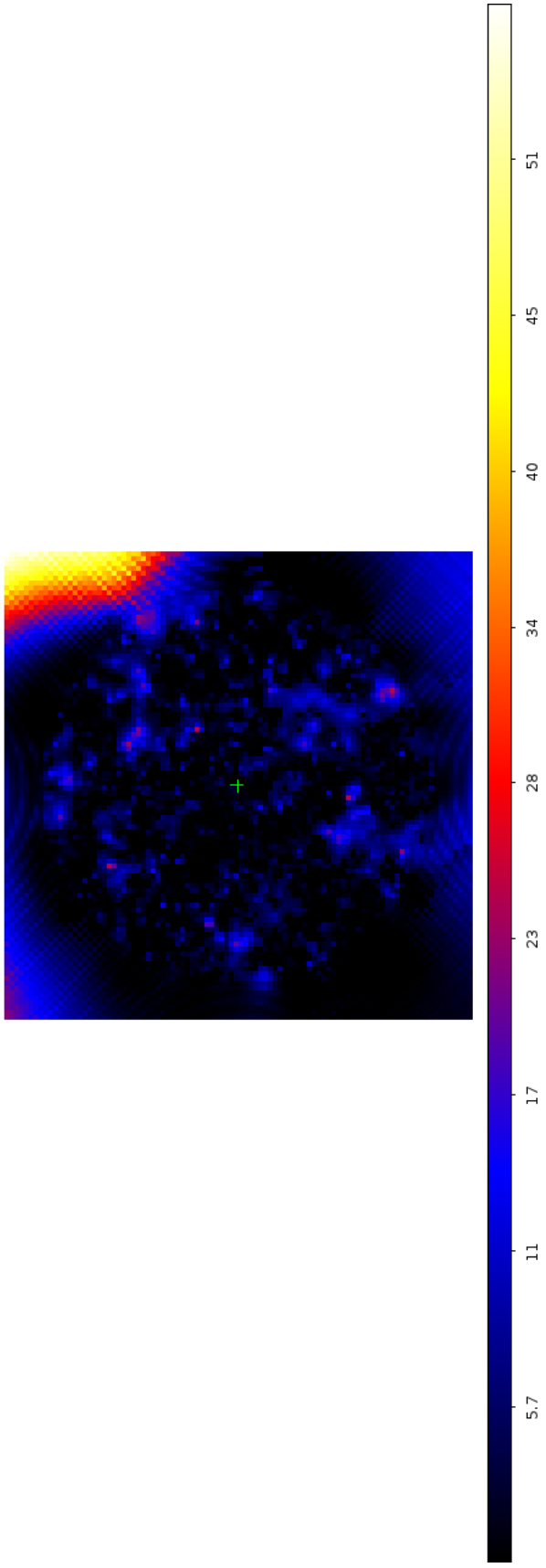

FIGURE 6.50. Fermi LAT, W Comae 12° TS map after background subtraction. Note the different TS scale. A lower TS scale is required to ensure the lower TS sources in the ROI are seen clearly.

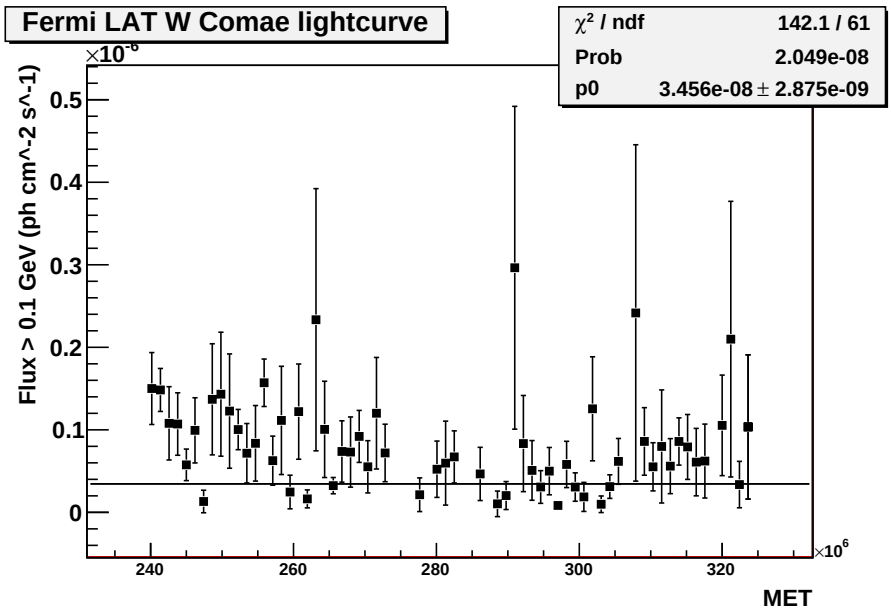

FIGURE 6.51. W Comae Fermi LAT 2 week-interval lightcurve, showing variability. VERITAS observations are contemporaneous throughout the entire dataset.

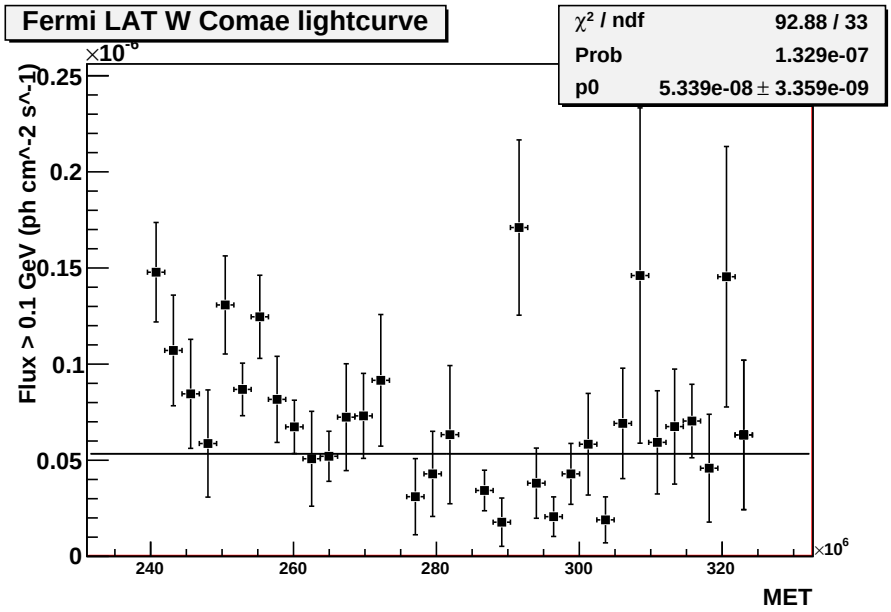

FIGURE 6.52. W Comae Fermi LAT monthly lightcurve showing variability detected. VERITAS observations are contemporaneous throughout the entire dataset.

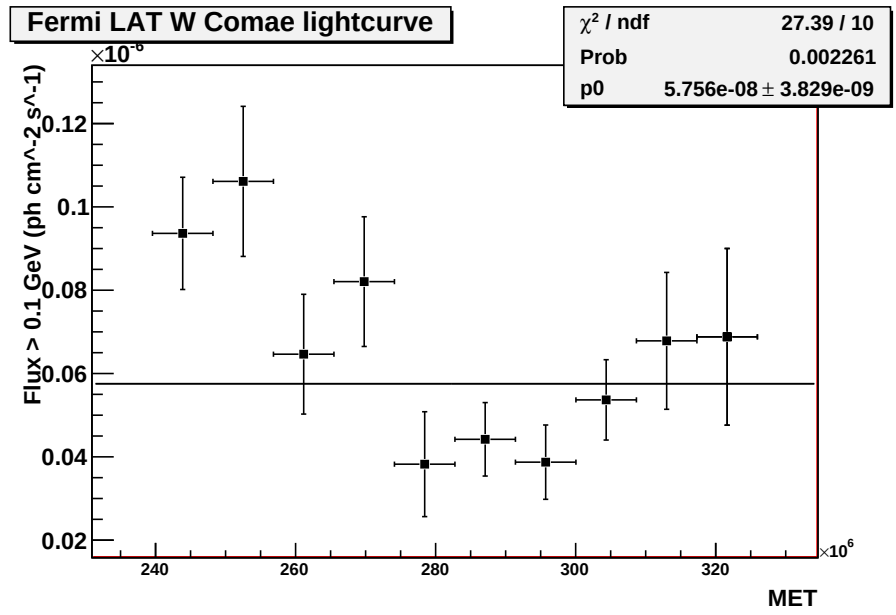

FIGURE 6.53. W Comae Fermi LAT 3 month-long interval lightcurve showing no variability. VERITAS observations are contemporaneous throughout the entire dataset.

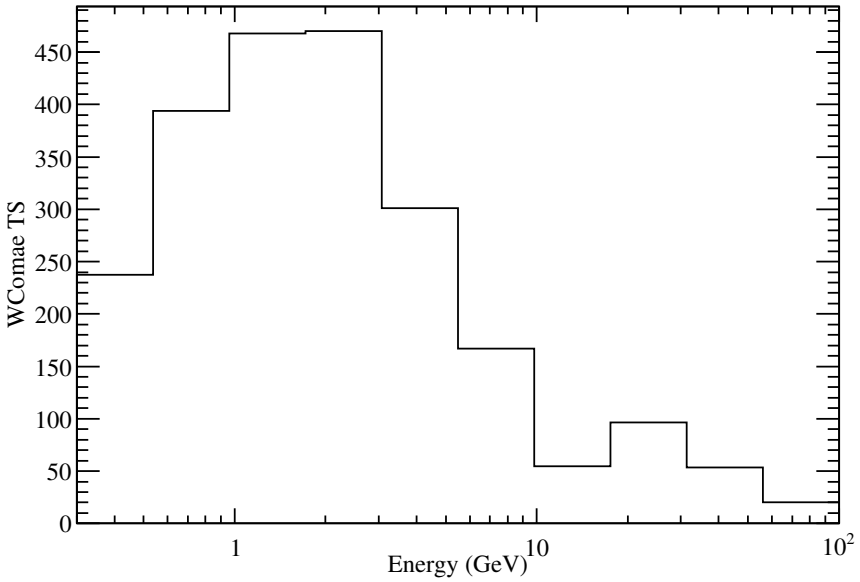

FIGURE 6.54. W Comae Fermi LAT TS as a function of energy in 10 bins.

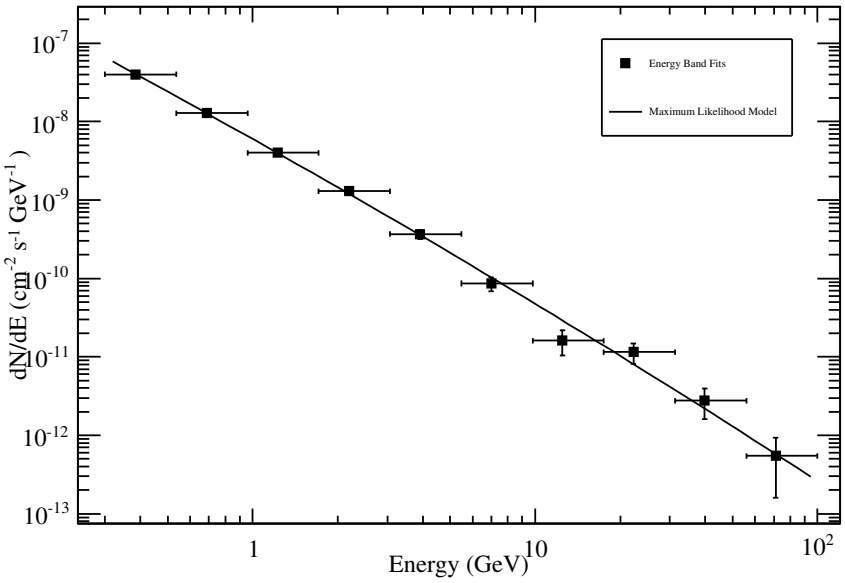

FIGURE 6.55. W Comae Fermi LAT dN/dE spectrum in 10 bins.

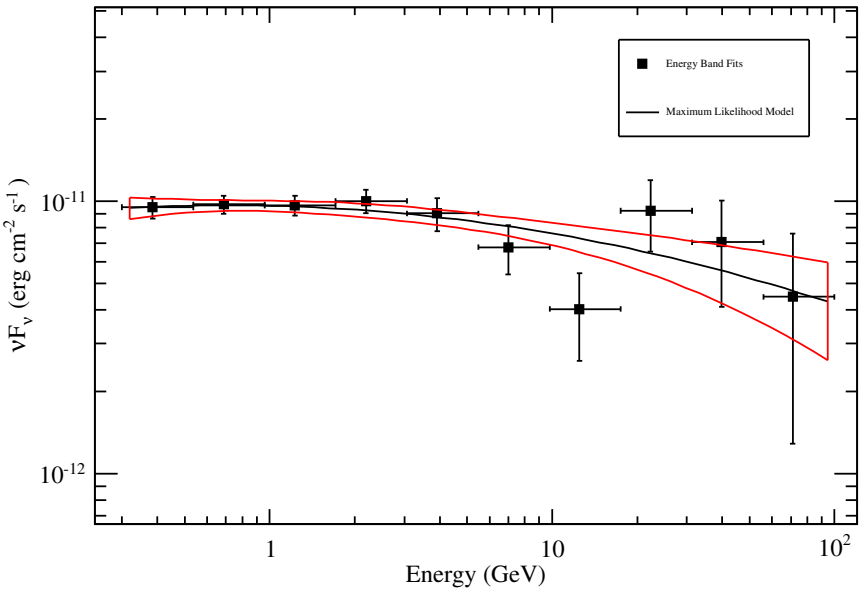

FIGURE 6.56. W Comae Fermi LAT E ^{2} dN/dE spectrum in 10 bins, fit best by a log parabolic curve.

6.7. 3C66A

3C66A is an IBL detected by both VERITAS and Fermi LAT as described below.

6.7.1. VERITAS. The soft TeV spectrum IBL 3C66A was observed between September 13^{th} 2007 and January 8^{th} 2010 with the total livetime of the dataset calculated to be $\sim$ 46 hours. A wobble analysis (table 6.9) yielded a γ-ray event rate of 0.82 $\pm$ 0.04 γ's min^{-1} resulting in a detection of $\sim$ 19.59 sigma. The detection is clearly evident in the θ^2 plot and 2D significance map as shown in figures 6.57 and 6.58.

The spectrum is fit, χ^2/n.d.f = 0.0008/1, by a powerlaw of $(1.12 \pm 0.43)\times10^{-8}$ $\left(\frac{E}{1TeV}\right)^{-4.39\pm0.30}$ with an integral flux (E > 1 TeV) of $(2.32 \pm 0.16)\times10^{-8}$ m^{-2}s^{-1} (figure 6.62). Due to sparse observations, it is difficult to discern variability in the day, week and month lightcuves (figures 6.59, 6.60 and 6.61)

TABLE 6.9. VERITAS Wobble 3C66A results

	2007-2008	2008-2009	2010-2011	total
Total On Events	1.42×10^3	8.11×10^3	3.24×10^3	1.28×10^4
Total Off Events	7.65×10^3	3.78×10^4	1.77×10^4	6.31×10^4
Total Exposure Time (min)	3.50×10^2	1.85×10^3	5.65×10^2	2.76×10^3
Significance (σ)	4.05	20.12	4.72	19.59
γ-ray Rate (γ's min^{-1})	0.45 $\pm$ 0.11	0.98 $\pm$ 0.05	0.50 $\pm$ 0.11	0.82 $\pm$ 0.04
Background Rate (γ's min^{-1})	3.59	3.41	5.23	3.81

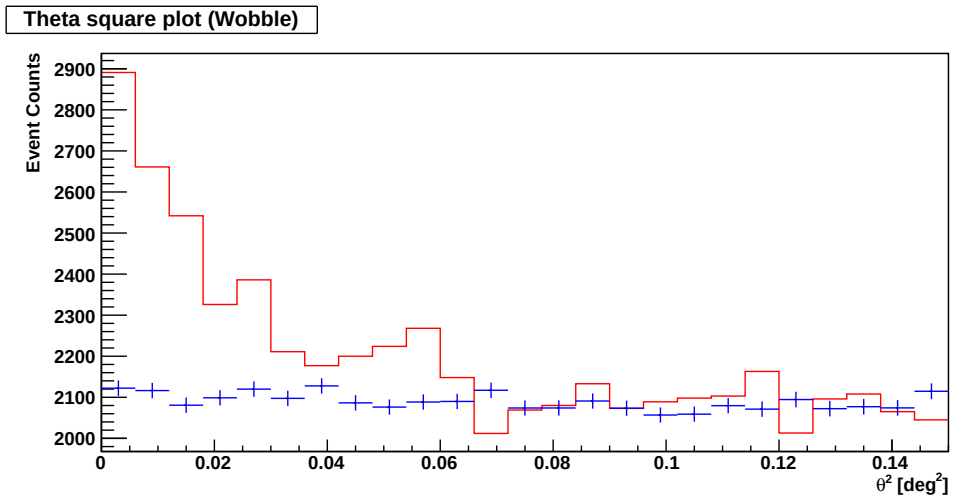

FIGURE 6.57. 3C66A VERITAS θ^2 plot (red = source, blue = background).

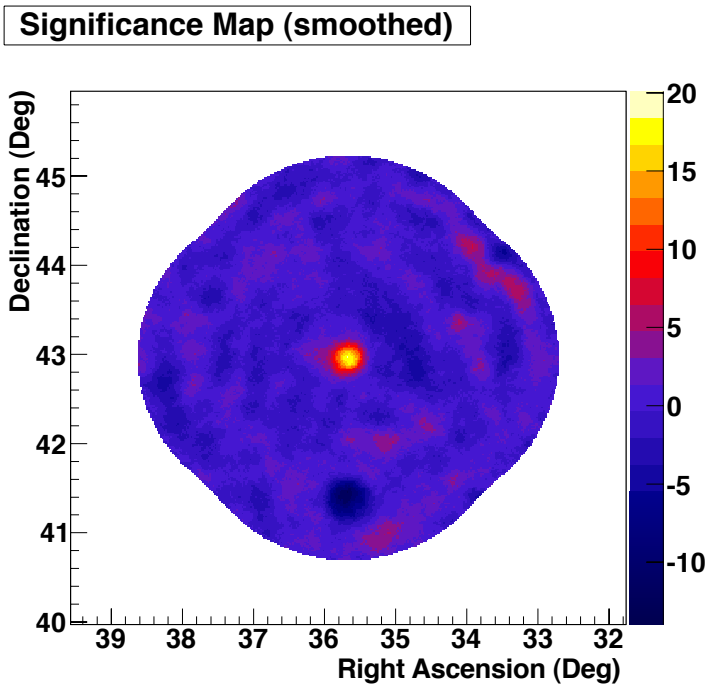

FIGURE 6.58. 3C66A VERITAS 2D significance map.

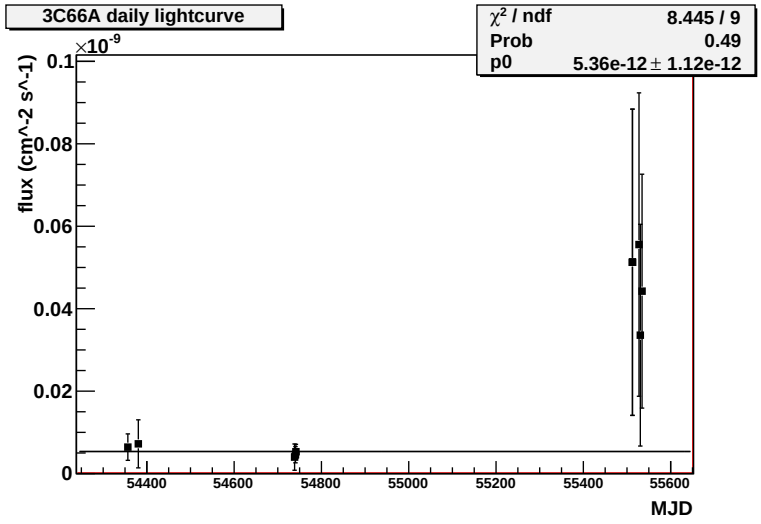

FIGURE 6.59. 3C66A TeV lightcurve binned in daily intervals timescales, does not suggest variability.

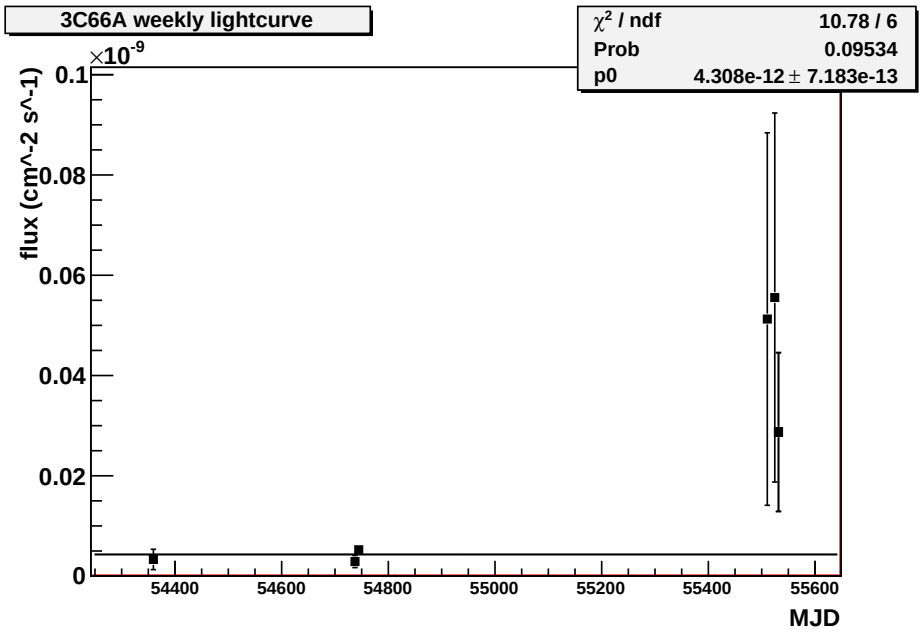

FIGURE 6.60. 3C66A TeV lightcurve binned in weekly timescales, does not suggest variability.

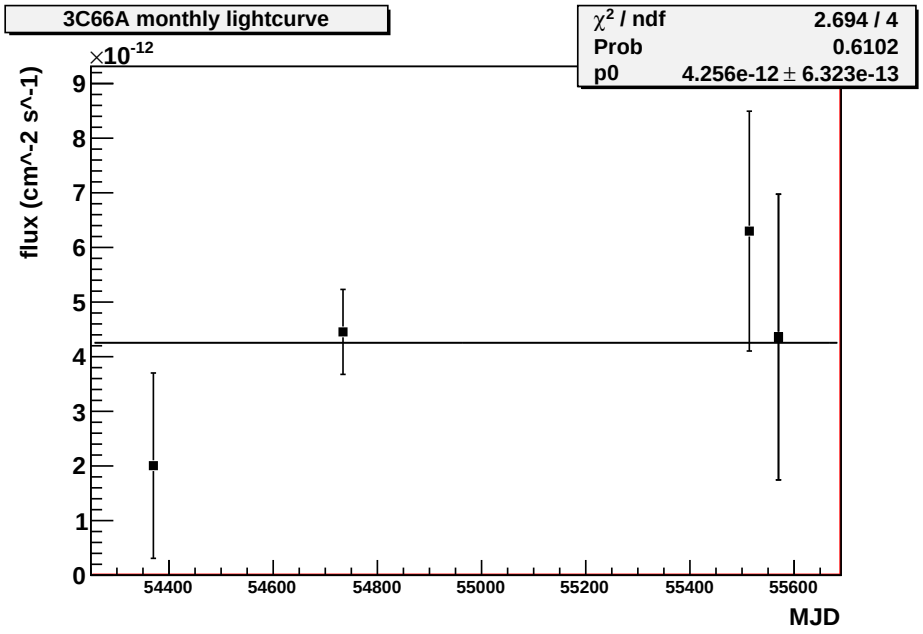

FIGURE 6.61. 3C66A TeV lightcurve binned in monthly timescales, does not suggest variability.

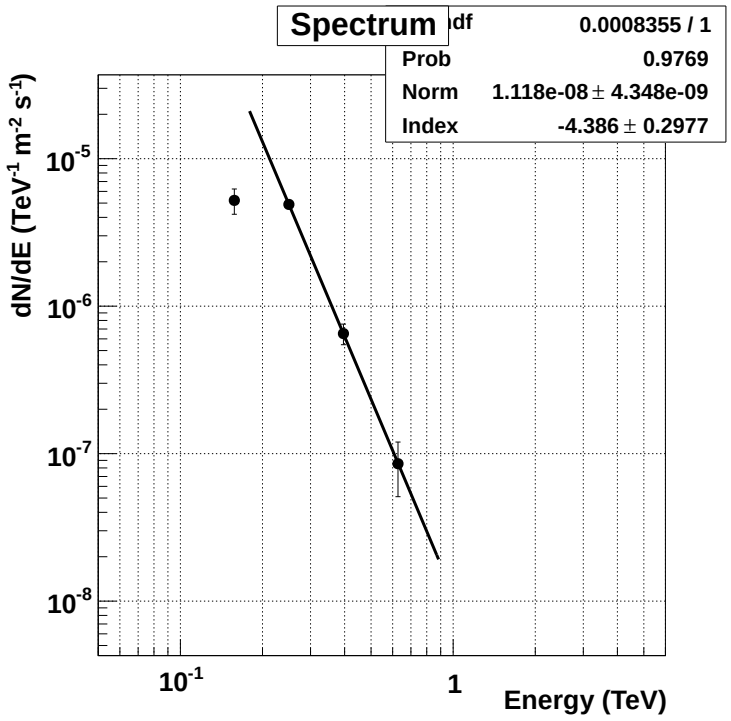

FIGURE 6.62. 3C66A TeV dN/dE spectrum fit by a powerlaw.

6.7.2. Fermi analysis. 3C66A is detected with a flux (> 300 MeV) of $(7.69 \pm 0.14) \times 10^{-8}$ ph cm^{-2} s^{-1} and an index of -1.95 $\pm$ 0.01 at a TS of 14382.8, equivalent to a significance of $\sim 120\ \sigma$. Figures 6.63 and 6.64 show the background before the addition of other γ-ray sources in the ROI and after. There were 18 "unknown source" or TS bumps required in the model in order to generate a flat background. Table 6.10 give a list of the 24 month catalog sources, in addition to the Unbinned Maximum Likelihood analysis results for each source. There were seven (> 100 GeV) photons detected within 1° of the source location throughout the dataset; 260 GeV, 167 GeV, 130 GeV, 123 GeV, 123 GeV, 123 GeV, 111 GeV and 106 GeV.

Apart from a flare in October 2008, the lightcurves (figures 6.65 and 6.66) do not show significant variability in 2 week and monthly. This could be due to the large error bars on two of the data points. The dataset is divided into ten equal bins for spectral analysis. The TS as a function of energy (figure 6.67) exhibits a high peak at ~ 2 GeV. The dN/dE spectrum is shown in figure 6.68.

The E^2 dN/dE spectrum is best fitted by a log parabolic curve demonstrating the the peak of the IC bump at ~ 4 GeV (figure 6.69).

TABLE 6.10. 3C66A Fermi LAT Gtlike Unbinned Maximum Likelihood results

Source	Index	Flux (ph cm^{-2} s^{-1})	TS	Npred	ROI Distance
3C66A	-1.95 ± 0.01	$(7.69 \pm 0.14)\times10^{-8}$	14382.8	5690.1	0.00
1FGL J0128.6+4439	-2.45 ± 0.12	$(4.91 \pm 0.73)\times10^{-9}$	90.93	196.12	9.86
1FGL J0136.5+3905	-1.77 ± 0.03	$(1.34 \pm 0.07)\times10^{-8}$	1950.44	785.08	9.54
1FGL J0137.0+4751	-2.38 ± 0.03	$(3.13 \pm 0.10)\times10^{-8}$	2392.48	1775.38	9.34
1FGL J0155.0+4433	-2.37 ± 0.10	$(4.64 \pm 0.59)\times10^{-9}$	133.30	325.49	5.21
1FGL J0208.6+3522	-2.11 ± 0.12	$(2.53 \pm 0.49)\times10^{-9}$	78.11	169.59	9.11
1FGL J0221.0+3555	-2.28 ± 0.03	$(2.39 \pm 0.10)\times10^{-8}$	2054.55	1626.84	7.10
1FGL J0226.0+3922	-2.90 ± 0.15	$(5.07 \pm 0.64)\times10^{-9}$	92.91	336.23	3.67
1FGL J0230.8+4031	-2.67 ± 0.07	$(9.55 \pm 0.72)\times10^{-9}$	324.47	648.54	2.88
1FGL J0248.7+5127	-1.97 ± 0.10	$(3.60 \pm 0.69)\times10^{-9}$	98.62	204.64	9.55
1FGL J0254.2+5107	-2.34 ± 0.10	$(6.88 \pm 0.97)\times10^{-9}$	109.69	343.48	9.64
1FGL J0303.1+4711	-2.24 ± 0.05	$(1.05 \pm 0.08)\times10^{-9}$	419.04	706.80	8.33
1FGL J0307.5+4916	-1.71 ± 0.10	$(3.01 \pm 0.66)\times10^{-9}$	112.35	124.88	9.93
24M0202	-2.62 ± 0.09	$(6.89 \pm 0.61)\times10^{-9}$	224.65	460.97	6.23
24M0248	-2.50 ± 0.10	$(6.86 \pm 1.02)\times10^{-9}$	165.22	460.46	6.38
24M0282	-2.02 ± 0.10	$(5.03 \pm 0.85)\times10^{-9}$	84.59	198.20	9.94
24M0356	-2.57 ± 0..09	$(2.04 \pm 0.18)\times10^{-9}$	247.67	550.31	10.14
PSR J0218+4232	-2.38 ± 0.04	$(2.52 \pm 0.11)\times10^{-8}$	100.75	307.48	3.77
AS1	-2.48 ± 0.11	$(4.43 \pm 0.58)\times10^{-9}$	100.75	307.48	3.77
AS2	-2.71 ± 0.16	$(3.31 \pm 0.58)\times10^{-9}$	48.09	217.66	6.55
AS3	-2.73 ± 0.18	$(3.10 \pm 0.61)\times10^{-9}$	42.16	180.69	8.84
AS4	-2.48 ± 0.16	$(2.54 \pm 0.51)\times10^{-9}$	43.77	172.72	6.66
AS5	-2.29 ± 0.16	$(2.25 \pm 0.52)\times10^{-9}$	47.70	155.45	5.74
AS6	-2.58 ± 0.17	$(3.29 \pm 0.61)\times10^{-9}$	51.18	228.68	2.81
AS7	-2.61 ± 0.14	$(3.64 \pm 0.57)\times10^{-9}$	71.57	231.15	8.15
AS8	-3.13 ± 0.21	$(3.49 \pm 0.60)\times10^{-9}$	44.07	226.05	4.67
AS9	-2.80 ± 0.20	$(3.51 \pm 0.74)\times10^{-9}$	32.88	207.27	8.73
AS10	-2.73 ± 0.18	$(2.99 \pm 0.58)\times10^{-9}$	37.80	166.75	9.06
AS11	-2.82 ± 0.22	$(2.31 \pm 0.56)\times10^{-9}$	27.15	134.25	8.86
AS12	-2.67 ± 0.21	$(3.07 \pm 0.75)\times10^{-9}$	32.75	184.61	8.70
AS13	-2.43 ± 0.18	$(2.02 \pm 0.50)\times10^{-9}$	34.02	134.10	7.45
AS14	-2.80 ± 0.16	$(3.89 \pm 0.61)\times10^{-9}$	56.03	233.31	8.71
AS15	-3.09 ± 0.22	$(3.33 \pm 0.68)\times10^{-9}$	33.00	190.71	8.70
AS16	-3.25 ± 0.22	$(3.56 \pm 0.64)\times10^{-9}$	43.61	222.92	6.91
AS17	-2.87 ± 0.21	$(2.79 \pm 0.56)\times10^{-9}$	32.55	182.10	6.15
AS18	-4.18 ± 0.45	$(3.17 \pm 0.67)\times10^{-9}$	25.58	197.66	4.07

AS = Additional Source

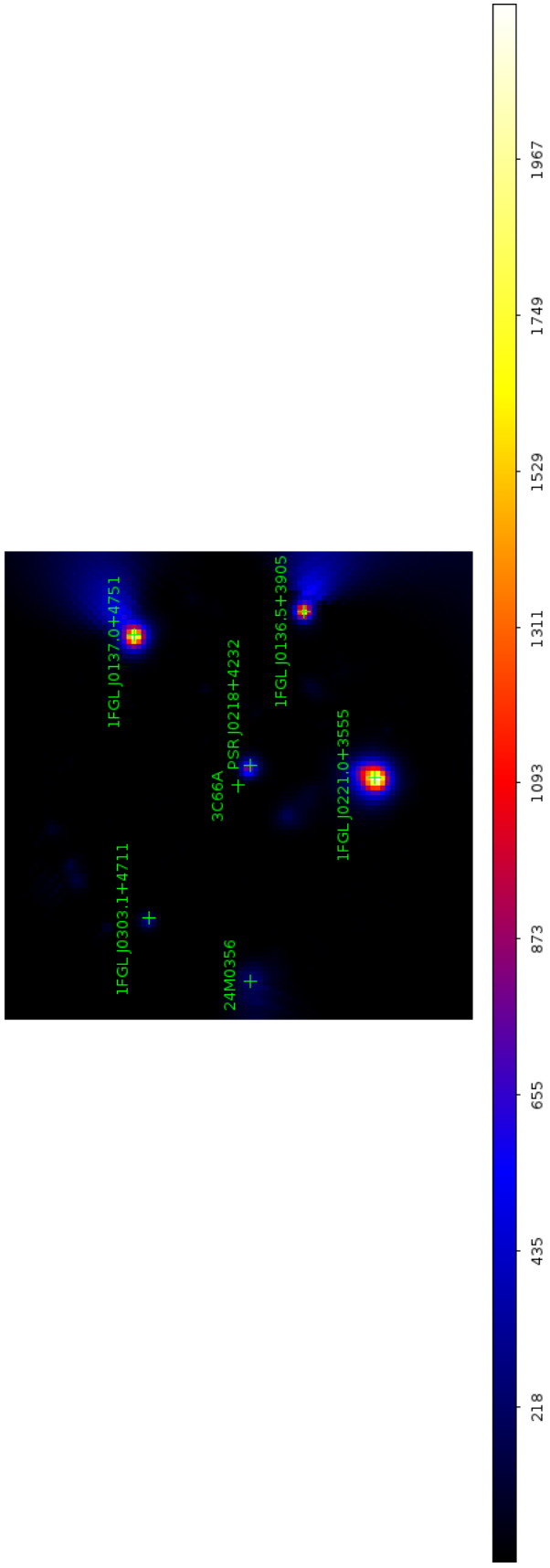

FIGURE 6.63. 3C66A Fermi LAT 12° TS map before background sources in ROI are subtracted, highlighting 6 high TS source in the ROI.

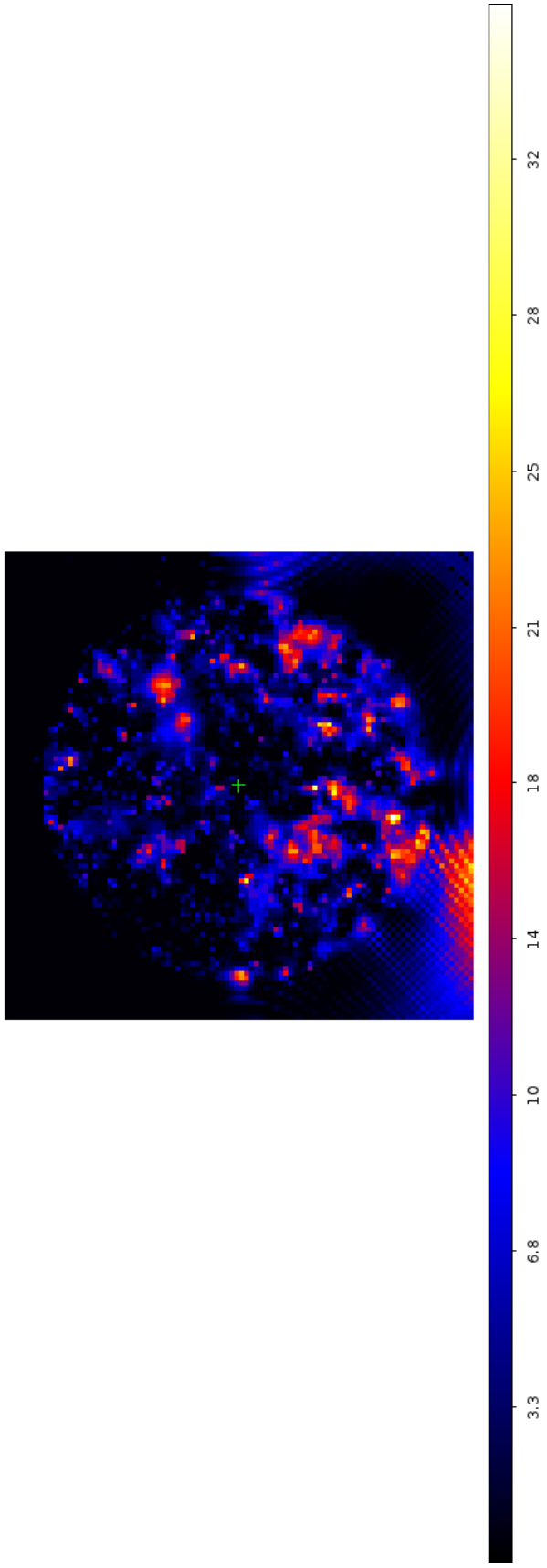

FIGURE 6.64. 3C66A Fermi LAT 12° TS map after background subtraction. Note the different TS scale. A lower TS scale is required to ensure the lower TS sources in the ROI are seen clearly.

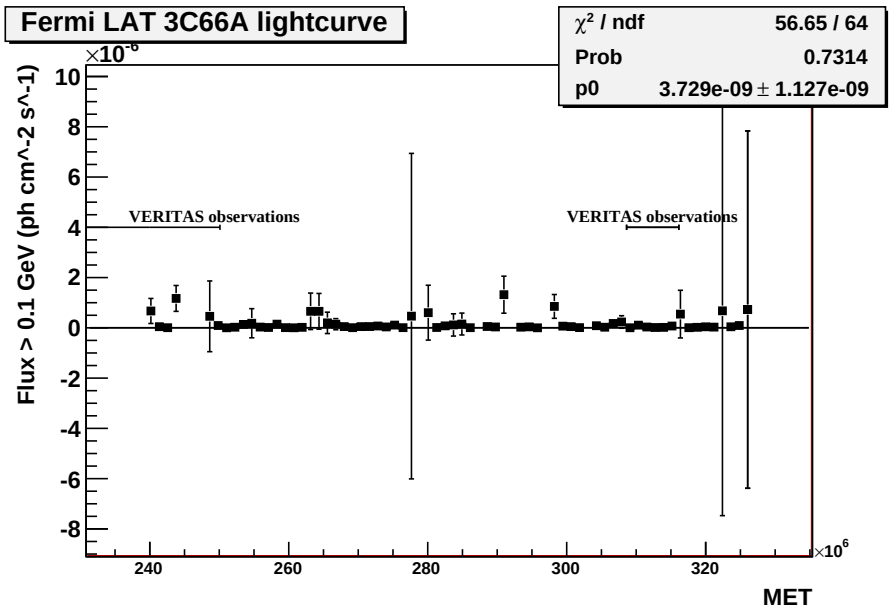

FIGURE 6.65. 3C66A Fermi LAT 2week-long lightcurve. Apart from a flare in October 2008 there is no significant variability observed. Due to the error bars on 3 of the points the majority of the points appear to be zero, this is not the case. Note the contemporaneous VERITAS observations.

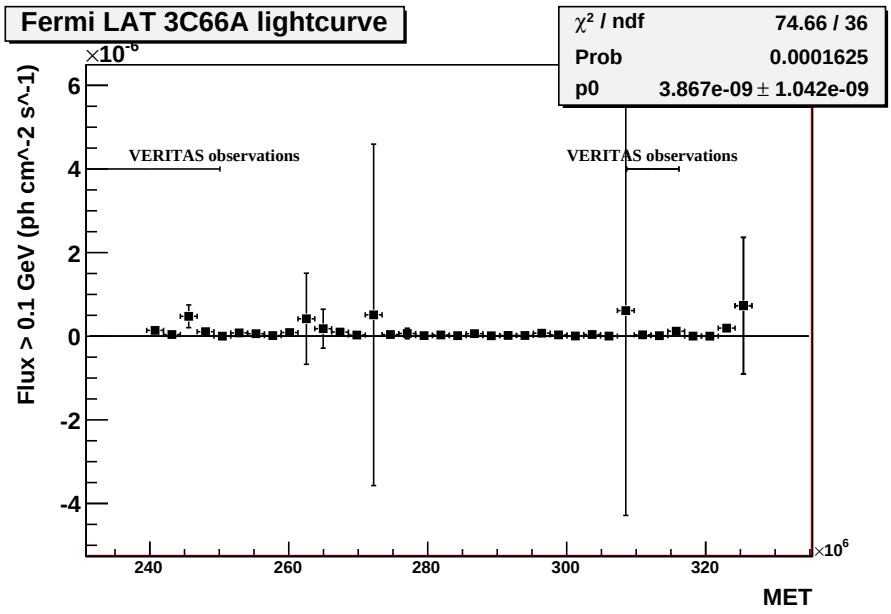

FIGURE 6.66. 3C66A Fermi LAT monthly Lightcurve. Apart from a flare in October 2008 there is no significant variability observed. Due to the error bars on 2 of the points the majority of the points appear to be zero, this is not the case. Note the contemporaneous VERITAS observations.

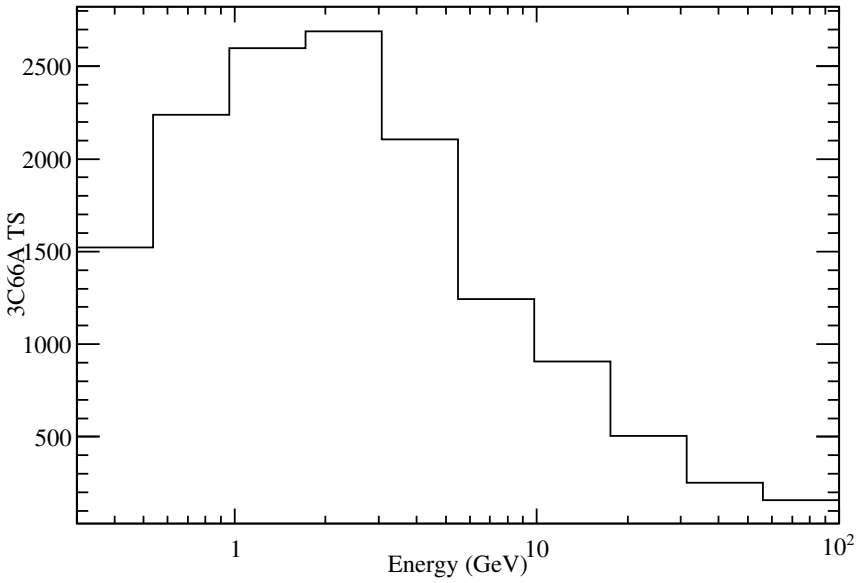

FIGURE 6.67. 3C66A Fermi LAT TS as a function of Energy in 10bins.

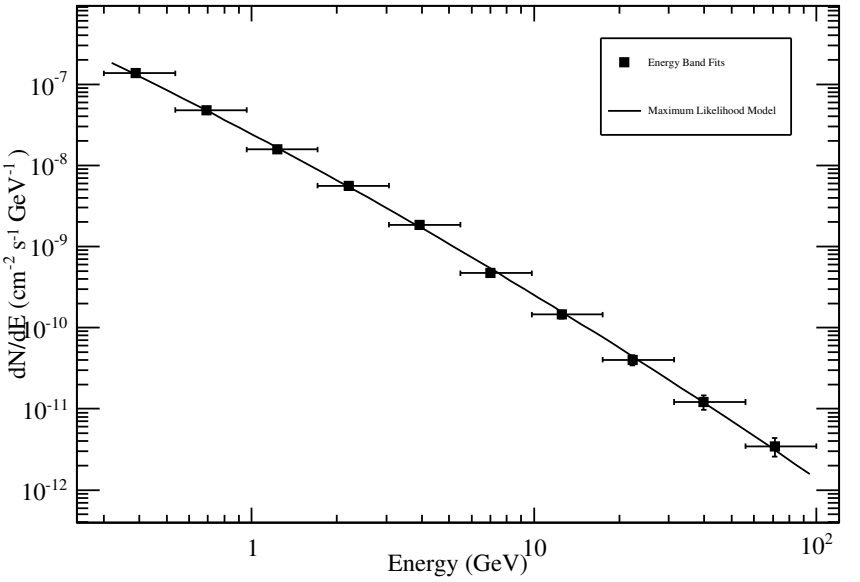

FIGURE 6.68. 3C66A Fermi LAT dN/dE spectrum in 10 bins.

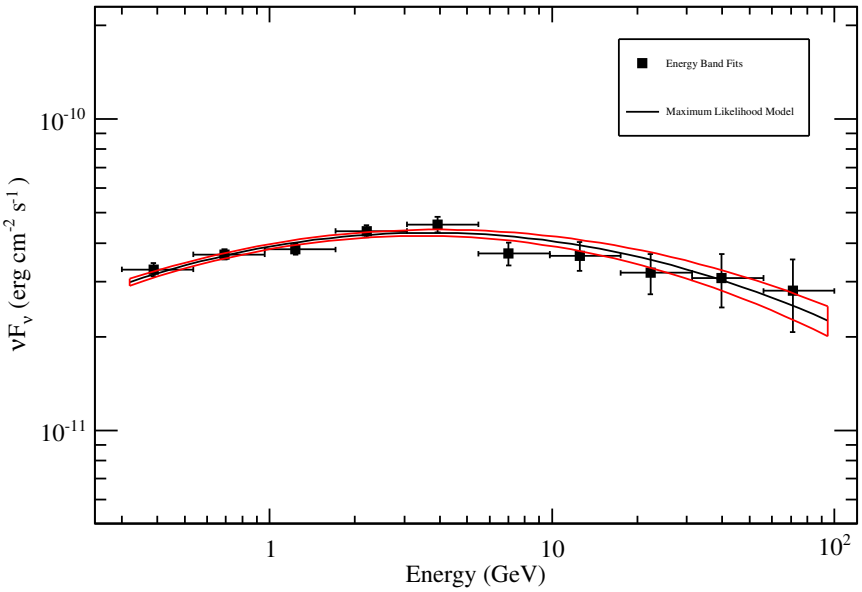

FIGURE 6.69. 3C66A Fermi LAT E^2 dN/dE spectrum in 10 bins fit best by a log parabolic function.

6.8. PKS 1424+240

PKS 1424+240 is an IBL detected by both VERITAS and Fermi LAT as described below.

6.8.1. VERITAS. The soft TeV spectrum IBL PKS1424+240 was observed between February 18^{th} 2009 and April 11^{th}2011 with the total livetime of the dataset calculated to be $\sim$ 28 hours. A wobble analysis (table 6.11) yielded a γ-ray event rate of 0.40 $\pm$ 0.05 γ's min^{-1} resulting in a detection of $\sim$ 7.79 σ. The detection is clearly evident in the θ^2 plot and 2D significance maps as shown in figures 6.70 and 6.71.

The spectrum is fit, χ^2/n.d.f = 6.227/1, by a powerlaw of $(7.14 \pm 5.55)\times10^{-9}$ $\left(\frac{E}{1TeV}\right)^{-3.104\pm0.4441}$ with an integral flux (E > 1 TeV) of $(1.45 \pm 0.19)\times10^{-8}$ m^{-2}s^{-1} (figure 6.72 for the TeV spectrum. Due to the limited amount of observations it is difficult to discern variability in the day, week and month timescale lightcurves (figure 6.73 and 6.74).

TABLE 6.11. VERITAS Wobble PKS 1424+240 results

	2008-2009	2010-2011	total
Total On Events	$4.21\times^{3}$	$2.46\times^{3}$	$6.67\times^{3}$
Total Off Events	$2.31\times^{4}$	$1.31\times^{4}$	$3.62\times^{4}$
Total Exposure Time (min)	$8.17\times^{2}$	$8.68\times^{2}$	$1.68\times^{3}$
Significance (σ)	5.74	5.33	7.79
γ-ray Rate (γ's min^{-1})	0.48 $\pm$ 0.09	0.32 $\pm$ 0.06	0.395 $\pm$ 0.052
Background Rate (γ's min^{-1})	4.68	2.51	3.56

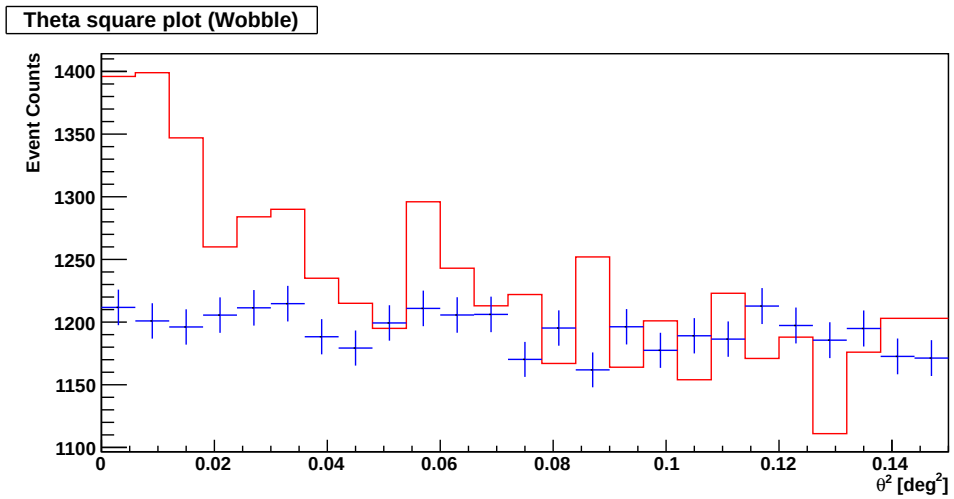

FIGURE 6.70. PKS1424+240 VERITAS θ^2 (red = source, blue = background).

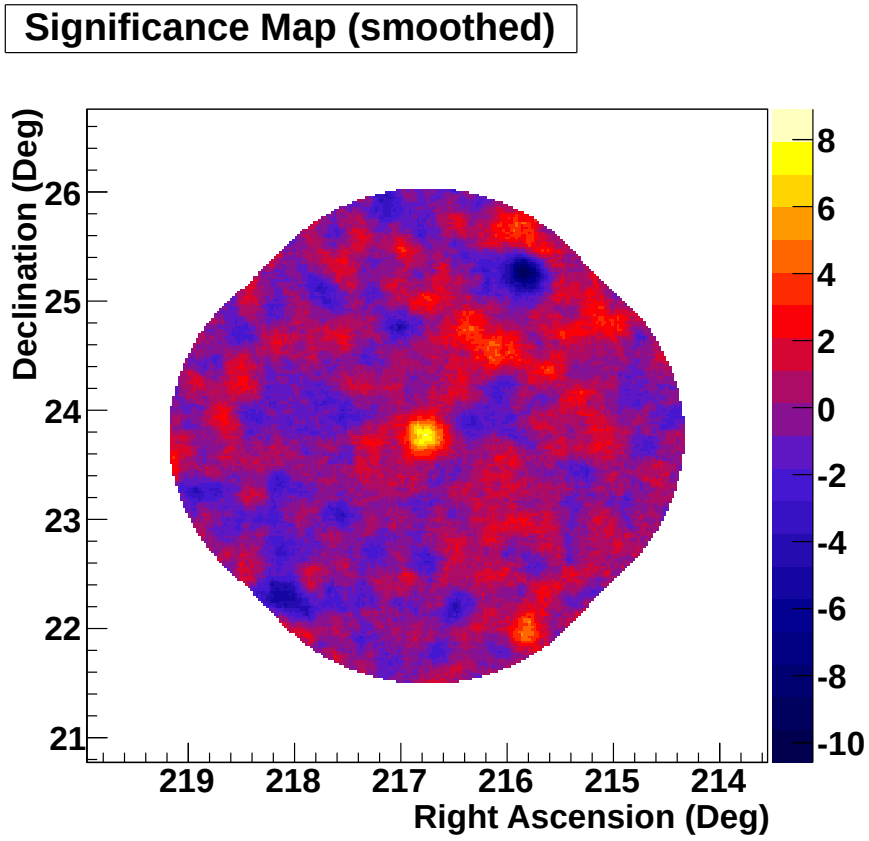

FIGURE 6.71. PKS 1424+240 VERITAS 2D significance map.

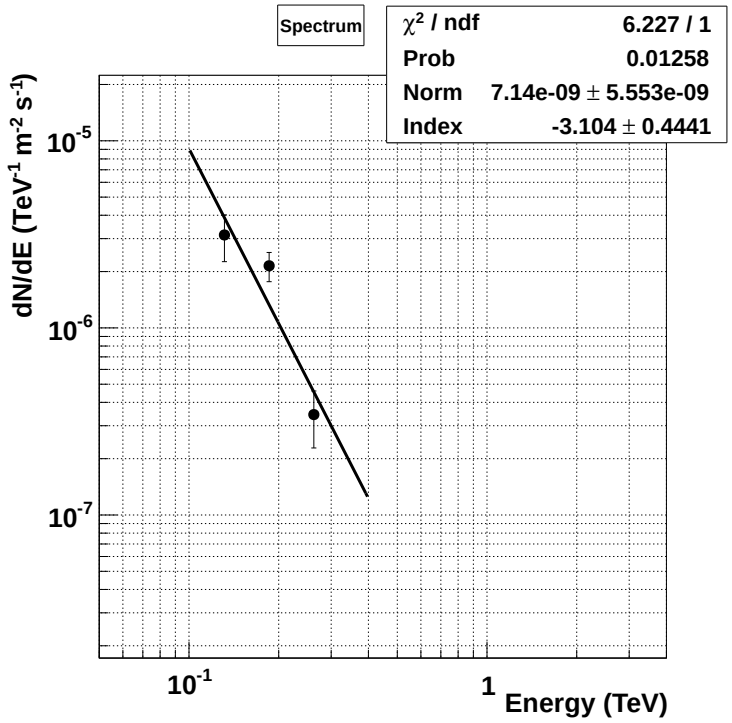

FIGURE 6.72. PKS 1424+240 TeV spectrum fit best by a powerlaw.

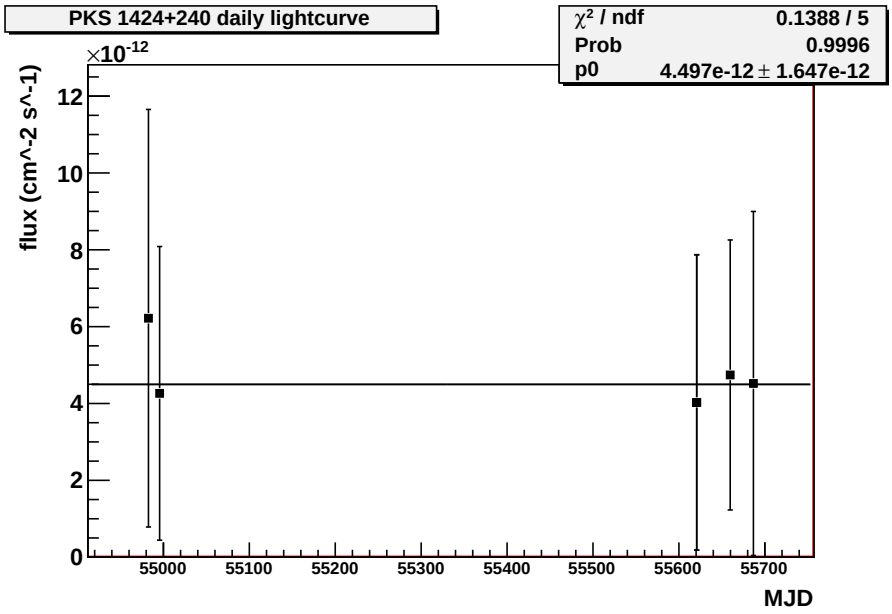

FIGURE 6.73. PKS 1424+240 TeV lightcurve in 1 day-long time bins. Due to the limited number of observations it is difficult to detect variability.

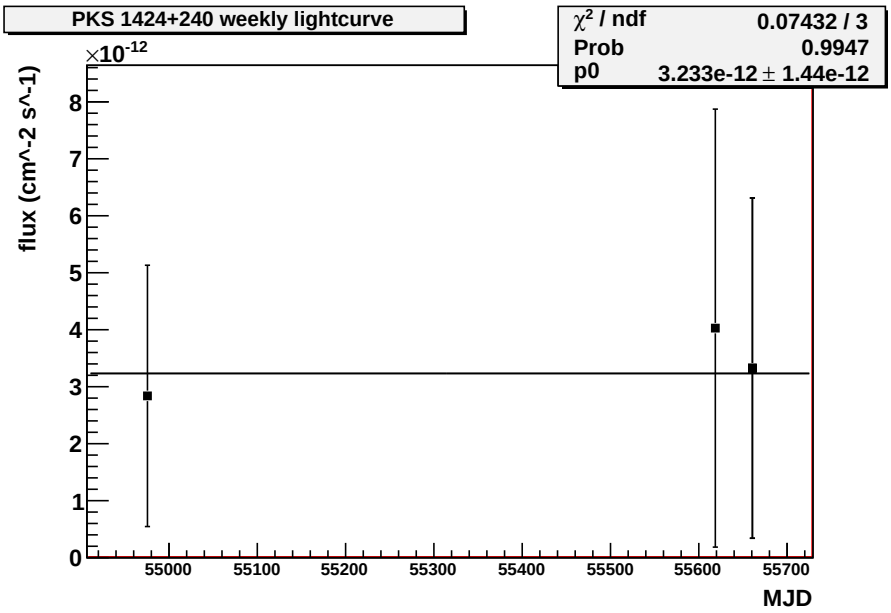

FIGURE 6.74. PKS 1424+240 TeV lightcurve in 1 week-long time bins. Due to the limited number of observations it is difficult to detect variability.

6.8.2. Fermi. PKS 1424+240 is detected with a flux (> 300 MeV) of $(3.41 \pm 0.10) \times 10^{-8}$ ph cm^{-2} s^{-1} and an index of -1.82 $\pm$ 0.02 at a TS of 6296.77, equivalent to a significance of $\sim 80\sigma$. Figures 6.75 and 6.76 show the background before the addition of other γ-ray sources in the ROI and after. There was one "unknown source" or TS bump required in the model in order to generate a flat background. Table 6.12 give a list of the 24 month catalog sources, in addition to the Unbinned Maximum Likelihood analysis results for each source. There were three (> 100 GeV) photons detected within 1° of the source location throughout the dataset: 148 GeV, 137 GeV and 117 GeV.

The lightcurves (see figures 6.77, 6.78 and 6.79) do not show significant variability in biweekly, monthly and 3 month timescales. The dataset is divided into ten equal bins for spectral analysis. The TS as a function of energy (figure 6.80) exhibits a high peak at ~ 20 GeV at < 1200 TS. The dN/dE spectrum is shown in figure 6.81.

The E^2 dN/dE spectrum is best fitted by a log parabolic law demonstrating the the peak of the IC bump at ~ 20 GeV (figure 6.82). This is higher than WComae and 3C66A, both spectra turning over at ~ 4 GeV.

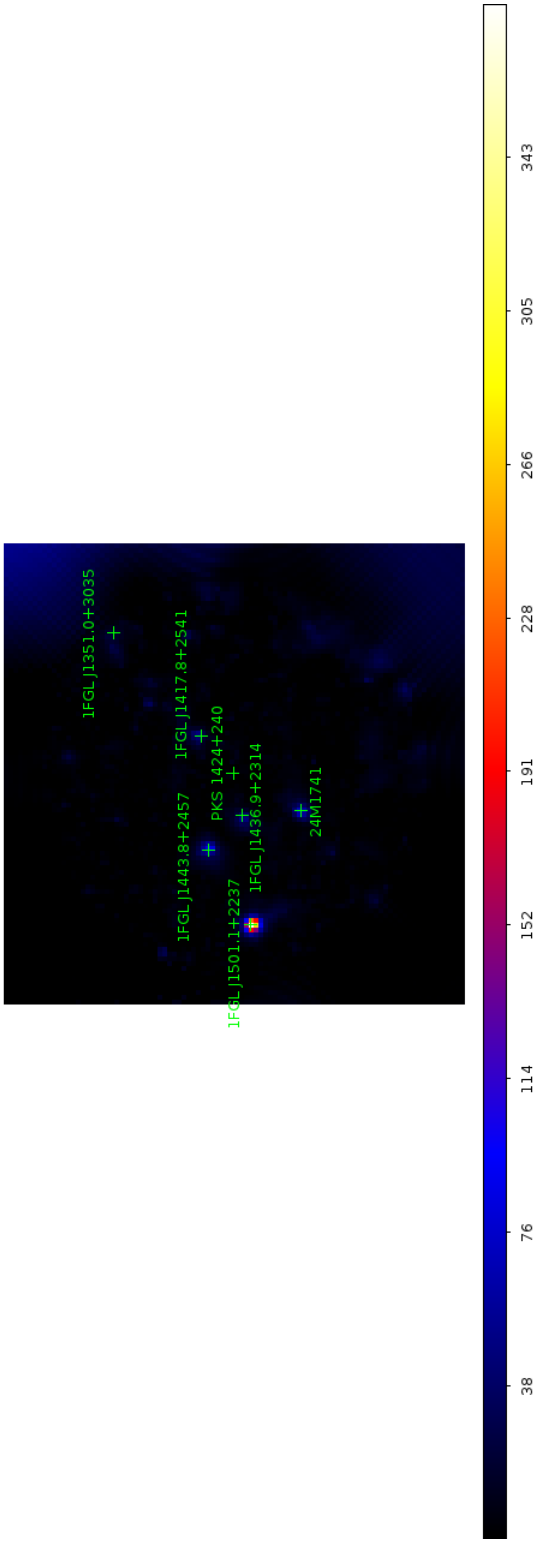

FIGURE 6.75. PKS 1424+140 Fermi LAT 12° TS map before sources in the ROI are background subtracted, highlighting 2 high TS sources in the ROI that need to be included in the background model

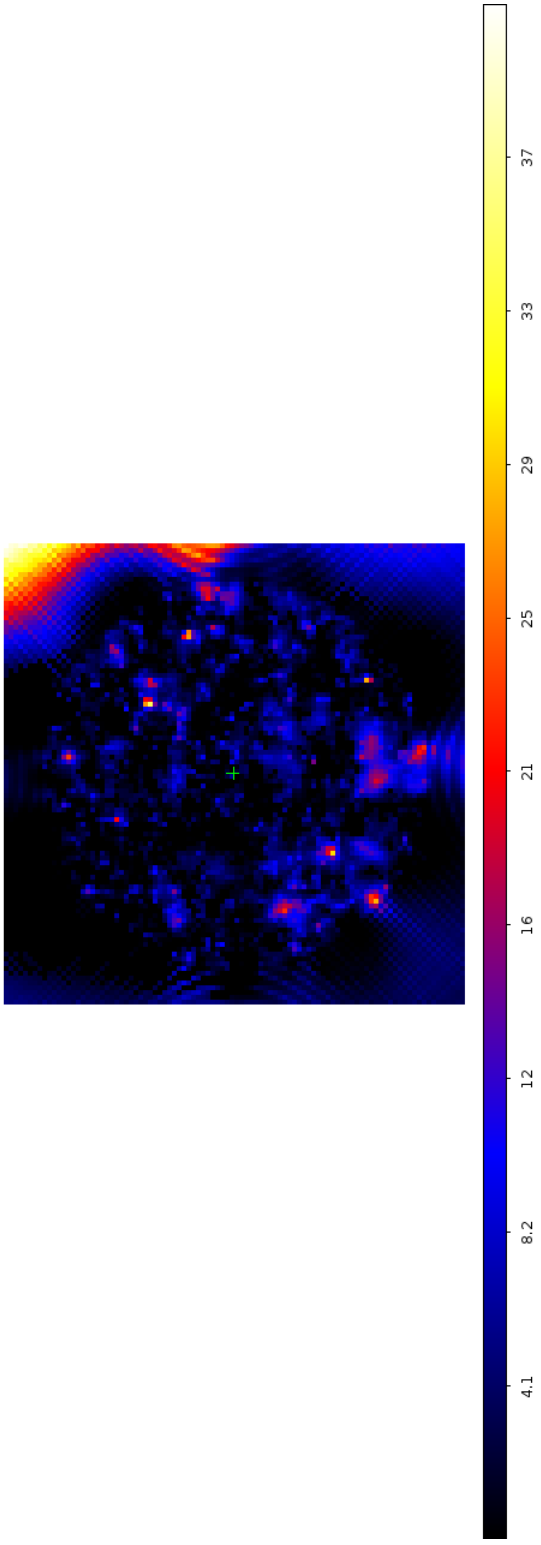

FIGURE 6.76. PKS1424+140 Fermi LAT 12° TS map after background subtraction. Note the different TS scale. A lower TS scale is required to ensure the lower TS sources in the ROI are seen clearly.

TABLE 6.12. PKS 1424+240 Fermi LAT Gtlike Unbinned Maximum Likelihood results

Source	Index	Flux (ph cm^{-2} s^{-1})	TS	Npred	ROI Distance (°)
PKS 1424+240	-1.82 ± 0.02	$(3.41 \pm 0.10)\times10^{-8}$	6296.77	2361.41	0
1FGL J1417.8+2541	-2.09 ± 0.17	$(1.91 \pm 0.47)\times10^{-9}$	54.35	127.81	
1FGL J1436.9+2314	-2.31 ± 0.18	$(2.73 \pm 0.60)\times10^{-9}$	60.15	177.53	2.32
1FGL J1443.8+2457	-2.13 ± 0.13	$(3.18 \pm 0.58)\times10^{-9}$	102.06	211.62	4.07
1FGL J1501.1+2237	-1.87 ± 0.07	$(5.42 \pm 0.60)\times10^{-9}$	425.56	356.27	7.94
24M1741	-2.27 ± 0.14	$(3.44 \pm 0.59)\times10^{-9}$	88.37	222.12	3.91
24M1802	-1.39 ± 0.25	$(6.29 \pm 3.05)\times10^{-10}$	42.59	23.95	9.96
AS1	-3.16 ± 0.36	$(2.96 \pm 0.65)\times10^{-9}$	29.22	160.57	8.34

AS = Additional Source

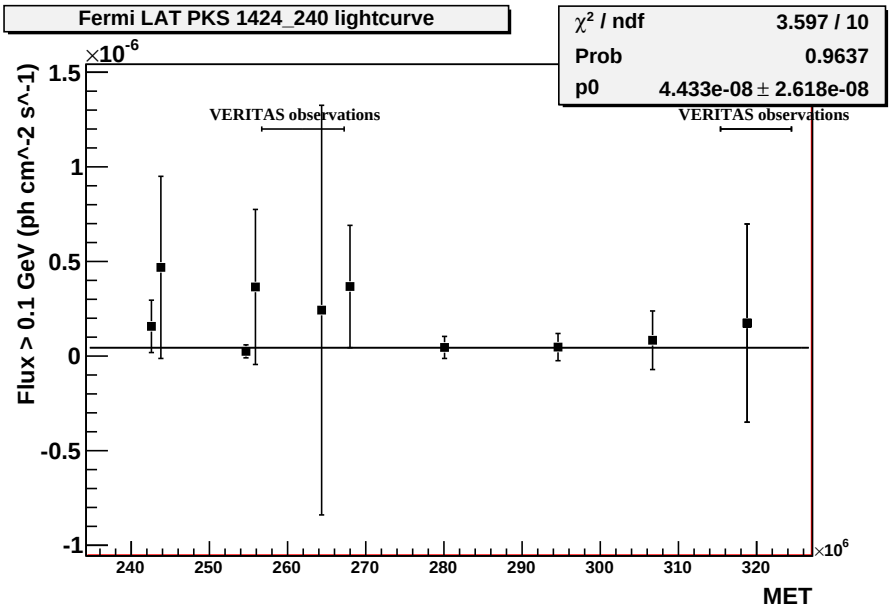

FIGURE 6.77. PKS1424+240 Fermi LAT lightcurve in 2 week bins, showing little variability. Note the contemporaneous VERITAS observations.

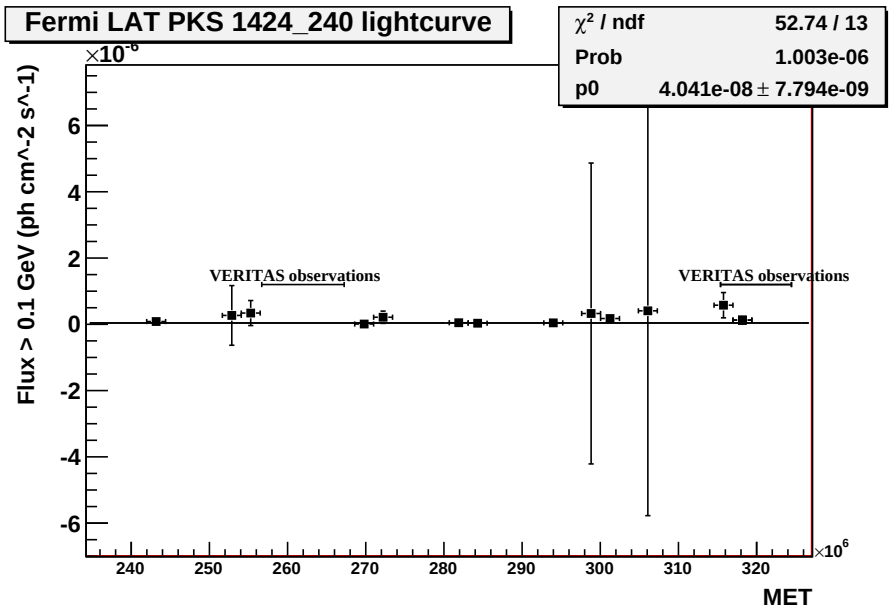

FIGURE 6.78. PKS1424+240 Fermi LAT monthly lightcurve, showing variability. Note the contemporaneous VERITAS observations.

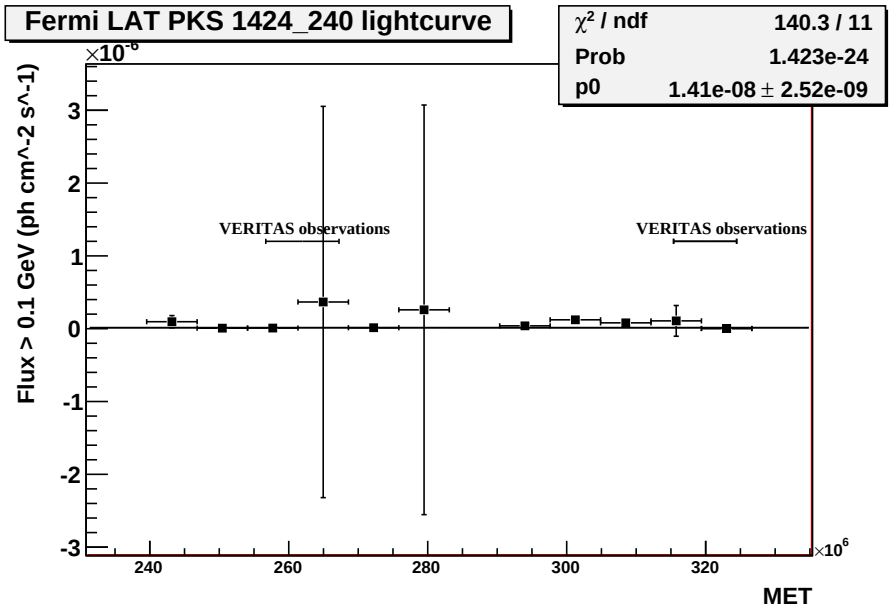

FIGURE 6.79. PKS1424+240 Fermi LAT lightcurve in 3 month-long time intervals, demonstrating extreme variability. Note the contemporaneous VERITAS observations.

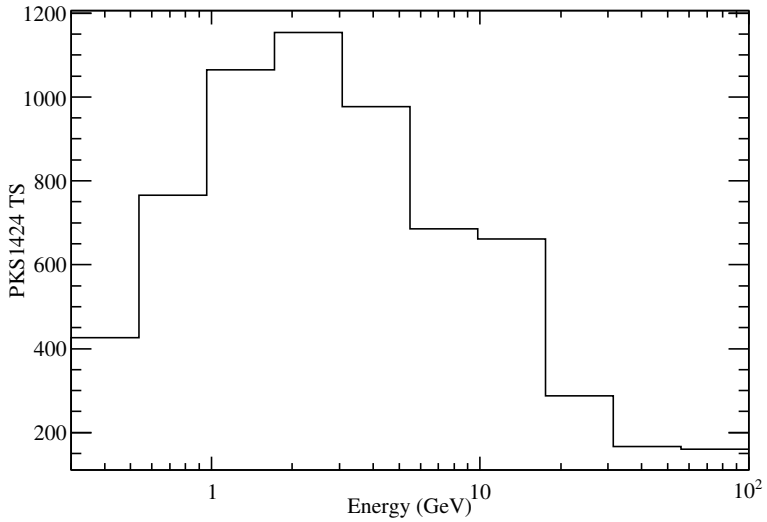

FIGURE 6.80. PKS 1424+240 Fermi LAT TS as a function of energy in 10 bins

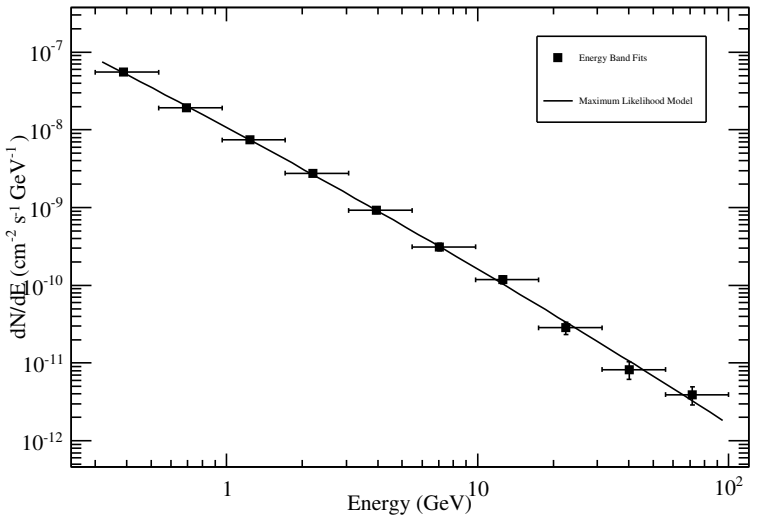

FIGURE 6.81. PKS 1424+240 Fermi LAT dN/dE spectrum in 10 bins.

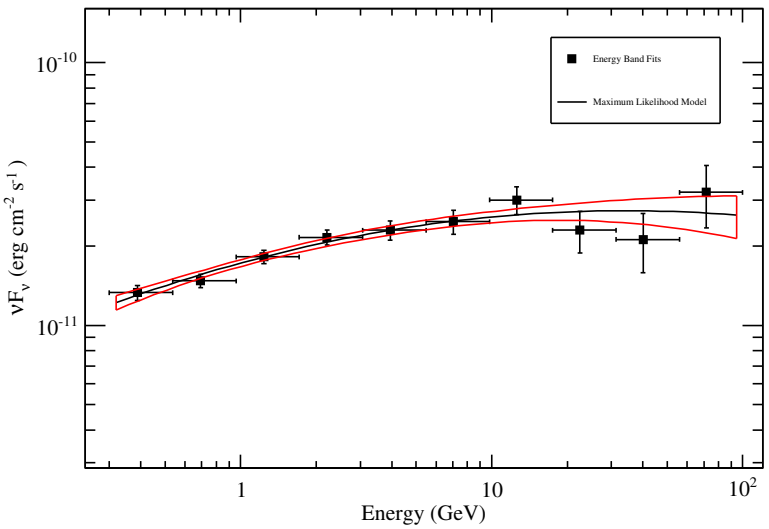

FIGURE 6.82. PKS 1424+240 Fermi LAT E^2 dN/dE spectrum in 10 bins fit best by a log parabolic curve.

6.9. Constraining the IC peak

As mentioned in the motivations for this thesis (section 2.9), one of the main objectives was to constrain the IC peak. In order to do this, the redshift value is required for all six sources. Unfortunately due to weak or absent emission lines to their optical spectra, the redshifts of 1ES 0502+675, 3C66A and PKS 1424+240 are uncertain. To compensate for this and to place preliminary upper limits on the redshifts, the VERITAS spectra were de-absorbed, using the Franceschini (2008) EBL model, for a range of redshift values. The upper limit on the redshifts were then obtained when the dN/dE Fermi LAT - VERITAS spectra were approximately a powerlaw. From this and for the remaining three sources (1ES 0806+524, 1ES1959+650 and W Comae), the TeV spectra were de-absorbed according to their redshifts (or upper limits) and the E^2dN/dE Fermi LAT - VERITAS spectra were constructed and fitted with log parabolic functions to constrain the peak of the IC emission. In the case of 1ES 0502+675, the upper limit on redshift was estimated to be z=0.3 from the Fermi LAT - VERITAS dN/dE spectrum (figure 6.83). Using this value, the E^2dN/dE Fermi LAT - VERITAS spectrum was constructed (figure 6.84). However, the peak of the IC emission could not be constrained as the TeV spectrum continued to rise indicating that the IC peak occurred at higher the TeV energies or (more probably) the redshift was over-estimated.

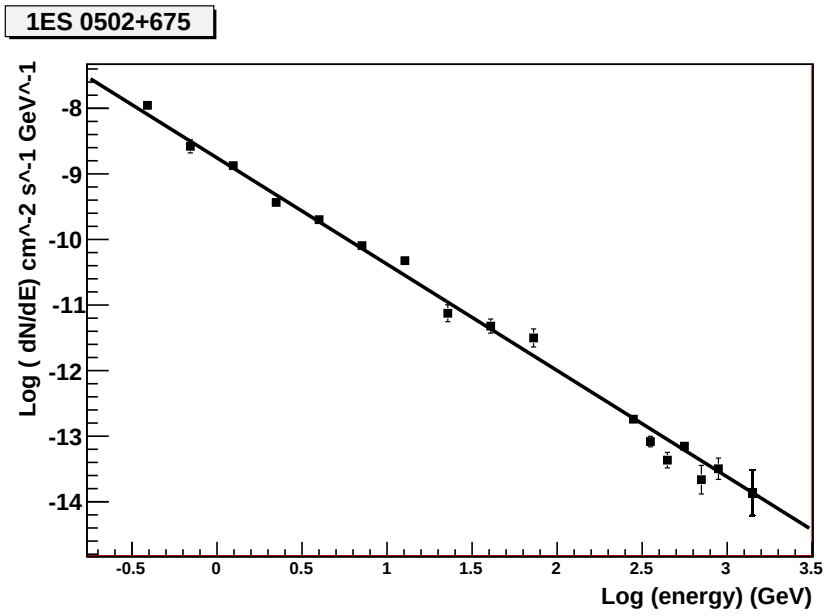

FIGURE 6.83. 1ES 0502+675 Fermi LAT and de-absorbed VERITAS dN/dE spectra at a redshift of z = 0.3.

Using a redshift of z=0.138 (Acciari et al., 2009), the TeV spectrum of 1ES 0806+524 was de-absorbed and the E^2 dN/dE MeV - TeV spectrum was constructed (figure 6.85). The spectrum

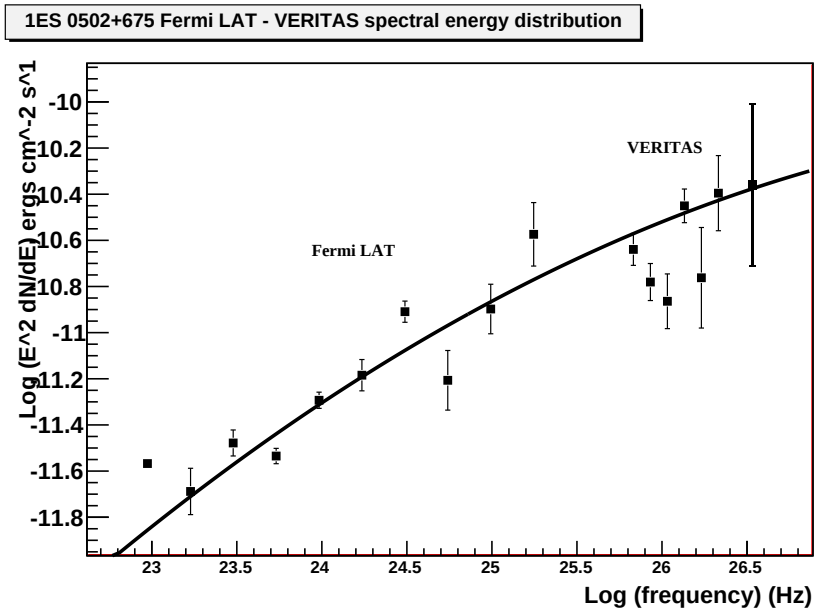

FIGURE 6.84. 1ES 0502+675 Fermi LAT and de-absorbed VERITAS E^2dN/dE spectra at a redshift of z = 0.3.

was fitted with a log parabolic curve and the peak of the IC emission was constrained to $\sim 10^{24}$ Hz.

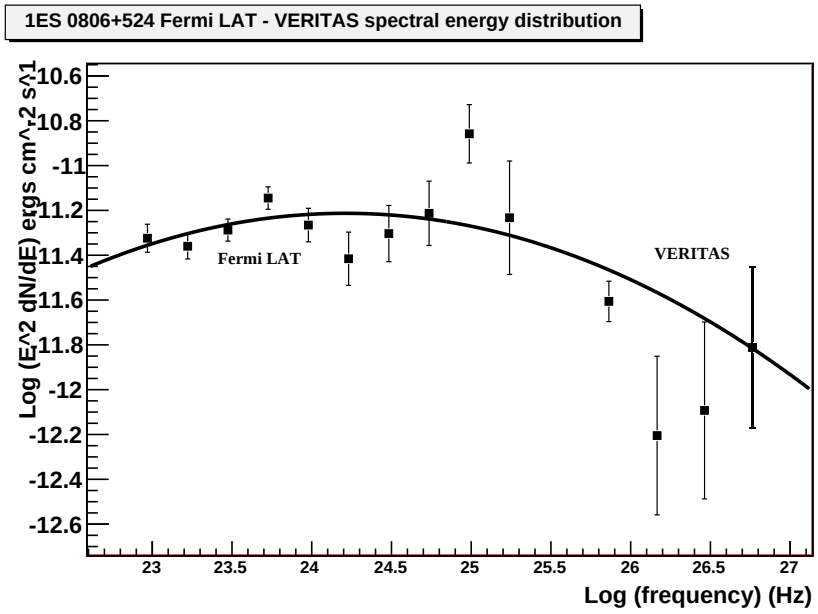

FIGURE 6.85. 1ES 0806+524 Fermi LAT and de-absorbed VERITAS E^2dN/dE spectra at a redshift of z = 0.138.

With a redshift of z=0.047 (Krawczynski et al., 2004), the TeV spectrum of 1ES 1959+650 was de-absorbed and the E^2 dN/dE MeV - TeV spectrum was constructed (figure 6.86). The spectrum was fitted with a log parabolic curve and the peak of the IC emission was constrained to $\sim 10^{24}$ Hz.

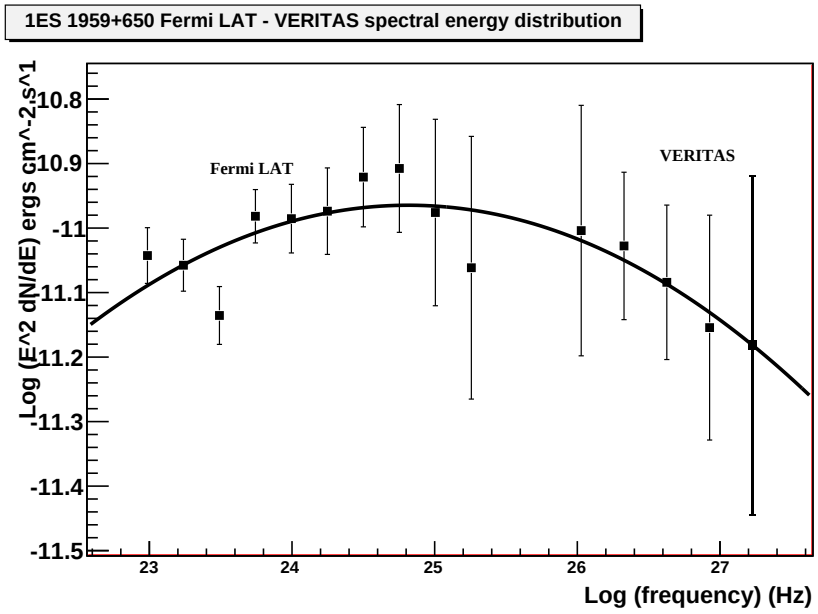

FIGURE 6.86. 1ES 1959+650 Fermi LAT and de-absorbed VERITAS E^2dN/dE spectra at a redshift of z = 0.047.

Using a redshift of z=0.102 (Acciari et al., 2009), the TeV spectrum of W Comae was de-absorbed and the E^2 dN/dE MeV - TeV spectrum was constructed (figure 6.87). The spectrum was fitted with a log parabolic curve and the peak of the IC emission was constrained to $\sim 10^{23}$ Hz.

In the case of 3C66A, the upper limit on redshift was estimated to be z=0.3 from the Fermi LAT - VERITAS dN/dE spectrum (figure 6.88). Using this value, the E^2dN/dE Fermi LAT - VERITAS spectrum was constructed (figure 6.89). The spectrum was fitted with a log parabolic curve and the peak of the IC emission was constrained to $\sim 10^{24}$ Hz. Earlier Fermi LAT analysis of this source demonstrates that the Fermi LAT dN/dE points are actually fit better by a log parabolic curve than a powerlaw, indicating the IC peak emission is occurring $\sim 10^{23}$ Hz. This suggests the redshift could be over estimated or that there is a spectral dip between 10^{23} and 10^{24} Hz. The turnover of the IC peak was then assumed to be $\sim 10^{23}$ Hz and the TeV spectrum was deabsorbed for different redshifts in order to see which redshift suited best. The results indicated that if the IC turnover does in fact occur $\sim 10^{23}$ Hz the redshift would be z=0.05 at the most (figure 6.90).

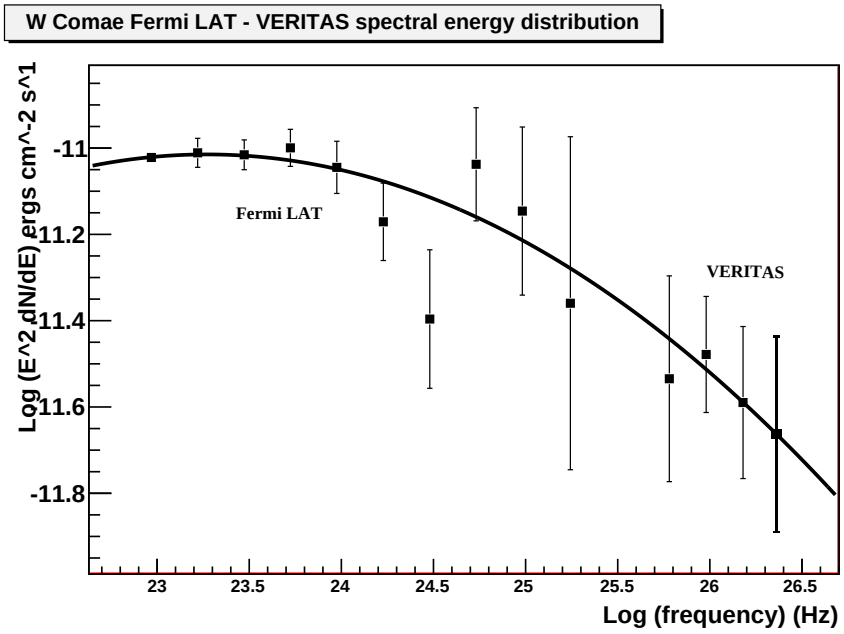

FIGURE 6.87. W Comae Fermi LAT and de-absorbed VERITAS E^2dN/dE spectra at a redshift of z = 0.102.

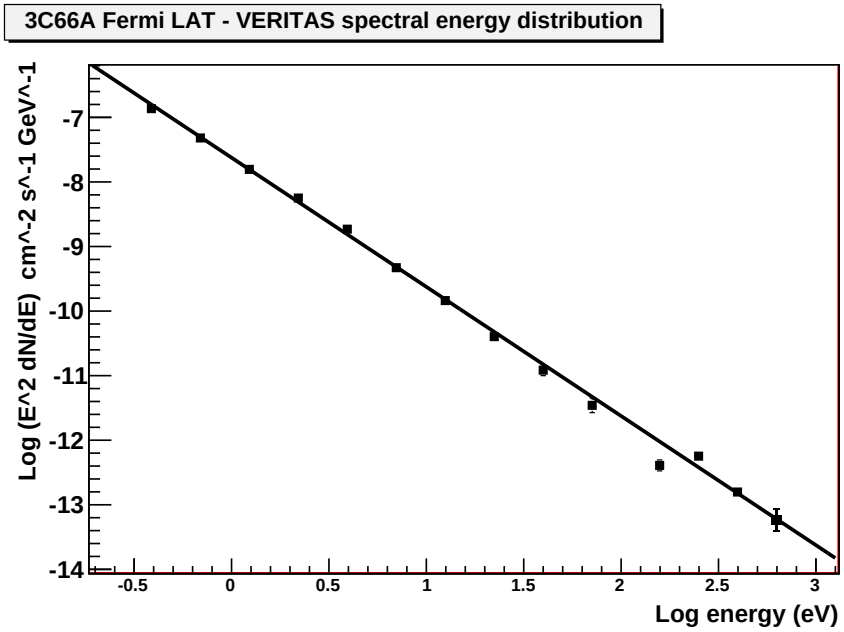

FIGURE 6.88. 3C66A Fermi LAT and de-absorbed VERITAS dN/dE spectra at a redshift of z = 0.3.

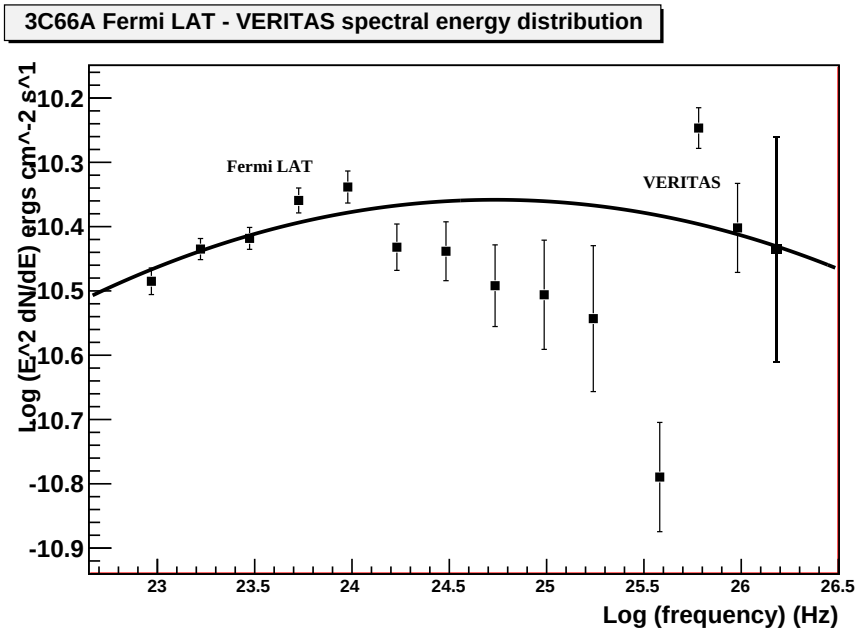

FIGURE 6.89. 3C66A Fermi LAT and de-absorbed VERITAS E^2dN/dE spectra at a redshift of z = 0.3.

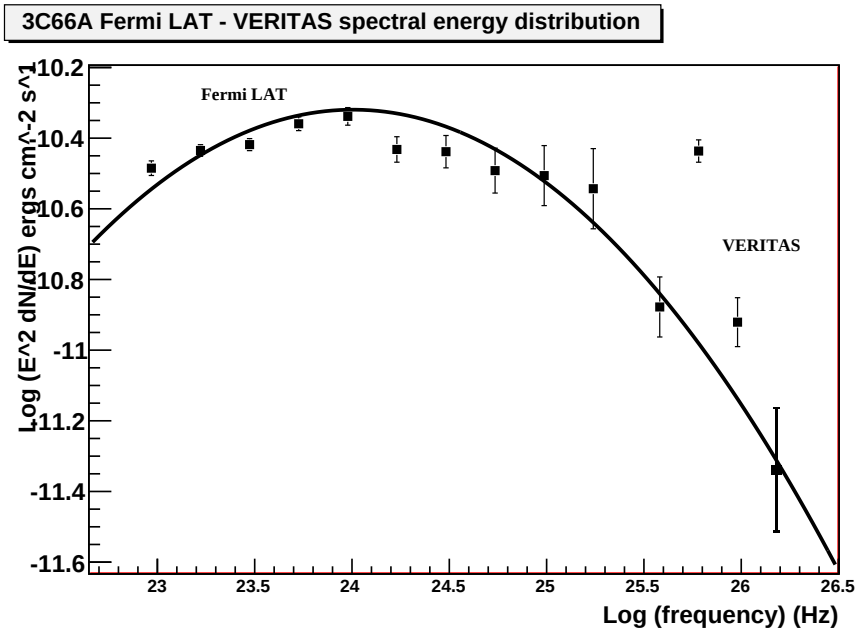

FIGURE 6.90. 3C66A Fermi LAT and de-absorbed VERITAS E^2dN/dE spectra at a redshift of z = 0.05.

In the case of PKS 1424+240, the upper limited on redshift was estimated to be z = 0.6 from the Fermi LAT - VERITAS dN/dE spectrum (figure 6.91). Using this value, the E^2dN/dE Fermi LAT - VERITAS spectrum was constructed (figure 6.92). The spectrum was fitted with a log parabolic curve and the peak of the IC emission was constrained to $\sim 10^{24.5}$ Hz. This frequency is larger than expected from the Fermi LAT dN/dE (figure 6.82)‘ spectrum indicating the redshift is actually less than the redshift upper limit used here. See table 6.13 for a comparison of the previously published synchrotron and IC peaks for the different sources and for the different subclass of blazar.

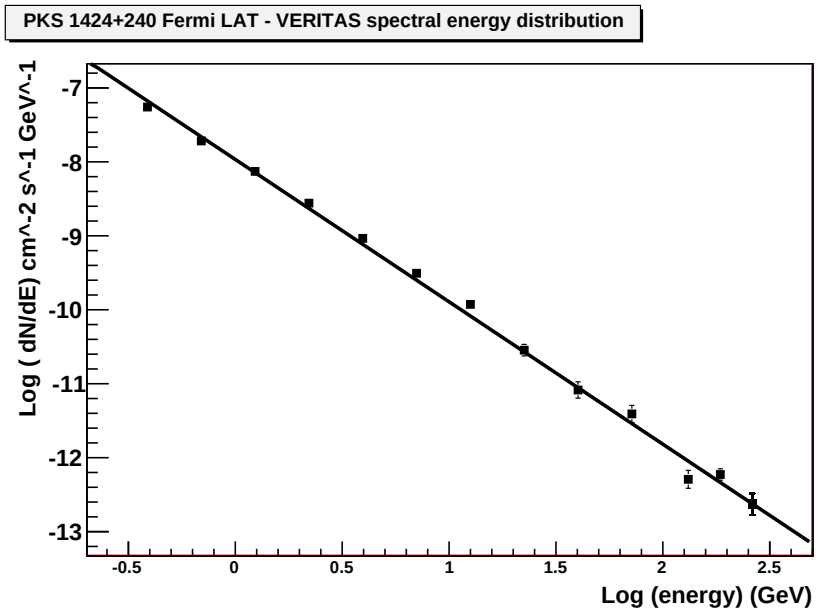

FIGURE 6.91. PKS 1424+240 Fermi LAT and de-absorbed VERITAS dN/dE spectra at a redshift of z = 0.6.

TABLE 6.13. A comparison of the synchrotron and IC peaks, * denotes sources of uncertain redshift

Source	Blazar subclass	Synchrotron peak (Hz)	IC peak (Hz)
1ES 0502+675*	HBL	10^{16}	Inconclusive
1ES 0806+524	HBL	8.3×10^{15}	10^{24}
1ES 1959+650	HBL	10^{17} - 10^{18}	10^{24}
W Comae	IBL	10^{14} - 10^{16}	10^{23}
3C66A*	IBL	10^{15} - 10^{16}	10^{23}
PKS 1424+240*	IBL	10^{15} - 10^{17}	$10^{24.5}$

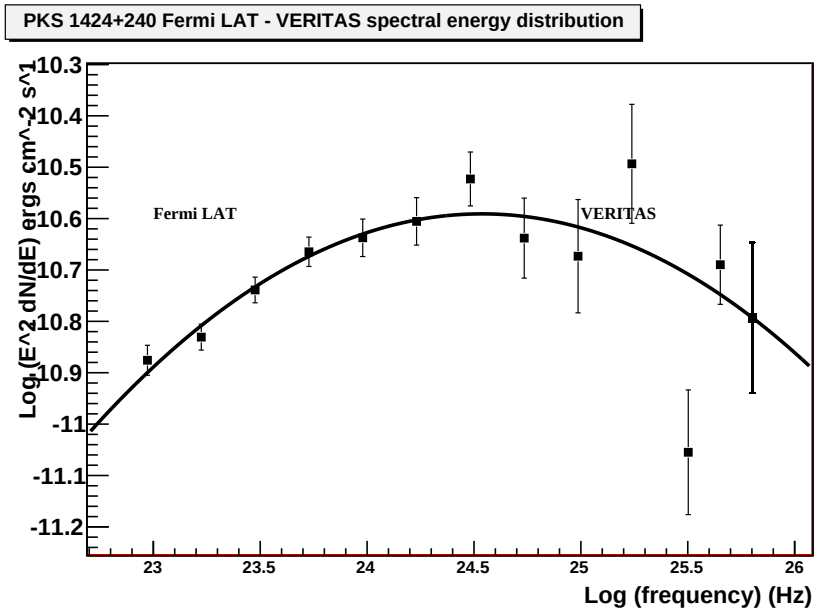

FIGURE 6.92. PKS 1424+ 240 Fermi LAT and de-absorbed VERITAS E^2dN/dE spectra at a redshift of z = 0.6

6.10. SED modeling

Multiwavelength SEDs were constructed with the addition of multiwavelength data to the Fermi LAT - VERITAS spectral points, and fitted with both the SSC and SSC + EC model as described in section 2.7.4. The fits were then compared and a best model fit was established. The SED parameters from were also compared for each source.

• 1ES 0502+675:

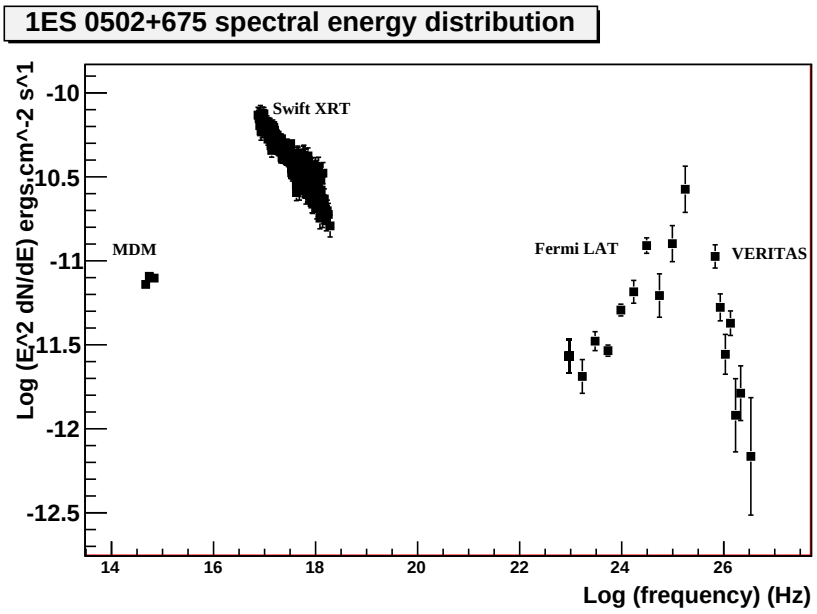

FIGURE 6.93. 1ES 0502+675 multiwavelength E^2 dN/dE spectra including VERITAS and Fermi LAT data with quasi-contemporaneous MDM and Swift XRT data. The data is taken from Acciari et al. (in prep).

Figure 6.93 shows the Fermi LAT and VERITAS spectral data points in addition to contemporaneous MDM and Swift XRT data (Acciari et al., in prep). The redshift was originally reported to be z=0.341 from a private communication (Perlman, 1996) which would make it one of the largest redshift blazars detected at TeV energies. This redshift measurement has since been deemed unreliable, due to the absence of emission lines in the optical spectra, and more detailed redshift measurements have also been inconclusive. Despite this, for the purpose of the SED modeling of this source, the redshift value of z=0.341 has been used. In addition to the redshift being held constant, the angle to the observer's line of sight θ is set to 1.91° for the modeling process (Acciari et al., in prep). The low-energy electron spectral index is fixed at 1.5 due to the sharp IC peak with the high-energy electron spectral index left at 3. Figures 6.94 and 6.95 show the best fit SSC and SSC+EC models and table 6.14 for model parameters. As evident in the SED modeled plots, the pure one-zone SSC model fits well and accounts for the sharp IC peak and steep GeV and TeV spectra. Also, the fits yields realistic SED model parameters such as

bulk Lorentz factor and magnetic field strength. The SSC + EC combination fits the IC bumps well but over-estimates the synchrotron radiation. From this, it is reasonable to conclude the SSC model fits the data best. To date, no short variability timescales has been detected. This could be the result of the combination of the lack of observations and a period of low activity, i.e. no flaring. As a consequence of this, the radius of the emitting region can only be constrained from SED modeling. This means it is difficult to determine whether a low Doppler factor/large radius or a high Doppler factor/small radius works best. The extremely soft TeV spectrum could be indicative of EBL absorption, suggesting a large redshift. The increase in the de-absorbed TeV spectra (black dashed lines) in the SSC+EC model, suggests the emitting radius may be too small and attenuation from γ-γ pair production is limiting the TeV emission.

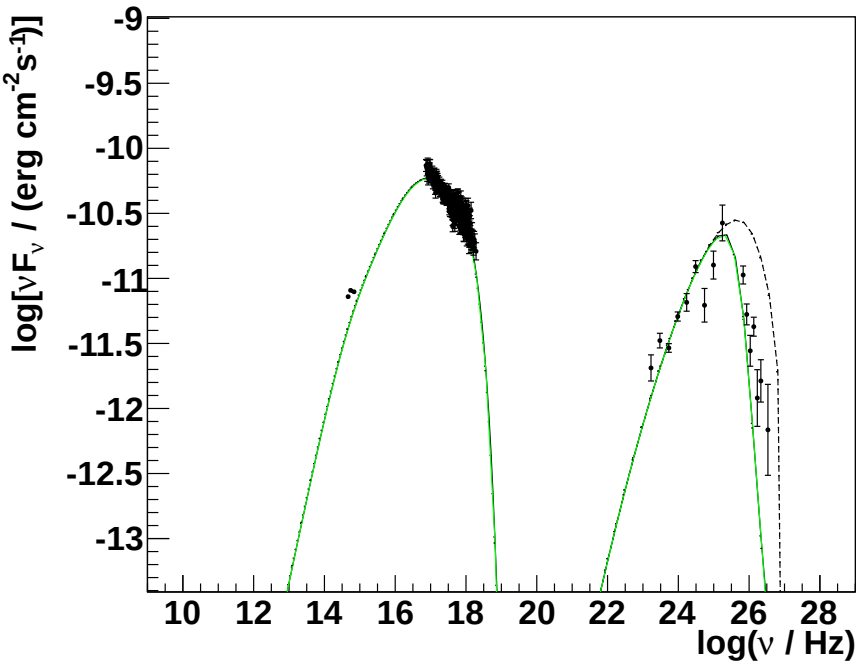

FIGURE 6.94. 1ES 0502+675 SSC E^2 dN/dE spectra with VERITAS, Fermi LAT, Swift XRT and MDM data. Black = SSC, dashed black = deabsorbed spectrum, Green is the SSC fit.

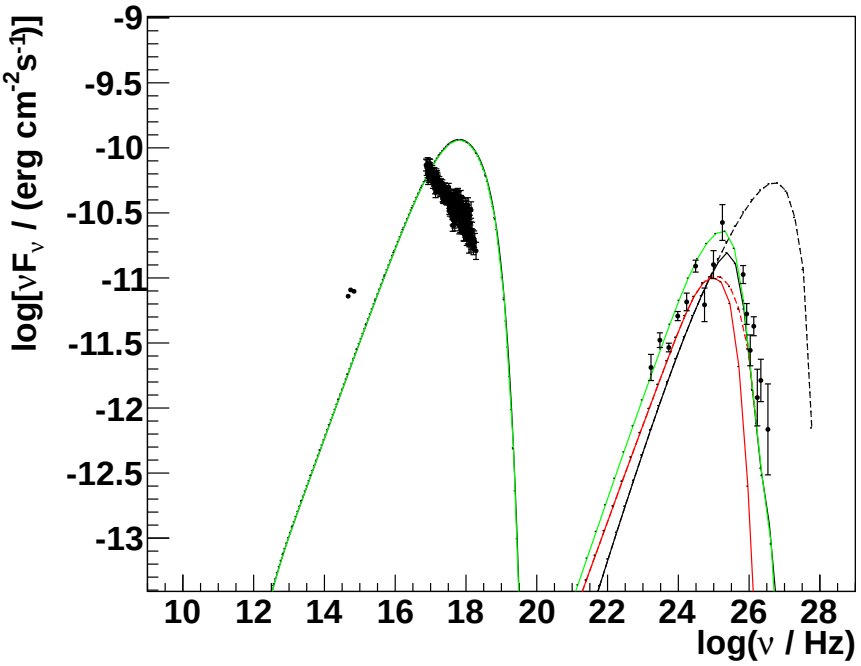

FIGURE 6.95. 1ES 0502+675 SSC + EC E^2 dN/dE spectra with VERITAS, Fermi LAT, Swift XRT and MDM data. Black = SSC, dashed black = deabsorbed spectrum, red = EC, Green is the sum of the SSC+ EC.

TABLE 6.14. SSC and SSC+EC model fit parameters, 1ES 0502+675

	SSC	SSC + EC
Redshift	0.341	0.341
Bulk Lorentz factor	30	30
Angle to observer's line of sight (°)	1.91	1.91
Magnetic field strength (G)	0.1	0.01
Radius of emitting volume (m)	2.7×10^{14}	1×10^{15}
Energy Density of electrons (erg cm^{-3})	0.003	0.001
Minimum electron energy (eV)	1×10^{9}	1×10^{9}
Maximum electron energy (eV)	3.16×10^{11}	1×10^{12}
Electron powerlaw break energy (eV)	1×10^{11}	1×10^{11}
Low energy electron spectral index	1.5	1.5
High energy electron spectral index	3	3
Black hole mass in solar masses*	∼	1×10^{9}
Accretion rate in solar masses*	∼	4
Height of emitting volume in Schwarzchild radius*	∼	6500

* not applicable in the case of pure SSC

• 1ES 0806+524:

The Fermi LAT and VERITAS data is combined with archival data radio and x-ray data (figure 6.96). The redshift is fixed at z=0.138 (Acciari et al., 2009). The low-energy electron spectral index is fixed at 2.6 to compensate for the broad IC peak with the high energy electron spectral index left at 3. Table 6.15 shows the best fit SSC and SSC+EC parameters (figures 6.97 and 6.98, respectively). Both the pure SSC and the SSC + EC combination agree quite well in the case of 1ES 0806+524 and the model parameters are very similar. The SSC fit reproduces the hard Fermi LAT spectrum and the steep VERITAS spectrum but under-produces the maximum of the IC peak. Due to a limited quantity of radio to x-ray data, it is difficult to see if the model constrains the synchrotron peak adequately. The SSC fit model parameters are within reasonable limits and suggest variability on the timescales of $\sim$ 5 hours is possible. Despite the SSC+EC combination generating reasonable model parameter results, the model does not adequately explain the hard Fermi spectrum and similarly to the pure SSC model, under-produces the flux of the IC peak. Again it is difficult to constrain the synchrotron peak due to the lack of data. The SSC+EC model also suggests variability on the timescales of $\sim$ 5 hours is possible. From these results, it can be concluded that pure SSC emission processes dominate here.

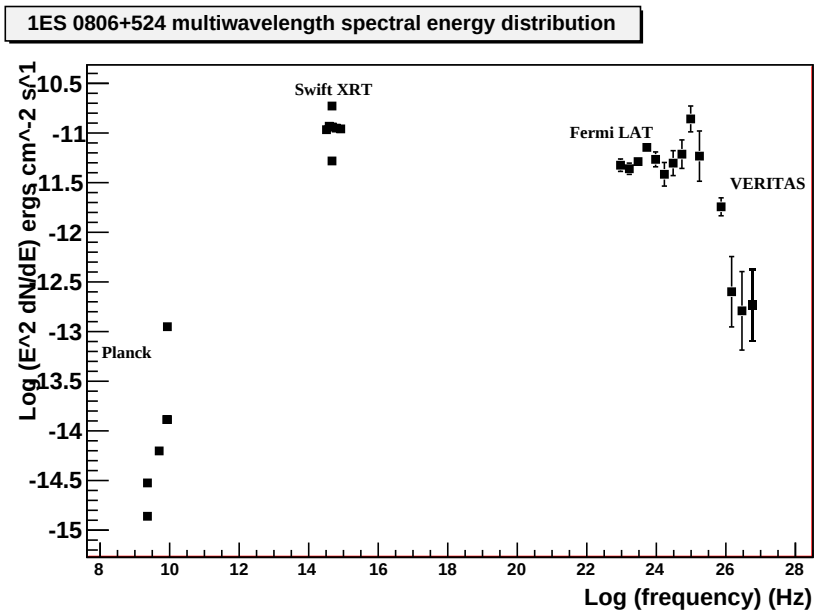

FIGURE 6.96. 1ES 0806+524 SED with Planck upper limits and Swift XRT data points (Planck Collaboration, 2011) combined with Fermi LAT and VERITAS data points.

TABLE 6.15. SSC and SSC+EC model fit parameters, 1ES 0806+524

	SSC	SSC + EC
Redshift	0.138	0.138
Bulk Lorentz factor	35	35
Angle to observer's line of sight (°)	3	3
Magnetic field strength (G)	0.2	0.2
Radius of emitting volume (m)	1.8×10^{14}	7×10^{14}
Energy Density of electrons (erg cm^{-3})	0.3	0.005
Minimum electron energy (eV)	3162	3162
Maximum electron energy (eV)	1×10^{12}	1×10^{12}
Electron powerlaw break energy (eV)	1×10^{11}	1×10^{11}
Low energy electron spectral index	2.6	2.6
High energy electron spectral index	3	3
Black Hole mass in solar masses*	∼	1×10^{9}
Accretion rate in solar masses*	∼	4
Height of emitting volume in Schwarzchild radii*	∼	1400

* not applicable in the case of pure SSC

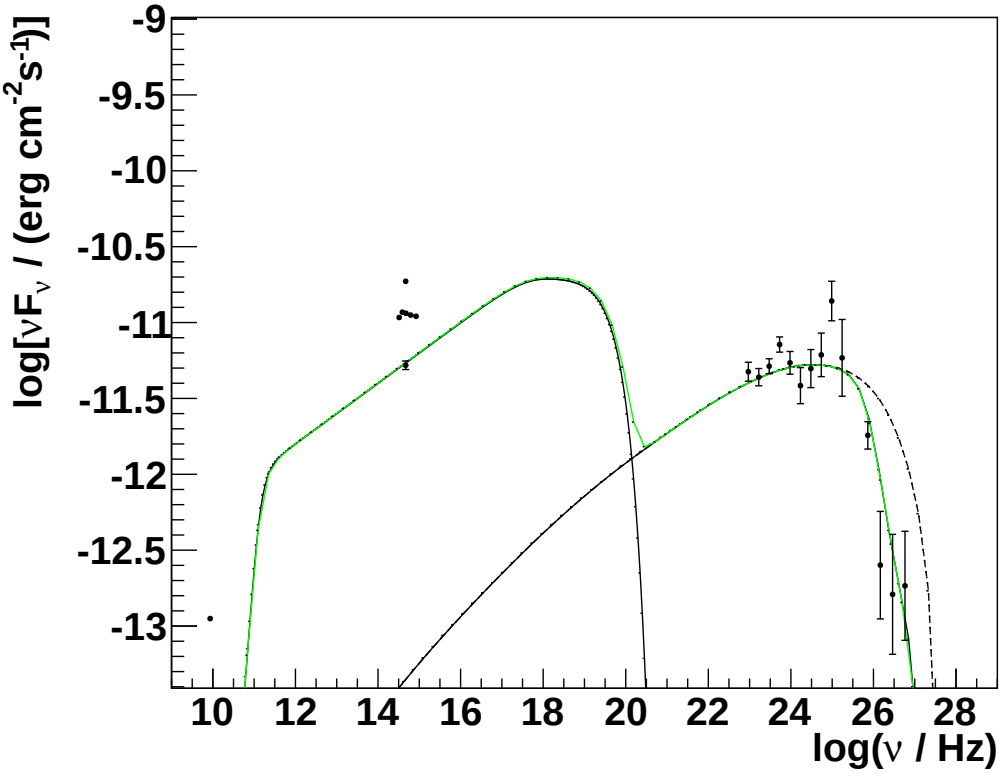

FIGURE 6.97. 1ES 0806+524 SSC fit to multiwavelength data. Black = SSC, dashed black = deabsorbed spectrum, red = EC, Green is the SSC curve.

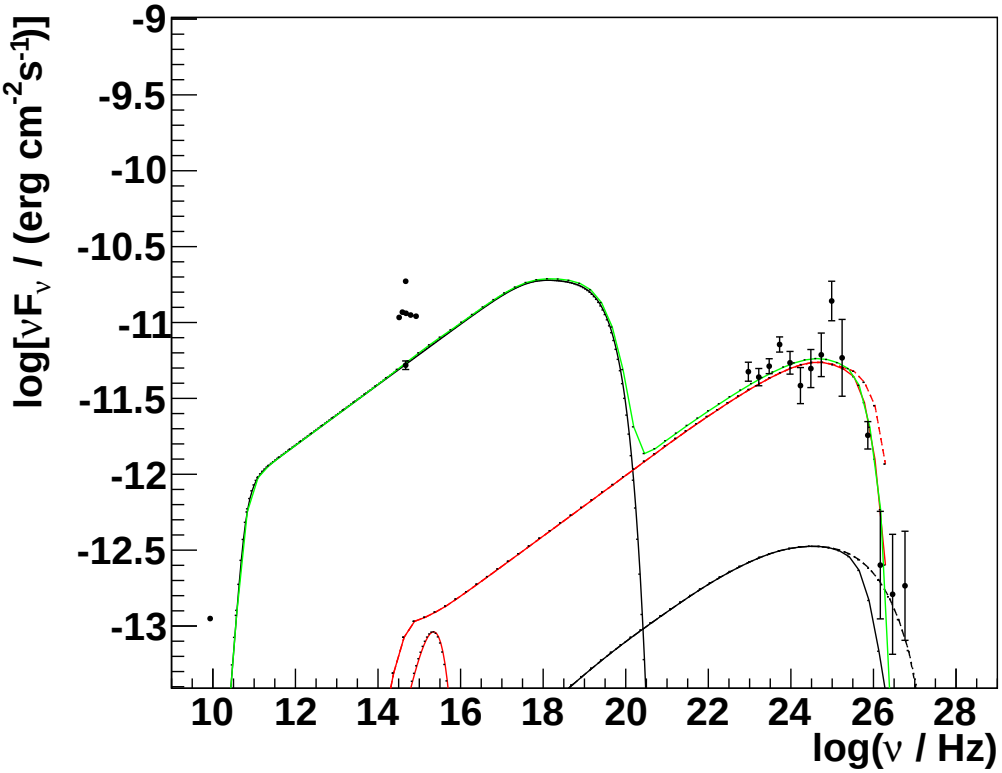

FIGURE 6.98. 1ES 0806+524 SSC+EC fit to multiwavelength data. Black = SSC, dashed black = deabsorbed spectrum, red = EC, Green is the sum of the SSC + EC.

TABLE 6.16. SSC and SSC+EC model fit parameters, 1ES 1959+650

	SSC	SSC + EC
Redshift	0.047	0.047
Bulk Lorentz factor	35	35
Angle to observer's line of sight (°)	2.7	2.7
Magnetic field strength (G)	0.12	0.12
Radius of emitting volume (m)	2.3×10^{14}	4.5×10^{14}
Energy Density of electrons (erg cm^{-3})	0.1	0.01
Minimum electron energy (eV)	3162	3162
Maximum electron energy (eV)	1×10^{12}	3.16×10^{13}
Electron powerlaw break energy (eV)	1×10^{11}	1×10^{12}
Low energy electron spectral index	2.6	2.6
High energy electron spectral index	3	3
Black Hole mass in solar masses*	$\sim$	1×10^{9}
Accretion rate in solar masses*	$\sim$	4
Height of emitting volume in Schwarzchild radii*	$\sim$	2100

* not applicable in the case of a pure SSC model.

• 1ES 1959+650:

The Fermi LAT and VERITAS data are combined with Planck upper limits, and Swift UVOT and Swift XRT data (figure 6.99), taken from Planck Collaboration (2011). The redshift is fixed at z=0.047 (Krawczynski et al., 2004) The low-energy electron spectral index is fixed at 2.6 due to the broad IC peak with the high energy electron spectral index left at 3. Table 6.16 shows the best fit SSC and SSC+EC parameters (figures 6.100 and 6.101, respectively). Both models are in good agreement with the majority of the data points. The SSC model adequately describes the hard Fermi spectrum and the IC peak maximum. However it underproduces the TeV spectrum and does not agree with the VERITAS data points unless the model is de-absorped. The SSC+EC model produces a TeV spectrum similar to the VERITAS data and fits the IC peak well. Both models produce synchrotron peaks (though somewhat broad) that are consistent with the data. The SSC fit model parameters are within reasonable limits and in agreement with previously published datasets (Krawczynski et al., 2004) and suggest variability on the timescales of $\sim$ 6 hours is possible. Variability on timescales shorter than this would imply the radius of the emitting region is too high. Decreasing the radius parameter would then lead to the synchrotron and IC peaks being underproduced by the model. This coupled with orphan flares from IES 1959+650 (Krawczynski et al, 2004), suggests that a one zone SSC model does not adequately describe the processes taking place.

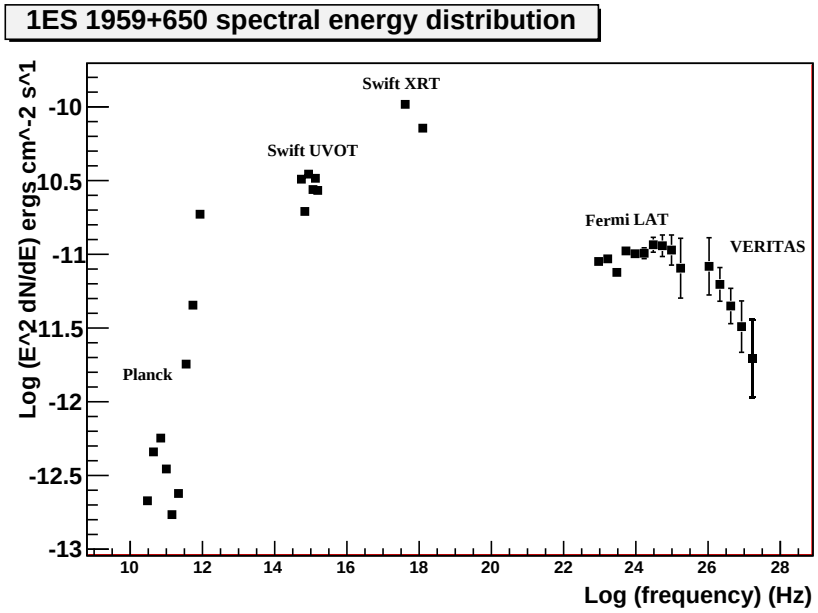

FIGURE 6.99. 1ES 1959+650 multiwavelength data SED including Planck upper limits and Swift UVOT and XRT data points (Planck Collaboration, 2011).

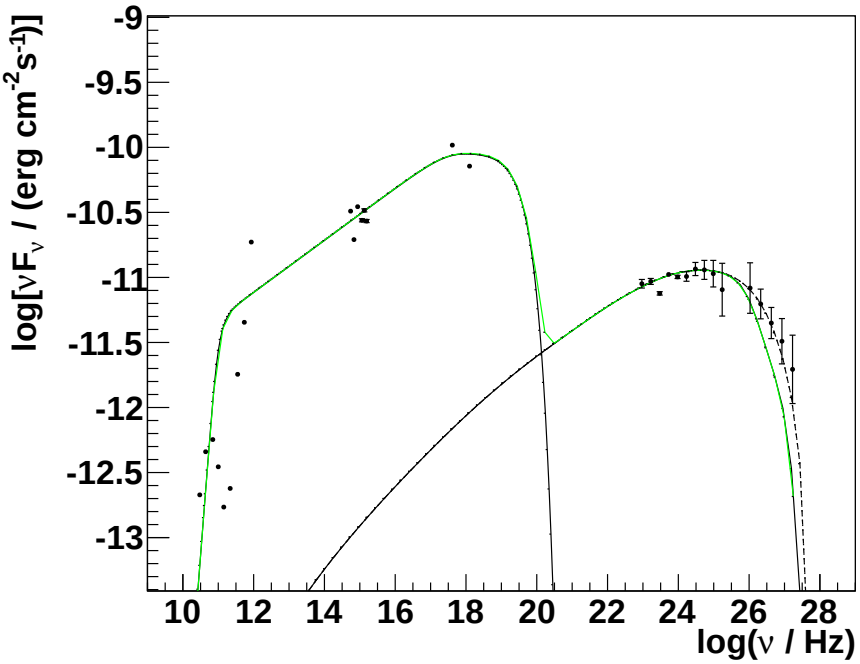

FIGURE 6.100. 1ES 1959+650 SSC fit to multiwavelength data. Black = SSC, dashed black = deabsorbed spectrum, Green = SSC.

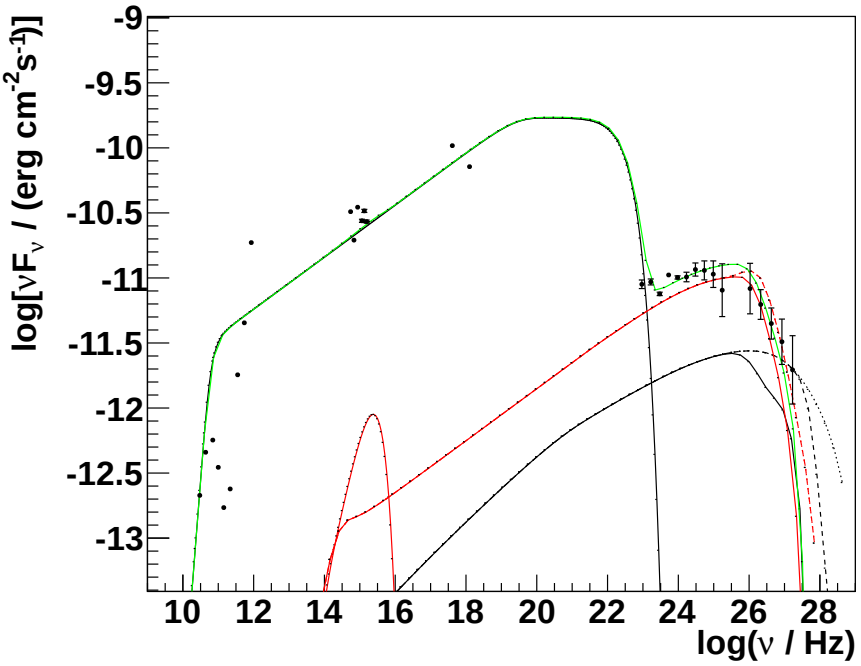

FIGURE 6.101. 1ES 1959+650 SSC + EC fit to multiwavelength data. Black = SSC, dashed black = deabsorbed spectrum, red = EC, Green = sum over SSC +EC.

• W Comae:

The Fermi LAT and VERITAS data are combined with Planck upper limits and Swift UVOT and Swift XRT data (figure 6.102), the data is taken from Planck Collaboration (2011). The redshift is fixed at z=0.102 (Acciari et al., 2009) The low energy electron spectral index is fixed at 2.6 due to the broad IC peak with the high energy electron spectral index left at 3. Table 6.17 shows the best fit SSC and SSC+EC parameters (figures 6.103 and 6.104, respectively). The SSC model fits bests, constraining both peaks. Previous results show an SSC+EC model fits the data best. However, this is the first published large dataset of W Comae analysis since the launch of Fermi LAT and in order to fit the hard Fermi LAT spectrum and constrain the IC peak, the synchrotron peak is over-estimated.

Both SED models produce realistic model parameters, that are in agreement with previous results and over-produce the synchrotron peak in x-ray energies. The predicted radius of the emitting region in both cases infers a variability timescale of $\sim$ 11 hours. This is quite a large estimate and observed variability timescales shorter than this would indicate that the emitting region radius may have been over-estimated. This suggest a one zone SSC model does not fit best and possibly a multi-zone model is required.

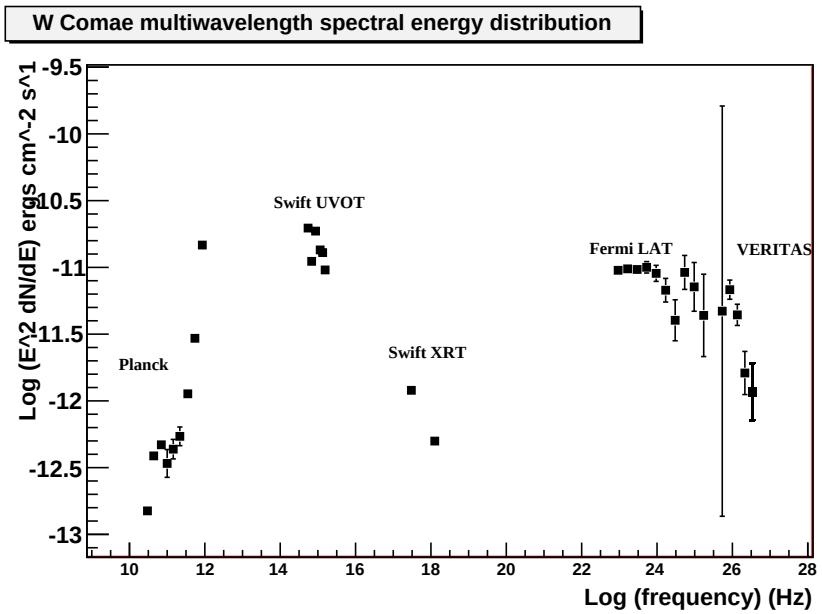

FIGURE 6.102. W Comae multiwavelength SED with quasi-contemporaneous Planck (data points and upper limits), Swift XRT, Swift UVOT (Planck Collaboration, 2011), Fermi LAT and VERITAS.

TABLE 6.17. SSC and SSC+EC model fit parameters, W Comae

	SSC	SSC + EC
Redshift	0.102	0.102
Bulk Lorentz factor	20	20
Angle to observer's line of sight (°)	3	3
Magnetic field strength (G)	0.1	0.1
Radius of emitting volume (m)	2.2×10^{14}	5×10^{14}
Energy Density of electrons (erg cm^{-3})	0.35	0.05
Minimum electron energy (eV)	7943	7943
Maximum electron energy (eV)	1×10^{12}	1×10^{12}
Electron powerlaw break energy (eV)	1×10^{10}	1×10^{10}
Low energy electron spectral index	2.6	2.6
High energy electron spectral index	3	3
Black Hole mass in solar masses*	∼	1×10^{9}
Accretion rate in solar masses*	∼	4
Height of emitting volume in Schwarzchild radii*	∼	1600

* not applicable in the case of a pure SSC model.

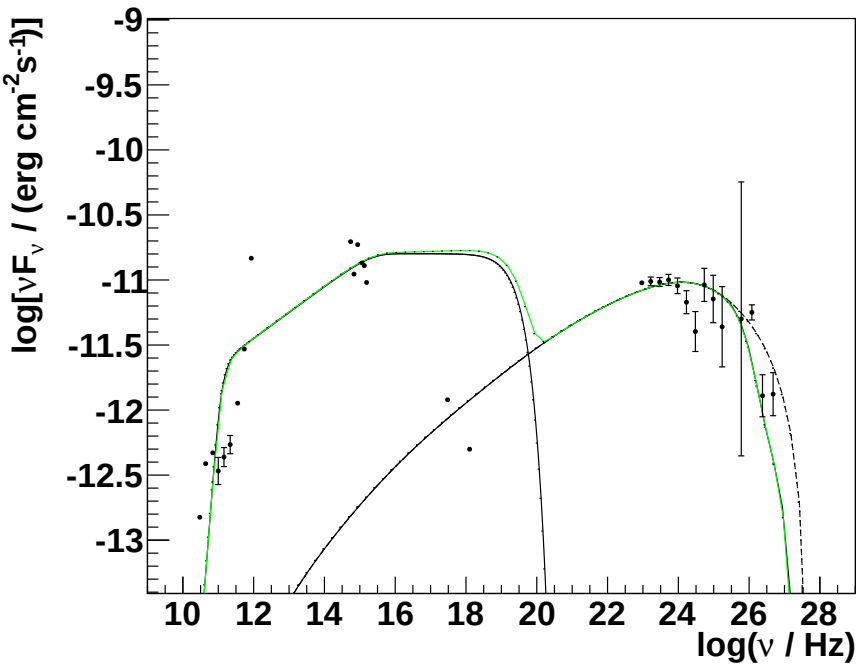

FIGURE 6.103. W Comae SSC fit to multiwavelength data (quasi-contemporaneous Planck (data points and upper limits), Swift XRT, Swift UVOT, Fermi LAT and VERITAS). Black = SSC, dashed black = de-absorbed spectrum, Green = SSC.

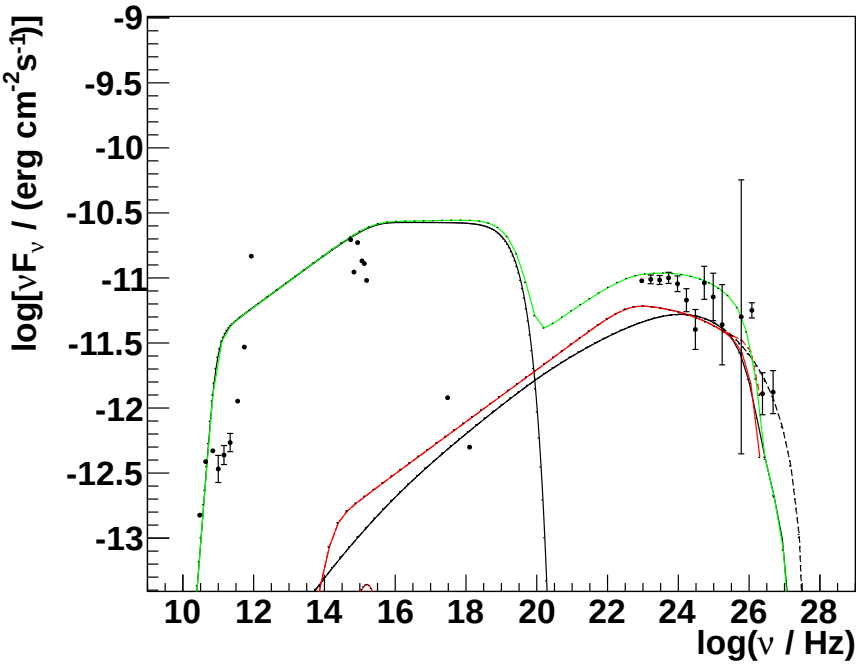

FIGURE 6.104. W Comae SSC + EC fit to multiwavelength data (quasi-contemporaneous Planck (data points and upper limits), Swift XRT, Swift UVOT, Fermi LAT and VERITAS). Black = synchrotron, dashed black = de-absorbed spectrum, red = EC, Green = sum of SSC+EC.

TABLE 6.18. SSC and SSC+EC model fit parameters, 3C66A

	SSC	SSC + EC
Redshift	0.444	0.444
Bulk Lorentz factor	35	35
Angle to observer's line of sight (°)	1.9	1.9
Magnetic field strength (G)	0.4	0.4
Radius of emitting volume (m)	1.4×10^{14}	2.5×10^{14}
Energy Density of electrons (erg cm^3	0.8	0.3
Minimum electron energy (eV)	1×10^{5}	1×10^{4}
Maximum electron energy (eV)	1×10^{13}	1×10^{12}
Electron powerlaw break energy (eV)	1×10^{12}	1×10^{10}
Low energy electron spectral index	2.6	2.6
High energy electron spectral index	3	3
Black Hole mass in solar masses*	$\sim$	1×10^{9}
Accretion rate in solar masses*	$\sim$	1
Height of emitting volume in Schwarzchild radii*	$\sim$	1080

* not applicable in the case of a pure SSC model.

• 3C66A

The Fermi LAT and VERITAS data are combined with quasi- contemporaneous FGASP, MDM, Swift UVOT and Swift XRT data (Acciari et al., 2009) shown in figure 6.105. The redshift is fixed at z=0.444 (Acciari et al., 2009). The low energy electron spectral index is fixed at 2.6 due to the broad IC peak with the high energy electron spectral index left at 3. Table 6.18 for the best fit SSC and SSC+EC parameters (figures 6.106 and 6.107, respectively). The pure SSC model predicts a synchrotron peak that is consistent with observations however, it does not describe adequately both the Fermi LAT and VERITAS spectra. To explain the hard Fermi LAT spectrum and estimate the IC peak turnover, the model underproduces the TeV spectra and vice versa. One explanation for this is that the redshift is uncertain. In comparison to this, the SSC + EC combination fits the IC turnover and the steep TeV spectrum but over predicts the synchrotron radiation significantly. While neither model explains the data fully, the SSC+EC model looks to be the better fit. The redshift value was then fixed to 0.05 as demonstrated in 6.90. Table 6.19 for the best fit SSC and SSC+EC parameters (figures 6.108 and 6.109, respectively). Both the SSC and SSC+EC models fit well and describe both the synchrotron and IC emission adequately.

TABLE 6.19. SSC and SSC+EC model fit parameters, 3C66A

	SSC	SSC + EC
Redshift	0.05	0.05
Bulk Lorentz factor	35	35
Angle to observer's line of sight (°)	1.9	1.9
Magnetic field strength (G)	0.045	0.045
Radius of emitting volume (m)	1.4×10^{14}	1.4×10^{14}
Energy Density of electrons (erg cm^3	0.8	0.8
Minimum electron energy (eV)	3981	3000
Maximum electron energy (eV)	1×10^{11}	1×10^{11}
Electron powerlaw break energy (eV)	1×10^{12}	1×10^{10}
Low energy electron spectral index	2.6	2.6
High energy electron spectral index	3	3
Black Hole mass in solar masses*	$\sim$	1×10^{9}
Accretion rate in solar masses*	$\sim$	1
Height of emitting volume in Schwarzchild radii*	$\sim$	2000

* not applicable in the case of a pure SSC model.

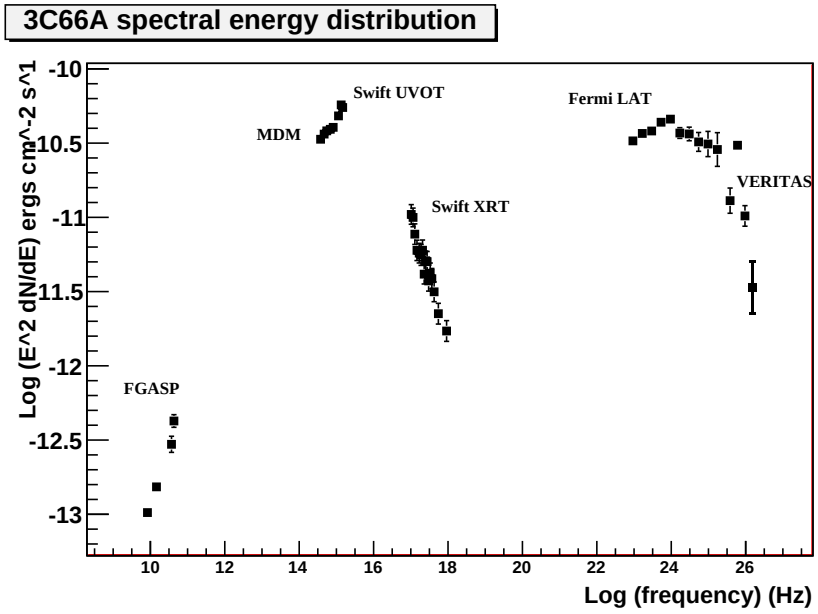

FIGURE 6.105. 3C66A multiwavelength SED with quasi-contemporaneous FGASP, MDM, Swift XRT, Swift UVOT (taken from Acciari et al, 2009), Fermi LAT and VERITAS data.

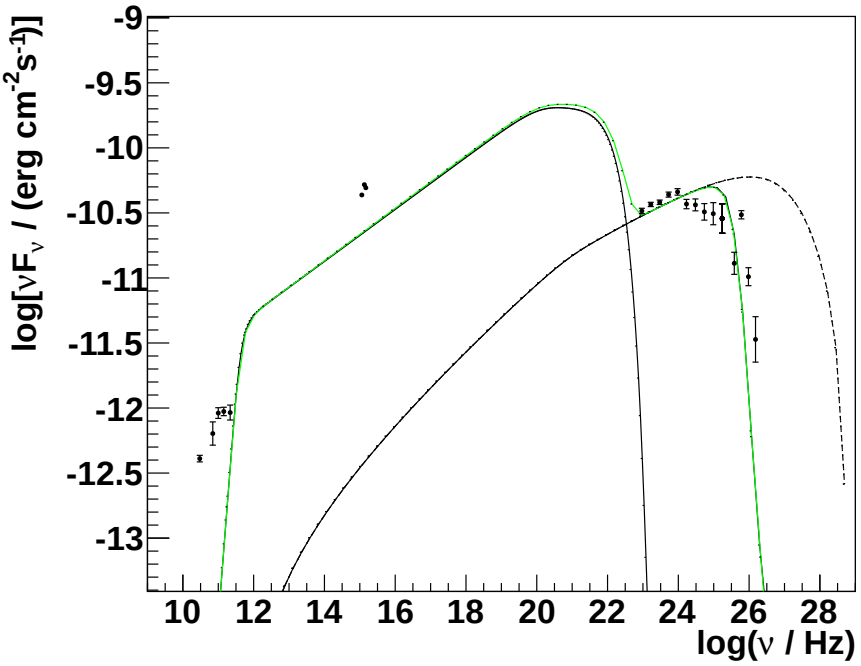

FIGURE 6.106. 3C66A SSC fit (z=0.444) to multiwavelength data (quasi-contemporaneous FGASP, MDM, Swift XRT, Swift UVOT, Fermi LAT and VERITAS data). Black = SSC, dashed black = deabsorbed spectrum, red = EC, Green = SSC.

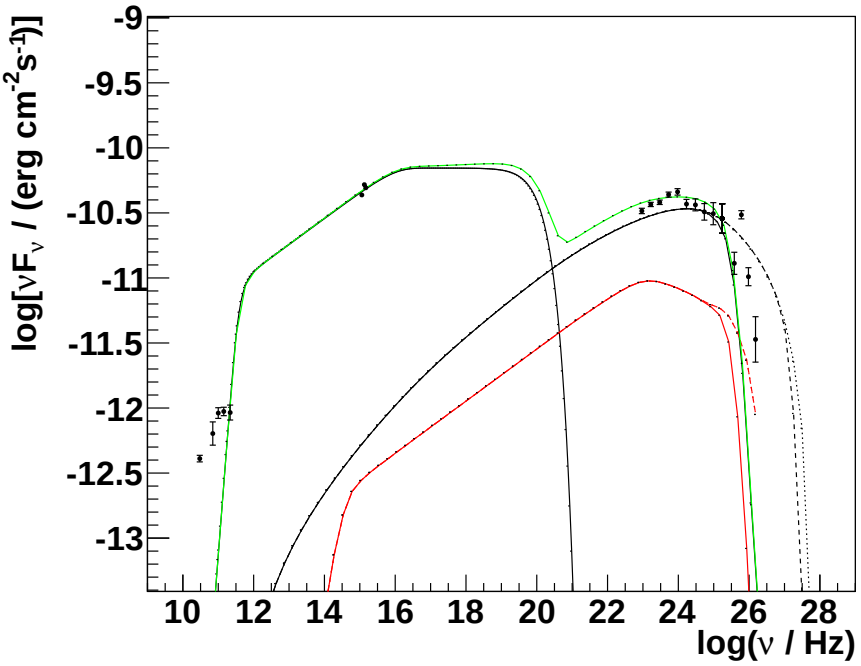

FIGURE 6.107. 3C66A SSC + EC fit (z=0.444) to multiwavelength data (quasi-contemporaneous FGASP, MDM, Swift XRT, Swift UVOT, Fermi LAT and VERITAS data). Black = SSC, dashed black = deabsorbed spectrum, red = EC, Green = sum of SSC +EC.

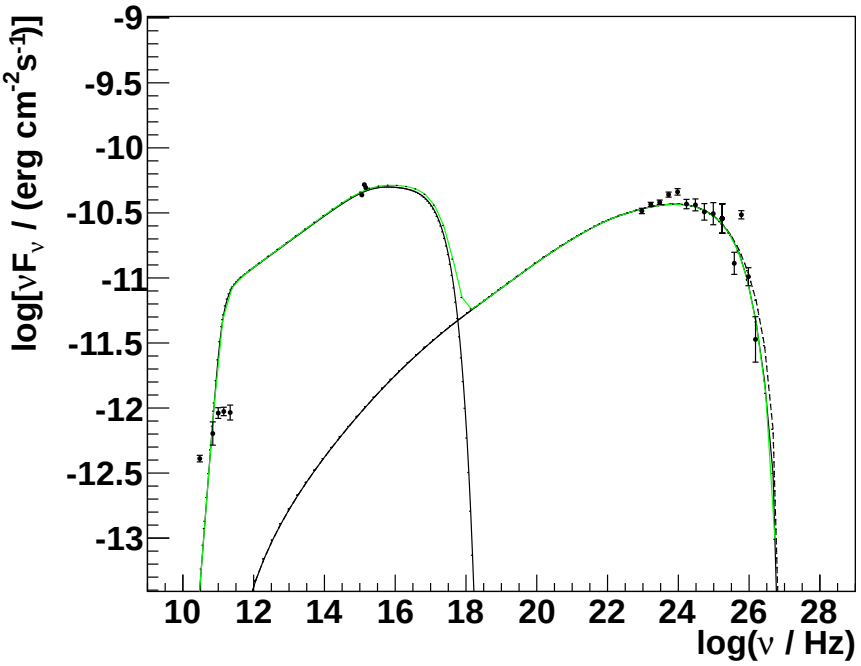

FIGURE 6.108. 3C66A SSC fit (z=0.05) to multiwavelength data (quasi-contemporaneous FGASP, MDM, Swift XRT, Swift UVOT, Fermi LAT and VERITAS data). Black = SSC, dashed black = deabsorbed spectrum, red = EC, Green = SSC.

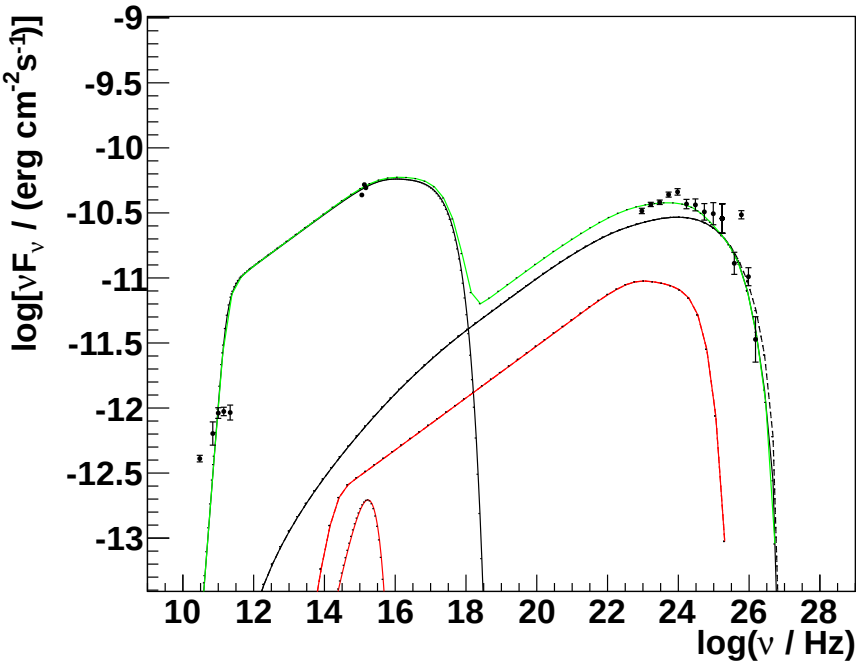

FIGURE 6.109. 3C66A SSC + EC fit (z=0.05) to multiwavelength data (quasi-contemporaneous FGASP, MDM, Swift XRT, Swift UVOT, Fermi LAT and VERITAS data). Black = SSC, dashed black = deabsorbed spectrum, red = EC, Green = sum of SSC +EC.

TABLE 6.20. SSC and SSC+EC model fit parameters, PKS1424

Parameter	SSC	SSC + EC
Redshift	0.66	0.66
Bulk Lorentz factor	35	35
Angle to observer's line of sight (°)	3	3
Magnetic field strength (G)	1.5	1.7
Radius of emitting volume (m)	2.45×10^{14}	2.45×10^{14}
Energy Density of electrons (erg cm^{-3})	0.32	0.25
Minimum electron energy (eV)	1×10^{2}	1×10^{2}
Maximum electron energy (eV)	1×10^{12}	1×10^{12}
Electron powerlaw break energy (eV)	1×10^{12}	1×10^{12}
Low energy electron spectral index	2.6	2.6
High energy electron spectral index	3	3
Black Hole mass in solar masses*	$\sim$	1e9
Accretion rate in solar masses*	$\sim$	4
Height of emitting volume in Schwarzchild radii*	$\sim$	600

* not applicable in the case of a pure SSC model.

• PKS1424+240

The Fermi LAT and VERITAS data are combined with Planck, Swift UVOT and Swift XRT (Planck Collaboration, 2011) shown in figure 6.110. The redshift is estimated and fixed at z=0.3, this was the best result from Acciari et al. (2009). The low energy electron spectral index is fixed at 2.6 due to the broad IC peak with the high energy electron spectral index left at 3. Table 6.20 shows the best fit SSC and SSC+EC parameters (figures 6.111 and 6.112, respectively). Both models produced reasonable model parameters, however they under-predict the synchrotron peak and over-produce the TeV spectrum. The SSC+EC model is marginally a better fit. Similarly to 3C66A, it is difficult to model the broad-band emission without a measured redshift value.

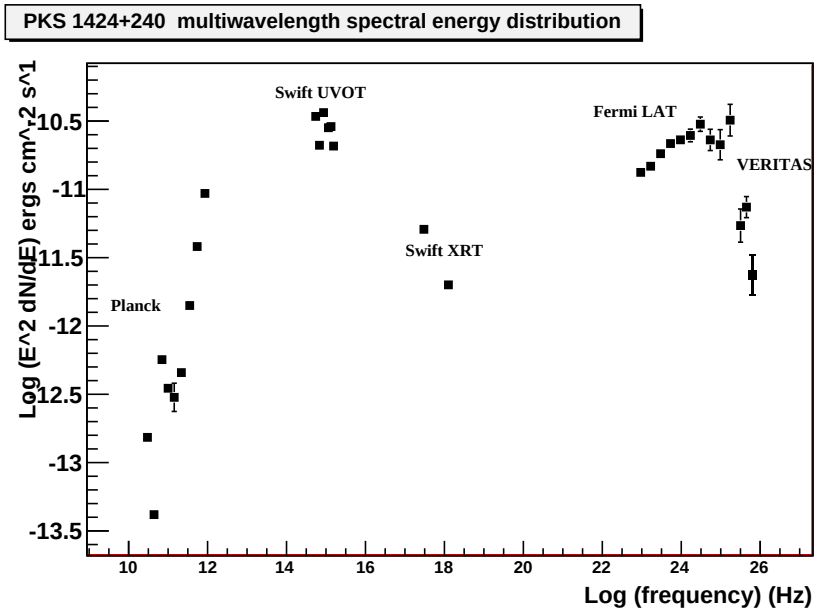

FIGURE 6.110. PKS 1424+240 multiwavelength SED with quasi-contemporaneous Planck (data= error bars and upper limits=no error bars, Planck Collaboration, 2011), Swift UVOT, Swift XRT(Acciari et al, 2010), Fermi LAT and VERITAS data.

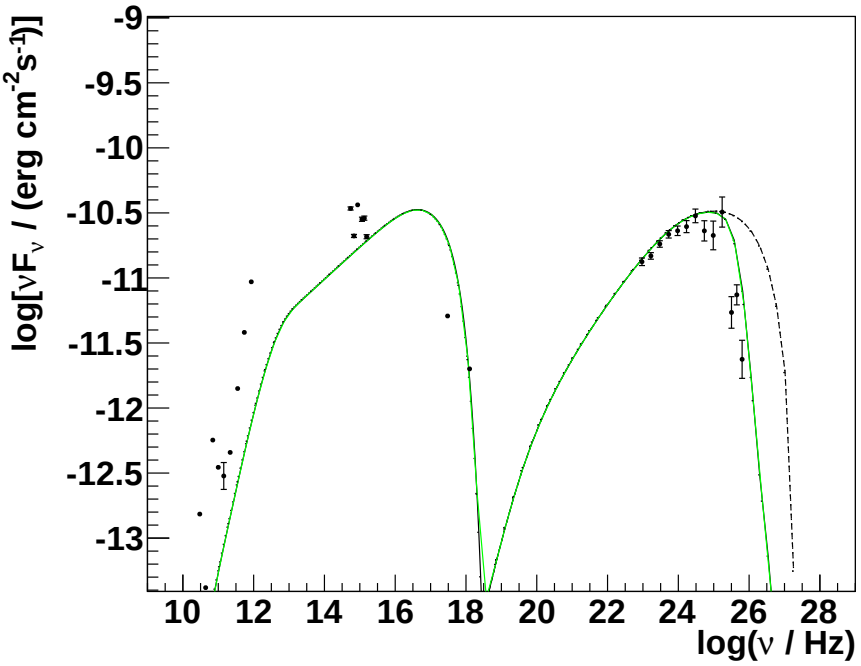

FIGURE 6.111. PKS 1424+240 SSC fit to multiwavelength data (quasi-contemporaneous Planck (Planck Collaboration, 2011), Swift UVOT, Swift XRT (Acciari et al, 2010), Fermi LAT and VERITAS data). Black = SSC, dashed black = deabsorbed spectrum, Green = SSC.

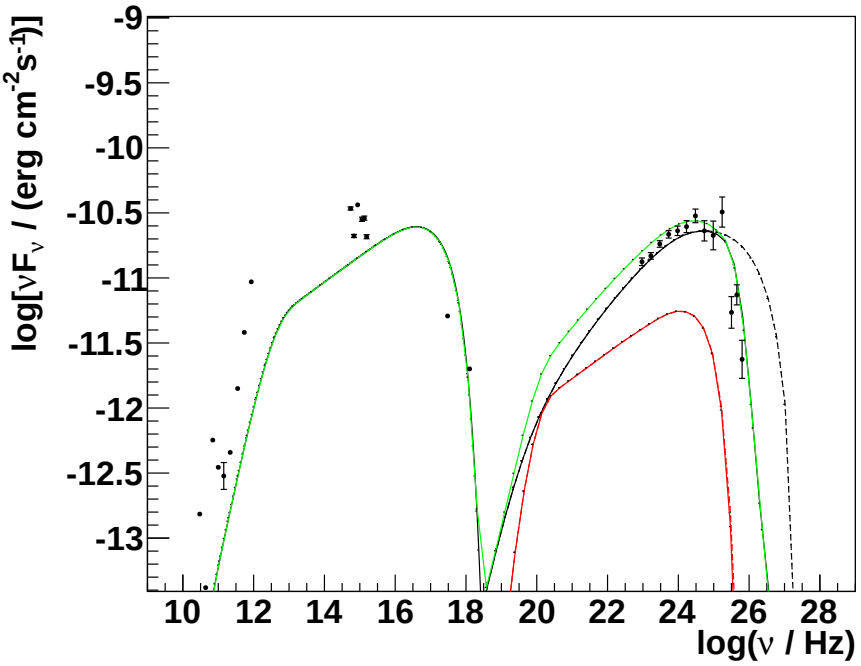

FIGURE 6.112. PKS 1424+240 SSC +EC fit to multiwavelength data (quasi-contemporaneous Planck, Swift UVOT, Swift XRT, Fermi LAT and VERITAS data). Black = SSC, dashed black = deabsorbed spectrum, red = EC, Green = sum of SSC+EC.

6.11. GeV dip

The $>$ 10 GeV dip seen in most Fermi blazar spectra cannot be the result of Klein-Nishina effects or electron cooling as the spectrum would continue to decrease and not turn up again. Two possible explanations are discussed here.

The first is that the dip is the result of the Fermi effective areas being underestimated $\sim$ 12% between 10 -150 GeV by underestimating the level of γ - γ absorption caused by γ-rays from the Earth, also known as γ-ray albedo. The Earth is the brightest γ-ray source detectable by Fermi LAT with a spectrum that extends from MeV into TeV energies (Abdo et al., 2009). Studies are on-going to update the IRFs to compensate for this.

The $>$ 10 GeV spectral break as seen in all but one (3C66A) of the blazars analyzed in this thesis can also be explained by HeII and HI Lyman recombinations absorption occurring in the BLR.Unlike the IRFs Earth's Limb theory, the shifting of the dip to higher or lower energies can be explained. The BLR is made up of HeII and HI Lyman photons that are available for absorption interactions with nearby photons (Poutanen, 2011). As shown in figure 6.113 (γ - γ cross sections weighted with the BLR spectrum), the opacity of the BLR is at its highest after $\sim$ 10 GeV, which corresponds to the Fermi spectral dip seen in blazars.

The level of absorption would provide intrinsic details about the size of the BLR; a larger BLR will have lower density of BLR photons which means less γ - γ absorption and a smaller $>$ GeV dip.

This hypothesis implies the γ-ray emitting region is located within the BLR. Studies have shown that the significance of the sip decreases with respect to increasing flux which suggests:

• Higher flux sources have their emitting regions further from the BLR and therefore undergo less γ - γ absorption.

• During flaring episodes or periods of increased flux, the emitting region could be moving out from the BLR. Detailed temporal studies are required to verify this.

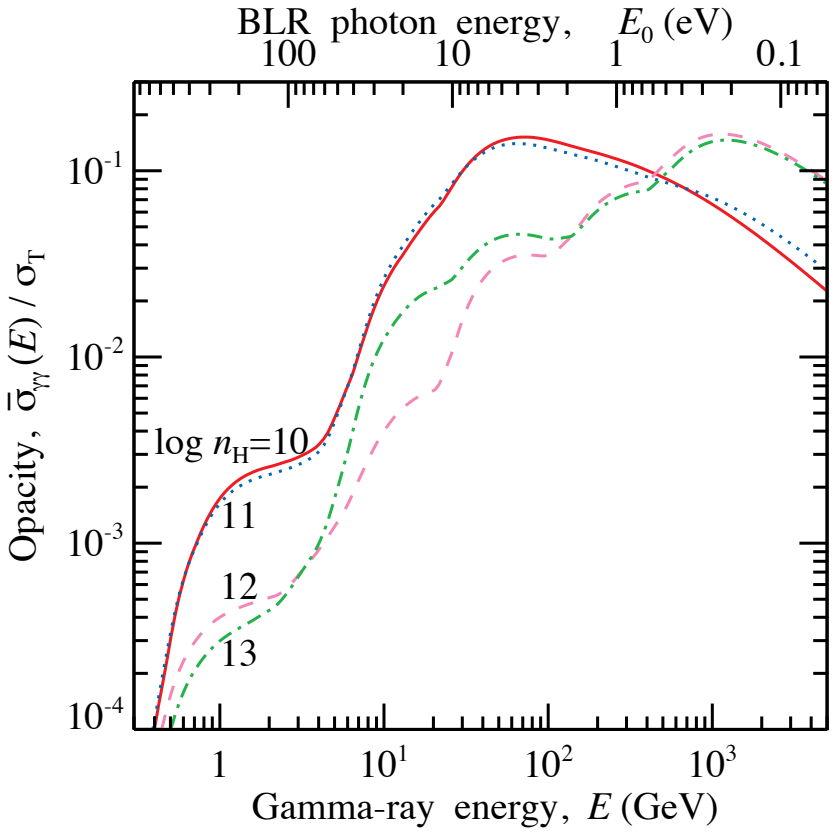

FIGURE 6.113. Corresponding γ - γ cross sections weighted with the BLR spectrum are shown by the solid, dotted, dashed and dot-dashed curves, respectively. n_H refers to column density - taken from Poutanen (2011)

6.12. Discussion

This chapter presented the comprehensive analysis and results of an extensive comparison study between two subclass of blazars: Intermediate frequency Bl Lacs (IBLs) and High frequency Bl Lacs (HBLs). 3 IBLs (W Comae, 3C66A and PKS 1424+240) and 3 HBLs (1ES 0502+675, 1ES 0806+524 1ES 1959+650) were selected based on previously published data. This is one of the first extensive contemporaneous MeV - TeV datasets produced, thanks to the addition of Fermi LAT data.

The Fermi LAT data used in this study was taken in survey mode with an energy range of 300 MeV - 100 GeV, zenith angle cut of $> 105°$ and a $10°$ ROI cut were applied to the datasets. The backgrounds were modeled, with a combination of extragalactic and galactic diffuse emission and other γ-ray sources in the ROI, and subtracted. A detailed Unbinned Maximum Likelihood analysis was performed in each case to determine the detection level (TS), flux and spectral index. The datasets were then binned in energy and time intervals to produce spectra and lightcurves.

The VERITAS data used in this study were taken in $0.5°$ wobble mode and selected based on weather and L3 rates (as described in section 6.2.1). The data sets were calibration corrected, NSB background was removed and all Cherenkov images underwent quality cuts. Hillas parameterization then discriminated against muons and hadron-initiated Cherenkov showers. Wobble and RBM analyses were run on each dataset to determine detection level (σ), flux and spectral index. The data sets were divided into pre- and post- T1 relocation and binned in energy and time intervals to produce spectra and lightcurves. The results were then combined to generate complete spectra and lightcurves.

6.12.1. Variability. For each source the VERITAS and Fermi LAT data were divided into short- and long- term timescales to search for significant flaring (large amplitude/short timescales) that would require a separate analysis. Day-long VERITAS and 2 week-long Fermi LAT time periods are referred to as short-term timescales due to the differences in sensitivity of both instruments. Table 6.21 provides a summary of the variability of each source for both instruments on short- and long- term timescales. The majority of the sources analyzed demonstrated evidence for variability in the VERITAS data in short-term timescales and in fact, only W Comae exhibited any significant long-term variability when binned in week-long time intervals: χ^2/n.d.f. = 44.97/13, probability = 2.11×10^{-5}. This variability is also seen in the Fermi LAT biweekly lightcurve with a χ^2/n.d.f. of 142.1/61 and a probability of being at a constant flux of 2.049×10^{-8}. All of the blazars (excluding 3C66A) demonstrate extreme Fermi LAT variability on long-term timescales and 1ES 0502+675, 1ES 0806+524, 1ES 1959+650 and W Comae also display significant short-term variability. 3C66A, apart from a documented flare in October 2009 (Acciari et al., 2009) does not display evidence for variability in either 2 week-long or monthly timescales. With similar results from the VERITAS data, it is reasonable to conclude the source has been in a low activity state for the majority of the analysis period. Due to the limited VERITAS observations and the poor sensitivity of the Fermi LAT to short timescales,

TABLE 6.21. Fermi LAT and VERITAS Detected Flux Variability

Source	VERITAS$_{short}$	VERITAS$_{long}$	Fermi LAT$_{short}$	Fermi LAT$_{long}$
1ES 0502+675	No	No	Yes	Yes*
1ES 0806+524	No	No	Yes	Yes
1ES 1959+650	No	No	Yes	Yes
W Comae	No	Yes	Yes	Yes
3C66A	No	No	No	No
PKS 1424+240	No	No	No	Yes

* month-long timescales indicate variability while 3 month-long do not

it is difficult to conclude with any certainty whether variability timescales or amplitudes are different for each subclass.

6.12.2. Blazar subclass and IC peak correlation. As described in section 6.9, the IC peaks were constrained for all sources (excluding 1ES 0502+675). It is reasonable to assume a correlation between IC peak frequency and blazar subclass, as the IBL synchrotron peak occurs lower in frequency than the HBL (Abdo et al., 2010). Unfortunately, a correlation is not observed with respect to IC emission in this dataset. A possible cause for this is the uncertain redshifts. As the maximum possible redshifts, to ensure the extrapolated Fermi LAT dN/dE spectra (powerlaw) do not turn up in TeV energies, are used to de-absorb the VERITAS spectral points, it is possible the resultant E^2dN/dE de-absorbed TeV spectra are too hard. If this was true, the IC emission peak would appear broader than it actually is, pushing the IC peak higher in frequency. For example, the 3C66A VERITAS E^2dN/dE spectrum was de-absorbed with a redshift of z = 0.03 (the maximum value allowed as explained above) and the E^2dN/dE MeV - TeV spectra is displayed (figure 6.89) showing a maximum at $> 10^{24}$ Hz. An earlier Fermi LAT E^2dN/dE (figure 6.69) fit by a log parabolic curve suggests the peak actually occurs $\sim 10^{23}$ Hz. The TeV spectrum was then deabsorbed for a range of redshifts and a redshift of z=0.05 produced a GeV - TeV curve that peaked at 10^{23} Hz In fact, the Fermi LAT dN/dE spectrum is fit better with a log parabolic curve than a powerlaw indicating the IC turnover is occurring in the Fermi LAT energy range. This is also seen with PKS 1424+240.

The HBL 1ES 0502+675 was the only case where the IC peak could not be constrained. As shown in figure 6.83, the maximum upper limit of z = 0.3 ensures the extrapolated Fermi LAT dN/dE spectrum continues to rise into the TeV energies with no sign of an IC turnover (figure 6.84). Previous publications have estimated the redshift of this source to be at z = 0.341 through the analysis of optical spectra. The result here however, suggests the redshift is highly over-estimated and as a consequence of this, the TeV spectrum is over-corrected for EBL absorption. It is unlikely, the IC frequency turnover is higher energy than demonstrated here, due to effects of the Klein Nishina limit.

There could be, however, a correlation evident between IC peak frequency and blazar subclass in the 3 remaining (known redshifts) blazars, but more sources, better statistics, are required to

verify this. The synchrotron (10^{14} Hz - 10^{16} Hz) and IC peak frequencies (10^{23} Hz) of IBL W Comae are lower than the frequency peaks for the HBLs 1ES 0806+524 ($\upsilon_{synchrotron} = 8 \times 10^{15}$ Hz, $\upsilon_{IC} = 10^{24}$ Hz) and 1ES 1959+650 ($\upsilon_{synchrotron} = 10^{16}$ Hz, $\upsilon_{IC} = 10^{24}$ Hz).

6.12.3. Modeling results. For this dataset the SSC model is a better fit to multiwavelength data over the SSC+EC, except in the case of the 1ES 1959+650 and 3C66A. The interesting modeling results are discussed here.

In the 1ES 1959+650 dataset, the addition of an EC component did improve the fit and would also explain "orphan" TeV flares often seen with this blazar. This would mean that a population of electrons from outside the jet are contributing to the IC emission. W Comae was originally fit best by a SSC +EC model (Acciari et al., 2009) before the addition of the Fermi LAT data. However, to account for the hard Fermi LAT spectrum, the synchrotron peak is overproduced.

Neither model explained the TeV spectrum from 3C66A, while adequately fitting both the synchrotron peak and the Fermi LAT spectrum. While increasing magnetic field strength, Lorentz factor or emitting radius did increase the amplitude (flux) of the IC emission, both the SSC and SSC+EC models did not extend to high enough frequency to describe the TeV data. Increasing these model parameters also led to the synchrotron peak becoming over-produced. The most probable reason behind this is that the uncertain redshift of z = 0.444 (Acciari et al., 2009) is too high. As discussed in section 6.9, the maximum allowed value for the redshift based on the extrapolated Fermi LAT dN/dE spectrum, is z = 0.3. A similar result is described in Acciari et al. (2009). The redshift was then fixed to z=0.05 and the SED was remodeled producing good fits for both the SSC and SSC + EC models. Tables 6.22 provide the SSC and SSC+EC modeling parameters for each source.

The SSC+EC model allows for a lower electron energy density but required a larger emitting radius. Measured short-term timescale variability could constrain the modeling process i.e., the SSC model favors a smaller emitting region which is suggested by flaring activity. As it stands, the emission models to not appear to differ with respect to blazar subclass. In the majority of modeled cases the magnetic field strength is below equipartition. This infers that the condition of minimum power does not hold. The addition of an EC component in the leptonic modeling generally required an lower electron energy density in order to produce the IC spectrum. This brings the magnetic field strength closer to equipartition. From this, it can be inferred that in terms of energy equipartition, the SSC+EC is a closer fit. However, as it is still below equipartition hadronic processes or leptonic-hadronic hybrid processes could be required to accelerate the particles sufficiently.

To conclude, the addition of Fermi LAT data has massively contributed to the constraint of the IC emission. In some of the cases, the IC spectrum is in fact broader than previously expected. Modeling this broad emission leads to an over produced (in frequency) synchrotron peak. This infers an EC component or a multi-zone SSC model may be required.

TABLE 6.22. SSC model fit parameters for each source

Subclass	HBL	HBL	HBL	IBL	IBL	IBL
SSC model parameter	1ES 0502+675	1ES 0806+524	1ES 1959+650	W Comae	PKS 1424+240	3C66A
Bulk Lorentz factor	30	35	35	20	20	35
Magnetic field strength (G)	0.1	0.2	0.12	0.1	0.01	0.4
Radius of emitting volume (m)	2.7×10^{14}	1.8×10^{14}	2.3×10^{14}	2.2×10^{14}	2.45×10^{14}	1.4×10^{14}
Energy Density of electrons (erg cm^{-3})	0.003	0.3	0.1	0.35	0.0005	0.8
SSC +EC model parameter						
Bulk Lorentz factor	30	35	35	20	20	35
Magnetic field strength (G)	0.1	0.2	0.12	0.1	0.01	0.4
Radius of emitting volume (m)	1×10^{15}	7×10^{14}	4.5×10^{14}	5×10^{14}	2.45×10^{14}	2.5×10^{14}
Energy Density of electrons (erg cm^{-3})	0.001	0.005	0.01	0.05	0.0005	0.3

.

The investigation into whether SED modeling is influenced by blazar subclass is inconclusive, largely due to the uncertain redshift values and also due to the fact that the SSC model include only one emitting zone. Possible future steps could involve:

- modeling the SEDs for a range of redshift values for the sources of uncertain redshift
- multi-zone SSC models
- a comparison study of different SSC and SSC+EC models
- hadronic models.

The SED modeling results produced here, though consistent with previously published results, are preliminary. In-depth modeling and interpretation of the results with the aim to distinguish clearly between emission models is beyond the scope of this thesis.

6.12.4. Conclusion. Data from Fermi LAT and VERITAS were analyzed to examine at the spectra and temporal characteristics of each source. Time-averaged spectra were used for both instruments to combine the quasi-simultaneous continuous Fermi LAT observations with spaced-out VERITAS snapshots.

Lightcurves were produced for a range of timescales to search for significant flaring activity, which would have required a separate dedicated analysis. Although extreme variability was observed in the Fermi LAT data, this was the result of flickering in flux with small flux uncertainties and not distinctive flaring. From the comparison of HBL and IBL lightcurves (both Fermi LAT and VERITAS), variability timescales and amplitudes do not differ with each subclass.

Lightcurves were produced to look for correlations in short- and long- term timescales in the lower temporal-sensitivity but continuous, Fermi LAT data and the high sensitivity VERITAS snapshots. Fermi LAT is ideal for studying long-term variability while VERITAS can measured short timescales as short as minutes. Variability was also examined as a function of blazar subclass.

The GeV - TeV spectra for each source was constructed to constrain the IC emission peak and in the case of 1ES 0502+675, 3C66A and PKS 1424+240, to place upper limits on the redshifts. The measured IC peaks were then used with previously published synchrotron emission peaks to investigate if the HBLs had higher frequency peaks than the IBLs. These results were inconclusive due to uncertain redshifts. In fact, the results of this thesis indicate that some of the previously published redshift measurements are inaccurate, in particular in the cases of 3C66A, 1ES 0502+675 and PKS 1424+240. Using available multiwavelength data, broad-band SEDs were constructed. SSC and SSC+EC models were then fit to each SED to determine which model and therefore which emission process fit best and compared to distinguish between emission process for both blazar subclass. All results were then compared with previously published subset results.

CHAPTER 7

Conclusions and Future work

7.1. Thesis results

This thesis presents the analysis and results of an extensive comparison study of HBLs and IBLs. 3 HBLs (1ES 0502+675, 1ES 0806+524 and 1ES 1959+650) and 3 IBLs (W Comae, 3C66A and PKS 1424+240) were selected based on previous results and publications. Quasi-contemporaneous Fermi LAT and VERITAS data for each source were analysis and combined to look closely at spectra.

Lightcurves were produced for a range of timescales to search for significant flaring activity which would have required a separate dedicated analysis. Short- and Long-time timescale lightcurves generated for both instruments, did not show any significant flaring activity for any source. Time-averaged spectra were used for both instruments to combine the quasi continuous Fermi LAT observations with spaced-out VERITAS snapshots. The lightcurves also demonstrate that there are no obvious differences between the variability timescales and amplitudes seen in both subclasses.

For the first time the IC peak can be constrained fully thanks to the addition of Fermi LAT data. This was achieved for all the sources (excluding 1ES 0502+675) by constructing GeV - TeV spectra with Fermi LAT and the de-absorbed VERITAS spectra. The GeV - TeV spectra were then fit with a log parabolic curve and the peak frequency was measured. Due to uncertain and possibly over-estimated redshifts leading to the over-correction of EBL absorption, it is difficult to see if the frequency of the IC peak is different for the blazar subclasses. Constraints on the uncertain redshifts are required to investigate this further. Multiwavlength SEDs were construction for each source and fit with both a homogenous one-zone SSC and an SSC+EC model. The results of this thesis indicate that with the addition of the Fermi LAT MeV - GeV data, a simple one zone SSC model does not actually fit the data adequately, in particular the IC peak. The addition of the EC component does not improve the fit in the majority of cases and although it allows for lower electron energy densities it does require large emitting volumes radii which are not conducive to flaring activity on very short (minutes to hours) timescales. As a consequence of this , the investigation into whether the emission processes differ for each blazar subclass in inconclusive. Possible future steps could involve multi-zone SSC models, hadronic models and leptonic-hadronic hybrid models.

This study highlights the need for high quality simultaneous multiwavelength data from radio to γ-ray energies to aim in distinguishing between emission models. Determining which

emission model fits best is required in order to learn more about the emission process taking place. The emission models also provide information on the surrounding environments, the properties intrinsic to the sources themselves and properties that are characteristic of blazars and blazar subclass.

To conclude, the addition of Fermi LAT data has substantially changed the shape and frequency of the IC emission peak. One-zone SSC and SSC+EC models do not explain the broad-band emission completely. A measured redshift is required for both SED modeling and constraining the IC peak frequency. A larger quantity of contemporaneous multiwavelength data is required to verify this.

7.2. The Future of γ-ray Blazar Science

The collection of knownγ-ray sources has expanded massively since the launch of the Fermi satellite. The 24 months catalog released this year contains 1873 γ-ray source detections with at least 781 of these being associated with blazars. This is a substantial advancement from the third EGRET catalog which contained 27 blazar-associated γ-ray sources (Hartman et al., 1999). Currently, there are at least 2 years of Fermi LAT operations remaining. During that time many more γ-ray blazar discoveries and detections are expected along with on-going monitoring of previously known sources. The survey-mode observations of the LAT means there are continuous MeV - GeV observations of the TeV blazars, important for multiwavelength campaigns and studies.

The VERITAS array has been operating since its first light ceremony in April 2007. During that time, the instrument has partaken in numerous multiwavelength campaigns and follow up observations of interesting activity e.g. the 2008 M87 campaign from radio to γ rays (Wagner et al., 2009). Planned upgrades are due to take place in the near future, such as PMT upgrades, which will increase the sensitivity of the instruments. Currently, analysis and software improvements are underway to extend the energy range to lower energies, increasing the chances of overlap in MeV - GeV and GeV - TeV spectra.

CTA (Cherenkov Telescope Array) is a joint European/U.S. collaboration experiment which is currently in its design and development stage. The experiment will consist of two array of different types of IACT telescopes; one in the northern hemisphere and the second in the southern. The experiment plans to expand the energy range of γ-ray astronomy to $\sim$ 100 TeV with greater stereoscopic imaging, better angular and energy resolution and improved sensitivity of at least one order of magnitude. At present, the proposed design is three sizes of telescope in the southern hemisphere with two in the northern to cover three energy ranges : 10's GeV, 100 GeV - 1 TeV and $>$ 10 TeV. The HAWC (High Altitude Water Cherenkov) experiment is a joint U.S./Mexico collaboration experiment under construction in Sierra Negra, Mexico. The experiment proposes an improvement in sensitivity of as much as 15% with respect to its predecessor Milagro and should be able to detect fluxes of 5 $\times$ crab in 10 minutes making it an impressive instrument for catching blazar flares.

This third generation of TeV γ-ray instruments and the further upgrades to the current generation in addition to the continued Fermi LAT operations ensure that γ-ray astronomy will continue for the foreseeable future. Increasing the γ-ray blazar catalog will lead to population studies, better modeling statistics and multiwavelength correlation studies with respect to spectra and flux varability.

Bibliography

[1] A. A. Abdo, M. Ackermann, M. Ajello, A. Allafort, E. Antolini, W. B. Atwood, M. Axelsson, L. Baldini, J. Ballet, G. Barbiellini, and et al. Fermi Large Area Telescope First Source Catalog. *Astrophysical Journal Supplements*.

[2] A. A. Abdo, M. Ackermann, M. Ajello, W. B. Atwood, M. Axelsson, L. Baldini, J. Ballet, D. L. Band, G. Barbiellini, D. Bastieri, and et al. Fermi/Large Area Telescope Bright Gamma-Ray Source List. *Astrophysical Journal Supplements*, 183:46–66, July 2009.

[3] A. A. Abdo, M. Ackermann, M. Ajello, L. Baldini, J. Ballet, G. Barbiellini, D. Bastieri, K. Bechtol, R. Bellazzini, B. Berenji, and et al. Multi-wavelength Observations of the Flaring Gamma-ray Blazar 3C 66A in 2008 October. *Astrophysical Journal Letters*.

[4] V. Acciari, E. Aliu, T. Arlen, M. Bautista, M. Beilicke, W. Benbow, M. Boettcher, S. M. Bradbury, J. H. Buckley, V. Bugaev, Y. Butt, K. Byrum, A. Cannon, O. Celik, A. Cesarini, Y. C. Chow, L. Ciupik, P. Cogan, P. Colin, W. Cui, R. Dickherber, C. Duke, T. Ergin, A. Falcone, S. J. Fegan, J. P. Finley, G. Finnegan, P. Fortin, L. Fortson, A. Furniss, D. Gall, K. Gibbs, G. H. Gillanders, J. Grube, R. Guenette, G. Gyuk, D. Hanna, E. Hays, J. Holder, D. Horan, C. M. Hui, T. B. Humensky, A. Imran, P. Kaaret, N. Karlsson, M. Kertzman, D. Kieda, J. Kildea, A. Konopelko, H. Krawczynski, F. Krennrich, M. J. Lang, S. LeBohec, G. Maier, A. McCann, M. McCutcheon, J. Millis, P. Moriarty, R. Mukherjee, T. Nagai, R. A. Ong, A. N. Otte, D. Pandel, J. S. Perkins, D. Petry, M. Pohl, J. Quinn, K. Ragan, L. C. Reyes, P. T. Reynolds, E. Roache, J. Rose, M. Schroedter, G. H. Sembroski, A. W. Smith, D. Steele, S. P. Swordy, M. Theiling, J. A. Toner, L. Valcarcel, A. Varlotta, V. V. Vassiliev, R. G. Wagner, S. P. Wakely, J. E. Ward, T. C. Weekes, A. Weinstein, R. J. White, D. A. Williams, S. Wissel, M. Wood, and B. Zitzer. Discovery of Very High Energy Gamma-ray Radiation from the BL Lac 1ES 0806+524. *Astrophysical Journal Letters*, 690:L126–L129, January 2009.

[5] V. A. Acciari, E. Aliu, T. Arlen, T. Aune, M. Bautista, M. Beilicke, W. Benbow, M. Boettcher, D. Boltuch, S. M. Bradbury, and et al. Discovery of Very High Energy Gamma Rays from PKS 1424+240 and Multiwavelength Constraints on Its Redshift. *Astrophysical Journal Letters*, 708:L100–L106, January 2010.

[6] V. A. Acciari, E. Aliu, T. Arlen, M. Beilicke, W. Benbow, M. Boettcher, S. M. Bradbury, J. H. Buckley, V. Bugaev, Y. Butt, K. Byrum, A. Cannon, O. Celik, A. Cesarini, Y. C. Chow, L. Ciupik, P. Cogan, W. Cui, M. K. Daniel, R. Dickherber, T. Ergin, A. Falcone, S. J. Fegan, J. P. Finley, P. Fortin, L. Fortson, A. Furniss, D. Gall, K. Gibbs, G. H. Gillanders, S. Godambe, J. Grube, R. Guenette, G. Gyuk, D. Hanna, E. Hays, J. Holder, D. Horan, C. M. Hui, T. B. Humensky, A. Imran, P. Kaaret, N. Karlsson, M. Kertzman, D. Kieda, J. Kildea, A. Konopelko, H. Krawczynski, F. Krennrich, M. J. Lang, S. LeBohec, G. Maier, A. McCann, M. McCutcheon, J. Millis, P. Moriarty, R. Mukherjee, T. Nagai, R. A. Ong, A. N. Otte, D. Pandel, J. S. Perkins, D. Petry, F. Pizlo, M. Pohl, J. Quinn, K. Ragan, L. C. Reyes, P. T. Reynolds, E. Roache, H. J. Rose, M. Schroedter, G. H. Sembroski, A. W. Smith, D. Steele, S. P. Swordy, M. Theiling, J. A. Toner, A. Varlotta, V. V. Vassiliev, R. G. Wagner, S. P. Wakely, J. E. Ward, T. C. Weekes, A. Weinstein, D. A. Williams, S. Wissel, M. Wood, and B. Zitzer. Veritas Observations of a Very High Energy *gamma*-Ray Flare From the Blazar 3C 66A. *Astrophysical Journal Letters*, 693:L104–L108, March 2009.

[7] V. A. Acciari, E. Aliu, T. Aune, M. Beilicke, W. Benbow, M. Boettcher, D. Boltuch, J. H. Buckley, S. M. Bradbury, V. Bugaev, K. Byrum, A. Cannon, A. Cesarini, L. Ciupik, P. Cogan, W. Cui, R. Dickherber, C. Duke, A. Falcone, J. P. Finley, P. Fortin, L. Fortson, A. Furniss, N. Galante, D. Gall, K. Gibbs, G. H. Gillanders, J. Grube, R. Guenette, G. Gyuk, D. Hanna, J. Holder, C. M. Hui, T. B. Humensky, P. Kaaret, N. Karlsson, M. Kertzman, D. Kieda, A. Konopelko, H. Krawczynski, F. Krennrich, M. J. Lang, S. Le Bohec, G. Maier, S. McArthur, A. McCann, M. McCutcheon, J. Millis, P. Moriarty, R. A. Ong, A. N. Otte, D. Pandel, J. S. Perkins, A. Pichel, M. Pohl, J. Quinn, K. Ragan, L. C. Reyes, P. T. Reynolds, E. Roache, H. J. Rose, G. H. Sembroski, A. W. Smith, D. Steele, M. Theiling, S. Thibadeau, A. Varlotta, V. V. Vassiliev, S. Vincent, S. P. Wakely, J. E. Ward, T. C. Weekes, A. Weinstein, T. Weisgarber, D. A. Williams, S. Wissel, M. Wood, E. Pian, S. Vercellone, I. Donnarumma, F. D'Ammando, A. Bulgarelli, A. W. Chen, A. Giuliani, F. Longo, L. Pacciani, G. Pucella, V. Vittorini, M. Tavani, A. Argan, G. Barbiellini, P. Caraveo, P. W. Cattaneo, V. Cocco, E. Costa, E. Del Monte, G. De Paris, G. Di Cocco, Y. Evangelista, M. Feroci, M. Fiorini, T. Froysland, M. Frutti, F. Fuschino, M. Galli, F. Gianotti, C. Labanti, I. Lapshov, F. Lazzarotto, P. Lipari, M. Marisaldi, M. Mastropietro, S. Mereghetti, E. Morelli, A. Morselli, A. Pellizzoni, F. Perotti, G. Piano, P. Picozza, M. Pilia, G. Porrovecchio, M. Prest, M. Rapisarda, A. Rappoldi, A. Rubini, S. Sabatini, P. Soffitta, M. Trifoglio, A. Trois, E. Vallazza, A. Zambra, D. Zanello, C. Pittori, P. Santolamazza, F. Verrecchia, P. Giommi, S. Colafrancesco, L. Salotti, M. Villata, C. M. Raiteri, H. D. Aller, M. F. Aller, A. A. Arkharov, N. V. Efimova, V. M. Larionov, P. Leto, R. Ligustri, E. Lindfors, M. Pasanen, O. M. Kurtanidze, S. D. Tetradze, A. Lahteenmaki, M. Kotiranta, A. Cucchiara, P. Romano, R. Nesci, T. Pursimo, J. Heidt, E. Benitez, D. Hiriart, K. Nilsson, A. Berdyugin, R. Mujica, D. Dultzin, J. M. Lopez, M. Mommert, M. Sorcia, and I. de la Calle Perez. Multiwavelength Observations of a TeV-Flare from W Comae. *Astrophysical Journal*, 707:612–620, December 2009.

[8] V. A. Acciari, E. Aliu, T. Aune, M. Beilicke, W. Benbow, M. Boettcher, S. M. Bradbury, J. H. Buckley, V. Bugaev, Y. Butt, and et al. Simultaneous Multiwavelength Observations of Markarian 421 During Outburst. *Astrophysical Journal*, 703:169–178, September 2009.

[9] V. A. Acciari, E. Aliu, M. Beilicke, W. Benbow, M. Boettcher, S. M. Bradbury, J. H. Buckley, V. Bugaev, Y. Butt, O. Celik, A. Cesarini, L. Ciupik, Y. C. K. Chow, P. Cogan, P. Colin, W. Cui, M. K. Daniel, T. Ergin, A. D. Falcone, S. J. Fegan, J. P. Finley, G. Finnegan, P. Fortin, L. F. Fortson, A. Furniss, D. Gall, G. H. Gillanders, J. Grube, R. Guenette, G. Gyuk, D. Hanna, E. Hays, J. Holder, D. Horan, C. M. Hui, T. B. Humensky, A. Imran, P. Kaaret, N. Karlsson, M. Kertzman, D. B. Kieda, A. Konopelko, H. Krawczynski, F. Krennrich, M. J. Lang, S. LeBohec, K. Lee, G. Maier, A. McCann, M. McCutcheon, P. Moriarty, R. Mukherjee, T. Nagai, J. Niemiec, R. A. Ong, D. Pandel, J. S. Perkins, D. Petry, M. Pohl, J. Quinn, K. Ragan, L. C. Reyes, P. T. Reynolds, E. Roache, H. J. Rose, M. Schroedter, G. H. Sembroski, A. W. Smith, D. Steele, S. P. Swordy, J. A. Toner, V. V. Vassiliev, R. Wagner, S. P. Wakely, J. E. Ward, T. C. Weekes, A. Weinstein, R. J. White, D. A. Williams, S. A. Wissel, M. Wood, and B. Zitzer. VERITAS Discovery of gt200 GeV Gamma-Ray Emission from the Intermediate-Frequency-Peaked BL Lacertae Object W Comae. *Astrophysical Journal Letters*, 684:L73–L77, September 2008.

[10] F. Aharonian, A. Akhperjanian, J. Barrio, K. Bernloehr, H. Boerst, H. Bojahr, O. Bolz, J. Contreras, J. Cortina, S. Denninghoff, V. Fonseca, J. Gonzalez, N. Goetting, G. Heinzelmann, G. Hermann, A. Heusler, W. Hofmann, D. Horns, A. Ibarra, C. Iserlohe, I. Jung, R. Kankanyan, M. Kestel, J. Kettler, A. Kohnle, A. Konopelko, H. Kornmeyer, D. Kranich, H. Krawczynski, H. Lampeitl, E. Lorenz, F. Lucarelli, N. Magnussen, O. Mang, H. Meyer, R. Mirzoyan, A. Moralejo, L. Padilla, M. Panter, R. Plaga, A. Plyasheshnikov, J. Prahl, G. P"uhlhofer, A. Roehring, W. Rhode, G. Rowell, V. Sahakian, M. Samorski, M. Schilling, F. Schroeder, M. Siems, W. Stamm, M. Tluczykont, H. J. Voelk, C. A. Wiedner, and W. Wittek. Rejection of the Hypothesis That Markarian 501 TEV Photons Are Pure Bose-Einstein Condensates. *Astrophysical Journal Letters*, 543:L39–L42, November 2000.

[11] F. Aharonian, A. Akhperjanian, M. Beilicke, K. Bernloehr, H. Boerst, H. Bojahr, O. Bolz, T. Coarasa, J. Contreras, J. Cortina, L. Costamante, S. Denninghoff, V. Fonseca, M. Girma, N. Goetting, G. Heinzelmann, G. Hermann, A. Heusler, W. Hofmann, D. Horns, I. Jung, R. Kankanyan, M. Kestel, J. Kettler, A. Kohnle, A. Konopelko, H. Kornmeyer, D. Kranich, H. Krawczynski, H. Lampeitl, M. Lopez, E. Lorenz, F. Lucarelli, O. Mang, H. Meyer, R. Mirzoyan, M. Milite, A. Moralejo, E. Ona, M. Panter, A. Plyashesh-nikov, G. P"uhlhofer, G. Rauterberg, R. Reyes, W. Rhode, J. Ripken, G. Rowell, V. Sahakian, M. Samorski, M. Schilling, M. Siems, D. Sobzynska, W. Stamm, M. Tluczykont, H. J. Voelk, C. A. Wiedner, W. Wittek, and R. A. Remillard. Variations of the TeV energy spectrum at different flux levels of Mkn 421 observed with the HEGRA system of Cherenkov telescopes. *Astronomy and Astrophysics*, 393:89–99, October 2002.

[12] J. Aleksi'c, L. A. Antonelli, P. Antoranz, M. Backes, J. A. Barrio, D. Bastieri, J. Becerra Gonz'alez, W. Bednarek, A. Berdyugin, K. Berger, E. Bernardini, A. Biland, O. Blanch, R. K. Bock, A. Boller, G. Bonnoli, D. Borla Tridon, I. Braun, T. Bretz, A. Ca nellas, E. Carmona, A. Carosi, P. Colin, E. Colombo, J. L. Contreras, J. Cortina, L. Cossio, S. Covino, F. Dazzi, A. De Angelis, E. De Cea del Pozo, B. De Lotto, C. Delgado Mendez, A. Diago Ortega, M. Doert, A. Dom'inguez, D. Dominis Prester, D. Dorner, M. Doro, D. Elsaesser, D. Ferenc, M. V. Fonseca, L. Font, C. Fruck, R. J. Garc'ia L'opez, M. Garczarczyk, D. Garrido, G. Giavitto, N. Godinovi'c, D. Hadasch, D. H"afner, A. Herrero, D. Hildebrand, D. Hoehne-Moench, J. Hose, D. Hrupec, B. Huber, T. Jogler, S. Klepser, T. Kr"ahenb"uhl, J. Krause, A. La Barbera, D. Lelas, E. Leonardo, E. Lindfors, S. Lombardi, M. L'opez, E. Lorenz, M. Makariev, G. Maneva, N. Mankuzhiyil, K. Mannheim, L. Maraschi, M. Mariotti, M. Mart'inez, D. Mazin, M. Meucci, J. M. Miranda, R. Mirzoyan, H. Miyamoto, J. Mold'on, A. Moralejo, D. Nieto, K. Nilsson, R. Orito, I. Oya, D. Paneque, R. Paoletti, S. Pardo, J. M. Paredes, S. Partini, M. Pasanen, F. Pauss, M. A. Perez-Torres, M. Persic, L. Peruzzo, M. Pilia, J. Pochon, F. Prada, P. G. Prada Moroni, E. Prandini, I. Puljak, I. Reichardt, R. Reinthal, W. Rhode, M. Rib'o, J. Rico, S. R"ugamer, A. Saggion, K. Saito, T. Y. Saito, M. Salvati, K. Satalecka, V. Scalzotto, V. Scapin, C. Schultz, T. Schweizer, M. Shayduk, S. N. Shore, A. Sillanp"a"a, J. Sitarek, D. Sobczynska, F. Spanier, S. Spiro, A. Stamerra, B. Steinke, J. Storz, N. Strah, T. Suri'c, L. Takalo, F. Tavecchio, P. Temnikov, T. Terzi'c, D. Tescaro, M. Teshima, M. Thom, O. Tibolla, D. F. Torres, A. Treves, H. Vankov, P. Vogler, R. M. Wagner, Q. Weitzel, V. Zabalza, F. Zandanel, R. Zanin, MAGIC Collaboration, Y. T. Tanaka, D. L. Wood, and S. Buson. MAGIC Discovery of Very High Energy Emission from the FSRQ PKS 1222+21. *Astrophysical Journal Letters*, 730:L8+, March 2011.

[13] R. V. Ambartsumian. Book Reviews: A life in astrophycis. Selected papers of Viktor A. Ambartsumian. Edited by Rouben V. Ambartsumian, with an Introduction by Geoffrey Burbidge, Allerton Press, Inc., 150 Fifth Avenue, New York NY 1001, Fax (212) 463-9684. *Astrophysics*, 41:328–330, October 1998.

[14] W. B. Atwood, A. A. Abdo, M. Ackermann, W. Althouse, B. Anderson, M. Axelsson, L. Baldini, J. Ballet, D. L. Band, G. Barbiellini, and et al. The Large Area Telescope on the Fermi Gamma-Ray Space Telescope Mission. *Astrophysical Journal*, 697:1071–1102, June 2009.

[15] W. B. Atwood, R. Bagagli, L. Baldini, R. Bellazzini, G. Barbiellini, F. Belli, T. Borden, A. Brez, M. Brigida, G. A. Caliandro, C. Cecchi, J. Cohen-Tanugi, A. de Angelis, P. Drell, C. Favuzzi, Y. Fukazawa, P. Fusco, F. Gargano, S. Germani, R. Giannitrapani, N. Giglietto, F. Giordano, T. Himel, M. Hirayama, R. P. Johnson, H. Katagiri, J. Kataoka, N. Kawai, W. Kroeger, M. Kuss, L. Latronico, F. Longo, F. Loparco, P. Lubrano, M. M. Massai, M. N. Mazziotta, M. Minuti, T. Mizuno, A. Morselli, D. Nelson, M. Nordby, T. Ohsugi, N. Omodei, M. Ozaki, M. Pepe, S. Rain‘o, R. Rando, M. Razzano, D. Rich, H. F.-W. Sadrozinski, G. Scolieri, C. Sgr‘o, G. Spandre, P. Spinelli, M. Sugizaki, H. Tajima, H. Takahashi, T. Takahashi, S. Yoshida, C. Young, and M. Ziegler. Design and initial tests of the Tracker-converter of the Gamma-ray Large Area Space Telescope. *Astroparticle Physics*, 28:422–434, December 2007.

[16] P. M. S. Blackett. A possible contribution to the night sky from the Cerenkov radiation emitted by cosmic rays. In *The Emission Spectra of the Night Sky and Aurorae*, pages 34–+, 1948.

[17] R. D. Blandford and D. G. Payne. Hydromagnetic flows from accretion discs and the production of radio jets. *Monthly Notices of the Royal Astronomical Society*, 199:883–903, June 1982.

[18] M. Boettcher and J. Chiang. X-ray spectral and variability modeling of low-frequency peaked BL Lac objects. In *American Astronomical Society Meeting Abstracts*, volume 34 of *Bulletin of the American Astronomical Society*, pages 1109–+, December 2002.

[19] E. Bottacini, M. Boettcher, P. Schady, A. Rau, X.-L. Zhang, M. Ajello, C. Fendt, and J. Greiner. Probing the Transition Between the Synchrotron and Inverse-compton Spectral Components of 1ES 1959+650. *Astrophysical Journal Letters*, 719:L162–L166, August 2010.

[20] S. M. Bradbury and H. J. Rose. Pattern recognition trigger electronics for an imaging atmospheric Cherenkov telescope. *Nuclear Instruments and Methods in Physics Research A*, 481:521–528, April 2002.

[21] R. Buehler, F. D'Ammando, A. Cannon, and et al. Fermi LAT detection of a new enhanced gamma-ray emission from the Crab Nebula region. *The Astronomer's Telegram*, 3276:1, 2011.

[22] M. R. Calabretta and E. W. Greisen. Representations of celestial coordinates in FITS. *Astronomy and Astrophysics*, 395:1077–1122, December 2002.

[23] A. Cannon and et al. Fermi LAT detection of increasing gamma-ray activity of blazars PKS 0537-441 and PKS 0301-243. *The Astronomer's Telegram*, 2591:1, 2010.

[24] A. Cannon and et al. Fermi LAT observations of increasing gamma-ray activity of blazar 3C279. *The Astronomer's Telegram*, 2886:1, September 2010.

[25] A. Cannon and et al. Fermi LAT detection of increased gamma-ray activity from blazar S5 0716+71. *The Astronomer's Telegram*, 3487:1, 2011.

[26] G. Cocconi. An air shower telescope and the detection of 10^{12} eV photon sources. In *International Cosmic Ray Conference*, volume 2 of *International Cosmic Ray Conference*, pages 309–+, 1960.

[27] P. Cogan. *Nanosecond Sample of Atmospheric Cherenkov radiation Applied to TeV Gamma-ray Observations of Blazars with VERITAS, PhD thesis, UCD*. 2006.

[28] L. Costamante and G. Ghisellini. TeV candidate BL Lac objects. *Astronomy and Astrophysics*, 384:56–71, March 2002.

[29] C. D. Dermer and Dermer. Blazar jet physics in the age of Fermi. In G. E. Romero, R. A. Sunyaev, T. Belloni, editor, *IAU Symposium*, volume 275 of *IAU Symposium*, pages 111–121, February 2011.

[30] C. D. Dermer and R. Schlickeiser. On the location of the acceleration and emission sites in gamma-ray blazars. *Astrophysical Journal Supplements*, 90:945–948, February 1994.

[31] C. E. Fichtel, R. C. Hartman, D. A. Kniffen, D. J. Thompson, H. Ogelman, M. E. Ozel, T. Tumer, and G. F. Bignami. High-energy gamma-ray results from the second small astronomy satellite. *Astrophysical Journal*, 198:163–182, May 1975.

[32] V. P. Fomin, A. A. Stepanian, R. C. Lamb, D. A. Lewis, M. Punch, and T. C. Weekes. New methods of atmospheric Cherenkov imaging for gamma-ray astronomy. I. The false source method. *Astroparticle Physics*, 2:137–150, May 1994.

[33] G. Fossati, L. Maraschi, A. Celotti, A. Comastri, and G. Ghisellini. A unifying view of the spectral energy distributions of blazars. *Monthly Notices of the Royal Astronomical Society*, 299:433–448, September 1998.

[34] A. Franceschini, G. Rodighiero, and M. Vaccari. Extragalactic optical-infrared background radiation, its time evolution and the cosmic photon-photon opacity. *Astronomy and Astrophysics*, 487:837–852, September 2008.

[35] R. Fr"u'hwirth, M. Regler, R. K. Bock, H. Grote, and D. Notz. *Data Analysis Techniques for High-Energy Physics*. August 2000.

[36] J. A. Gaidos, C. W. Akerlof, S. Biller, P. J. Boyle, A. C. Breslin, J. H. Buckley, D. A. Carter-Lewis, M. Catanese, M. F. Cawley, D. J. Fegan, J. P. Finley, J. B. Gordo, A. M. Hillas, F. Krennrich, R. C. Lamb, R. W. Lessard, J. E. McEnery, C. Masterson, G. Mohanty, P. Moriarty, J. Quinn, A. J. Rodgers, H. J. Rose, F. Samuelson, M. S. Schubnell, G. H. Sembroski, R. Srinivasan, T. C. Weekes, C. L. Wilson,

and J. Zweerink. Extremely rapid bursts of TeV photons from the active galaxy Markarian 421. *Nature*, 383:319–320, September 1996.

[37] W. Galbraith and J. V. Jelley. Light Pulses from the Night Sky associated with Cosmic Rays. *Nature*, 171:349–350, February 1953.

[38] G. Ghisellini and P. Madau. On the origin of the gamma-ray emission in blazars. *Monthly Notices of the Royal Astronomical Society*, 280:67–76, May 1996.

[39] V. L. Ginzburg and S. I. Syrovatskii. Developments in the Theory of Synchrotron Radiation and its Reabsorption. *Annual Review of Astronomy and Astrophysics*, 7:375–+, 1969.

[40] J. L. Greenstein. Red-Shift of the Unusual Radio Source: 3C 48. *Nature*, 197:1041–1042, March 1963.

[41] R. C. Hartman, D. L. Bertsch, S. D. Bloom, A. W. Chen, P. Deines-Jones, J. A. Esposito, C. E. Fichtel, D. P. Friedlander, S. D. Hunter, L. M. McDonald, P. Sreekumar, D. J. Thompson, B. B. Jones, Y. C. Lin, P. F. Michelson, P. L. Nolan, W. F. Tompkins, G. Kanbach, H. A. Mayer-Hasselwander, A. M"ucke, M. Pohl, O. Reimer, D. A. Kniffen, E. J. Schneid, C. von Montigny, R. Mukherjee, and B. L. Dingus. The Third EGRET Catalog of High-Energy Gamma-Ray Sources. *Astrophysical Journal Supplements*, 123:79–202, July 1999.

[42] W. Heitler. *Quantum theory of radiation*. 1954.

[43] W. Hermsen, B. N. Swanenburg, G. F. Bignami, G. Boella, R. Buccheri, L. Scarsi, G. Kanbach, H. A. Mayer-Hasselwander, J. L. Masnou, and J. A. Paul. New high energy gamma-ray sources observed by COS B. *Nature*, 269:494–+, October 1977.

[44] A. M. Hillas. Cerenkov light images of EAS produced by primary gamma. In F. C. Jones, editor, *International Cosmic Ray Conference*, volume 3 of *International Cosmic Ray Conference*, pages 445–448, August 1985.

[45] J. Holder, R. W. Atkins, H. M. Badran, G. Blaylock, S. M. Bradbury, J. H. Buckley, K. L. Byrum, D. A. Carter-Lewis, O. Celik, Y. C. K. Chow, P. Cogan, W. Cui, M. K. Daniel, I. de La Calle Perez, C. Dowdall, P. Dowkontt, C. Duke, A. D. Falcone, S. J. Fegan, J. P. Finley, P. Fortin, L. F. Fortson, K. Gibbs, G. Gillanders, O. J. Glidewell, J. Grube, K. J. Gutierrez, G. Gyuk, J. Hall, D. Hanna, E. Hays, D. Horan, S. B. Hughes, T. B. Humensky, A. Imran, I. Jung, P. Kaaret, G. E. Kenny, D. Kieda, J. Kildea, J. Knapp, H. Krawczynski, F. Krennrich, M. J. Lang, S. Lebohec, E. Linton, E. K. Little, G. Maier, H. Manseri, A. Milovanovic, P. Moriarty, R. Mukherjee, P. A. Ogden, R. A. Ong, D. Petry, J. S. Perkins, F. Pizlo, M. Pohl, J. Quinn, K. Ragan, P. T. Reynolds, E. T. Roache, H. J. Rose, M. Schroedter, G. H. Sembroski, G. Sleege, D. Steele, S. P. Swordy, A. Syson, J. A. Toner, L. Valcarcel, V. V. Vassiliev, S. P. Wakely, T. C. Weekes, R. J. White, D. A. Williams, and R. Wagner. The first VERITAS telescope. *Astroparticle Physics*, 25:391–401, July 2006.

[46] J. Holder, I. H. Bond, P. J. Boyle, S. M. Bradbury, J. H. Buckley, D. A. Carter-Lewis, W. Cui, C. Dowdall, C. Duke, I. de la Calle Perez, A. Falcone, D. J. Fegan, S. J. Fegan, J. P. Finley, L. Fortson, J. A. Gaidos, K. Gibbs, S. Gammell, J. Hall, T. A. Hall, A. M. Hillas, D. Horan, M. Jordan, M. Kertzman, D. Kieda, J. Kildea, J. Knapp, K. Kosack, H. Krawczynski, F. Krennrich, S. LeBohec, E. T. Linton, J. Lloyd-Evans, P. Moriarty, D. M"uller, T. N. Nagai, R. Ong, M. Page, R. Pallassini, D. Petry, B. Power-Mooney, J. Quinn, P. Rebillot, P. T. Reynolds, H. J. Rose, M. Schroedter, G. H. Sembroski, S. P. Swordy, V. V. Vassiliev, S. P. Wakely, G. Walker, and T. C. Weekes. Detection of TeV Gamma Rays from the BL Lacertae Object 1ES 1959+650 with the Whipple 10 Meter Telescope. *Astrophysical Journal Letters*, 583:L9–L12, January 2003.

[47] D. Horan, H. M. Badran, I. H. Bond, S. M. Bradbury, J. H. Buckley, M. J. Carson, D. A. Carter-Lewis, M. Catanese, W. Cui, S. Dunlea, D. Das, I. de la Calle Perez, M. D'Vali, D. J. Fegan, S. J. Fegan, J. P. Finley, J. A. Gaidos, K. Gibbs, G. H. Gillanders, T. A. Hall, A. M. Hillas, J. Holder, M. Jordan, M. Kertzman, D. Kieda, J. Kildea, J. Knapp, K. Kosack, F. Krennrich, M. J. Lang, S. LeBohec, R. Lessard, J. Lloyd-Evans, B. McKernan, P. Moriarty, D. Muller, R. Ong, R. Pallassini, D. Petry, J. Quinn, N. W. Reay, P. T. Reynolds, H. J. Rose, G. H. Sembroski, R. Sidwell, N. Stanton, S. P. Swordy, V. V. Vassiliev, S. P.

Wakely, and T. C. Weekes. Detection of the BL Lacertae Object H1426+428 at TeV Gamma-Ray Energies. *Astrophysical Journal*, 571:753–762, June 2002.

[48] E. P. Hubble. Extragalactic nebulae. *Astrophysical Journal*, 64:321–369, December 1926.

[49] J. V. Jelley. v Cerenkov radiation in the atmosphere. *planss*, 1:105–+, April 1959.

[50] R. W. Klebesadel, I. B. Strong, and R. A. Olson. Observations of Gamma-Ray Bursts of Cosmic Origin. *Astrophysical Journal Letters*, 182:L85+, June 1973.

[51] W. Kraushaar, G. W. Clark, G. Garmire, H. Helmken, P. Higbie, and M. Agogino. Explorer XI Experiment on Cosmic Gamma Rays. *Astrophysical Journal*, 141:845–+, April 1965.

[52] H. Krawczynski, S. B. Hughes, D. Horan, F. Aharonian, M. F. Aller, H. Aller, P. Boltwood, J. Buckley, P. Coppi, G. Fossati, N. Goetting, J. Holder, D. Horns, O. M. Kurtanidze, A. P. Marscher, M. Nikolashvili, R. A. Remillard, A. Sadun, and M. Schroeder. Multiwavelength Observations of Strong Flares from the TeV Blazar 1ES 1959+650. *Astrophysical Journal*, 601:151–164, January 2004.

[53] H. Krawczynski, Working Group on the Status, and F. o. Ground Based Gamma-Ray Astronomy. White Paper On The Status And Future Of Ground-based Gamma-ray Astronomy. In *American Astronomical Society Meeting Abstracts*, volume 38 of *Bulletin of the American Astronomical Society*, pages 874–+, December 2007.

[54] J. H. Krolik. *Active galactic nuclei : from the central black hole to the galactic environment*. 1999.

[55] J. E. Ledden, S. L. Odell, W. A. Stein, and W. Z. Wisniewski. The spectral flux distribution of the candidate BL Lacertae object 1218 + 304 /identically equal to 2A 1219 + 305/. *Astrophysical Journal*, 243:47–52, January 1981.

[56] M. S. Longair. *High Energy Astrophysics*. 2010.

[57] C. D. Mackay. Observations of the structure of radio sources in the 3C catalogue V. The properties of sources in a complete sample. *Monthly Notices of the Royal Astronomical Society*, 154:209–277, 1971.

[58] E. Massaro, M. Maesano, F. Montagni, R. Nesci, G. Tosti, M. Fiorucci, M. Luciani, L. O. Takalo, A. Sillanp"a"a, S. Katajainen, P. Kein"anen, T. Pursimo, M. Villata, C. M. Raiteri, G. de Francesco, G. Sobrito, Y. S. Efimov, and N. M. Shakhovskoy. The extraordinary optical outburst of ON 231 (W Com) in spring 1998. *aap*, 342:L49–L52, February 1999.

[59] J. R. Mattox, D. L. Bertsch, J. Chiang, B. L. Dingus, S. W. Digel, J. A. Esposito, J. M. Fierro, R. C. Hartman, S. D. Hunter, G. Kanbach, D. A. Kniffen, Y. C. Lin, D. J. Macomb, H. A. Mayer-Hasselwander, P. F. Michelson, C. von Montigny, R. Mukherjee, P. L. Nolan, P. V. Ramanamurthy, E. Schneid, P. Sreekumar, D. J. Thompson, and T. D. Willis. The Likelihood Analysis of EGRET Data. *Astrophysical Journal*, 461:396–+, April 1996.

[60] A. A. Moiseev, R. C. Hartman, J. F. Ormes, D. J. Thompson, M. J. Amato, T. E. Johnson, K. N. Segal, and D. A. Sheppard. The anti-coincidence detector for the GLAST large area telescope. *Astroparticle Physics*, 27:339–358, June 2007.

[61] A. A. Moiseev, J. F. Ormes, R. C. Hartman, T. E. Johnson, J. W. Mitchell, and D. J. Thompson. Observation and simulations of the backsplash effects in high-energy *gamma*-ray telescopes containing a massive calorimeter. *Astroparticle Physics*, 22:275–283, November 2004.

[62] T. Nagai, R. McKay, G. Sleege, and et al. Focal Plane Instrumentation of VERITAS. In *International Cosmic Ray Conference*, volume 3 of *International Cosmic Ray Conference*, pages 1437–1440, 2008.

[63] T. Nishiyama. Detection of a new TeV gamma-ray source of BL Lac object 1ES 1959+650. In *International Cosmic Ray Conference*, volume 3 of *International Cosmic Ray Conference*, pages 370–+, August 1999.

[64] R. A. Ong and et al. Discovery of VHE Gamma-Ray Emission from the Fermi-LAT Source 1ES 0502+675. *The Astronomer's Telegram*, 2301:1, November 2009.

[65] D. E. Osterbrock and R. A. R. Parker. Physical Conditions in the Nucleus of the Seyfert Galaxy NGC 1068. *Astrophysical Journal*, 141:892–+, April 1965.

[66] P. Padovani. Unified Schemes and the Two Classes of BL Lacs. In L. O. Takalo A. Sillanp"a"a, editor, *BL Lac Phenomenon*, volume 159 of *Astronomical Society of the Pacific Conference Series*, pages 339–+, 1999.

[67] P. Padovani. The blazar sequence: validity and predictions. *Astrophysics and Space Science*, 309:63–71, June 2007.

[68] P. Padovani and P. Giommi. The ROSAT X-ray spectra of BL Lacertae objects. *Monthly Notices of the Royal Astronomical Society*, 279:526–534, March 1996.

[69] Planck Collaboration, P. A. R. Ade, N. Aghanim, M. Arnaud, M. Ashdown, J. Aumont, C. Baccigalupi, M. Baker, A. Balbi, A. J. Banday, and et al. Planck Early Results: The Planck mission. *ArXiv e-prints*, January 2011.

[70] J. Poutanen and B. E. Stern. Fermi Observations of Blazars: Implications for Gamma-ray Production. *ArXiv e-prints, 1109.0946*, September 2011.

[71] M. Punch, C. W. Akerlof, M. F. Cawley, M. Chantell, D. J. Fegan, S. Fennell, J. A. Gaidos, J. Hagan, A. M. Hillas, Y. Jiang, A. D. Kerrick, R. C. Lamb, M. A. Lawrence, D. A. Lewis, D. I. Meyer, G. Mohanty, K. S. O'Flaherty, P. T. Reynolds, A. C. Rovero, M. S. Schubnell, G. Sembroski, T. C. Weekes, and C. Wilson. Detection of TeV photons from the active galaxy Markarian 421. *Nature*, 358:477–+, August 1992.

[72] J. Quinn, J. Buckley, T. C. Weekes, M. Catanese, D. A. Carter-Lewis, F. Krennrich, R. C. Lamb, J. Zweerink, C. W. Akerlof, D. Meyer, M. Schubnell, J. Gaidos, G. Sembroski, C. Wilson, D. J. Fegan, R. Lessard, J. McEnery, M. F. Cawley, S. Biller, A. M. Hillas, A. Rodgers, and J. Rose. Markarian 501. *iaucirc*, 6178:1–+, June 1995.

[73] R. Rando and for the Fermi LAT Collaboration. Post-launch performance of the Fermi Large Area Telescope. *ArXiv e-prints, 0907.0626*, July 2009.

[74] P. F. Rebillot, J. H. Buckley, P. Dowkontt, and K. Kosack. The VERITAS Flash ADC Electronics System. In *International Cosmic Ray Conference*, volume 5 of *International Cosmic Ray Conference*, pages 2827–+, July 2003.

[75] P. T. Reynolds, C. W. Akerlof, M. F. Cawley, M. Chantell, D. J. Fegan, A. M. Hillas, R. C. Lamb, M. J. Lang, M. A. Lawrence, D. A. Lewis, D. Macomb, D. I. Meyer, G. Mohanty, K. S. O'Flaherty, M. Punch, M. S. Schubnell, G. Vacanti, T. C. Weekes, and T. Whitaker. Survey of candidate gamma-ray sources at TeV energies using a high-resolution Cerenkov imaging system - 1988-1991. *Astrophysical Journal*, 404:206–218, February 1993.

[76] E. Roache, R. Irvin, J. S. Perkins, and et al. Mirror Facets for the VERITAS Telescopes. In *International Cosmic Ray Conference*, volume 3 of *International Cosmic Ray Conference*, pages 1397–1400, 2008.

[77] C. Sauty, K. Tsinganos, and E. Trussoni. Jet Formation and Collimation. In A. W. Guthmann, M. Georganopoulos, A. Marcowith, K. Manolakou , editor, *Relativistic Flows in Astrophysics*, volume 589 of *Lecture Notes in Physics, Berlin Springer Verlag*, pages 41–+, 2002.

[78] J. F. Schachter, J. T. Stocke, E. Perlman, M. Elvis, R. Remillard, A. Granados, J. Luu, J. P. Huchra, R. Humphreys, C. M. Urry, and J. Wallin. Ten new BL Lacertae objects discovered by an efficient X-ray/radio/optical technique. *Astrophysical Journal*, 412:541–549, August 1993.

[79] M. Schmidt. 3C 273 : A Star-Like Object with Large Red-Shift. *Nature*, 197:1040–+, March 1963.

[80] J. L. Schmitt. BL Lac identified as a Radio Source. *Nature*, 218:663–+, May 1968.

[81] C. K. Seyfert. Five thousand external galaxies and a new dense group. *The Astronomical Journal*, 53:203–+, 1948.

[82] M. Sikora and G. Madejski. On Pair Content and Variability of Subparsec Jets in Quasars. *Astrophysical Journal*.

[83] H. Sol, G. Pelletier, and E. Asseo. Two-flow model for extragalactic radio jets. *Monthly Notices of the Royal Astronomical Society*, 237:411–429, March 1989.

[84] H. C. Spruit. Magnetohydrodynamic jets and winds from accretion disks. In R. A. M. J. Wijers, M. B. Davies, C. A. Tout, editor, *NATO ASIC Proc. 477: Evolutionary Processes in Binary Stars*, pages 249–286, 1996.

[85] F. W. Stecker, O. C. de Jager, and M. H. Salamon. Predicted Extragalactic TeV Gamma-Ray Sources. *Astrophysical Journal Letters*, 473:L75+, December 1996.

[86] B. N. Swanenburg, K. Bennett, G. F. Bignami, R. Buccheri, P. Caraveo, W. Hermsen, G. Kanbach, G. G. Lichti, J. L. Masnou, H. A. Mayer-Hasselwander, J. A. Paul, B. Sacco, L. Scarsi, and R. D. Wills. Second COS B catalog of high-energy gamma-ray sources. *Astrophysical Journal Letters*, 243:L69–L73, January 1981.

[87] M. Theiling. *Observations of very high energy gamma-ray emission from supervova remnants with VERTIAS, PhD thesis, Clemson university*. 2009.

[88] D. J. Thompson, D. L. Bertsch, C. E. Fichtel, R. C. Hartman, R. Hofstadter, E. B. Hughes, S. D. Hunter, B. W. Hughlock, G. Kanbach, D. A. Kniffen, Y. C. Lin, J. R. Mattox, H. A. Mayer-Hasselwander, C. von Montigny, P. L. Nolan, H. I. Nel, K. Pinkau, H. Rothermel, E. J. Schneid, M. Sommer, P. Sreekumar, D. Tieger, and A. H. Walker. Calibration of the Energetic Gamma-Ray Experiment Telescope (EGRET) for the Compton Gamma-Ray Observatory. *Astrophysical Journal Supplements*, 86:629–656, June 1993.

[89] K. E. Turver and T. C. Weekes. Gamma-ray astronomy from 10 to 100 GeV. *Nuovo Cimento B Serie*, 45:99–108, May 1978.

[90] Y. Uchida and K. Shibata. Magnetodynamical acceleration of CO and optical bipolar flows from the region of star formation. *Publications of the Astronomical Society of Japan*, 37:515–535, 1985.

[91] C. M. Urry and P. Padovani. Unified Schemes for Radio-Loud Active Galactic Nuclei. *Publications of the Astronomical Society of the Pacific*, 107:803–+, September 1995.

[92] C. M. Urry and P. Padovani. The Unification of Radio-Loud AGN. In R. D. Ekers, C. Fanti, L. Padrielli, editor, *Extragalactic Radio Sources*, volume 175 of *IAU Symposium*, pages 379–+, 1996.

[93] P. A. v Cerenkov. Visible Radiation Produced by Electrons Moving in a Medium with Velocities Exceeding that of Light. *Physical Review*, 52:378–379, August 1937.

[94] L. Valcarcel. *VERITAS, 1ES 1218 + 30.4 and the Extragalactic Background Light, PhD thesis, McGill University*. 2008.

[95] A. E. Vladimirov, S. W. Digel, G. J'ohannesson, P. F. Michelson, I. V. Moskalenko, P. L. Nolan, E. Orlando, T. A. Porter, and A. W. Strong. GALPROP WebRun: An internet-based service for calculating galactic cosmic ray propagation and associated photon emissions. *Computer Physics Communications*, 182:1156–1161, May 2011.

[96] J. E. Ward. *VERITAS Survey of the Cygnus Region of the Galactic Plane, PhD thesis, UCD*. 2010.

[97] T. C. Weekes. *Very high energy gamma-ray astronomy*. 2003.

[98] T. C. Weekes. TeV Gamma-ray Astronomy: The Story So Far. In F. A. Aharonian, W. Hofmann, F. Rieger, editor, *American Institute of Physics Conference Series*, volume 1085 of *American Institute of Physics Conference Series*, pages 3–17, December 2008.

[99] T. C. Weekes, M. F. Cawley, D. J. Fegan, K. G. Gibbs, A. M. Hillas, P. W. Kowk, R. C. Lamb, D. A. Lewis, D. Macomb, N. A. Porter, P. T. Reynolds, and G. Vacanti. Observation of TeV gamma rays from the Crab nebula using the atmospheric Cerenkov imaging technique. *Astrophysical Journal*, 342:379–395, July 1989.

[100] A. Weinstein. The VERITAS Trigger System. In *International Cosmic Ray Conference*, volume 3 of *International Cosmic Ray Conference*, pages 1539–1542, 2008.

[101] R. J. White, H. J. Rose, S. M. Bradbury, and et al. The VERITAS Digital Asynchronous Transceiver. In *International Cosmic Ray Conference*, volume 3 of *International Cosmic Ray Conference*, pages 1527–1530, 2008.

[102] R. Winston. Light Collection within the Framework of Geometrical Optics. *Journal of the Optical Society of America (1917-1983)*, 60:245–+, February 1970.

[103] D. M. Worrall and B. J. Wilkes. X-ray spectra of compact extragalactic radio sources. *Astrophysical Journal*, 360:396–407, September 1990.

APPENDIX A

Astronomer's Telegrams

Fermi LAT detection of increasing gamma-ray activity of blazars PKS 0537-441 and PKS 0301-243

ATel #2591; *A. Cannon (University College Dublin, NASA/GSFC) on behalf of the Fermi Large Area Telescope Collaboration*
on 30 Apr 2010; 19:37 UT
Credential Certification: Teddy Cheung (ccheung@milkyway.gsfc.nasa.gov)

Subjects: Gamma Ray, >GeV, AGN

Referred to by ATel #: 2610

The Large Area Telescope (LAT), one of the two instruments on the Fermi Gamma-ray Space Telescope, has observed over 27th and 28th April 2010, increasing gamma-ray activity in sources positionally consistent with PKS 0537-441 (1FGL J0538.8-4404) and PKS 0301-243 (1FGL J0503.5-2406).

PKS 0537-441 (z=0.894, Peterson et al. 1976, ApJ, 207, L5) is one of the most variable BL Lac objects. Preliminary analysis indicates that the source gradually brightened over the previous weeks. On 27th April 2010, the source peaked at a daily gamma-ray flux (E>100MeV) of (1.2+/-0.2)x10^-6 ph cm-2 s-1, reaching a 6 hr peak flux of (2.0+/-0.7)x10^-6 ph cm-2 s-1 (statistical uncertainty only). Similar activity was previously reported in ATEL #1759 (October 2008) and ATEL #2124 (July 2009).

PKS 0301-243 (RA:03h03m26.50s Dec:-24d07m11.3s, J2000, Healey et al., 2007 ApJS, 171, 61) is also a BL Lac with redshift z=0.26 (Falomo et al 1993 AJ, 106, 11). It is a steep spectrum radio source with spectral index ~ -0.5. Fermi LAT observations indicate a daily flux (E>100MeV) of (1.4+/-0.3)x10^-6 ph cm-2 s-1 on 28th April 2010, with a peak 6 hr flux of (2.0+/-0.6)x10^-6 ph cm-2 s-1, which is ~40x larger than the average flux for this source over the first 11 months of LAT operation (arXiv:1002.2280v1). This is the first Fermi ATEL on this source.

Because Fermi operates in an all-sky scanning mode, regular gamma-ray monitoring of these sources will continue. In consideration of the ongoing activity of these sources we strongly encourage multiwavelength observations. The Fermi LAT contact persons for these sources are Gino Tosti (tosti@pg.infn.it) for PKS 0537-441 and Dave J. Thompson (David.J.Thompson@nasa.gov) for PKS 0301-243.

The Fermi LAT is a pair conversion telescope designed to cover the energy band 20 MeV to greater than 300 GeV. It is the product of an international collaboration between NASA and DOE in the U.S. and many scientific institutions across France, Italy, Japan and Sweden.

FIGURE A.1. Fermi LAT detection of increasing gamma-ray activity of blazars PKS 0537-441 and PKS 0301-243

Fermi LAT observations of increasing gamma-ray activity of blazar 3C279

ATel #2886; *A. Cannon (University College Dublin, NASA/GSFC), on behalf of the Fermi Large Area Telescope Collaboration*
on 29 Sep 2010; 22:54 UT
Distributed as an Instant Email Notice Transients
Credential Certification: Teddy Cheung (ccheung@milkyway.gsfc.nasa.gov)

Subjects: Gamma Ray, >GeV, Blazar

The Large Area Telescope (LAT), one of the two instruments on the Fermi Gamma-ray Space Telescope, has observed over 27th and 28th September 2010, a sharp increase in gamma-ray activity from the blazar 3C279.

Preliminary analysis indicates that the source rapidly reached a daily flux (E>100MeV) of (3.9+/-1.4) x10^-6 ph cm^-2 s^-1 on the 27th (errors are statistical only), more than a factor of 4 greater than reported in the Fermi-LAT 1st year catalog (1FGL J1256.2-0547, Abdo et al. 2010, ApJS 188, 405). This intense gamma-ray flare follows a slowly increasing trend during the course of the last month. The source was detected again on the 28th with a daily flux (E>100MeV) of (2.0+/-0.1) x10^-6 ph cm^-2 s^-1.

This well-known blazar, classified as a flat spectrum radio quasar (FSRQ), has a redshift of 0.536 (Marziani et al. ApJS, 1996, 104, 37). Increased gamma-ray activity from this source was previously reported in Atel #2154 (August 2009) and Atel #1864 (December 2008).

The Fermi-LAT contact people for this source are Greg Madejski (madejski@slac.stanford.edu) and Masaaki Hayashida (mahaya@slac.stanford.edu). Because Fermi operates in an all-sky scanning mode, regular gamma-ray monitoring of this source will continue. In consideration of the ongoing activity of this source we strongly encourage multiwavelength observations.

The Fermi LAT is a pair conversion telescope designed to cover the energy band from 20 MeV to greater than 300 GeV. It is the product of an international collaboration between NASA and DOE in the U.S. and many scientific institutions across France, Italy, Japan and Sweden.

FIGURE A.2. Fermi LAT observations of increasing gamma-ray activity of blazar 3C279

Fermi LAT detection of a new enhanced gamma-ray emission from the Crab Nebula region

ATel #3276; *R. Buehler (SLAC/KIPAC), F. D'Ammando (INAF-IASF Palermo, CIFS), A. Cannon (University College Dublin, NASA/GSFC) on behalf of the Fermi Large Area Telescope Collaboration*

on 12 Apr 2011; 16:21 UT
Distributed as an Instant Email Notice Transients
Credential Certification: Rolf Buehler (buehler@slac.stanford.edu)

Subjects: Gamma Ray, >GeV, Neutron Star, Transient, Pulsar

Referred to by ATel #: 3279, 3282, 3283, 3284, 3286

The Large Area Telescope (LAT), one of the two instruments on the Fermi Gamma-ray Space Telescope, has observed a renewed increase of the gamma-ray activity from a source positionally consistent with the Crab Nebula in the period April 9-11, 2011.

Preliminary LAT analysis indicates that the gamma-ray emission (E >100 MeV) observed at the location of the Crab Nebula started to increase on 9 April with a flux of (4.7 +/- 0.6) x10^-6 ph/cm2/sec (only statistical errors are given), and a peak in the period between 2011-04-11 05:59:58 UT and 2011-04-11 23:44:56 UT of (5.7 +/- 0.7) x10^-6 ph/cm2/sec, corresponding to an increase of a factor of 2 with respect to the average flux from the direction of the Crab nebula of (2.9 +/- 0.1) x10^-6 ph/cm2/sec, estimated for the entire Fermi operation period. All given fluxes are the sum of the pulsar and nebula emission.

A gamma-ray flux increase from the direction of the Crab Nebula was reported previously by the AGILE and LAT collaborations in September 2010 (ATel #2855 and ATel #2861). We strongly encourage further multifrequency observations of that region. For this source the Fermi LAT contact person is Rolf Buehler (buehler@stanford.edu).

The Fermi LAT is a pair conversion telescope designed to cover the energy band from 20 MeV to greater than 300 GeV. It is the product of an international collaboration between NASA and DOE in the U.S. and many scientific institutions across France, Italy, Japan and Sweden.

FIGURE A.3. Fermi LAT detection of a new enhanced gamma-ray emission from the Crab Nebula region

Fermi LAT detection of increased gamma-ray activity from blazar S5 0716+71

ATel #3487; *A. Cannon (University College Dublin, GSFC) on behalf of the Fermi Large Area Telescope Collaboration*
on 15 Jul 2011; 13:42 UT
Credential Certification: Filippo D'Ammando (filippo.dammando@iasf-roma.inaf.it)

Subjects: Gamma Ray, >GeV, Request for Observations, AGN, Black Hole, Blazar

The Large Area Telescope (LAT), one of two instruments on-board the Fermi Gamma-ray Space Telescope, has observed an increase in gamma-ray activity from a source positionally coincident with the Low-frequency BL Lac object S5 0716+71 (also known as 1FGL J0721.9+7120, Abdo et al. 2010, ApS, 188, 405; R.A.= 07h21m53.4484s, Dec.=+71d20m36.363s, J2000, Johnston et al. 1995, AJ 110, 880). Nilsson et al. (2008, A&A 487, L29) derived a photometric redshift for this source of z = 0.31+/- 0.08.

Preliminary analysis indicates that the source on July 12th, 2011, was detected in a high state with an average daily flux (E>100 MeV) of (1.4+/-0.3)x10^-6 ph cm^-2 s^-1 (statistical uncertainty only), peaking with a flux (E>100 MeV) of (2.6+/-0.7)x10^-6 ph cm^-2 s^-1 in the 6-hour interval starting at 12:00 UT of the same day. The source continued to be bright on July 13th, 2011, with a similar average daily flux (E>100 MeV) of (1.4+/-0.2) x10^-6 ph cm^-2 s^-1. This represents a greater than one order of magnitude increase in flux with respect to the average flux reported in the first Fermi LAT catalog (Abdo et al. 2010, ApS, 188, 405) and is the first flare from this source reported by Fermi. The source was also observed on July 9th and 10th, 2011, with average daily fluxes of (0.7+/-0.2) x10^-6 ph cm^-2 s^-1 and (0.9+/-0.2) x10^-6 ph cm^-2 s^-1, respectively.

Because Fermi operates in an all-sky scanning mode, regular gamma-ray monitoring of this source will continue. In consideration of the activity of this source we strongly encourage multiwavelength observations. The Fermi LAT contact person for this source is D. Bastieri (bastieri@pd.infn.it).

The Fermi LAT is a pair conversion telescope designed to cover the energy band from 20 MeV to greater than 300 GeV. It is the product of an international collaboration between NASA and DOE in the U.S. and many scientific institutions across France, Italy, Japan and Sweden.

FIGURE A.4. Fermi LAT detection of increased gamma-ray activity from blazar S5 0716+71